PROEFSCHRIFT

ter verkrijging van de graad van doctor

aan de Technische Universiteit Delft,

op gezag van de Rector Magnificus Prof. ir. K. C. A. M. Luyben,

voorzitter van het College voor Promoties,

in het openbaar te verdedigen op 11-03-2015 om 12.30 uur

door

Andrea FORZONI

Master of Science, Earth Sciences VU Amsterdam

geboren te Pistoia, Italië.

Dit proefschrift is goedgekeurd door de promotoren:

Prof. Dr. S.M. Luthi.

Dr. J.E.A. Storms

Samenstelling promotiecommissie:

Rector Mangificus	voorzitter
Prof. Dr. S.M. Luthi	Delft University of Technology, promotor
Dr. J.E.A. Storms	Delft University of Technology, co-promotor
Prof. Dr. Tom Coulthard	University of Hull
Prof. Dr. William Helland-Hansen	University of Bergen
Prof. Dr. Ir. Marcel Stive	Delft University of Technology
Prof. Dr. Jakob Wallinga	University of Wageningen
Prof. Dr. Ronald van Balen	Vrije Universiteit Amsterdam
Prof. Dr. Giovanni Bertotti	Delft University of Technology

Contents

CHAPTER 1

Introduction

1.1. Relevance

How are climatic, sea-level, and tectonic histories transmitted across a river system and how are they recorded in the stratigraphic record? What is the impact of the changing boundary conditions on fluvio-deltaic stratigraphy? These are still outstanding questions in the fields of geomorphology and stratigraphy and have both a scientific and a commercial relevance. Investigating and quantifying sediment erosion, transport and deposition processes in present day river systems and sedimentary basins is the key, in actualistic terms, for reconstructing climatic, tectonic, and sea-level histories of the past, which are written in the stratigraphic record. Furthermore, by modelling river systems response to forcing, we can better predict the impact of climatic changes and sea-level rise on the hydrologic and sedimentary evolution of river deltas, and on human infrastructures and activities. Finally, understanding the evolution of river systems is crucial for predicting the stratal architecture and the properties of sedimentary basins in the sub-surface, which is one of the key challenges in the hydrocarbon and shallow and deep subsurface engineering industries.

1.2. Background and open questions

River systems are the key motor in delivering water and sediments to the ocean. Sediments are mainly produced in the upland part of river systems, where chemical and mechanical processes degrade and erode rocks. The fresh sediments are transported towards rivers, which carry them downstream either in suspension, solution or as bedload. Sediments can get transported, accumulated and again remobilized several times during their years-to-millennia downstream journey, on hillslopes, within channels, in floodplains, and in river deltas, before reaching their final sink in a deep marine environment. The major natural controls on this journey, called source-to-sink, are tectonics, climate, and sea-level. Tectonic processes creates topography and allows gravitational processes to operate. Climate furnishes the energy (water and heat) to modify and degrade topography, produce and transport

sediments. Base-level is the main control on accommodation, which is the amount of space available for sediments to be accumulated. At the end of the journey to the sink, the pattern in which sediments are distributed and accumulated in river deltas is controlled by accommodation, a function of sea-level and subsidence, sediment supply from rivers, and marine processes, i.e. waves and tides.

The impact of external forcing on river systems has been extensively investigated by geomorphologists and stratigraphers during the last decades, by interpreting field data (Busschers et al., 2007; Vis et al., 2008; Whittaker et al., 2009), and simulating natural processes with numerical and analogue models (Tucker and Slingerland, 1997; Muto and Steel, 2004; Syvitski and Milliman, 2007). Although surface processes are qualitatively well understood, it is still difficult to quantify them, with a reasonable level of uncertainty, on a geological time scale. River systems are often called complex systems because of their non-linear response to forcing (Coulthard and Van De Wiel, 2007; Jerolmack and Paola, 2010). First, the non-linearity is caused by the fact that it takes times for perturbations to be transmitted across the river system (Gaudemer and Metivier, 1999; Allen, 2008). These perturbations are either the upstream migration of tectonic-induced incision, or the downstream migration of a climate-induced high sediment pulse. Consequently the response of the system is delayed and buffered (Fig. 2). Second, the system is affected by thresholds or tipping points, beyond which the system response is no longer proportional to the perturbation, such as the threshold for bedrock incision on channel beds (Wiel and Coulthard, 2010). Third, a large amount of variability in sediment flux from river systems is caused by autogenic processes, such as avulsions and bed armouring.

Consequently, in order to predict the sediment flux to river deltas and to better read the external forcing history from the stratigraphic record it is important to incorporate the non-linear response of river systems to forcing into both conceptual and numerical models. At the same time, it is equally important to work with models of reduced complexity. This becomes fundamental the farther we move back in the geological past, because it is often very difficult to constrain past boundary conditions (climate, tectonics, base-level). Models should be simple, or better, simple enough to simulate only the first order processes with a reasonable processing time, and the level of output precision should be comparable to the level of uncertainty of the required input.

1.3. Objective and approach

The objectives of this PhD project are (i) to develop and apply a numerical catchment model to simulate the transient landscape and sediment flux response of river systems to external forcing, and (ii) to investigate and disentangle sea level and sediment supply histories in fluvio-deltaic stratigraphy. First, a catchment model, PaCMod, was developed and tested on three river systems: the Waipaoa (New Zealand), the Meuse (the Netherlands) and the Celano, (Italy). PaCMod was then applied to reconstruct the sedimentary history of a well-studied, Late Quaternary river system, the Golo (Corsica, France). Modelling results were compared to new sediment ages, and topographic, sedimentological, and geophysical data acquired in the field, to investigate the impact of climate, sea-level, and tectonic forcing on the geomorphic and stratigraphic evolution of the Golo river system. Finally, the architecture and the heterogeneities of a Cretaceous river delta, the Panther Tongue (Utah, USA) were studied by means of outcrop observations, stratigraphic logs correlation, and petrological analysis of rock samples. These stratigraphic data on the Panther Tongue form the basis for current and future work with forward and inverse stratigraphic model to quantify the impact of sediment supply and sea-level change on stratigraphic architecture.

1.4. Background on numerical modelling

The simplest approach to simulate river systems processes is represented by spatially lumped models, which are based on spatially averaged parameters representing the behaviour of the system in time (e.g., Bogaart and van Balen, 2000; Syvitski and Milliman, 2007). A more advanced and complex approach is a two-dimensional landscape evolution or cellular model (e.g., Tucker and Slingerland, 1997; Coulthard et al., 200), where all variables are functions of time and spatial coordinates. However, the generally poor control on palaeo-climate and catchment morphology hampers the applicability of cellular models, as they require a high level of input detail, which is usually unavailable the further we move back in time. In contrast, reduced complexity models, with one or zero spatial dimensions, are more parsimonious with the required input, computation, and output resolution, and they produce results that have the same resolution as the input boundary conditions. Lumped and one-dimensional models usually focus on a single set of geomorphic processes, such as the evolution of a fluvial longitudinal profile (Kirby and Whipple, 2001), and they rely on important assumptions, such that they may not fully replicate the internal dynamics of the system that we know to be important

(cf. Armitage et al., 2011; Rohais et al., 2012). Nevertheless, they are useful tools to investigate catchment evolution and sediment flux in ancient settings, where parameters have a high degree of uncertainty, or where long timescales are considered (10^5–10^7 a).

By developing PaCMod, an attempt was made to bridge the gap between cellular and spatially-lumped approaches, by using the maximum level of simplicity necessary for palaeo-applications, and by a process-response approach to simulate the transient response of landscape morphology to external forcing. PaCMod calculates long time series of water and sediment flux from any given catchment. The key aspects of the first version of the model is the parameterization of sediment routing and storage in the catchment (Chapter 2). The three-dimensional morphology of a real catchment was collapsed into four spatial domains, where different processes occur and sediment is routed and temporarily stored: hillslopes, fluvial network, catchment lower reaches, and catchment outlet. In the second version of the model the model was implemented with new routines to simulate the evolution of landscape morphology and erosion rates under tectonic and climatic forcing (Chapter 3).
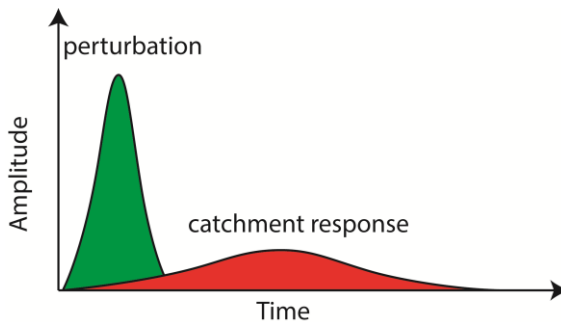
Figure 1.1: Conceptual model of delayed and buffered response of a catchment to an external perturbation (from Metivier and Gaudemer, 1999)

1.5. Background on the Golo River System

The Golo river system (Corsica, France) was chosen as modern system to apply and test PaCMod. Because of its small size, the well constrained coastal and offshore sedimentary archives, and the limited storage area within the catchment, the Golo River system is an excellent laboratory to investigate the transmission of climatic and eustatic sea level fluctuations across a fluvial system. The Golo has received significant attention from academia and industry during the last decade. Research has focused mainly on the geometries of the deep-marine basin floor fans, the final

sink of the system. More recently the whole source-to-sink system was investigated to understand the pattern of sediment dispersal and the mechanisms controlling alluvial and marine stratigraphy (Somme et al., 2011; Calves et al., 2013).

The Golo River is the main fluvial system on the island of Corsica. The present day rugged relief of the catchment is a result of the recent phase of regional uplift (Plio-Quaternary), which rejuvenated the Miocene low-relief landscape (Fellin et al., 2005). Terraced remnants of ancient floodplains and alluvial fans are preserved in the Marana Plain, the alluvial-coastal plain bordering the Tyrrhenian Sea (Somme et al., 2011). Here, the Golo River accumulated thick conglomeratic wedges during the Late Pleistocene (Conchon, 1972; Skyles, 2003) and repeatedly incised into these deposits, as a result of tectonic uplift, climatic and sea-level changes (Somme et al., 2011). These coarse braidplain deposits are organized in a cut-and-fill pattern, with the younger units located at progressively lower topographic levels.

The Marana Plain was the area of two fieldwork campaigns, in collaboration with colleagues from the TU Delft, IFREMER, Brest, and the Netherlands Center for Luminescence dating NCL (Wageningen). The field data included geophysical data (S-wave reflection seismics, seismic interferometry, electro-magnetic profiles), sedimentological observations (outcrops, cores), and sediment dating (optical stimulated luminescence OSL and radiocarbon ^{14}C). The 4D model of the Marana Plain, constructed integrating all the data, was compared to numerical simulations with PaCMod, in order to investigate the relative impact of climate and sea-level changes on the Golo fluvial system (Chapter 4). This 4D model forms a good conditioning dataset for the ongoing and future work with stratigraphic modeling.

1.6. Background on the Panther Tongue, Utah, USA

After developing PaCMod and studying a relatively well-constrained fluvial system, the Golo, the focus of the research project switched to the sediment sink, and in particular, to an ancient deltaic system with poorly-constrained boundary conditions, the Panther Tongue delta on the Wasatch Plateau (Utah, USA). The Panther Tongue was chosen because its continuous exposures, sub-parallel to the regional depositional strike of deltaic shorelines, allow reconstructing the stratigraphic architecture and the along-strike variability of the deltaic system.
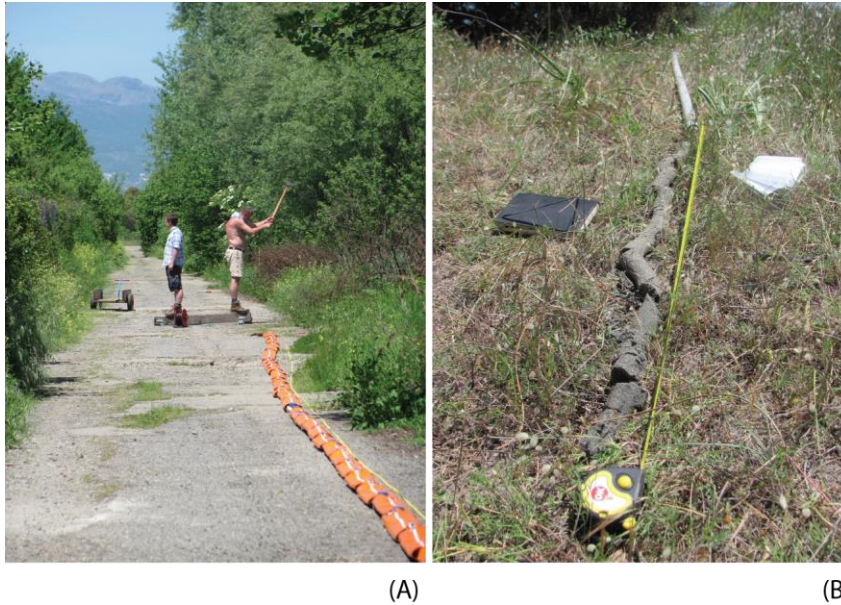
Figure 1.2: Two examples of field techniques used in the fieldwork campaign in Corsica. (A) S-wave seismics using a 96 m length array of geophones as reveivers and a manually operated active source. (B) Sediment cored using the Van der Staay corer and described in the field.

Based on detailed outcrop studies in the northern Wasatch Plateau, the Panther Tongue is considered a typical fluvial-dominated river delta, which is used as a potential analogue for hydrocarbon reservoirs. Although it is interpreted to record forced regression (Posamentier and Morris, 2000; Hwang and Heller, 2002), the architecture of the Panther Tongue as a coastal system and the heterogeneities on the spatial scale of the whole Wasatch Plateau are still poorly understood. In the final part of this research project, the 3D architecture of the Panther Tongue deltaic system was characterized, with special emphasis on the connection between the different sedimentary environments within the stratigraphic units. During a two-weeks fieldwork campaign stratigraphic logs were recorded and rock samples were collected. The stratigraphic logs were correlated with previous literature and wireline log, and the samples were analysed with thin sections, CT-scans and XRF (X-ray fluorescence). The stratigraphic architecture and the lithological properties of the Panther Tongue are the basis for current and future research with forward and inverse numerical modelling.

1.7. Thesis outline

The structure of this thesis follows three parallel paths through space and time. First, the structure represents the chronological order of the PhD project workflow. Second, it follows a spatial shift in focus, migrating from the upstream part of the catchment, the sediment source, towards the river delta, the sediment sink. Third, it forms a path back in time, from Holocene river systems with a well-constrained evolution, to Pleistocene and then Cretaceous river systems, whose evolution is poorly constrained.

In chapter 2 the numerical model PaCMod and its testing on the present-day Waipaoa and the Meuse River are described. The integration of PaCMod with new routines for catchment transient response to climate and tectonics and the application of the model to the tectonically-perturbed Celano catchment, are the focus of chapter 3. Chapter 4 presents field data and modelling work on the Golo River system. Chapter 5 describes the architecture and the heterogeneities of the Cretaceous Panther Tongue coastal system. Finally, in chapter 6, a synthesis is made of the findings from the previous chapters, and lines for potential future research are presented.
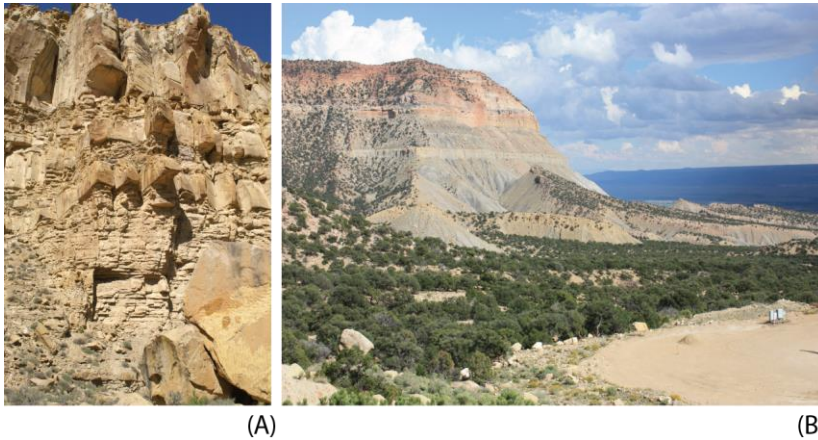
Figure 1.3: Ksp040 field impression from (A) Muddy Creek and (B) Des Bee Dove Mine
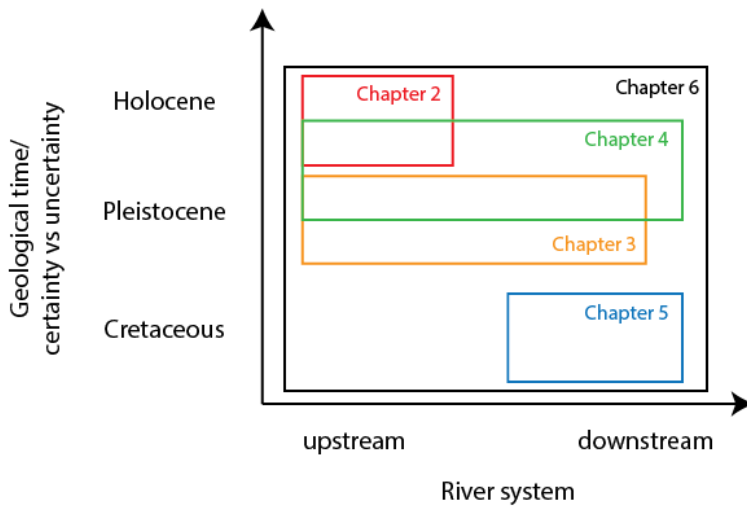
Figure 1.4: Thesis outline conceptual scheme showing the relation between the different chapters to geological time and to the position within a river system

CHAPTER 2

PaCMod: a spatially lumped model to investigate downstream sediment flux propagation within a fluvial catchment

Abstract. A spatially lumped process-response model, PaCMod, is presented, which calculates long time series (thousands to million years) of fluvial water discharge and sediment load at the river catchment outlet, based on climatic data, drainage basin characteristics and user-defined parameters. Key aspects of the model are (i) the lumped approach, allowing for fast simulations and preserving the same resolution from palaeoclimatic conditions and geomorphological reconstructions; (ii) the parameterization of sediment routing and storage within the catchment. PaCMod was successfully tested on observed data from three present-day fluvial systems: the Meuse, the Waipaoa, and the Po Rivers. Moreover, the simulated sediment flux for the Meuse and for the Waipaoa Rivers in the late Quaternary is in agreement with published field and modeling work. PaCMod experiments show how the downstream propagation of the original climatic signal is hampered by sediment routing and storage within the catchment.

2.1 Introduction

Understanding the effects of palaeoclimate forcing on catchment sediment yield and on basin stratigraphy is still an outstanding research objective in sedimentary geology. Numerical simulations have shown that Quaternary climatic changes produced clear sediment flux pulses (e.g., Tucker and Slingerland, 1997; Tebbens et al., 2000a; Kettner et al., 2009; van Balen et al., 2010). Sediment budgeting works have indicated that, for certain source-to-sink systems, the sediment flux signal is preserved in the stratigraphic record (e.g., Busschers et al., 2007; Vis et al., 2008; Somme et al., 2011), while for other systems it is lacking or strongly buffered (e.g., Trimble, 1977; Metivier and Gaudemer, 1999; Phillips, 2003; Brommer et al., 2009).

The role of sediment supply in basin stratigraphy has received more and more attention in the last decades because understanding the palaeo sediment supply fluxes can provide a better interpretation of the available core and seismic data and can help interpretation at the parasequence and event-bed scale (Blum and Törnqvist, 2000; Hampson and Storms, 2003; Blum and Aslan, 2006; Helland-Hansen and Hampson, 2009; Charvin et al., 2011; Holbrook and Bhattacharya, 2012). Numerical simulations of fluviodeltaic and shoreface-shelf systems have clearly shown a relation between sediment supply and stratal response (Hampson and Storms, 2003; Storms and Swift, 2003; Kubo et al., 2006; Charvin et al., 2011). This implies that we are able to detect a climatic signal in marine stratigraphy, but we still poorly understand the modification of such signal during its downstream propagation toward the marine domain.

The simplest approach to simulate catchment processes is a spatially lumped model, which is based on spatially averaged parameters representing the behavior of the system in time (e.g. Weltje et al., 1998; Bogaart and van Balen, 2000; Bogaart et al., 2003; Syvitski and Milliman, 2007; Kettner and Syvitski, 2008). A more advanced and complex approach is a two-dimensional landscape evolution model (e.g., Tucker and Slingerland, 1997; Whipple and Tucker, 1999; Coulthard et al., 2002; Armitage et al., 2011) where all dependent variables are functions of time and spatial coordinates. These models include internal catchment dynamics, such as landscape thresholds, sedimentation and erosion waves propagation that contribute to the generation as well as intra catchment modification and dampening of a climatic or tectonic signal (Walling, 1982; Phillips and Slattery, 2006; Coulthard and Van De Wiel, 2007; Whittaker et al., 2010; Armitage et al., 2011).

The generally poor control on palaeoclimate and catchment morphology hampers the applicability of two-dimensional models, as they require a high level of input detail, which is usually unavailable the further we move back in time. Spatially lumped models produce results that have the same resolution as the input boundary conditions instead. As such, they could be used for palaeo settings for which catchment properties and climate reconstructions are poorly known. However, because of the spatial lumping, they do not simulate catchment memory, i.e. the inheritance of previous climatic and morphologic conditions, which is enhanced by sediment routing and storage.

We have developed a spatially lumped model, PaCMod, that simulates time series of fluvial water discharge and sediment load from any given catchment. It combines new modeling algorithms and parameterizations for environmental response to climatic changes, sediment routing, and storage (catchment memory) with existing and modified routines from Hydrotrend (Syvitski et al., 1998; Kettner and Syvitski, 2008) and PALAEOFLOW (Bogaart et al., 2003a). The aims of this paper are (i) to describe the new modeling technique, its potential and limitations; (ii) to test the model on real-world present-day and late Pleistocene—Holocene cases, and (iii) to investigate how the sediment flux signal is generated, transmitted, and buffered in a river drainage system.

2.2. PaCMod outline

A schematic overview of the PaCMod modeling approach is shown in Fig. 2.1. The main inputs are climatic conditions and catchment properties. We define the catchment as the upland, mainly erosional part of a drainage basin in which sedimentation occurs only temporarily, as alluvial fans, confined floodplains, and channel deposits. PaCMod consists of three connected routines operating at different timescales: the long-term routine, the epochs routine, and the yearly routine.

In the long-term routine, the long-term climatic and environmental boundary conditions are defined. We consider the long-term climate as a series of discrete points in time, which we call epochs. The spacing between epochs (typically 500-1000 years) is based on the discreteness of the palaeoclimatic proxies data and on computational demand. For each epoch (epochs routine), PaCMod performs short simulations (10-30 years) at a daily timescale, producing daily weather conditions (*weather module*) and river discharge values (*hydrological module*). In addition, erosion rates, long-term suspended load, and channel pattern are calculated for each epoch

based on average environmental conditions (*erosion module and channel pattern module*).

Spatial domains	Sediment reservoirs	Processes	Memory
Hillslopes	Regolith	Erosion	Climate and weather history
Fluvial network	Fine /Coarse fraction Qfines'/Qcoarse'	Selective transport	Bedload routing
Catchment lower reaches	Confined floodplain / Fluvial Terraces	Accumulation and incision	Sediment storage
Catchment outlet	Suspended Bedload load	Fluvial transport	

Figure 2.1: Schematic overview of PaCMod modeling approach. The three-dimensional morphology of a real catchment is collapsed into four spatial domains where different processes occur and sediment is routed and temporary stored. The processes occurring in the catchment operate simultaneously but at different time scales (e.g., decennia to millennia for hillslope erosion and days for fluvial transport). Therefore the model structure is composed of three different routines working at different timescales.

Finally, the yearly routine interpolates the daily values obtained from the epochs routine over the whole simulation timespan on a yearly scale. A long time series of fluvial water discharge is generated, and the bedload transport capacity is calculated for each time step (*discharge and transport capacity module*). The sediment supply from hillslopes, the suspended sediment load, and the bedload transport capacity are eventually balanced in a global sediment transport module (*sediment balance module*).

2.2.1 Long-term routine

In the long-term routine, the climatic boundary conditions (temperature and precipitation), derived from palaeoclimate proxies, are related to three

environmental parameters: vegetation cover *Veg*, soil holding capacity H_c, and runoff/ infiltration coefficient *R/I*. We define *Veg* as the area of the catchment covered by arboreal species (0-1); H_c is defined as the amount of water that can be held by soils (mm); and *R/I* is defined as the ratio (0-1) between overland flow and water that infiltrates under the surface (Bogaart et al, 2003a). The relation between total annual precipitation P_a (mm/ y) and *Veg* is modeled as a logarithmic function, with the constant of proportionality set by the coefficient *v*1. The relation between mean annual temperature T_a (°C) and *Veg* is treated as a Gaussian function (Eq. 2.1), similar to Weltje et al. (1998), with a thermal optimum set by the coefficient *v*2 (Fig. 2.2A).
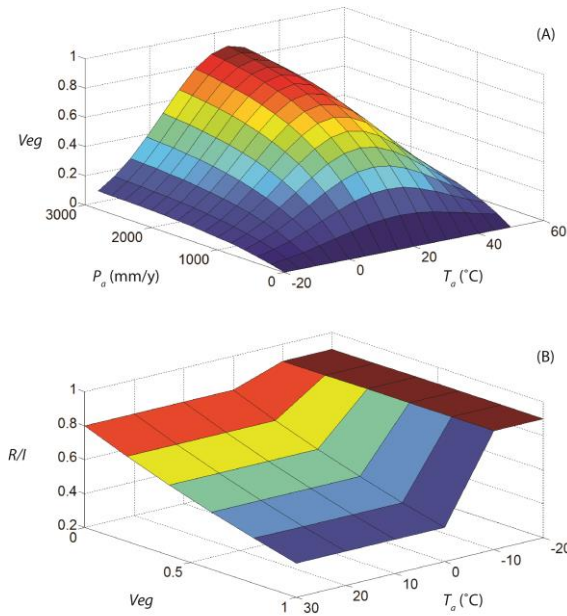
Figure 2.2: (A) Vegetation cover as a function of temperature (°C) and annual precipitation (mm/ y); (B) *R/I* coefficient as a function of temperature and vegetation cover (0-1). The values of the user-defined coefficients are: *v*1 (0.001), *v*2 (20), *v*3 (20), *x*1 (0.5), *x*2 (0.2), *x*3 (0.01), and x4 (0.03).

$$Veg = \left(-\frac{1}{e^{(v1 \cdot P_a)}} + 1\right) \cdot \left(\frac{e^{-(T_a - v2)^2}}{2 \cdot v3^2}\right) \tag{2.1}$$

H_c is assumed to be directly related to vegetation cover (Weltje et al., 1998) with a range of 0-100 mm (Bogaart et al., 2003a). The *R/I* is modeled as inversely proportional to vegetation cover (Eq. 2.2) and directly proportional to temperature, when $T_a > 0°C$. For $T_a < 0°C$ we assumed a value of 0.9 for *R/I* based on Bogaart (2003a). In this way we simulate the effect of permafrost (or soil frost), which inhibits the infiltration capacity (Fig. 2.2B) (Couture and Pollard, 2007).

$$R/I = x1 - Veg^{x2} + x3^{x4 \cdot Ta} \tag{2.2}$$

for $T_a > 0°C$

where $v3$, $x1$, $x2$, $x3$, and $x4$ are user-defined coefficients.

2.2.2. Epochs routine

Weather module and hydrological module

Values of daily temperature, precipitation, vegetation cover, soil storage capacity, and *R/I* ratio conditions are created by a weather module that adds seasonal and synoptic variations to the average climatic signal (Bogaart and van Balen, 2000; Bogaart et al, 2003a) (see appendix A). Precipitation may be water or snow, depending on elevation and temperature. In the model, the precipitation that infiltrates under the surface can contribute to the soil water reservoir. The soil water reservoir can lose water by evapotranspiration and by infiltration to a deep groundwater reservoir. The actual evapotranspiration is a function of the availability of water in the soil water reservoir and of the potential evaporation. The fluvial water discharge at the outlet of the river catchment is calculated as the daily sum of superficial runoff, snowmelt and base flow from the groundwater. A flow diagram of the hydrological module is shown in Fig. 2.3.

The algorithms used in the weather and hydrological module are based on Bogaart and van Balen (2000). Yet, we modified them in order to consider hypsometry and for nonuniform distribution of precipitation, which are major controls on volumes and timing of water discharge pulses, particularly for high relief catchments. Because palaeotemperature reconstructions usually refer to sea level, we need to account for elevation to obtain representative temperature values for the whole catchment. PaCMod calculates daily temperature, precipitation, and ratio between snow and rain for 10 hypsometric classes (see Appendix B).
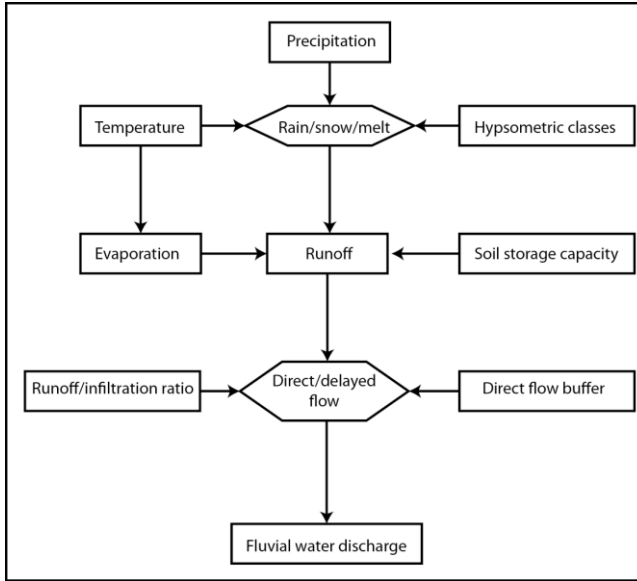
Figure 2.3: Flow diagram of the hydrological module (within the Epochs routine). Arrows indicate input/ output relation between model components.

Precipitation data is based on present-day observations from weather stations, which are generally located at low altitudes. However, most of the precipitation occurs at higher altitudes. To correct for this, we calculate an extra amount of precipitation (*EP*) for every hypsometric class as a function of precipitation gradient P_g (mm d^{-1} m^{-1}), i.e. the increase of precipitation with altitude *H* (m) (Eq. 2.3):

$$EP = P_g \cdot H \tag{2.3}$$

The P_g can be calibrated on present-day precipitation data. Daily potential evaporation *PET* (mm d^{-1}) is calculated following the Linacre method (Eq. 8 in Linacre, 1977). The delay of the peak discharge with respect to a precipitation event is calculated using the user-defined direct flow buffer parameter, which can be calibrated using real-world precipitation and discharge data. Finally, PaCMod calculates the river bankfull discharge (m^3 s^{-1}) Q_p as the average peak discharge for each epoch.

Erosion module

Erosion in a catchment occurs through different processes (e.g. rill and gully erosion, soil creep, mass wasting) in different parts of the catchment and with specific rates (Tucker and Slingerland, 1997). The spatial distribution and intensity

of these processes is predominantly controlled by local hillslope angle and vegetation cover (Bogaart et al., 2003b). We apply the method proposed by Zhang (2002) to calculate the long-term average soil erosion rate (mm y^{-1}) (Eq. 2.4),

$$E = K_{soil} \cdot runoff^2 \cdot S_h^{1.67} + e^{7 \cdot Veg} \tag{2.4}$$

where K_{soil} is a coefficient for soil erodibility, *runoff* is the mean long-term predicted runoff (mm d^{-1}), S_h is the average hillslope angle, and *Veg* is the mean vegetation cover. The K_{soil} can be calculated based on soil properties (USDA) or calibrated when all other variables in Eq. (2.4) are known. Regolith eroded from hillslopes is transported by the river discharge as bedload or suspended load. Suspended load is coupled to fluvial discharge, while bedload is delayed in the fluvial channel, depending on the drainage system morphology and on the grain size. In PaCMod, bedload is modeled as the balance between sediment supply from hillslopes and bedload transport capacity (section 2.3.2). The long-term potential suspended load is calculated with the BQART equation (based on Eq. 7 in Syvitski and Milliman, 2007; Kettner and Syvitski, 2008):

$$Q_s = BQ'ART \tag{2.5}$$

Here, Q_s (kg s^{-1}) is the long-term potential suspended load, R is maximum relief (km), T is the average temperature (°C), A is the catchment area (km^2), Q' is the long term-average fluvial discharge (m^3 s^{-1}), and B is a coefficient that incorporates the effect of glacial erosion and outcropping lithology. Equation (2.4) and (2.5) assume unlimited availability of regolith on hillslopes. To account for regolith availability, we apply the BQART equation as a potential suspended load transport capacity; the long-term potential suspended load Q_s and E can be compared by introducing a term E' (kg s^{-1}):

$$E' = E/N \cdot A \cdot \rho_s \tag{2.6}$$

where N is the number of seconds in one year, A is the catchment area, and ρ_s is the average sediment density that we assume to be 2700 kg m^{-3}. The calculated potential suspended load Q_s can exceed E'. In such case, we assume that Eq. (2.5) is overpredicting the suspended load. The actual long-term suspended load Q_{fines}' is a fraction (0.9) of E', because suspended load generally accounts for most of of the total sediment load (Summerfield and Hulton, 1994; Burbank and Anderson, 2008; Kettner and Syvitski, 2008). When $Q_s < E'$ then $Q_{fines}' = Q_s$. The fraction of coarse

sediment derived from hillslope erosion E available for bedload transport, Q_{coarse}, is calculated as the difference between total erosion from hillslopes and actual long-term suspended load (Eq. 2.7):

$$Q_{coarse\prime} = E\prime - Q_{fines\prime} \tag{2.7}$$

2.2.3.   *Channel pattern module*

For each epoch, PaCMod predicts the river channel pattern in the lower reaches of the catchment using Millar's (2000) approach. A braided channel pattern is assumed to develop when the river gradient exceeds a critical gradient S_c (Eq. 2.8), and vice versa for a meandering pattern:

$$S_c = 0.0002 \cdot BS^{1.75} \cdot D_{50}^{0.61} \cdot Q_p^{-0.25} \tag{2.8}$$

where Q_p is bankfull discharge (m^3 s^{-1}), D_{50} is the average grain size (mm), and BS is the river bank friction angle (°) that is defined as

$$BS = 20 + 0.5 \cdot Veg \cdot 100 \tag{2.9}$$

Vegetation has a stabilizing effect on river banks. The coefficients linking BS to average vegetation cover *Veg* were calibrated based on Millar (2000). We have applied the lowermost (20.1°) and the maximum value (79.1°) of bank friction angle in Millar (2000) to represent respectively 0% and 100% vegetation cover. With this approach we did not consider the impact of lithology on bank friction angle.

2.2.3.   **Yearly routine**

Discharge and transport capacity module

In the discharge and transport capacity module, we apply an upscaling method that captures long-term signal and extreme events. For each epoch, the main statistics are extracted (water discharge, suspended load, erosion rate, and fluvial channel pattern), and then interpolated over the whole simulation period. We chose four values to represent the statistical distribution of water discharge: peak discharge, average-low discharge, and their associated standard deviations. We refer to peak discharge as the average (over the epoch duration) yearly maximum discharge and to average-low discharge as the average discharge below the long term average (Fig. 2.4).
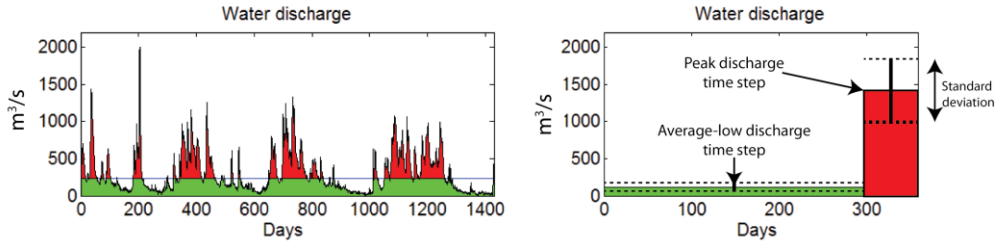
Figure 2.4. (Left) Meuse River water discharge above (red) and below (green) the long-term average (240 m^3/s) for four years (1980-1983). Based on this data, the average peak discharge, the average-low discharge, and the number of days with peak or average-low discharge are calculated. (Right) Two yearly time steps: average-low discharge and peak discharge time step. The number of days with peak or average-low discharge (Fig. 2.5A) determines the length of the two time steps.

In this way two time steps per year are modeled: the peak and the average-low discharge. The average length of the two time steps is determined based on present-day measurements (Fig. 2.4A) or on the reconstructed daily time series. A time series of yearly average, low-average, and peak discharge is generated stochastically from the statistical distribution of water discharge. The kind of distribution (exponential, normal, logarithmic) is user-defined and can be constrained by measurement data. The bedload transport capacity of the river TC is based on the bed shear stress (Tucker and Slingerland, 1997) and particle critical shear stress (USACE, 2007) approach (see Appendix C).

Sediment balance module

We interpolate the long-term actual suspended load Q_{fines}, to calculate the actual suspended load for each time step Q_{fines}, applying Morehead et al., (2003) formula:

$$\frac{Q_{fines}}{Q_{fines}'} = \psi \cdot \left(\frac{Q}{Q'}\right)^C \tag{2.10}$$

where Q is the water discharge per time step. All units are in m^3 s^{-1}; Ψ and C are coefficients based on catchment temperature, relief, and average discharge (Morehead et al., 2003).

The long-term coarse fraction of the material eroded from hillslopes, Q_{coarse}', is not directly available for transport in the catchment lower reaches, because it takes time

(10^2-10^4 years) for coarse sediment to be delivered from the hillslopes to the fluvial channel and then to the lower reaches (Tebbens and Veldkamp, 2000; Veldkamp and Tebbens, 2001; Coulthard et al., 2002; van Balen et al., 2010). The transport of coarse sediment is a diffusive process that buffers the downstream propagation of the hillslope erosion signal (Trimble, 1977; Walling, 1983; Meade, 1982; Church and Slaymaker, 1989; Frostick and Jones, 2002; Coulthard et al., 2005). The buffering effect is also enhanced by the mixing of different sediment sources within the catchment and by the slow movement of coarse sediments within the channel itself where transport is predominantly occurring during peak discharge periods.

We assume that hillslope erosion occurs only in the upper reaches of the catchment, and we define the lower reaches as the most downstream portion of the catchment, near the outlet, where sediment can be stored in confined floodplains, valley fill, and alluvial fans. In PaCMod we use a scaling parameter K_d to simulate bedload routing and hence delay in sediment transport downstream (Eq. 2.11):

$$Q_b = K_d \cdot Q_{coarse'} \tag{2.11}$$

where Q_b is the sediment available for bedload transport in the lower reaches of the catchment. The lower reaches of catchments provide accommodation space for sediment accumulation on confined floodplains, in case sediment availability prevails over fluvial transport capacity *TC*. Such confined floodplains may become incised when erosion capacity increases, and previously deposited sediments may be reworked. In addition, patches of such floodplain deposits may become preserved as fluvial terraces (Merrits et al., 1994; Blum and Törnqvist, 2000, Leigh et al., 2004; Blum and Aslan, 2006; Leigh, 2008). In PaCMod the actual availability of coarse-grained sediments for transport, $Q_{bactual}$, is the sum of the delayed bedload supply from hillslopes Q_b, added to a portion of the sediment n_1 previously stored in a confined floodplain reservoir R_v, in case floodplain deposition has occurred (Eq. 2.12).

$$Q_{bactual} = Q_b + n_1 \cdot R_v \tag{2.12}$$

The bedload leaving the catchment $Q_{bedload}$ equals $Q_{bactual}$ when $Q_{bactual}$ is exceeded by *TC*. Oppositely, when *TC* is lower than $Q_{bactual}$, $Q_{bedload}$ equals *TC* (Eq. 2.13):

$$when \; TC > Q_{bactual} \quad Q_{bedload} = Q_{bactual} \quad R_v = 0 \qquad (2.13)$$

$$when \; TC < Q_{bactual} \quad Q_{bedload} = TC \qquad R_v = Q_{bactual} - TC$$

In addition, PaCMod accounts for a constant fraction n_2 of the sediments stored in R_v that are never reworked and become part of a terrace reservoir R_t (Eq. 2.14):

$$R_t = n_2 \cdot R_v \qquad (2.14)$$

Our parameterized approach relies on some important assumption: (i) the coefficient n_1 and n_2 remain constant in time, (ii) bedload is represented only by D_{50}, and (iii) the fluvial channel gradient, like the hillslope angle, remains constant in time. The model results are sensitive to these assumptions. Using coefficient n_1 and n_2 constant in time implies that the geometry and the dimension of floodplains remains constant in time. This may result in an overestimation of sediment storage during periods of fluvial incision and consequent floodplain narrowing. The opposite may occur in the case of increase in accommodation leading to floodplain widening and enhaced sediment storage. Using assumption (ii) we did not consider temporal changes in bedload grain size and possible multimodal grain size distributions. Finally, assumption (iii) is valid in the case of catchment morphology in equilibrium with the tectonic regime. In addition, this approach neglects the changes in fluvial channel gradient and hillslope angle induced by climatic, tectonic, and eustatic changes. The impact of climatic and tectonic changes on catchment morphology is dealt with in chapter 3.

2.3. Tests
2.3.1. Hydrograph

PaCMod hydrological routines were tested on three present-day fluvial systems: the Meuse River in the Netherlands, the Po River in Italy, and the Waipaoa River in New Zealand. Meteorological data (Table 2.1) and catchment physiographic properties (Hydro1K digital elevation model) were used as input. We averaged precipitation and temperature from two weather stations in each catchment and corrected for altitude. The modeled hydrograph was compared to measured water discharge, and it was optimized by tuning the user-defined parameters: groundwater residence time, precipitation gradient, snowmelt coefficient, and direct flow buffer parameter (Table 2.2).

Table 2.1: input data and sources of information for the hydrograph calibration

River	Weather stations	Gauging station	Period	Data source
Meuse	Maastricht (NL) Luxemburg (L)	Borgharen	1980-2009	KNMI Rijswaterstaat
Waipaoa	Gisborne Waitangirua	Kanakanaia	1986-1991	NIWA TUTIEMPO.net
Po	Bologna (IT) Lugano (CH)	Pontelagoscuro	1950-1979	KNMI Rijswaterstaat
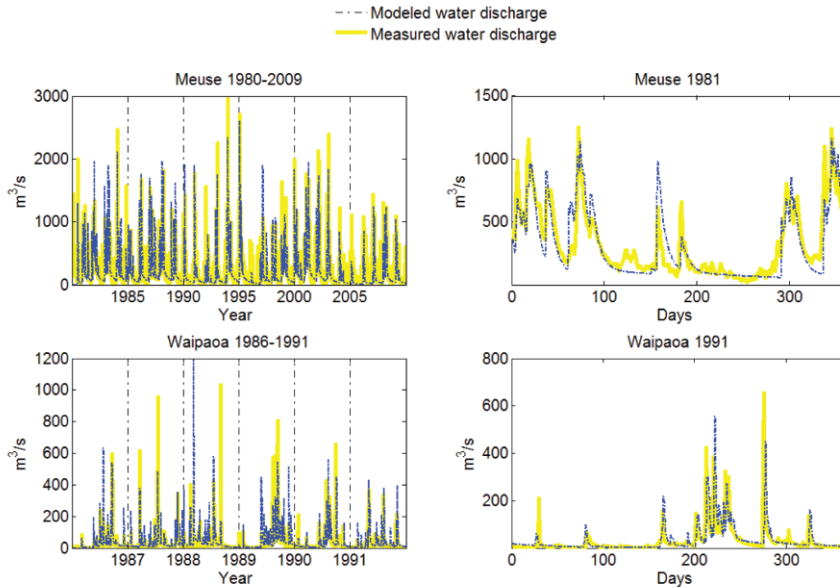
Figure 2.5: Daily measured and modeled water discharge of the Meuse River and of the Waipaoa River.
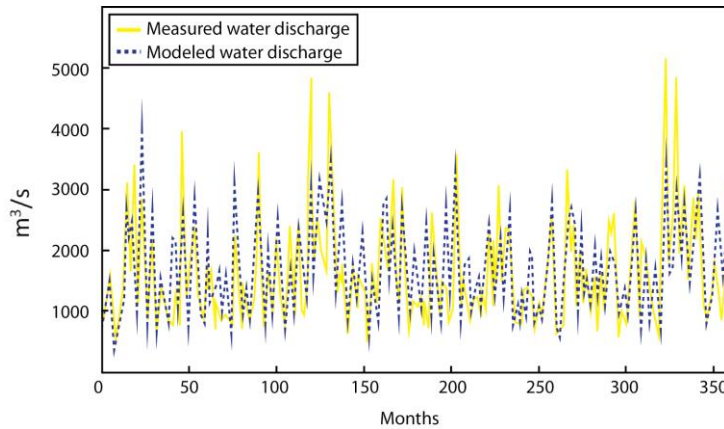
Figure 2.6: Monthly water discharge of the Po River during 30 years (1950-1979).

Table 2.2: Calibrated parameters for the three analyzed catchments

Parameter	Meuse	Waipaoa	Po	Unit
Precipitation gradient	10^{-4}	10^{-7}	10^{-4}	mm d^{-1} m^{-1}
Snowmelt coefficient	0,08	0,1	0,1	mm d^{-1} °C^{-1}
Groundwater residence time	400	90,0	1000,0	d
Direct flow buffer	8	2,0	15,0	d

PaCMod can be calibrated in such a way that it is able to simulate a realistic hydrograph for all the analyzed rivers based on only two weather stations (Figs. 2.5-2.7). The peaks in water discharge, which are influenced by superficial runoff, and the general decreasing trend after such peaks, which is influenced by base flow, are well represented. The main discrepancies between modeled and measured discharge, occurring during periods of very high and very low discharge, can be explained by the lack of spatial information for local storms. The probability and the magnitude of precipitation events can be very different from place to place across the catchment, and such heterogeneity cannot be captured by a spatially lumped model. In addition, the presence of dams affects the hydrograph by temporal storage and release of water in artificial reservoirs, which is not included in the model.
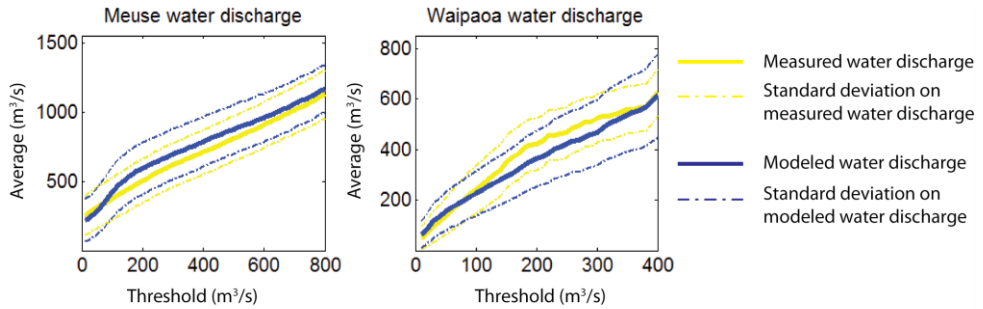
Figure 2.7: Average daily water discharge above a water discharge threshold. We calculated the average water discharge (vertical axis) of the days, when water discharge was above a defined threshold (horizontal axis), and the standard deviation on the average. We used these statistics to compare measured and modeled water discharge for the Meuse River and for the Waipaoa River.

2.3.2. Sediment flux

We tested PaCMod performance applying it to the late Quaternary fluvial development of two river systems, the Meuse River and the Waipaoa River, both well documented in terms of geomorphological evolution, sediment flux, and palaeoclimatic conditions.

Meuse River

We ran a 20-ky simulation from the late Pleniglacial to the present, based on palaeoclimatic proxies (Table 2.3; Fig. 2.8) and catchment morphology (Fig. 2.9). We applied a bedload travel time K_d of 1 ky, based on Veldkamp and Tebbens (2001) and van Balen et al. (2010). PaCMod simulated high delayed bedload supply (Q_{coarse}') and hillslopes erosion rate during cold phases (Fig. 2.11A), because of low vegetation cover and high runoff/ infiltration ratio. Simulated erosion rates varied between 0.005 to 0.05 mm y^{-1}, which is in the same range as the long-term erosion rates calculated with cosmogenic nuclides for the last 20 ky (van Balen et al., 2010) (0.014-0.08 mm/ y). The simulated bedload and suspended load supply were out of phase between 14 and 8 ky BP. During the late Pleniglacial and the Younger Dryas, bedload supply exceeded suspended load supply, while the opposite occurred during early Bølling-Allerød and Holocene.
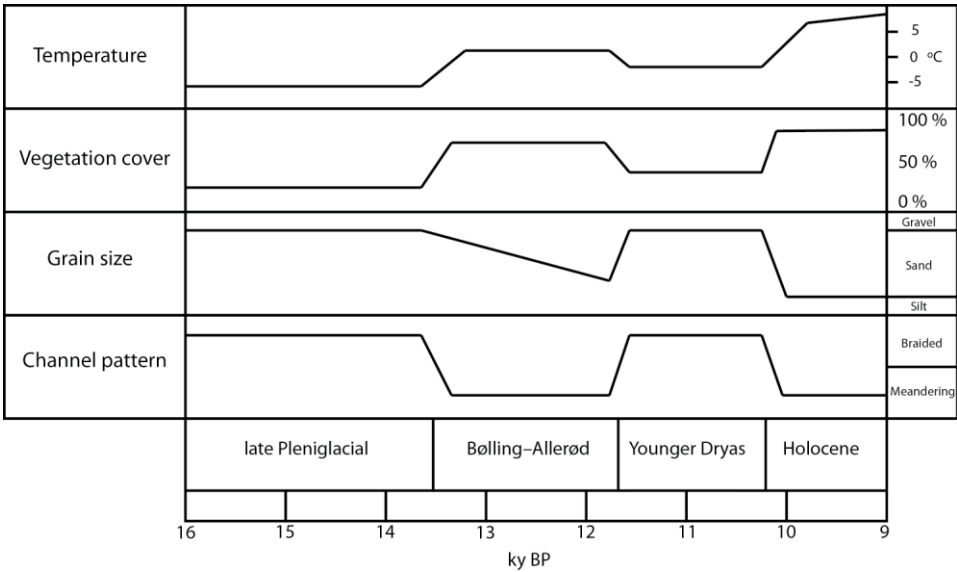
Figure 2.8: Summary of reconstructed late Quaternary temperature (Huisink, 1999; Bogaart et al., 2003b), vegetation cover (Hoek, 1997; Busschers et al., 2007), terraces grain size trend (Huisink, 1999; Busschers et al., 2007), and channel pattern (Huisink, 1999; Vandenberghe et al., 1994) for the Meuse River.

Because fine sediments are generally transported as suspended load while coarse sediment as bedload, we considered the ratio bedload/suspended load a proxy for average grain size. The model simulation indicates predominantly coarser material being supplied during cold–dry phases and finer material during warm–wet phases, which is in general agreement with the observations from Meuse River fluvial terraces (Huisink, 1999). During phases of high bedload supply and low transport capacity (Fig. 2.11B), most of the sediment was stored in the confined floodplain reservoir R_v (Fig. 2.12C). For this simulation, we assumed that 90% of the sediments in R_v can be reworked at a later stage ($n_1 = 0.9$), and that 10 % of R_v ($n_2 = 0.9$) is preserved as a fluvial terrace reservoir R_t (Fig. 2.11C).

Table 2.3: Input parameters for the Meuse River and Waipaoa River simulations

Parameter	Meuse	Waipaoa
S_h	5,0	17,0
A	31000,0	2050,0
R	710,0	1710,0
D_{50}	3,0	3,0
S_f	0,3	12,.0
K_{soil}	0,03	0,04
K_b	1000,0	100,0
$n1$	0,5	0,9
$n2$	0,9	0,9

Table 2.4: Comparison between PaCMod sediment flux and erosion rate predictions and values from literature for the last 20 ky

	PaCMod	Test	Unit	Source
Suspended load	0,3433	0,7354	km^3ky^{-1}	Ward (2008)
Bedload	0,0218	0,0500	km^3ky^{-1}	Doomen (2008)
Total sediment load	0,3651	0,19-0,70	km^3ky^{-1}	Murillo-Nuñoz et al., (2006)
Long term erosion rate	0,005-0,05	0,014-0,08	$m ky^{-1}$	van Balen et al., (2010)
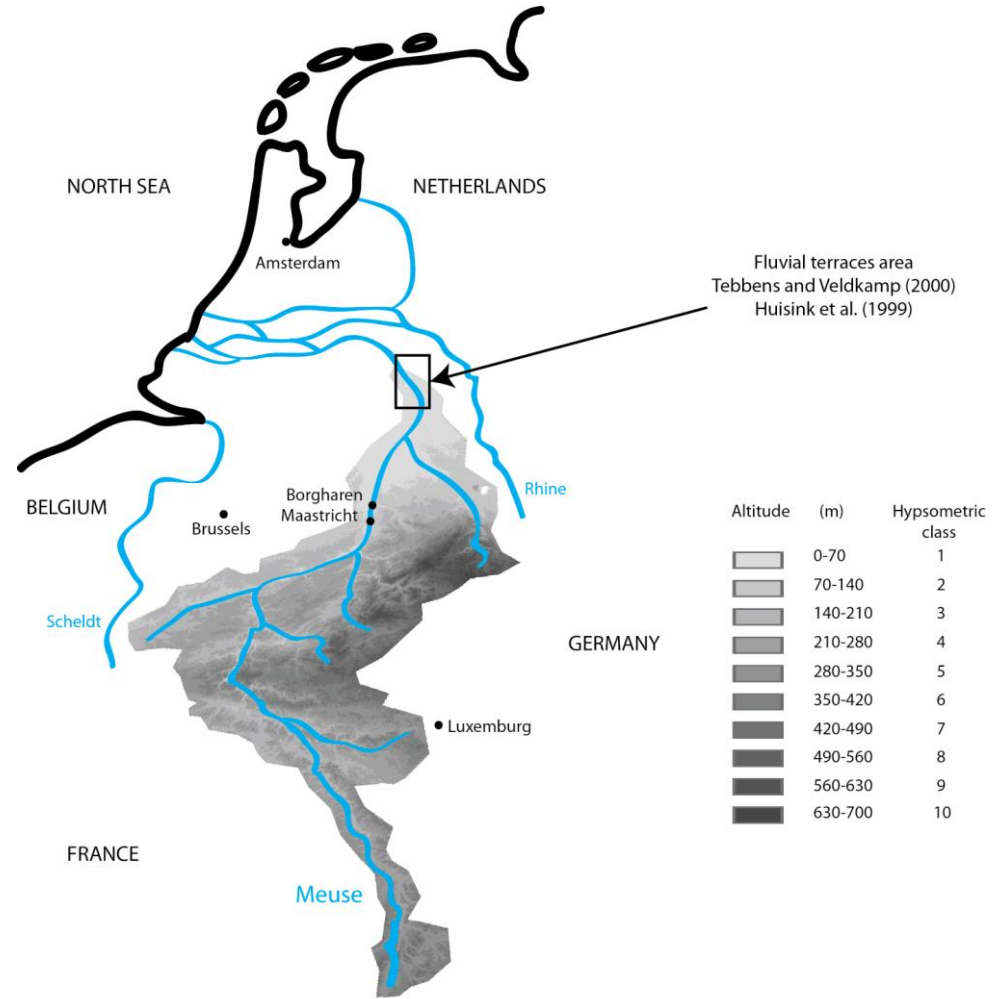
Figure 2.9: DEM of the Meuse River catchment (source: ASTER G-DEM), schematic map of the region around the Meuse River catchment, altitude, and hypsometric classes.
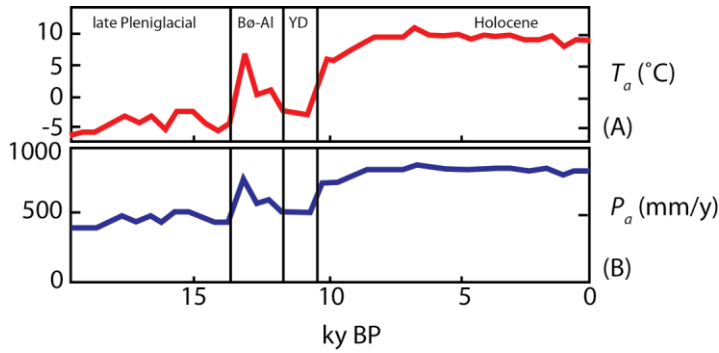
Figure 2.10: Climatic input for PaCMod for the past 20 ky of the Meuse catchment. The ice core deltaO^{18} signal (NGRIP, 2004) was used as input for all climatic boundary conditions. Such signal was calibrated based on permafrost structures (Huisink, 1999) and palaeoclimatic models (Bogaart et al., 2003b) in order to obtain temperature, precipitation, and storminess curves for the area of the Meuse catchment. Bo-Al = Bølling–Allerød; YD=Younger Dryas.

The model predicted accumulation of sediments in R_v during the late Pleniglacial and from the late Bølling-Allerød to the beginning of the Holocene. Bypass or incision occur from the late Pleniglacial to the early Bølling-Allerød and in the Holocene. These model results are in line with the observations by Vandenberghe et al. (1994) and Huisink (1999) and with model reconstructions by Bogaart et al. (2003b) and van Balen et al. (2010). The modeled cumulative volume of R_t is in the order of 10^8 m^3, which is in the same order of magnitude as the sediment volumes calculated by Huisink (1999) in the Meuse River terraces in southern Netherlands.

Applying a constant fluvial channel gradient (0.2 m km^{-1}) and a constant average grain size (3 mm) (Tebbens and Veldkamp, 2000; Murillo-Nuñoz et al., 2006), PaCMod predicted a braided channel pattern during cold phases and a meandering channel pattern during warm phases, similarly to findings by Vandenberghe (1994) and Huisink (1999) (Fig. 2.12A). The calculated vegetation cover (Fig. 2.12B) followed a similar trend as the arboreal/ nonarboreal curve in the southern Netherlands pollen record (Hoek, 1997; Busschers et al. 2007).

The modeled sediment flux signal (Fig. 2.13) was characterized by high discharge and suspended load during warm intervals and high bedload flux during stadials. Overall, suspended load and bedload simulated by PaCMod between 20 ky BP to present are comparable to those calculated in the literature (Table 2.4).
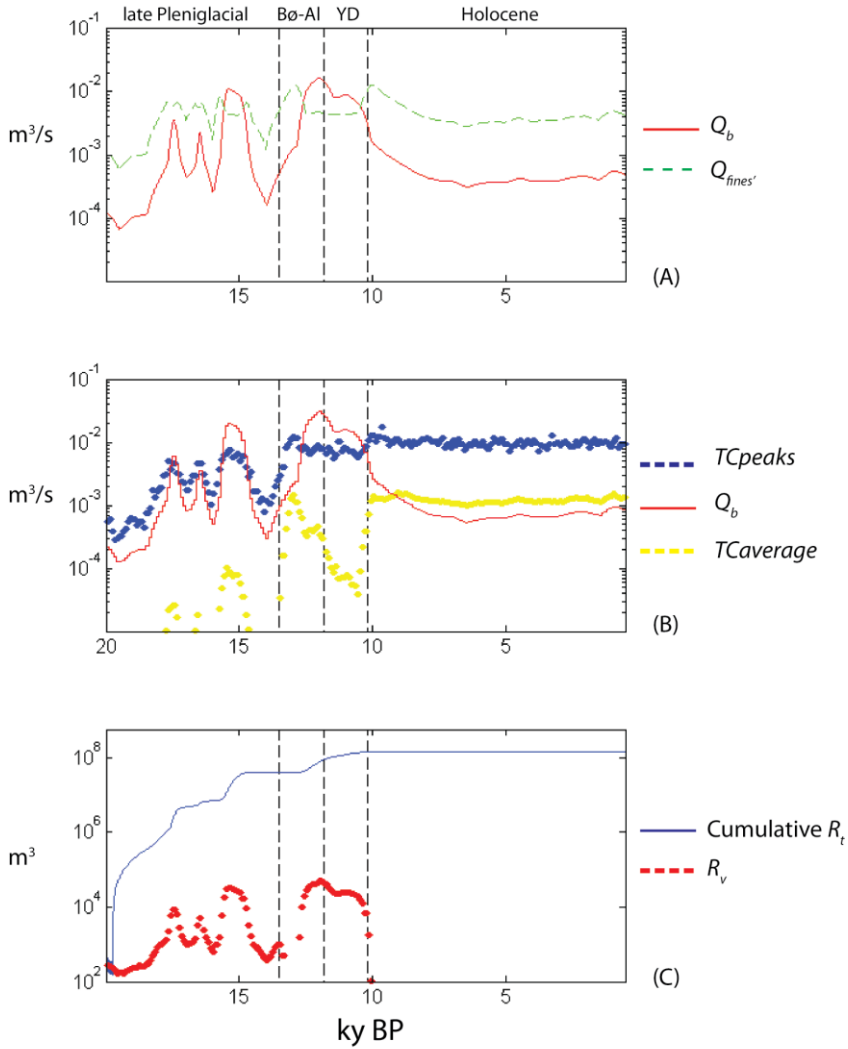
Figure 2.11: (A) Simulated delayed bedload supply Q_b and suspended load supply Q_{fines}; (B) relation between Q_b and fluvial transport capacity TC; (C) amount of bedload material stored in the confined floodplain reservoir R_v and cumulative amount of bedload material stored in the fluvial terrace reservoir R_t. Bø-Al = Bølling–Allerød. YD=Younger Dryas.
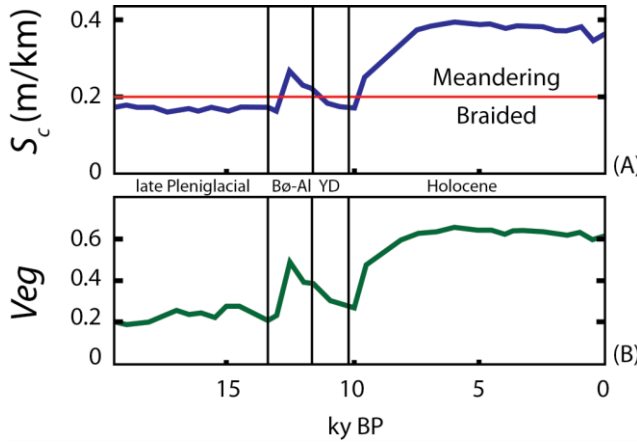
Figure 2.12: (A) Relation between fluvial channel gradient (0.2 m/ km) and critical gradient S_c. The fluvial channel pattern is braided when the fluvial channel gradient is above the critical gradient, while meandering if below. (B) Simulated vegetation cover *Veg*.

Waipaoa River

We applied PaCMod to reconstruct the sediment flux history of the Waipaoa River catchment, New Zealand, from 22.5 ky BP to Present, based on catchment morphology (Fig. 2.14 and Table 2.3) and on the hydrograph calibration (section 3.1). We used the same palaeoclimatic proxies applied by Upton et al. (2012) (Fig. 2.15) and we simulated the widespread, human-induced deforestation during the last 200 years (Marden et al., 2008), with a 50% decrease of vegetation cover *Veg*. From 22.5 to 15 ka, the low vegetation cover and high *R/I* ratio (Fig. 2.16A), induced high bedload supply Q_b (Fig. 2.16B), high bedload $Q_{bactual}$, and suspended load Q_{fines} (Fig. 2.17) (scenario W1). Because fluvial transport capacity *TC* was relatively low, compared to Q_b, a large amount of coarse material was stored in R_v and R_t (Fig. 2.16C). The Q_b decreased stepwise until 14 ka, with the major step at ca. 15 ka, while *TC* remained relatively constant throughout the whole simulation. As a result, the volume of sediments stored in R_v and in R_t drastically decreased at 15 ka and remained at low values until 200 BP.
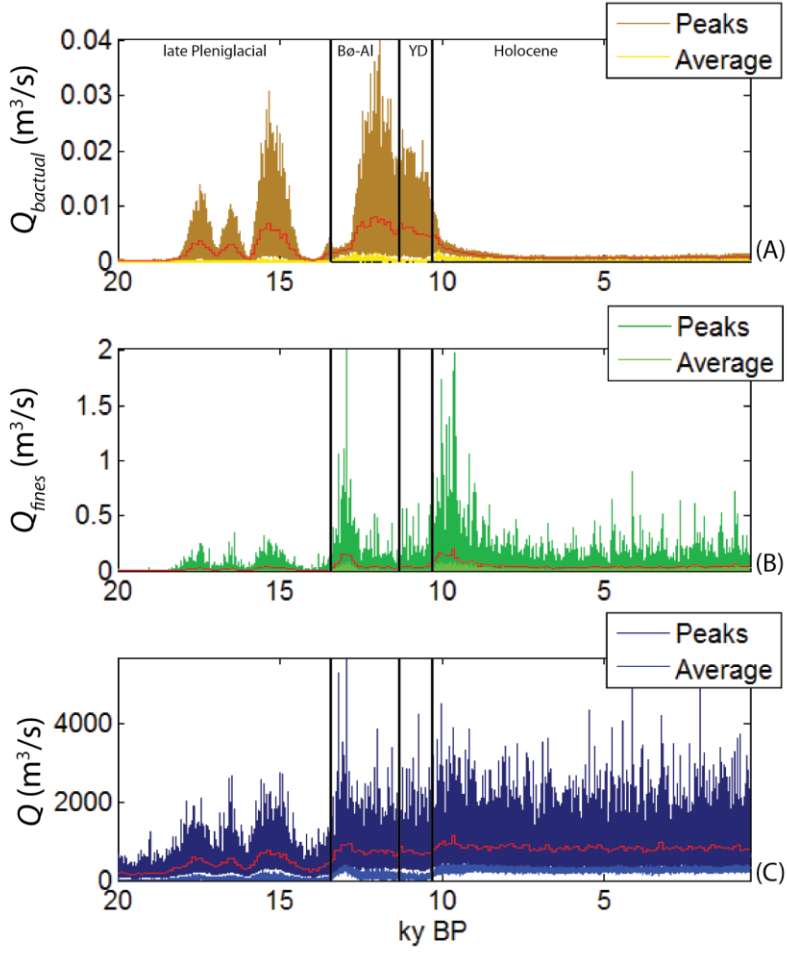
Figure 2.13: (A) Bedload $Q_{bactual}$, (B) suspended load Q_{fines}, and (C) water discharge Q out of the catchment.
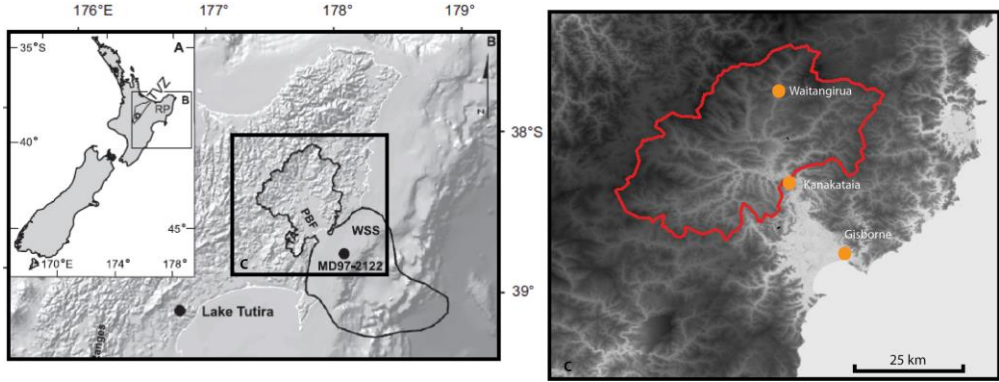
Figure 2.14: Location map (A and B, from Upton et al., 2012) and digital elevation model of the Waipaoa catchment (C) with the position of the gauging station of Kanakataia and the weather stations of Waintangirua and Gisborne. PBF=Poverty Bay Flats; WSS=Waipaoa sedimentary system. The core MD97-2122 was used by Phillips and Gomez (2007) to calculate the rate of terrigenous mass accumulation in the middle shelf. For the hydrograph test, we considered the Waipaoa catchments as the portion of the catchment upstream of Kanakataia (C), while for the sediment flux test we also considered all the Poverty Bay Flats and all its tributaries.
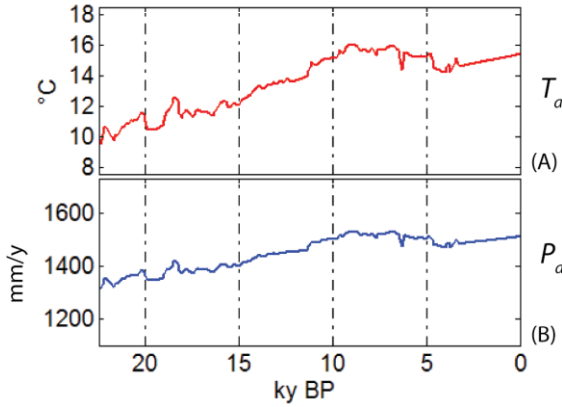
Figure 2.15: Input temperature T_a (A) and precipitation P_a (B) in the Waipaoa catchment from 22.5 ky to Present

Similarly, $Q_{bactual}$ decreased stepwise until 15 ka and then stabilized. The Q_{fines} diminished gradually from 15 to 10 ka, and except for a minor increase between 5 and 3 ka, it remained at low values until 200 BP. From 200 BP, because of deforestation, R_v, $Q_{bactual}$, and Q_{fines} sharply increased. The ages of 15 ky BP and ca. 200 BP were critical not only in the model simulation but also according to geomorphological evidence. The transition from floodplain aggradation to incision

and consequent formation of the Waipaoa1 terrace, upstream of Kanakataia (Brown, 1995; Berryman et al., 2000) is marked at 15 ky BP. The Waipaoa River started aggrading again, after ca. 200 BP, when Europeans colonized New Zealand (Phillips and Gomez, 2007; Marden et al., 2008). The phases of high R_v are thus correlated with phases of floodplain aggradation, while low R_v with incision.

Philips et al. (2007) calculated that, in the case of sediment supply exceeding transport capacity (Holocene), 30-40% of alluvial deposits was remobilized in the Waipaoa floodplain. Such percentage was likely higher in periods dominated by fluvial incision. We conducted another test (scenario W2) to evaluate the impact of sediment routing and sediment storage/remobilization on sediment flux, setting a high K_b value (2000 years) and $n_1 = 0.3$. The results were similar to scenario W1 (Fig. 2.18). Nevertheless, the higher K_b, and thus longer sediment travel times, produced a smoother Q_b and $Q_{bactual}$ signal, characterized by a gradual decrease from 15 to 5 ka. Because of the smaller n_1 value, and thus less sediment remobilization, R_v and R_t were almost one order of magnitude higher than in scenario W1.

Finally, we compared our modeled erosion rates to the sediment flux reconstruction by Kettner et al. (2009) and Upton et al. (2012) (Fig. 2.19). We calculated two end-members erosion rates, in order to account for uncertainty in average hillslope angle S_h and soil erodibility coefficient K_{soil}: a maximum erosion case, maximum E ($K_{soil} = 0.05$; $S_h = 20°$), and a minimum erosion case, minimum E ($K_{soil} = 0.03$; $S_h = 15°$). The long-term suspended load, calculated with the BQART equation Q_s, increased throughout the whole simulation. Differently, modeled erosion rates E drastically decreased from 5-15 Mton/y at 22.5 ky BP to 1-3 Mton/y at 10 ky BP, and remained stable until 200 BP, when they rose to 6-18 Mton/y. This trend is comparable to the *Qs(Eh)* calculated by Upton et al. (2012), although PaCMod predicted higher E than *Qs(Eh)* until 12 ky BP, whereas the opposite occurred afterward. During the last 3 ky, modeled erosion rates were comparable to the rate of terrigenous mass accumulation on the middle shelf at core site MD97-2122 (Phillips and Gomez, 2007).
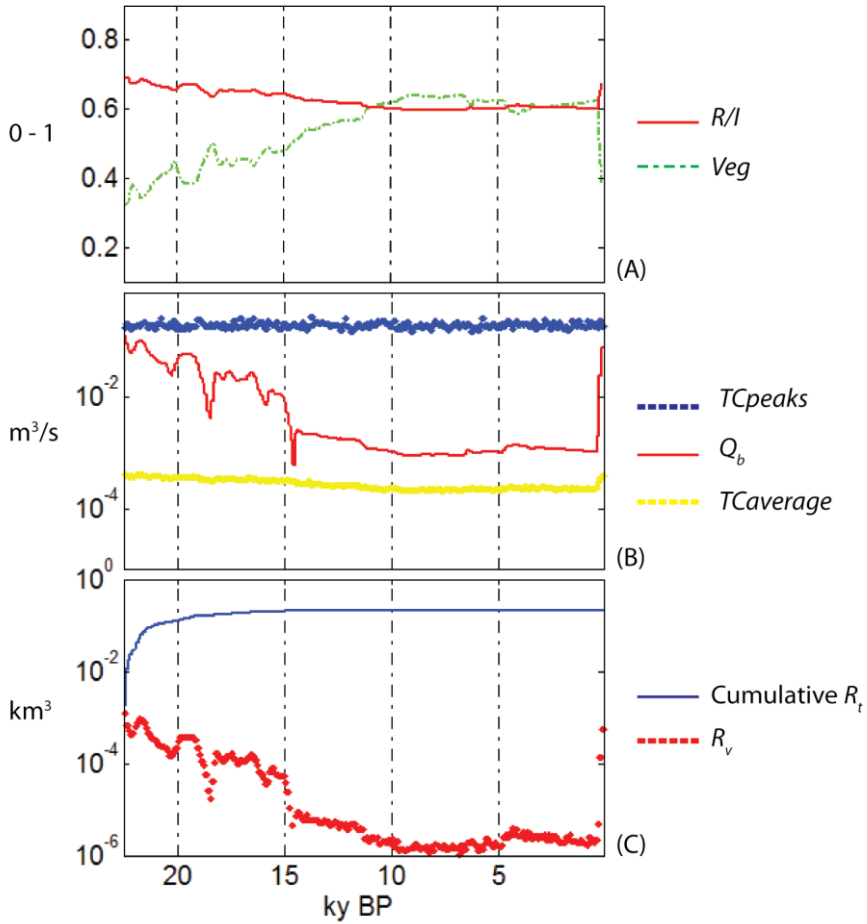
Figure 2.16: Waipaoa catchment geomorphic response to climatic changes for scenario W1, with $K_b = 100$ years, and $n1 = 0.9$: (A) vegetation cover *Veg* and runoff/ infiltration ratio *R/I*; (B) relation between delayed bedload supply Q_b and fluvial transport capacity *TCpeaks* and *TCaverage*, and (C) amount of bedload material stored in the confined floodplain reservoir R_v and cumulative amount of bedload material stored in the fluvial terrace reservoir R_t.
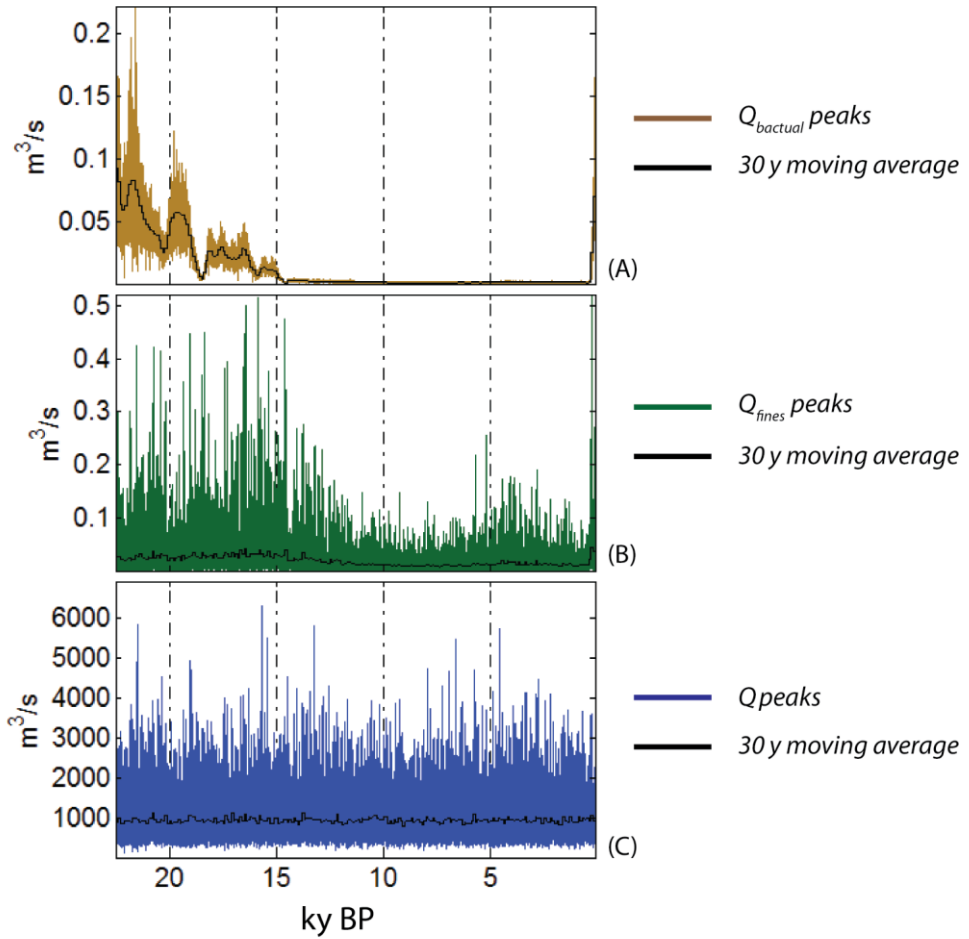
Figure 2.17: (A) Bedload peaks $Q_{bactual}peaks$, (B) suspended load peaks $Q_{fines}peaks$, and (C) water discharge peaks $Qpeaks$ from the Waipaoa catchment. Only peaks are shown, because water discharge and sediment flux during average conditions were too little for display.
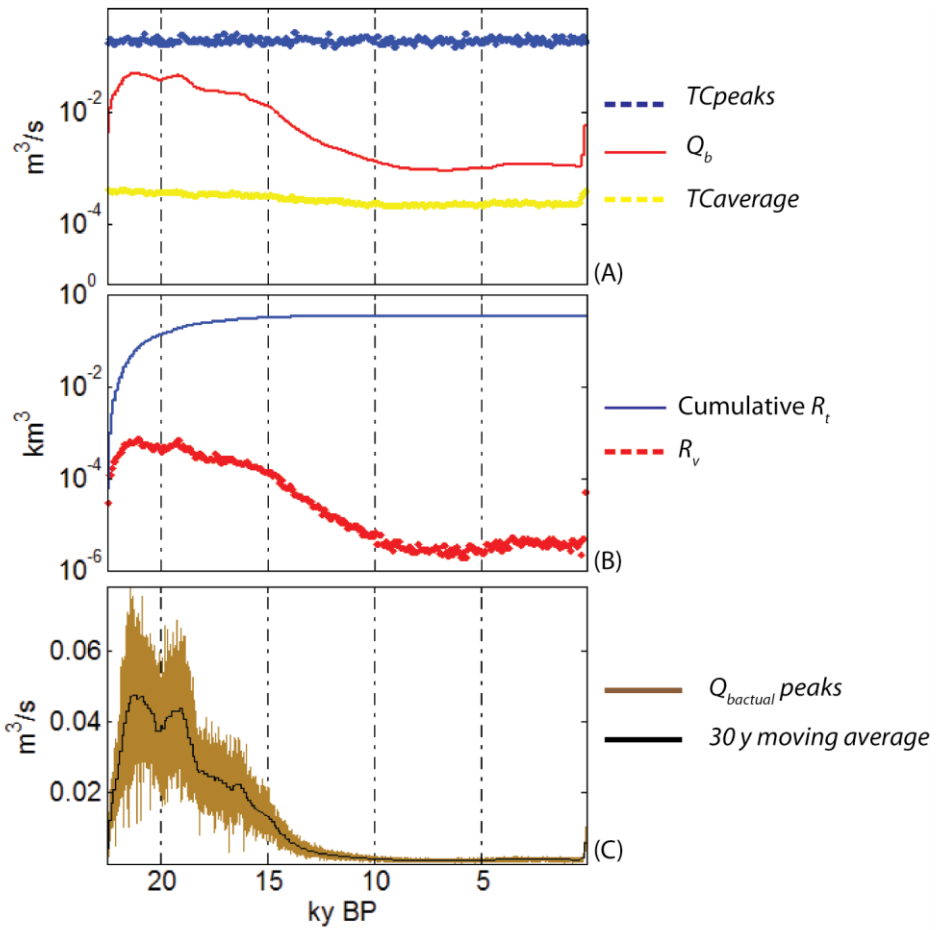
Figure 2.18: Waipaoa catchment geomorphic response to climatic changes for scenario W2. Relation between delayed bedload supply Q_b and fluvial transport capacity TC (A); bedload material stored in R_v and cumulative amount of bedload material stored in R_t (B), and bedload peaks $Q_{bactual} peaks$ (C).
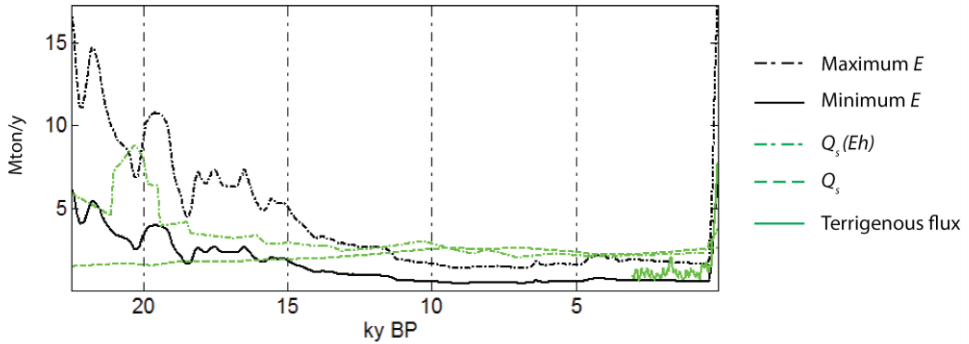
Figure 2.19: Comparison between PaCMod output, Hydrotrend output (Upton et al., 2012), and rate of terrigenous mass accumulation on the middle shelf at core site MD97-2122 (Phillips and Gomez, 2007). PaCMod output consists of maximum (Maximum E) and minimum (minimum E) erosion rates (Zhang, 2002 approach). Hydrotrend output consists of long-term suspended load Q_s (BQART approach, identical in PaCMod), and long-term suspended load calculated accounting for vegetation cover change and human impact $Q_s(Eh)$.

The modeled total volume of sediments transported out of the catchment from 18 ky BP to Present is in the range 10-30 km^3, assigning a dry bulk density of 1400 kg m^{-3} (Marden et al., 2008). In the same period, 20 km^3 of mud accumulated on the continental shelf (Foster and Carter, 1997) and 6.6 km^3 of gravel, sand, and mud accumulated in the Poverty Bay Flats (Marden et al., 2008). The present day measured mass of suspended load out of the catchment is 15 Mton y^{-1} (Marden et al.. 2008). Thus, the modeled volume of sediment eroded upstream, or at least the high end of the range, is comparable to the volume of material accumulated downstream and present day measurements.

2.4. Sensitivity analysis

A sensitivity analysis was conducted to evaluate the relative importance of the model parameters (Table 2.5) on PaCMod output. For each input parameter a realistic range was chosen and discretized into a minimum, mean, and maximum value, designated by -1, 0, and 1, respectively. This gave a choice of three input values for each of the 28 parameters. We ran PaCMod 10 times for all parameter combinations in order to account for the random components in the model. For each run, the average suspended and bedload flux volumes were calculated as well as (i) the suspended load and bedload cumulative volume, (ii) the RMSE (root mean

square error) with respect to a base case with all zero values, and (iii) the interannual standard deviation of suspended load and bedload.

The above retrieved data were used to perform an analysis of variance (ANOVA) (Hogg and Ledolter, 1987), a collection of statistical methods for hypothesis testing involving multiple groups of observations. Among the results of ANOVA, we used the F-test to quantify the relative statistical influence of each parameter (de Jager et al., 2009). Figure 2.20 shows the F-test values of the parameters that, combined, describe 95% of the model response variability. Ninety-five percent of the model output is controlled by only 11 parameters. Suspended load is mainly controlled by the parameters of the BQART equation. The most important parameter is temperature, followed by catchment area and maximum relief. Bedload flux is very sensitive to temperature, catchment area, and parameters controlling hillslope erosion (vegetation cover coefficients, hillslope angle) and is also importantly affected (47%) by the choice of user-defined parameters (vegetation cover and precipitation gradient).

2.5. Discussion

Validity of the model

PaCMod is able to produce a long time series of water discharge and sediment load and also simulated sediment storage and routing in the catchment. The use of empirical equations provides limitations and sources of uncertainty. Nevertheless, such an approach is valuable given the uncertainty in defining boundary conditions (climate, hypsometry, geology) of palaeo catchments. The PaCMod level of detail is sufficient to produce realistic scenarios of sediment flux in present-day systems and thus can also be applicable in palaeo settings.

Sediment routing and storage

The timing and the magnitude of modeled bedload pulses are affected by sediment routing and storage, as evidenced by PaCMod reconstructions of sediment flux from the Meuse and the Waipaoa catchments. Field studies (Phillips, 2003; Blum and Aslan, 2006; Leigh et al., 2006), modeling work (Coulthard and van de Wiel, 2007; van Balen et al., 2010), and studies on sediment provenance (Wittmann and von Blanckenburg, 2009; Alizai et al., 2011) evidenced the importance of sediment availability, storage and routing on the development of alluvial fans and on alluvial and deltaic sequences. For example, van Balen et al. (2010) suggested a 5-ky time lag

between upstream perturbation and fluvial system response in the lower reaches of the Rhine River catchment. Alizai et al. (2011) suggested a 5-10 ky time lag for the transport of zircon grains (bedload) from the Himalaya toward the delta of the Indus River. The bedload delay time may have a relation with catchment size and morphology. However, at present, such a relation is very difficult to establish and further systematic research should be done based on a bigger catchments database and modeling work.

Grain size

Weathering and selective transport processes in the catchment lead to a range of different grain sizes available for transport. So far, we have only modeled bedload and suspended load, not specifying for individual grain size classes. Such a model approach would require a good knowledge on outcropping lithology, on rock fabrics, and of the rate of grinding and selection. This is theoretically possible for modern systems, but it becomes increasingly harder for palaeo applications. The use of a semi quantitative weathering index (Weltje et al., 1998) or of a downstream sediment fining function (Whittaker et al., 2010) are interesting approaches to parameterize grain size fining and mixing in the catchment.
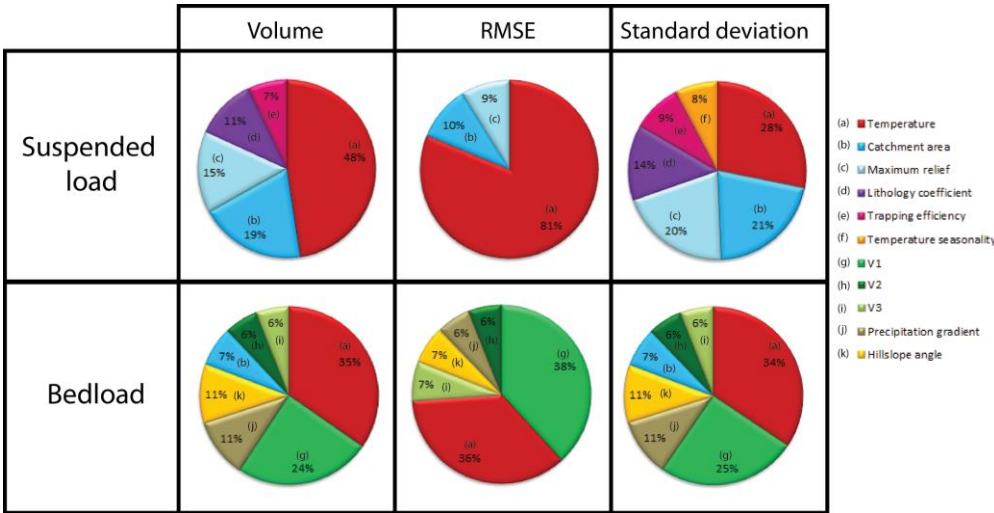
Figure 2.20: Sensitivity of PaCMod suspended load and bedload output to boundary conditions and parameters.

Table 2.5: Parameters and parameters values used in the sensitivity analysis

Parameter	Minimum	Mean	Maximum	Unit
R	200,0	4100,0	8000,0	m
Concavity exponent	0,5	2,75	5,0	
A	100,0	500050,0	1000000,0	km^2
D_{50}	0,1	50,05	100,0	mm
K_{soil}	0,2	0,4	0,6	
Trapping efficiency	0,0	0,35	0,7	
Lithology coefficient	0,5	1,5	2,5	
Groundwater residence time	100,0	300,0	500,0	d
Direct flow buffer	7,0	13,5	20,0	d
S_h	2,0	16,0	30,0	
S_f	0,1	50,0	100,0	m km^{-1}
Latitude	0,0	35,0	70,0	°
Snow melt coefficient	0,01	0,5	1,0	
P_g	0,00001	0,0005	0,001	
$v1$	0,0005	0,0012	0,002	
$v2$	15,0	20,0	25,0	
$v3$	10,0	15,0	20,0	
$x1$	0,5	1,0	1,5	
$x2$	1,0	2,0	3,0	
$x3$	0,2	0,5	0,8	
$x4$	0,002	0,003	0,004	
k_d	300,0	1150,0	2000,0	y
H_c	50,0	100,0	150,0	mm
P_a	200,0	1350,0	2500,0	mm y^{-1}
Storminess	0,2	0,5	0,8	
P_a seasonality	100,0	550,0	1000,0	mm y^{-1}
T_a	-5,0	10,0	25,0	°C
T_a variability	1,0	4,0	7,0	°C

Catchment nonlinear behaviour and implications for fluvio–deltaic stratigraphy

Water and sediment flux depend on a complex interaction of multiple processes, thresholds, and nonlinearity of system response (Tucker and Slingerland, 1997; Coulthard et al., 2005). For example, temperature, precipitation, vegetation development, and catchment morphology are all important controls for erosion rates and transport capacity. Neglecting one of these controls, when modelling, can lead to contrasting results (see Fig. 2.19). This means that a similar climatic change can induce a different sediment flux response in different catchments and in different parts of a catchment. Furthermore, favourable conditions for high sediment flux pulses may occur in transition phases (cold–warm or warm–cold), rather than during stable climate phases, as indicated for the Meuse River simulation and previously suggested by Vandenberghe et al. (2008).

The nonlinear behaviour of the catchment can influence fluvial and marine stratigraphy in different ways. Coarse sediment fractions have longer travel times than finer fractions (Alizai et al., 2011), which means that they may reach a delta 10^3 years later then the fine sediments. In a deltaic stratigraphic sequence, this may result in a coarsening-up signal superimposed on the typical coarsening-up trend caused by deltaic progradation. Furthermore the signal recorded in deltaic stratigraphy is the delayed and modified upstream forcing signal (Veldkamp and Tebbens, 2001; van Balen et al., 2010). This should be taken into account when chronologically and quantitatively linking sedimentary record and external forcing such as climate.

The balance between sediment erosion and fluvial transport capacity may also have an important effect on deltaic stratigraphy. During phases of high sediment availability, compared to transport capacity, the signal transmitted downstream is the one of transport capacity (c.f. dominated by precipitation). During such conditions, the stratigraphy may be more dominated by big floods events. When transport capacity is higher than sediment availability, the hillslope erosion signal is transmitted and also the small discharge events will be recorded.

2.6. Conclusions

We have developed a spatially lumped process-response model (PaCMod) that calculates long time series of fluvial water discharge and sediment load at the river catchment outlet including flood events. The PaCMod structure is a combination of existing and modified routines from Hydrotrend (Syvitski et al., 1998) and PALAEOFLOW (Bogaart and van Balen, 2000), complemented with new modeling algorithms and parameterizations for environmental response to climatic changes, sediment routing, and storage within the catchment. The PaCMod hydrological module was successfully tested on observed data from three present-day fluvial systems: the Meuse, the Waipaoa and the Po Rivers. In addition, we calculated the sediment load of the Meuse and the Waipaoa Rivers since 20 ky BP and 22.5 ky BP, respectively. Our results are in agreement with published field and modeling work. The results from a sensitivity analysis indicate that the main controls on simulated sediment flux are temperature, catchment area, maximum relief, and parameters controlling hillslope erosion.

PaCMod simulations have shown how the downstream propagation of a climatic signal is hampered by routing and storage of sediment within the catchment. This implies that, when reading and timing the climatic signal in fluvial or deltaic stratigraphy, we should take into account how the forcing signal is transmitted downstream and recorded in the stratigraphy. When boundary conditions are poorly constrained, spatially lumped, process-response numerical models (in this case PaCMod) are a valuable way to investigate the response of a catchment to perturbation and to make predictions about the sediment flux to sedimentary basins.

Table 2.6. Table of symbols

Parameter	Symbol	Unit
Catchment area	A	km^2
Actual evaporation	AET	$mm\ d^{-1}$
River bank friction angle	BS	°
Fluvial channel depth	D	m
Median grain size	D_{50}	mm
Potential long term erosion rate	E	$mm\ y^{-1}$
Extra amount of precipitation	EP	mm
Gravitational coefficient	g	$m\ s^{-2}$
Altitude	H	m
Altitude of hypsometric class	h	m
Absolute area of hypsometric class	H_{area}	m^2
Relative area of hypsometric class	H_{areal}	0-1
Soil holding capacity	H_c	mm
Bedload routing parameter	k_d	
Soil erodibility	K_{soil}	
Manning's flow resistance	n	
Fraction of bedload to floodplain reservoir	$n1$	0-1
Fraction of bedload to terrace reservoir	$n2$	0-1
Total annual precipitation	P_a	mm
Precipitation seasonal amplitude	P_{amp}	mm
Potential evaporation	PET	$mm\ d^{-1}$
Precipitation gradient	P_g	$mm\ d^{-1}\ m^{-1}$
Average daily precipitation	P_m	mm
Precipitation random component	P_n	0-1
Precipitation seasonal component	P_s	mm
Probability of a wet day	P_w	0-1
Water discharge per time step	Q	$m^3\ s^{-1}$
Long term average water discharge	Q'	$m3\ s^{-1}$
Sediment available for bedload transport	Q_b	$m^3\ s^{-1}$

Actual sediment available for bedload	$Q_{bactual}$	m^3 s^{-1}
Long term sediment available for bedload	$Q_{coarse'}$	kg s^{-1}
Actual suspended load per time step	Q_{fines}	kg s^{-1}
Actual long term suspended load	$Q_{fines'}$	kg s^{-1}
Bankfull discharge	Q_p	m^3 s^{-1}
Potential long term suspended load	Q_s	kg s^{-1}
Water density	ρ	kg m^{-3}
Average sediment density	ρ_s	kg m^{-3}
Maximum catchment relief	R	km^2
Hydraulic radius	R_h	m
Runoff/ infiltration coefficient	R/I	0-1
Terrace reservoir	Rt	m^3
Confined floodplain reservoir	Rv	m^3
Critical fluvial channel gradient	S_c	m km^{-1}
Fluvial channel gradient	S_f	m km^{-1}
Average hillslope angle	S_h	°
Bottom shear stress	τ	kg m^{-2} s^{-1}
Critical shear stress	τ_c	kg m^{-2} s^{-1}
Average catchment temperature	T	°C
Mean annual temperature	T_a	°C
Bedload transport capacity	TC	m^3 s^{-1}
Vegetation cover	Veg	0-1
Fluvial channel width	W	m
Width/ depth fluvial channel ratio	WDR	m m^{-1}

CHAPTER 3

Delayed delivery from the sediment factory: modeling the impact of catchment response time to tectonics on sediment flux and fluvio-deltaic stratigraphy

Abstract. The sediment flux from a catchment is driven by tectonics and climate but is moderated by the geomorphic response of the landscape system to changes in these two boundary conditions. Consequently, catchment response time and the non-linear behavior of landscapes in response to boundary condition change control the downstream propagation of climatic or tectonic perturbations from catchments to neighboring basins. In order to investigate the impact of catchment response time on sediment flux, we integrated a spatially-lumped numerical model PaCMod (Forzoni et al., 2013), with new routines simulating the evolution of landscape morphology and erosion rates under tectonic and climatic forcing. We subsequently applied the model to reconstruct the sediment flux from a tectonically perturbed catchment in Central Italy. Finally, we coupled our model to DeltaSim, a process-response model simulating fluvio-deltaic stratigraphy, and investigated the impact of catchment response time on stratigraphy, using both synthetic scenarios and a real world system (Fucino Basin, Central Italy). Our results demonstrate that the differential response of geomorphic elements to tectonic and climatic changes induces a complex sediment flux signal, and produces characteristic stratigraphic architectures and shoreline trajectories.

3.1. Introduction

Quantifying the response of river systems to tectonic and climatic changes is critical for predicting mass transfer across the Earth's surface, for determining the sediment fluxes to the oceans and for correctly interpreting geologic history from the stratigraphic archive. Allen (2008: p. 23) argued that "the more we make steps in understanding landscapes and sediment routing systems, the more we discern their complex response to perturbations of all types. Had such information been available previously to guide stratigraphic models, it is arguable that the entire field of sequence stratigraphy or genetic stratigraphy would have developed differently".

During the last twenty years, the role of sediment supply has become increasingly important in the field of stratigraphy. This is due both to the growth in studies that analyze landscape dynamics and sediment export from mountain belts (Tucker and Slingerland, 1997, Kirby and Whipple, 2001; Syvitski and Milliman, 2007; Whittaker et al., 2007; Armitage et al., 2012) and to the increasing use of concepts such as trajectory analysis, which explicitly document the migration pattern of shorelines and associated depositional systems as a function of sediment supply and sea level (Helland-Hansen and Hampson, 2009). Nevertheless, for many stratigraphers, the sediment supply signal is still often modeled or considered as a simple function of climatic or tectonic forcing (Van der Zwaan, 2002; Burgess et al., 2006; Kubo et al., 2006; Bhattacharya and MacEachern, 2009; Davidson and North, 2009). Geomorphologists argue that this is not the case.

Indeed, a number of recent studies have illustrated how the response of sediment flux and basin stratigraphy to external forcing is complex and highly non-linear, because it is a function of both the characteristics of the forcing and, more interestingly, of the internal dynamics of the fluvial system and of its response time to external perturbation (Tucker and Slingerland, 1997; Metivier and Gaudemer 1999; Whipple and Tucker, 1999; Allen 2008; Coulthard and Van de Wiel, 2013). The response time is defined as the time it takes for a perturbed system to adapt to the modified boundary conditions and to attain a new state of equilibrium, usually taken to be a topographic steady state (Whittaker et al., 2007; Allen, 2008; Armitage et al., 2008). A number of numerical experiments have shown that, even for very simple catchment configurations, a large amount of variability in sediment discharge can be caused through autogenic factors such as bed armoring, topographic changes, sediment storage and re-mobilization, and stochastic processes operating on a range of timescales (Coulthard and Van de Wiel, 2007; Jerolmack and Paola, 2010; van de Wiel and Coulthard, 2010). Additionally, large

floodplains have been shown to further enhance the inertia and the non-linear response of river systems to external forcing (Metivier and Gaudemer, 1999; Castellort and van Driesche, 2003; Allen et al., 2008).

Field studies provide good evidence for the transient response of erosional-depositional systems to changes in their external boundary conditions. For instance Whittaker et al. (2010) showed that, for transient catchments crossing active normal faults in central Italy, which had increased their slip rate within the last million years, most of the sediment export derived from the zone upstream of the fault (transient reach), as a consequence of enhanced incision and landsliding. Furthermore, their results indicated that grain size trends in hanging wall sedimentary basins are both a function of accommodation space creation and of the degree of tectonic perturbation affecting the footwall. In a related study that modeled the evolution of a coupled catchment-fan system crossing an active normal fault, Armitage et al. (2011) observed that an increase in fault slip rate resulted in a complex fan architecture and in different vertical grain size trends through the resulting stratigraphy, depending on the distance from the fan apex. Such complexity was fundamentally caused by the lag-time between the instantaneous generation of tectonic subsidence following the tectonic change, and the delayed response of sediment supply owing to the internal dynamics of the coupled catchment-fan system.

Using analogue models, Rohais et al. (2012) came to similar conclusions. In particular, their results indicated that fan stratigraphy and grain size trends recorded a non-linear response of the coupled catchment-fan system to tectonic and climatic perturbations. Such perturbations induce temporary disequilibrium between sediment supply and sediment transport capacity in the catchment. A new dynamic equilibrium is reached only after the catchment has adapted to the new boundary conditions.

The above studies all demonstrate that predicting the volume, characteristics and locus of sediment supply from perturbed catchments to basins is non-trivial, and it becomes increasingly more challenging the further we move back in the geological time, due to the poor control on palaeo-climate, tectonic rates and palaeo-catchment morphology. Consequently, while cellular models, such as GOLEM, CHILD, and CAESAR, are an excellent tool to investigate catchment evolution and sediment flux in tectonically and climatically perturbed areas over geomorphic time periods ≤ 1 My (Tucker and Slingerland, 1996; Coulthard and Kirby, 2002, Pepin et al., 2010), their applicability to ancient settings can be limited. This is

because they require a high level of input detail, such as rainfall or discharge records, which may be unobtainable (or even unknowable) for the geologic past. This problem significantly limits the utility of such models to simulate sediment flux from palaeo-catchments. In contrast, reduced complexity models, with one or zero spatial dimensions, are more parsimonious with the required input, computation, and output resolution, and they produce results that have the same resolution as the input boundary conditions. Zero and one dimension models usually focus on a single or a single set of geomorphic processes, such as the evolution of a fluvial longitudinal profile (Whipple and Tucker, 1999; Kirby and Whipple, 2001; Snyder et al., 2003), and they rely on important assumptions, so they may not fully replicate the internal dynamics of the system that we know to be important (c.f. Armitage et al, 2011, Rohais et al., 2012). Nevertheless, they are useful tools to investigate catchment evolution and sediment flux in ancient settings, where parameters have a high degree of uncertainty, or where long time scales are considered (10^5-10^7 y).

The objectives of this study are twofold. First, we aim to develop and test new numerical routines that simulate the response of the whole fluvial system to external perturbations using a spatially-lumped approach. We attempt to bridge the gap between cellular and spatially-lumped approaches, by using the maximum level of simplicity, necessary for palaeo-applications, which are intrinsically characterized by uncertain boundary conditions, and by a process-response approach to simulate the response of landscape morphology to external forcing. Second, we apply our model to investigate quantitatively the impact of catchment response time on sediment flux and fluvio-deltaic stratigraphy.We integrated a spatially-lumped model simulating sediment and water flux from a catchment, PaCMod (Forzoni et al., 2013), with new numerical routines simulating the evolution of landscape morphology and erosion rates under tectonic and climatic forcing. Next, we applied PaCMod to reconstruct the sediment flux history from the Celano catchment (Central Italy), for which field constraints already exist (Whittaker et al., 2007b; Whittaker et al., 2010), and we investigate the impact of catchment response times on sediment flux. Finally, we coupled PaCMod to DeltaSim (Overeem et al. 2003, Hoogendoorn et al. 2008), a process-based model simulating fluvio-deltaic stratigraphy, in order to investigate the impact of response time on stratigraphic architecture and shoreline trajectory, using synthetic scenarios and a real world system (Fucino Basin, Central Italy).

3.2. Methods

We developed new numerical routines to simulate the evolution of landscape morphology and erosion rates under tectonic and climatic forcing, and coupled these new routines to the catchment model known as PaCMod. A full description of PaCMod, with accompanying sensitivity analyses, is presented in detail in Forzoni et al. (2013). A summary of the relevant background model details for this study is provided in the Supplementary Online material.

3.2.1.   PaCMod

PaCMod is a numerical model, which calculates long time series of water and sediment flux out of any given catchment (Forzoni et al., 2013). The key aspects of the model are (1) a spatially lumped approach, allowing for fast simulations, and preserving the same resolution from palaeo-climatic proxies and (2) the parameterization of sediment routing and storage in the catchment. In PaCMod, the 3D morphology of a real catchment is collapsed into four spatial domains, where different processes occur and sediment is routed and temporary stored: hillslopes, fluvial network, catchment lower reaches, and catchment outlet.

Based on climatic and environmental conditions, PaCMod calculates a yearly time series of precipitation, runoff, and fluvial water discharge Q_w, with two time steps per year, one for flood conditions (peaks) and one for average conditions (average). In PaCMod hillslope erosion rate is calculated as a function of average hillslope angle, runoff and vegetation cover (Zhang et al., 2002). The fine fraction of eroded sediment is treated as suspended load and is calculated with the BQART approach (Syvitsky and Milliman, 2007). The coarse fraction of eroded sediment Q_{bss} (mm y^{-1}) is treated as bedload sediment supply. Q_{bss} is then balanced with the bedload fluvial transport capacity TC at the catchment outlet (m^3 s^{-1}) (Tucker and Slingerland, 1997), which is a function of fluvial channel gradient at the catchment outlet S_f (m km^{-1}), average bedload grain size D_{50} (mm), and Q_w. In PaCMod fluvial channel gradient and hillslope angle are constant in time, which means that they do not react to changes in climatic and tectonic conditions.

When Q_{bss} exceeds TC, i.e. more bedload is supplied to the river than the river can transport, the fraction of sediment in excess of this value is stored in a confined floodplain reservoir R_v. The actual bedload $Q_{bactual}$ (m^3 s^{-1}) available for transport in the following time step is the sum of Q_b and a fraction n_1 of R_v. Yearly bedload at the catchment outlet Q_{bed} equals $Q_{bactual}$ when $Q_{bactual} < TC$, whereas it equals TC when $Q_{bactual} > TC$. Finally, PaCMod calculates yearly suspended load at the catchment outlet Q_{susp} based on Morehead et al., (2003) approach.

3.2.2.   New routines

We coupled PaCMod (Forzoni et al., 2013) to new numerical routines which simulate the evolution of basic landscape morphological parameters in response to tectonic and climatic forcing. These new routines rely on the following assumptions: (1) we define the catchment as the upland, mainly erosional part of a drainage basin, in which sediments can be stored temporarily on hillslopes, alluvial fans, confined floodplains and channel deposits (Figure 3.1); (2) the catchment is uplifted as a single block; (3) all morphological parameters and processes are averaged, following the spatially-lumped modeling approach which characterizes PaCMod; (4) all coefficients are empirically defined by previous published studies or by calibration on real catchments; and (5) we model two landscape parameters, average hillslope angle, S_h, and the fluvial channel gradient at the catchment outlet, S_f, because these two parameters are the main morphological controls on hillslope erosion and fluvial transport capacity, respectively. In the new model routines, S_h is related to denudation rate D (mm year^{-1}) using a power law (Eq. 3.1), as suggested by Binnie et al. (2007), and Montgomery and Brandon (2002):

$$S_h = c1 \cdot D^{c2} \tag{3.1}$$

c1 and *c2* are hillslope evolution proportionality coefficients, which for this study were calibrated on three well-studied catchments in Central Italy (see Appendix for full details). S_h cannot exceed a critical hillslope angle (35°). Numerical and field studies (Whipple et al., 2004, Moglen et al., 1999; Gabet et al., 2004; Bogaart and Troch, 2006) have shown that more erosive climates induce lower fluvial relief, higher drainage density, and consequently gentler hillslope angle, whereas less erosive climates and high uplift rate result in steeper hillslope angles. In order to simulate this response of hillslope angle to tectonic and climatic perturbation in a spatially-lumped approach, we parameterize the overall catchment denudation rate, *D*, as:

$$D = (K_u \cdot U) \cdot \left(\frac{K_u \cdot U}{K_e \cdot E} \right) \tag{3.2}$$

where *U* is the imposed uplift rate (mm year^{-1}) and *E* is the overall catchment erosion rate (mm year^{-1}) and K_u and K_e are response time coefficients we discuss in detail below. We consider Summerfield (1991) definition of denudation, as the removal of material from the Earth surface by mechanical processes (erosion, *E*) and chemical processes. With this approach denudation rate, *D*, (and hence hillslope angle (Eq. 3.1)) is proportional to the imposed uplift rate and to the ratio

between uplift rate and erosion rate (right term of Eq. 3.2). When erosion rates exceed uplift rate, as a consequence of more erosive climate, hillslope angle decreases, while the opposite occurs when uplift rate exceeds erosion rates.

The response time coefficients K_u and K_e are diffusion coefficients dampening the response of denudation rate, and consequently hillslope angle (Eq. 3.1), to variations in tectonic uplift and climate-driven erosion rates. In real-world systems, the Earth's surface responds with inertia to tectonic and climatic changes. In other words, it takes a certain amount of time, the defined response time, for a landscape to react and reach and equilibrium with the modified conditions (Allen, 2008). During this period, landscape is in a transient state (Whipple, 2002, Whittaker and Boulton, 2012).

The response time is a function of the rate of different geomorphic processes and of the type of perturbation. Climatic perturbations induce changes in discharge across the whole catchment simultaneously, which can result in variations in fluvial erosion rates and hillslopes angle on a timescale of ~ 10^3 years (Tucker and Slingerland, 1997; Moglen et al., 1999; Gabet et al., 2004; Bogaart and Troch, 2006). In our numerical routines, these climate driven processes are captured in the response time coefficient of hillslope to erosion, K_e. Tectonic changes induce a more complex response. For upland bedrock rivers, an increase of fault-slip rate leads to the upstream migration of a wave of erosion (a knickzone) through the catchment, starting at the point where the channel crosses the fault (Whittaker et al., 2007; Allen et al., 2008). The perturbation immediately affects hillslope angle and erosion rate close to the fault, while the upstream part of the catchment are typically only affected after 10^4-10^6 years, depending on the celerity of the wave of erosion (Whittaker et al, 2007, Cowie et al., 2008, Whittaker and Boulton 2012). In our numerical routines, these processes are described by the response time coefficient of hillslopes to uplift K_u. We consider the response time of hillslopes, R_h (My), as the time it takes for hillslopes to react and reach and equilibrium with the modified tectonic and climatic conditions. The relationships between K_e, K_u, and R_h were calculated numerically (see Appendix for full details of this calculation).

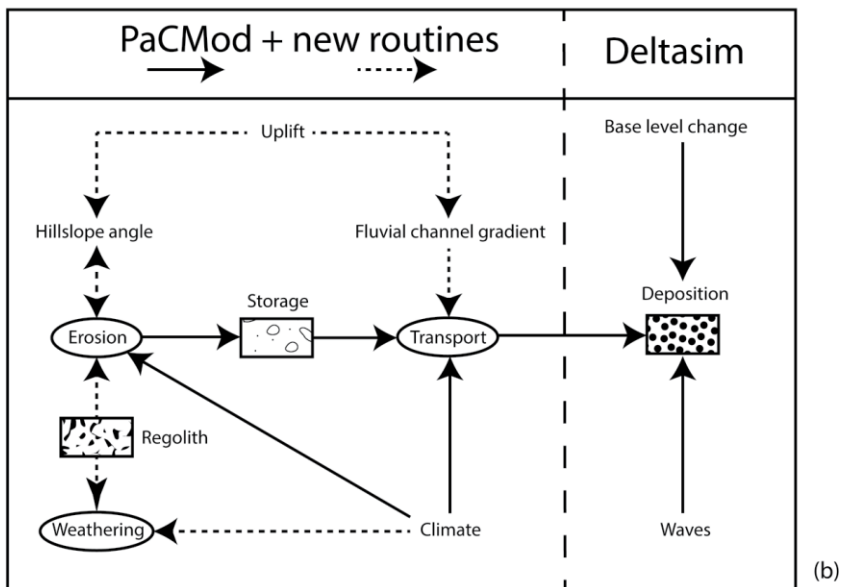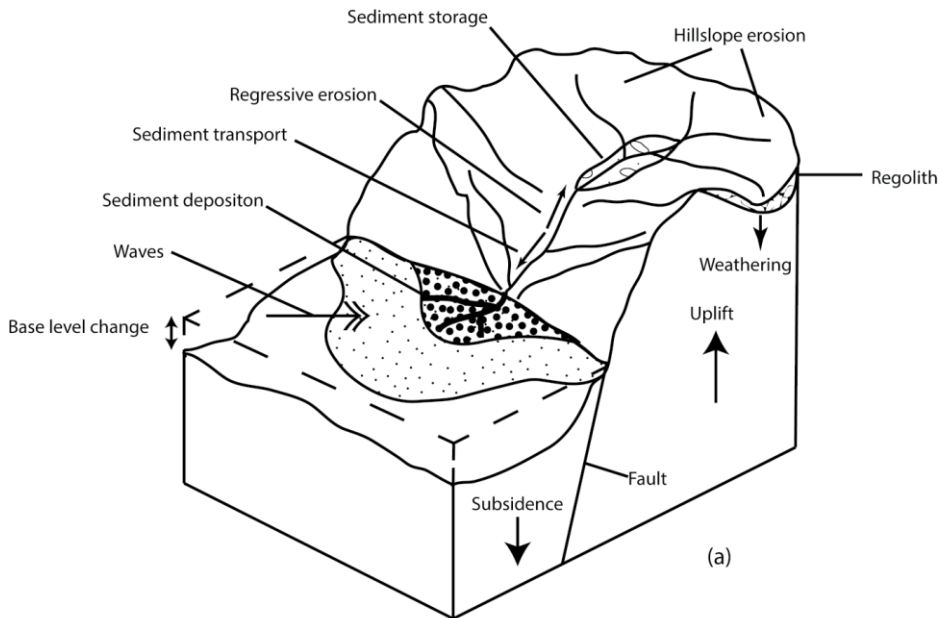**Figure 3.1**: (a) Geomorphic processes occurring in a real catchment-delta system and (b) modeled geomorphic processes in a catchment-delta system.

With our approach we are able to model both steady-state and transient-state landscape conditions. In steady-state conditions erosion rate is in equilibrium with uplift rate ($U = E$). In this case ($Ku{\cdot}U$)/ ($Ke{\cdot}E$) (Eq. 3.2) is unity, and denudation rate

is only dependent on uplift rate ($D = K_u \cdot U$). In transient conditions, D at any time depends on the balance between the imposed uplift and instantaneous catchment erosion rate and on their relative response times, controlled by K_u and K_e. The ratio K_u / K_e is thus a measure for the response time of the whole system to tectonic versus climatic perturbations. The maximum potential erosion rate in the model, E_p (mm year^{-1}) is calculated using Zhang's (2002) approach (eq. 3.3):

$$E_p = K_{soil} \cdot R^2 \cdot S_h^{1.67} + e^{0.07 \cdot Veg} \tag{3.3}$$

where K_{soil} is the soil erodibility coefficient, R is the mean yearly runoff (mm y^{-1}) and Veg is the average vegetation cover (0-1). We define E_p as the maximum achievable erosion rate, which is in the case of unlimited regolith availability. However, Equation 3 does not account for the availability of regolith for erosion. Field and modeling studies have indicated that under certain conditions such as with high erosion rate and resistant outcropping lithologies, regolith generation is much slower than the (potential) erosion rate (Tucker and Slingerland, 1997; Strudley et al., 2006). Therefore, only a minimum amount of regolith is available for erosion. This condition for hillslopes is usually defined as detachment limited. In contrast, if regolith generation is equal or exceeds erosion rate, conditions can be defined transport limited (Whipple, 2004). In our model, the actual erosion rate, E, is dependent on the potential erosion rate, E_p (mm year^{-1}), and on a regolith supply index SI (0-1), in order to simulate both detachment and transport limited conditions (eq. 3.4):

$$E = E_p \cdot SI \tag{3.4}$$

This means that actual erosion rates in the model approach the potential maximum only when regolith is abundant. We define the supply index as

$$SI = \frac{Reg}{R_t} \tag{3.5}$$

where Reg is regolith thickness (mm) and R_t is a (user-defined) regolith thickness threshold. SI decreases when Reg is below the critical regolith thickness threshold R_t, whereas it is assumed to equal unity when Reg is above R_t (unlimited regolith availability). Regolith thickness is modeled as the difference between weathering rate W and erosion rate E (eq. 3.6):

$$Reg = W - E \tag{3.6}$$

The weathering rate is given as:

$$W = SI \cdot \frac{(c3 \cdot I) \cdot e^{\frac{c4}{c5 \cdot Ta}}}{Reg}$$

(3.7)

where *c3, c4, c5* and *c6* are physical constants (Weltje et al., 1998), *I* is the soil infiltration rate (mm year^{-1}) and T_a (°C) is the yearly average catchment temperature. Equation 3.7 combines the Weltje et al. (1998) approach, which links weathering to climate, and the method of Strudley et al. (2006), which relates weathering to regolith thickness (c.f. Heimsath et al., 1999; Phillips et al., 2004). Equation 3.7 applies when $T_a > 1$°C. Finally, we model the fluvial channel gradient, S_f (m km^{-1}) at the catchment outlet, using a modified version of the steady-state formula of Whipple and Tucker (2002) which describes catchment slope-area scaling (eq. 3.8)

$$S_f = K_f \cdot \frac{U}{x} \cdot A^{-\theta}$$

(3.8)

where *A* is the catchment area referring to the catchment outlet, K_f is the response time coefficient of fluvial channel gradient to uplift, *x* is a dimensional coefficient of erosion (Whipple and Tucker, 2002), and θ is the concavity of the longitudinal river profile. The concavity of the longitudinal profile θ is defined by calibration (see Appendix). The relation between K_f and response time for fluvial channel gradient R_f (My) was also numerically constrained (see Appendix).

3.3. Impact of external forcing and catchment response time on sediment flux

Several field and modeling studies have demonstrated that the response of sediment flux and basin stratigraphy to external forcing is modulated by the fluvial system response time to external perturbation (Metivier and Gaudemer 1999; Whipple and Tucker, 1999; Allen 2008). Above, we have developed new modeling routines to simulate the inertial (damped) response of the fluvial system to perturbation using a spatially lumped approach in PaCMod (Forzoni et al., 2013). In order to test the model's ability to simulate catchment behavior in response to a change in boundary conditions, and to investigate the non-linear relation between external forcing and catchment response, we analyzed the impact of different boundary conditions on the output from the new routines. The external forcing signal used for these experiments was a time-dependent sinusoidal wave function combining climatic components (total annual precipitation P_a and catchment average temperature, T_a) and a tectonic component (uplift rate, *U*). The climate components varied with a periodicity of 200 ky, while the uplift rate component varied with a period of 500 ky. These input boundary conditions are shown in Figure 3.2.
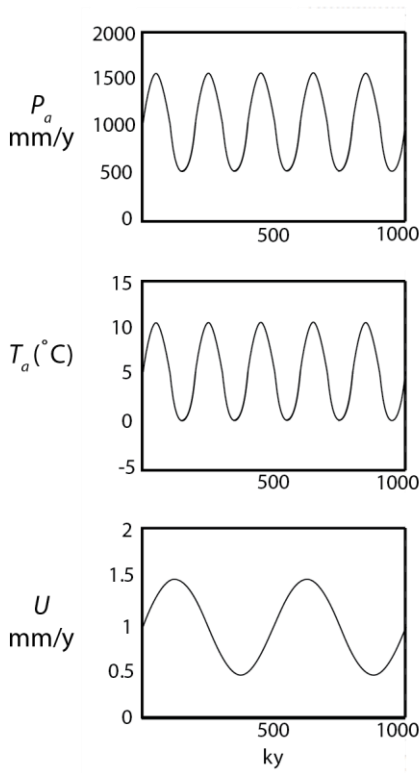
Figure 3.2: input boundary conditions used in the base case for sensitivity experiments. P_a is the total annual precipitation, T_a is the mean annual temperature and U is the uplift rate. In all sensitivity experiments we used K_{soil}=0.03, R_t=50, c1=15, and c2=0.2.

We subsequently ran three experiments in PacMod (Fig. 3.3): a base case with input boundary conditions shown in Figure 3.2 (P_a fluctuations between 500 and 1500 mm/y, average U = 1 mm/y), an experiment with high amplitude of P_a fluctuations (500-2500 mm/y) (case 1), and an experiment with high average U (3 mm/y) (case 2). Figure 3.3 illustrates the simulated evolution of hillslope angle S_h, potential erosion rate E_p, actual erosion rate, E, weathering rate W, and regolith thickness *Reg*, for case 1 and case 2 (green lines) compared to the base case (red lines). The input signal from these parameters was characterized by two periodicities, corresponding to the climatic and the tectonic forcing. In general terms, maximum erosion rates for both cases occurred during phases of high P_a and U (c.f. Fig. 3.3b and 3.3f).

In case 1, hillslope angle S_h (Fig. 3.3a) and regolith thickness *Reg* (Fig. 3.3d) decreased during periods of high erosion rate (Eq. 3.1 and 3.6), thereby acting as negative feedbacks. When weathering rate W (Figure 3.3c) could not keep pace with erosion rate, due to steep hillslope angle S_h, regolith thickness *Reg* went below

the regolith threshold R_t shown as a dotted line in Fig. 3.3d. This limited the regolith available for erosion, meaning that actual erosion rate E (solid green line, Fig. 3.3c) was less than potential erosion rate E_p (dotted green line, Fig. 3.3c) (c.f. eq. 3.4 and 3.5). Higher precipitation amplitudes caused higher E and a small decrease of S_h compared to the base case, shown in red. However, while the amplitude of the input forcing had almost doubled with respect to the base case, the amplitude hillslope angle S_h response remained similar to the base case.

In case 2, hillslope angles and regolith thickness also acted as negative feedback to erosion, similarly to case 1. In case 2, high average uplift rate U induced much steeper hillslope angles compared to the base case and case 1 (Figure 3.3e). As a result, regolith thickness (*Reg*) went considerably below the threshold, R_t, limiting the regolith available for erosion (Figure 3.3h), and thus actual erosion rate, E (Figure 3.3f). We found that E transiently decreased while uplift rate U and P_a continued to increase (t_a black marker line, Fig. 3.3f), and thus actual erosion (green line) was even lower than in the base case (red line) for parts of the model run. In addition, the timing of the erosion rate peaks in case 2 preceded the peaks in the base case by approximately 15 Ky (t_b red marker line, Fig. 3.3f) – this was driven by the fact that regolith thickness fell below the threshold value, R_t, earlier in the tectono-climatic cycle for case 2 relative to the base case. These sensitivity analyses show that while the input climatic and tectonic signals were transmitted to the model output, the transmission was buffered by hillslope angle and regolith availability response to changes in erosion rates. Finally, the exceeding of the regolith threshold induced a delayed and non-linear response of actual erosion rates to changes in precipitation and uplift.

After testing the sensitivity of the simulated hillslope angle, erosion, weathering and regolith thickness to changing boundary conditions, we investigated how the response time coefficients affect the sediment flux out of a theoretical catchment, applying the full integrated version of PaCMod (c.f. Forzoni et al., 2013), including our new routines. We ran three different scenarios, each with a 100 ky periodicity in climatic fluctuations and a 500 ky periodicity in tectonic fluctuations, and we applied different response time coefficients in each case. The variations in landscape morphological parameters and sediment flux as a result of tectonic and climatic changes are shown in Figure 3.4.
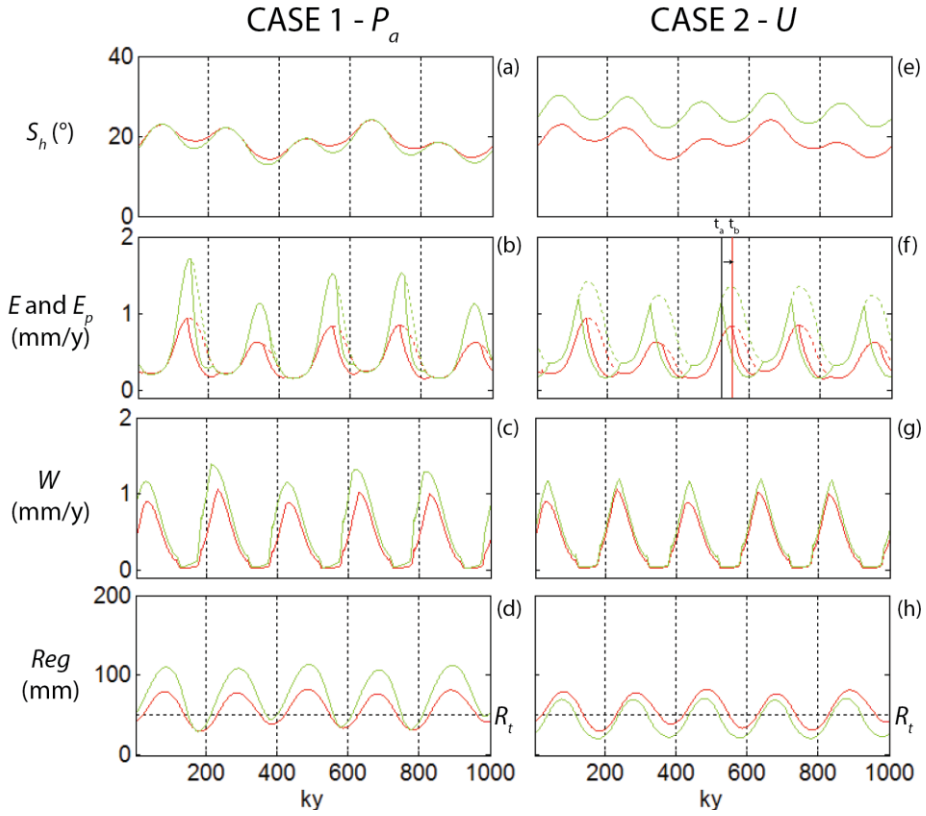
Figure 3.3: impact of total annual precipitation rate P_a (case 1), and uplift rate U (case 2) on average hillslopes angle S_h, potential erosion rate E_p (dotted line), actual erosion rate E (solid line), weathering rate W and regolith thickness Reg. When Reg is above the regolith threshold R_t, E equals E_p, while when Reg is below R_t, E is lower than E_p. The base case output is displayed in red, while the output for the three different cases is displayed in green. We assumed that half of P_a is able to infiltrate under the ground surface, and thus contribute to the infiltration rate.

In scenario S1, the response times of hillslopes and fluvial channels to uplift and erosion were shorter than the 100 kyr climatic and 500 kyr tectonic forcing wavelengths (i.e. the runs had small K_u, K_e and K_f, Eq. 3.2 and 3.8). In these circumstances, hillslope angle S_h and fluvial channel gradient S_f reacted without inertia to forcing (Figs 3.4a1 and 3.4b1). Consequently, both the tectonic and the climatic signals were transmitted via the catchment erosion rate E to the bedload sediment supply Q_{bss}, and the transport capacity TC (Figs 3.4c1 and 4d1), with high transport capacity during periods of high precipitation and high fluvial gradient, S_f. Consequently, we found that bedload Q_{bed} and suspended load Q_{susp} fluxes were a combination of the short wavelength climatic signal and the long wavelength tectonic signal (figs 3.4e1 and 3.4f1). In scenario S2, with small K_e (response time

coefficient of hillslopes to erosion), but long K_u and K_f (response time coefficient of hillslopes to uplift and response time coefficient of fluvial channel gradient to uplift, respectively) the tectonic signal was not transmitted to the hillslope gradient, S_h (Fig. 3.4a2). Additionally, the tectonic signal amplitude was significantly attenuated in fluvial channel gradient, S_f. (Fig. 3.4b2). Consequently, Q_{bed} and Q_{susp} were characterized only by short, climate-related wavelengths (Figs 3.4e2).

Finally, we considered the case of a long response time of the hillslope to erosion (large K_e, but small K_u and K_f, scenario S3). In this case, the climatic signal was not transmitted to the hillslope gradient, S_h (Fig. 3.4a3). However, it was still propagated to E, Q_{bed}, and Q_{susp} (Figs 3.4c3, 3.4e3, and 3.4f3), because of the climatically-driven variation in runoff, and vegetation cover (*Veg* parameter, Equation 3.3). Due to the damped response of S_h, the hillslopes did not act as negative feedback for erosion. This resulted in higher-amplitude short-wavelength fluctuations in the sediment flux signal, compared to scenario S1, with both "tectonic" and "climatic" signals present in bedload and sediment discharge (Figs 3.4e3 and 3.4ef). These scenarios therefore suggest that long response times to tectonic changes buffer the transmission of a tectonic signal to the sediment export from catchments, whereas climate forcing is more consistently transmitted to sediment flux because runoff and vegetation changes affected erosion rates, even without changes in landscape morphological parameters, i.e., hillslope angle and fluvial channel gradient.
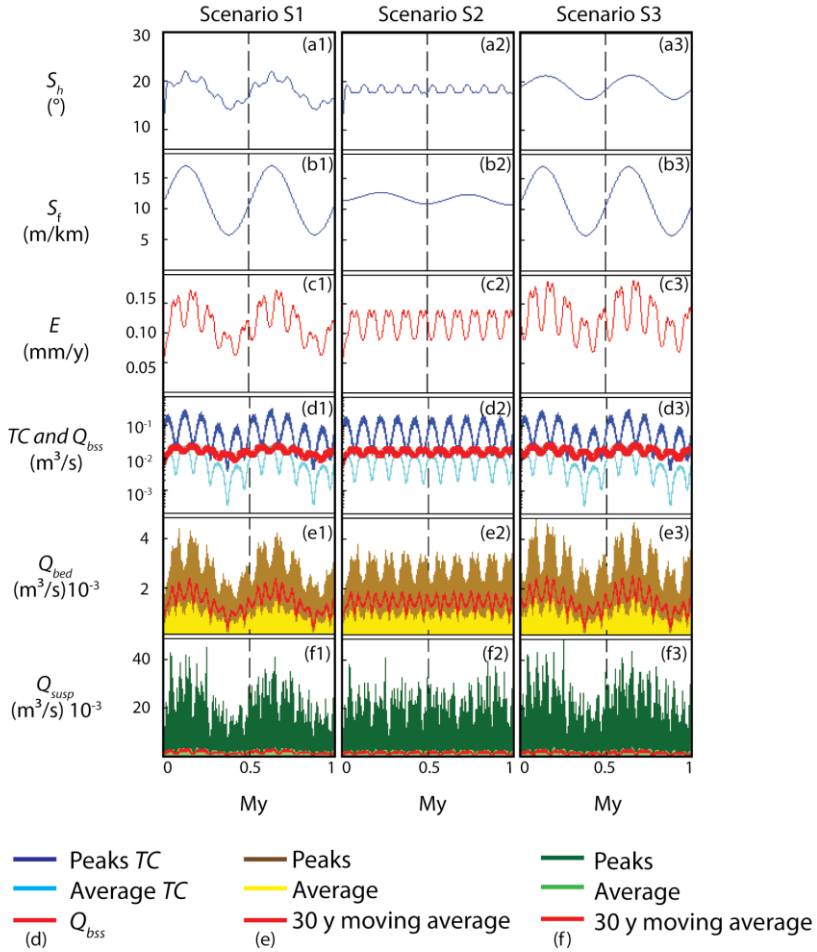
Figure 3.4: impact of response times on catchment morphology. Scenario S1 (short response time to tectonics): K_u =50; K_e =10; K_f =50. Scenario S2 (long response times to tectonics): K_u =1000; K_e =10; K_f =700. Scenario S3 (long response times to climate): K_u =50; K_e =500; K_f =50. All values are in ky. (a) Hillslopes angle; (b) fluvial channel gradient (c) actual erosion rate; (d) bedload sediment supply Q_{bss} and transport capacity TC; (e) bedload; (f) suspended load. Erosion rates and Q_{bed} 30 y moving average signals are characterized by two peaks within each climatic fluctuations, which are a consequence of regolith availability changes.

3.4. Impact of catchment response time on the sediment flux from the Celano catchment, central Italy

We applied the full integrated version of PaCMod to investigate the impact of catchment response time on the sediment flux from a real-world catchment in Abruzzo, Central Italy: the Celano catchment. We chose this catchment because it has been extensively studied, and its tectonic evolution is well constrained (Whittaker et al., 2007; Attal et al., 2008; Cowie et al., 2008; Whittaker et al., 2010). The Celano catchment is located in the footwall of an active normal fault, whose slip-rate increased 0.7 Ma ago in response to fault interaction and linkage. The increase in fault slip rate induced the upstream migration of an erosion wave front, leading to the steepening of hillslope angle and fluvial channel gradient, the generation of detachment-limited conditions in the lower reach of the catchment, and the formation of a substantial knickpoint in the fluvial longitudinal profile (Whittaker et al., 2010).

We ran a 3 My simulation, using the oxygen isotopes curve from Zachos et al. (2001) as the main climatic signal input, and the data from Whittaker et al. (2010) for the tectonic history (Fig. 3.5). To do this effectively, we empirically constrained the response times coefficients (K_e, K_u, and K_f, Eq. 3.2 and 3.8), based on the area of the catchment affected by the tectonically-induced wave of incision, so that our model was calibrated to the real-world data (Whittaker et al., 2010). The proportion of the catchment affected by the wave of incision is a function of knickzone migration rate; full details of our response time calculations are provided in the Appendix. We calculated the response time of hillslope angle R_h to be 4.6 My, and the response time of fluvial channel gradient R_f to be 2 My. This latter calibration is consistent with published field data (c.f. Whittaker et al., 2007). Next, we calibrated the hillslope parameters *c1* and *c2* (Eq. 3.1), and the concavity of the longitudinal river profile θ (Eq. 3.8), based on the change in average hillslope angle and fluvial channel gradient after 0.7 My BP. Finally, we calibrated regolith threshold R_t, by comparing the modeled and the measured excess volume of material eroded from the lower reach of the Celano catchment, *EV*, previously estimated by Whittaker et al (2010). Using these calibrations, we were then able to model, in PacMod, how sediment export and catchment morphology in a drainage basin like the Celano catchment had evolved in the last 3 My.

Figure 3.6 illustrates the evolution of morphological parameters and sediment flux from the model, over the last one million years of the 3 My PaCMod simulation using the Celano catchment calibrations as discussed above and in the Appendix. When the fault uplift rate, *U* increased at 0.7 My BP, average hillslope angle S_h (Fig.

3.6a, Eq. 3.1 and 3.2), channel gradient, S_f (Fig. 3.6b, Eq. 3.8) and potential erosion rate E_p (Fig. 3.6c, Eq. 3.3) gradually increased, which led hillslopes to detachment-limited conditions with limited regolith availability. Consequently, the modeled actual erosion rate, *E,* (red line, Fig. 3.6c, Eq. 3.4) was lower than the potential erosion rate E_p (green line, Fig. 3.6c). Before 0.7 Ma, bedload sediment supply Q_{bss} exceeded peak transport capacity *TC* (Fig. 6d). After 0.7 My BP, peak *TC* rose up to the same level of Q_{bss}, due to higher fluvial channel gradient S_f (Figure 3.6b). The switch from transport-limited to supply-limited conditions is both a function of the imposed shorter response time of fluvial channel gradient compared to hillslope angle and of the power relation between hillslope angle and transport capacity. Both bedload Q_{bed} (Fig. 3.6e) and suspended load Q_{susp} (Fig. 3.6f) gradually increased from 0.7 My BP, following the erosion rate trend.

Superimposed on this long term tectonic trend, driven by the increase in uplift rate at 0.7 Ma, climatic changes (Fig. 3.5) gave rise to high frequency-high amplitude fluctuations in the model output, with high *E*, low *TC*, high sediment load during cold-dry phases (glacials), and vice versa in warm-moist phases (interglacials). The 100 ky periodicity characterizing bedload and suspended load signal in the last 700 ky is clearly correlated with the periodicity of the climatic signal. During cold glacial periods, actual erosion rate *E* was lower than potential erosion rate E_p (Figure 3.6c), due to limited regolith availability on hillslopes (detachment-limited conditions), whereas *E* was almost equal to E_p during interglacials. The enhanced amplitude of climate-driven erosion cycles after 0.7 Ma was a result of the higher amplitude and wavelength of climatic fluctuations (Fig. 3.5).

Our model results suggest that erosion rates, averaged over the whole catchment, in for the Celano system gradually increased after the acceleration in fault slip-rate at 0.7 My BP, from 0.2 mm/y to 0.4 mm/y at present. These values are comparable to the long term average weathering rate calculated by Tucker et al., (2011). Due to the increase in transport capacity at 0.7 My BP, coarse sediments started being transported through the system. This is in accordance with previous modeling work and field data from Densmore et al. (2007) and Whittaker et al. (2010). Our simulations indicate that the maximum magnitude of sediment export from the Celano catchment has not yet been reached in the 0.7 My since the initial perturbation, and that the sediment flux response is delayed with respect to fault-slip rate increase (c.f. Armitage et al., 2011). The implications of such a delay for the basin stratigraphy are discussed below.
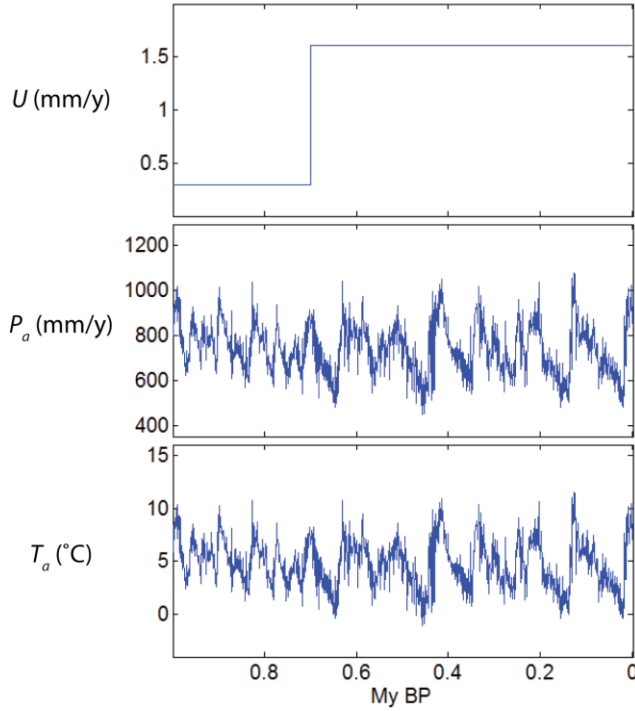
Figure 3.5: input for the Celano catchment sediment flux reconstruction in the last 1 My. The uplift rate signal U is based on Whittaker et al. (2010) and Tucker et al. (2010). We calibrated the Zachos curve (Zachos et al., 2001) based on present day temperatures and on palaeo-temperature reconstructions for the Last Glacial Maximum LGM (Allen et al., 2000; Tucker et al., 2010). We linked the total annual precipitation signal P_a to the mean temperature signal T_a and calibrated it using present day annual precipitation and LGM reconstruction (Allen et al., 2000; Tucker et al., 2010). We used the following parameters values in PaCMod: D_{50} (mm) = 40 mm (Whittaker et al., 2010); K_{soil} = 2 $\cdot 10^{-2}$; lithology coefficient L = 1 (Syvitski and Milliman, 2007); groundwater residence time GRT = 100 days; snow melt coefficient SMC = 0.5; precipitation gradient P_g = 2$\cdot 10^{-4}$; regolith threshold R_t = 45 mm; bedload delay K_b = 100 y.
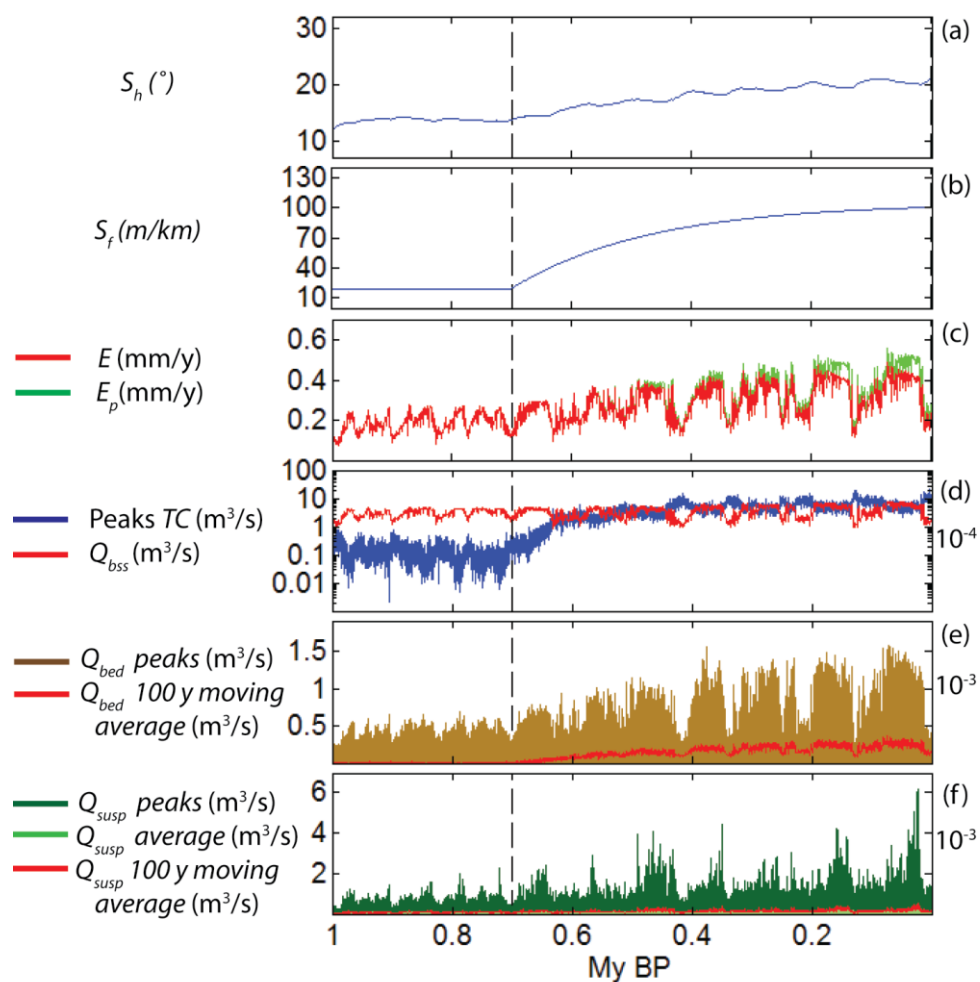
Figure 3.6: PaMod output from the Celano catchment sediment flux reconstruction in the last 1 My. Sh = average hillslopes angle; Sf = fluvial channel gradient; E = actual erosion rate; Ep = potential erosion rate; TC = bedload transport capacity; Qbss = bedload supply from hillslopes; Qbed = bedload; Qsusp = suspended load.
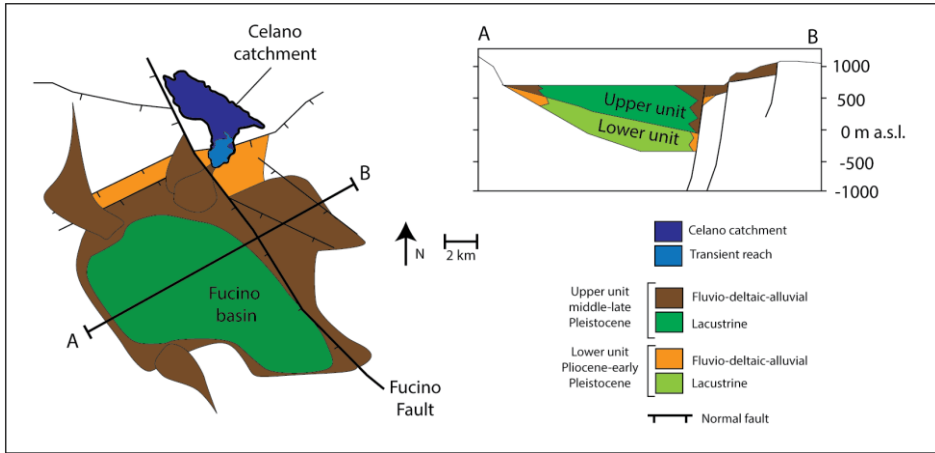
Figure 3.7: geological map of the Fucino basin, geological cross section across the basin, and location of the Celano catchment. This figure is based on Cavinato et al., 2002.

3.5. The stratigraphic signature of catchment response time

After reconstructing the sediment flux from the Celano catchment and noting that our model produced results that are comparable to existing field studies, we chose this catchment as a representative starting point for further analysis. We simulated the evolution of a delta fed by the Celano catchment, for instance entering the neighboring Fucino basin, using DeltaSim, a two dimensional process-response model. DeltaSim simulates erosion and sedimentation in a delta-shelf environment along a 2D longitudinal profile, based on simplified diffusion rules of cross-shore sedimentation (Overeem et al., 2003; Hoogendoorn et al., 2008) (see the Supplementary Information for the model overview). The purpose of this exercise was not to slavishly reproduce the observed stratigraphy in the basin, because of the paucity of detailed stratigraphic and borehole data, and because of the simplified modeling approach taken here. Instead we used the Celano-Fucino system a semi-realistic scenario to model the effect of catchment response times on typical delta stratigraphy that could be compared in general terms with a known example.

The Fucino basin (Fig. 3.7) is an intramontane half-graben, in the central part of the Apennines chain, Italy, which is filled by Plio–Quaternary alluvial and lacustrine deposits, (Cavinato et al., 2002). The basin sediment fill is subdivided into two units: the lower unit, Pliocene-Lower Pleistocene in age, with a 250 m maximum thickness, and the upper unit, deposited during the Middle Pleistocene-Present, reaching a maximum thickness of 700 m close to the major normal fault, the Fucino

Fault. The lower unit is characterized by lacustrine clays and silts, fluvial silts and sands, and alluvial fan conglomerates. The fluvial deposits were part of fluvio-deltaic systems prograding towards the basin center. The alluvial-fan conglomerates were formed by tectonically-driven mudflows and debris-flows. During this phase, the basin was overfilled, because regional uplift exceeded normal fault subsidence (Cavinato et al., 2002).

At around 0.7 My BP, the basin underwent a transition from overfilled to under-filled, as a result of increasing fault-slip rate, which led to increased accommodation space being generated (Whittaker et al., 2010; Armitage et al., 2011). During this phase the lake occupying the basin reached its maximum extent. In the outcrops at the basin edges, the transition from lower to upper unit is marked by an erosional unconformity. During the middle and late Pleistocene lacustrine deposits were accumulated in the central part of the basin, while fan-deltas (sands and silts) developed on the basin edges (upper unit). The fan-deltas prograded towards the basin center and, at the basin edges, the sandy-silty deposits graded upward to alluvial fans gravel and pebbles (upper Pleistocene). We compared the stratigraphy on the hanging wall in northern edge of the basin, near the Celano catchment outlet (Fig. 3.7), with DeltaSim simulations.

We ran three PaCMod-DeltaSim experiments using the input from Figure 3.6, and applying three different response times of hillslopes and fluvial channel gradient (R_h and R_f respectively). In DeltaSim we simulated an increase in accommodation space at 0.7 My BP by an increase in water level rise to mimic subsidence. The model output is visualized as 2D cross sections across the delta, and as 1D synthetic borehole logs with grain size (Fig. 3.8a). In all experiments, the simulated delta stratigraphy was characterized by two major sedimentary units: a 90 m thick, fine-grained, prograding lower unit (LPU), and a 210 m thick, coarser-grained, prograding upper unit (UPU). These two units were separated by a 40 m thick retrograding unit (RU). Superimposed on this general trend, we note that all borehole logs retain the 100 ky frequency climatic and sediment flux periodicity.

In scenario C1, we applied the response times calculated for the Celano catchment as described above. The resulting shoreline trajectory followed three steps: (1) slow ascending regression (3.0-0.7 My BP), (2) fast transgression (0.7-0.55 My BP), and (3) fast ascending regression (0.55 My BP-Present). The major shift from step 1 to step 2 was a direct result of long catchment response time, and corresponded to the transition from filled to under-filled conditions at 0.7 My BP. While the increase of accommodation affected the delta immediately, the increase in sediment supply

(shown in Figure 3.6) was slow and could not keep pace with lake-level rise. Only at 0.55 My BP did the sediment supply start to fill in the accommodation space and induced a regression. This indicates that the delayed response of the catchment to tectonic perturbation importantly affects the delta stratigraphic architecture.

The synthetic borehole log for scenario C1 shows a gradual coarsening upward trend in the upper prograding unit UPU, which is caused by the gradual increase in sediment supply and by delta progradation, and by second order grain size fluctuations related to climate-induced sediment and water flux variability.

In scenario C2 we used shorter response times than in scenario C1 ($R_h = R_f = 500$ ky). In this case, the coastline migrated only 1 km landward during transgression (step 2). After that, the delta aggraded with only minor progradation. In scenario C3, with very short response times ($R_h = R_f = 100$ ky), the coastline migrated only few hundreds of meters during transgression, and after that it remained stable until the end of the simulation. Due to the short extent of shoreline migration during transgression in the scenario C2 and C3, accumulation between 0 and 2 km along the x axis of the DeltaSim model output occurred in sub-aerial conditions during both simulations. As a consequence, in scenario C2 and C3 any well log between 0 and 2 km could not record sequence stratigraphic surfaces forming in subaqueous conditions, such as the ravinement erosion surface, resulting from sediment reworking by waves during water level rise. Finally, while in scenario C2 and C3 the shoreline position remained relatively stable, as a result of the equilibrium between accommodation and sediment supply, in scenario C1 the equilibrium was not achieved. Consequently, in scenario C1 the UPU in the synthetic borehole log was characterized by a coarsening upward sequence, which is only partly visible in scenario C2 and is completely absent in scenario C3. These scenarios demonstrate that sediment flux histories, driven by tectonic and climatic forcing can produce stratigraphies which are very different. Consequently, catchment response times determines how efficiently, and the characteristics with which the upland "sediment factory" fills available accommodation space.
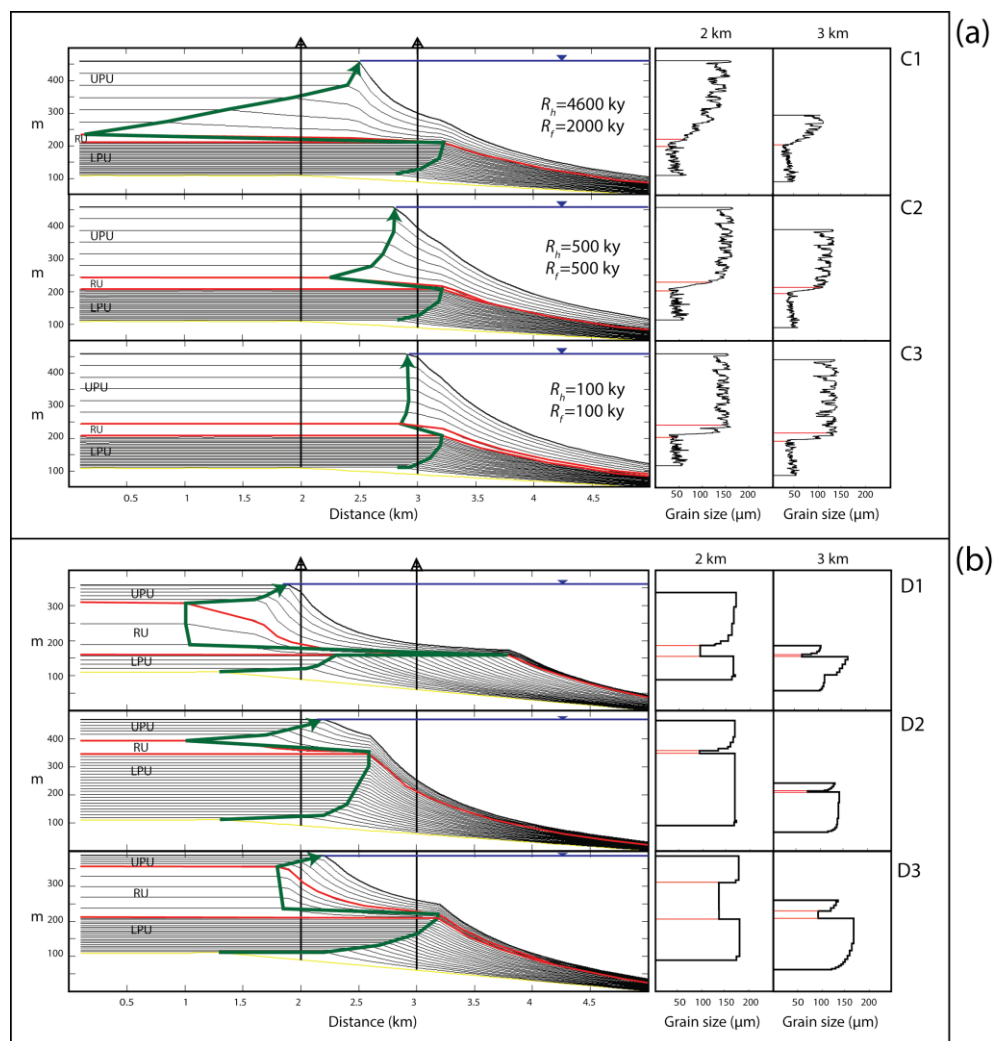
Figure 3.8: longitudinal 2D cross-section and synthetic borehole logs for scenarios (a) C1, C2 and C3, and (b) D1, D2, and D3. The shoreline trajectory is displayed with a green arrow. The boundary between lower and upper sedimentary unit is shown in red. Black lines indicate the delta profile every 100 ky. UPU=upper prograding unit; RU=retrograding unit; LPU=lower prograding unit. The boundaries between lower prograding, transgressive, and upper prograding sedimentary unit are shown in red. For all scenarios we used a time interval of 3 Ma. The simulated stratigraphy for all scenarios is described in the text.

How unique is the stratigraphic response to tectonics in the catchment? Does the delay of sediment flux from the simulated "Celano" catchment, induced by long response times, produce a distinctive stratigraphic pattern, distinguishable from

the product of other forcing mechanisms? Or can we produce similar looking stratigraphies by changing other boundary conditions, such as base level? To answer these questions, we ran different scenarios in DeltaSim with variable water level (i.e., base level) but with constant sediment flux (Fig. 3.9), in order to attempt to reproduce the stratigraphy in scenario C1. We considered scenario C1 to be our target, because this was generated using responses times which were calibrated to the real Celano catchment, and because among the three previous experiments, it is the one which better reproduced the known gradual coarsening upward trend in the upper prograding unit in the real Fucino Basin and the relative sedimentary units' thicknesses. We note that shoreline trajectories followed approximately the same trend in all three scenarios, but that the detail of these and the stratigraphic geometries produced differed markedly, as shown in Figure 3.8b.

In scenario D1 with a complex base level history, when water-level fell at 2.2 My BP (c.f. Fig. 3.9), the delta experienced progradation and erosion (descending regressive trajectory, not intersecting depositional slopes), and the shoreline migrated two kilometers basinward. Afterwards, a major transgression occurred during fast water level rise from 0.7 Ma, and a thick retrograding unit RU was deposited in the landward part of the delta. Finally, the delta prograded again during the recent slow sea level rise. Scenario D2 was characterized by water level rise throughout the whole simulation, with fast rise between 700-550 ky BP. In this case the shoreline trajectory was comparable to scenario C1, but the lower prograding unit LPU was much thicker than the upper prograding unit UPU, opposite to the scenario C1. Finally, with a very fast water-level rise in the time interval 700-550 ky BP (scenario D3), the thickness of the LPU was comparable to scenario C1, but the RU was much thicker.

These results suggest that the shoreline trajectory and the unit thicknesses of the Fucino basin, approximated by scenario C1, were not likely to be the result of water-level change only (i.e., creation of accommodation space), but are most easily and satisfyingly explained by the coupled response of the catchment-depositional system to tectonic perturbation, which included delayed sediment delivery from eroding upland to the basin. In other words, the moderating effect of response time on sediment supply produced a characteristic stratal architecture, which was a complex combination of delayed sediment supply and creation of accommodation. These model results suggest that, if different observations and sources of information are available, such as trajectory analysis, grain size, and thickness of sedimentary units, we should be able to distinguish stratal architecture from the product of a single forcing mechanism, such as water-level, from those created by

the coupled generation of accommodation and time-delayed surface processes response. Although we aimed to produce generic insights, rather than to reproduce explicitly the Fucino basin stratigraphy, we argue that a combination of scenario C1 and D1 might be the best ones to explain the observed stratigraphic data. In particular, a phase of water-level fall might be the cause for the erosional unconformity between the lower and the upper unit, and the delayed increase in sediment supply from the catchment contributed to the coarsening upward and fan delta progradation in the upper unit.
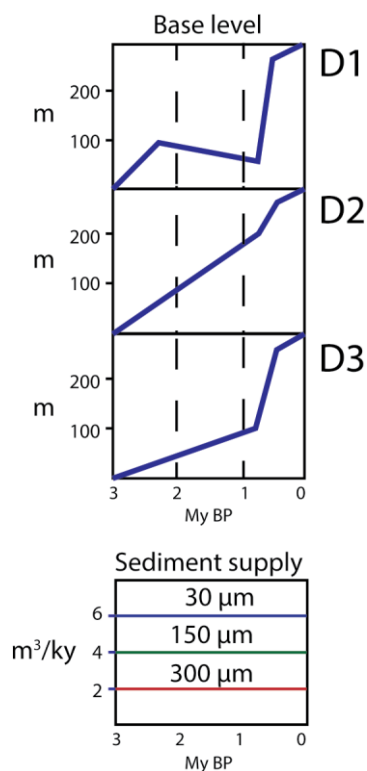
Figure 3.9: input sea level and sediment supply boundary conditions for scenario D1, D2, and D3. Sediment supply (three grain size fractions) is constant throughout all three simulations.

3.6. Discussion
3.6.1. Summary and model validity

Our results indicate that PaCMod is able to capture a non-linear response of a catchment to external forcing, and that amplitude and timing of erosion rate pulses are modulated by hillslope angle and regolith availability, which both act as negative feedbacks mechanisms. The modeling simulations confirm the idea that

long response times to tectonics buffer the transmission of a tectonic signal to sediment flux and stratigraphy, whereas long response times to climate can amplify the climatic signal (Densmore et al., 2007; Allen, 2008). Our model test on the Celano catchment (Central Italy), showed that the differential response of geomorphic elements to tectonic and climatic forcing induces a complex sediment flux output. In addition, model outcomes are comparable to previous studies on the area (Whittaker et al., 2010; Tucker et al., 2011).

Finally, DeltaSim simulations suggested that (1) the delayed response of sediment supply compared to accommodation space creation, which was induced by long catchment response time, significantly affects shoreline trajectory and the visibility of sequence stratigraphic surfaces in vertical borehole logs; (2) catchment response time moderates sediment supply and, combined with accommodation, produces a characteristic stratal architecture, which is distinguishable from the product of a single forcing mechanism, such as relative water-level. These results are important because they indicate that not only can we effectively apply our model for palaeo-sediment flux reconstructions, but we can also use it to gain new insight on the propagation of a tectonic-climatic forcing to sediment flux and to basin stratigraphy in a fluvio-deltaic setting. However, before discussing the implications our results in more detail, it is important to acknowledge that this kind of model is based on some important assumptions, three of which we discuss below.

(i) Our model uses a spatially lumped approach. All parameters and processes are averaged into single parameters. Such an approach neglects the detailed properties and processes heterogeneities across the catchment, as well as important processes such as glacial erosion, sediment sorting and grinding. Nevertheless, our model has the advantage of being parsimonious with required input, modeled processes, and processing capacity, in contrast to more complex cellular models, and is therefore particularly suited to ancient sediment routing systems.

(ii) Hillslopes and fluvial channel are treated as separate domains, whereas in reality they are coupled to various degrees (Harvey, 2002; Fryirs et al., 2007). Our approach neglects the control of hillslopes on fluvial channel gradient itself (e.g., due to downhill flux of sediment).

(iii) The increase of average hillslope angle is controlled by uplift and erosion rate. Previous research has shown a correlation between these three parameters (Ahnert , 1970; Whipple and Tucker, 1999; Montgomery and Brandon, 2002; Whipple, 2004; Roering et al., 2007). In the calibration section (Appendix) we attempted a

quantitative correlation of these variables, based on real catchments in Central Italy. Future research should perform a wider mathematical/ statistical analysis on a larger catchment dataset, in order to constrain the scaling coefficients between hillslope angle, uplift, and erosion rate, as well as regolith threshold. Nevertheless, we believe the model produces robust results, because it is able to simulate the first order response of landscape morphological parameters to external forcing, and to produce results comparable to geomorphological and stratigraphic observations.

3.6.2. Transmission of external forcing to sediment flux from the catchment

In a similar way to previous research (Tucker and Slingerland, 1997; Metivier and Gaudemer 1999; Whipple and Tucker, 1999; Allen 2008; Coulthard and Van de Wiel, 2013), our results show that long response times to tectonic changes buffer the transmission of a tectonic signal to the sediment export from catchments. On the other hand, climate forcing was consistently transmitted to sediment flux because environmental changes affected erosion rates even if hillslope angle S_h remained constant or responded slowly. Indeed, long response times of hillslopes to erosion amplified the input climatic signal, because hillslopes did not act as negative feedback to erosion.

Previous studies have illustrated how the sensitivity of hillslopes to external forcing is proportional to the degree of coupling of the fluvial system geomorphic elements (Fryirs, 2013), such as hillslopes and fluvial channels (Harvey, 2002; Macklin and Woodward, 2009). The degree of coupling varies both in time and in space across the catchment. A high degree of coupling is usually observed in the headwaters of a catchment (high relief), during high magnitude events like big floods (Fryirs, 2013), and in catchments characterized by easily erodible outcropping lithologies (Cowie et al. 2008). In our model, we have chosen two different response time coefficients K_f and K_h, for fluvial channel and hillslopes, respectively, in order to be able to simulate the various degrees of coupling.

In the simulation of the Celano catchment sediment flux, we observed that, even though we assigned similar response time coefficients, the impact of fluvial channel gradient on bedload transport capacity is much higher than the impact of hillslope angle on erosion rates (Figure 3.6). This caused the sudden switch from transport to supply-limited conditions at 0.7 My BP. This implies that the sediment flux signal recorded before 0.7 My is largely controlled by the fluvial discharge signal, whereas after 0.7 My BP, the sediment flux variations are primarily controlled by hillslope erosion. We suggest that, in the case of de-coupling between

hillslopes and fluvial gradient, the sediment flux response to external forcing might be even more complex.

So far in this section, we have addressed the propagation of a forcing signal through erosional processes. However, in real catchments, the transmission of a forcing signal to sediment flux is also controlled by sediment routing and storage within the catchment, especially in presence of extensive floodplains (Metivier and Gaudemer, 1999; Carrettier and Lucazeau, 2005; Forzoni et al., 2013). We propose a conceptual relation for the transmission of a tectonic perturbation to the sediment flux signal in catchments of equal size, as the balance between knickzone migration rate, controlled by erosion efficiency and uplift, and sediment storage. The transmission of a forcing signal is enhanced by fast knickzone migration rate (Figure 3.10), which is boosted by high degree of coupling in the fluvial system Fryirs (2013), high uplift rates, and erosional efficiency, i.e., higher runoff and/or weaker lithologies (Whittaker and Boulton, 2012).

On the other hand, sediment storage within the catchment buffers the signal transmission to the sediment flux and to stratigraphy (Metivier and Gaudemer, 1999; Castellort and van Den Driessche, 2003; Allen, 2008). Consequently, large drainage basins with plenty of accommodation space (such as the Amazon and Indus rivers), are likely to buffer the external forcing signal more effectively than smaller catchments with narrower floodplain, such as the Orange River, and even more effectively compared to mainly detachment-limited catchments in mountainous area, such as the Celano catchment. This means that even if short climatic changes easily affect erosion rates and water discharge in the uplands of a catchment, they may be less likely to affect the sediment flux to a marine basin, compared to longer wavelength climatic or tectonic changes. It also implies that workers should be careful about specifying the response timescale and length-scale to external perturbation when evaluating "catchment sensivity" to climate or tectonics.
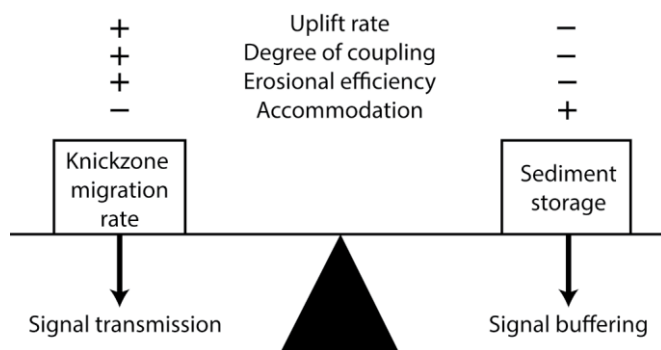
Figure 3.10: conceptual relation for forcing signal transmission or buffering in a catchment

3.6.3. Delayed delivery from the sediment factory: impact on stratigraphy

As we have seen above, because of the damped (inertial) response of the landscape system to external perturbation, the volumetric export of sediment from catchments to neighboring depositional basins can be delayed relative to the timing of a tectono-climatic perturbation. In the case of the modeled Celano catchment, the maximum magnitude of sediment export from the catchment was delayed with respect to the relative base level change, and has not yet been reached after 700 ky post the initial perturbation. Previous studies have shown how this delayed relationship results in different stratigraphic patterns in fluvial and deltaic environments (Van den Berg and Postma, 2008; van Strien, 2010; Armitage et al., 2011; Rohais et al., 2012).

Our experiments indicated that the sediment supply delay within the "sediment factory" with respect to base-level changes can significantly affect shoreline trajectories and stratigraphies (Fig. 3.8). Importantly, we find that only scenarios that explicitly incorporate the buffered sediment supply response of the catchment to a change in fault slip rate can satisfyingly explain real-world examples where stratigraphy records the transient response of a sediment routing system to an external perturbation (c.f. Cavinato et al., 2002; Whittaker et al., 2010). We also find that the lateral extent of a sequence stratigraphic surface, vertical grain size trends in borehole logs, and the relative thickness of the sedimentary units at different locations in a fluvio-deltaic system are indicative of different catchment responses and base level histories. This supports the idea that stratigraphic architectures in basins are likely to be diagnostic of external forcing and response times. This implies that using different observations and sources of information available, such as trajectory analysis, grain size, and thickness of sedimentary units, we might be

able distinguish such stratigraphic architecture from the product of single forcing mechanisms, i.e. base-level changes, sediment supply, and subsidence (Charvin et al., 2011).

In general, our model is able to simulate the basic response of catchment morphology and sediment flux perturbed by climate and tectonics. Its limited inputs and fast processing speed make it particularly suitable for palaeo-catchment applications, where it can be applied using a forward modeling approach to reconstruct sediment flux from upland areas to basins. Future research might initially focus on small transient landscape catchments (Snyder et al., 2003; Cowie et al., 2008; Whittaker and Boulton, 2012), in order to quantitatively disentangle the impact of climate, lithology and uplift rate on catchment response time. First, a database of transient landscape catchments with different climatic, lithological, morphologic and tectonic conditions should be built, by field and DEM analysis, extending Whittaker and Boulton (2012) data. Next, the data should be statistically analyzed in order to extract a mathematical relation between response time and boundary conditions. Finally, such relation should be implemented in PaCMod, which can be applied for palaeo-applications.

3.7. Conclusions

We developed and tested new numerical modeling routines using a spatially-lumped approach to model the evolution of landscape morphology and erosion rate in a catchment over time, in response to both tectonic and climatic forcing. We integrated these routines into PaCMod, a numerical model calculating sediment flux from a catchment, recently presented by Forzoni et al. (2013). Using this approach, we investigated the impact of tectonic and climatic forcing on sediment flux for synthetic scenarios. Next, we applied the model to reconstruct the expected sediment flux from a tectonically perturbed catchment in Central Italy, and investigate the impact of catchment response time on the sediment export over time. Finally, we coupled the fully implemented version of PaCMod to DeltaSim, a process-response model simulating fluvio-deltaic stratigraphy, to investigate the impact of catchment response time on stratigraphy, using synthetic scenarios and a real world system (Fucino Basin, Central Italy) as an exemplar. Our results showed that:

(i) Although PaCMod is a spatially lumped model with a high level of parameterization, the model is able to capture the first order non-linear response of a catchment to external forcing, caused by the interaction of

processes operating at different spatial and temporal scales, and by feedback mechanisms

(ii) Long response times of hillslopes and fluvial channel to tectonics buffer the transmission of a tectonic signal to sediment flux and stratigraphy, whereas long response times to climate tend to amplify the climatic signal. Climatic forcing (precipitation and temperature changes) is therefore translated to a sediment flux signal.

(iii) Hillslopes angle and regolith availability act as negative feedbacks, limiting erosion rates in periods of high precipitation and uplift rate, and are a major cause of catchment non-linear behavior.

(iv) Catchment response time modulates sediment supply to basins, and thus it significantly affects shoreline trajectories, stratal architecture, grain size trends and the visibility of sequence stratigraphic surfaces in borehole logs.

A key message from this paper is that the "sediment factory" (i.e. the upland catchment) behaves like many other natural systems: every time step depends on the previous ones, and on the interaction between the system and the continuously developing boundary conditions (Ruddiman, 2002). As a consequence, stratigraphy records a complex signal that cannot be understood without reference to landscape response times and sediment supply. The numerical methods proposed in this study give new insights into when and in what circumstances an inversion of climate and tectonic variables from the sedimentary record is possible, and could help us to disentangle other palaeo-catchment histories from the stratigraphic record.

Table 3.1: table of symbols

	Parameter	Unit
A	Total catchment area	km^2
A'	Area of the transient reach	km^2
A_c	Area of upper reach	km^2
$c1$	Proportionality coefficient between S_h and D	
$c2$	Exponential coefficient between S_h and D	
$c3$	Chemical weathering rate=4 10^6	m y^{-1}
$c4$	Arrhenius activation energy for weathering of bedrock	J mol -^{1}
$c5$	Gas constant	
C_e	Catchment erosion efficiency	
CT	Concentration time	days
D	Denudation rate	mm y^{-1}
D_{50}	Average grain size	mm
E	Actual erosion rate	mm y^{-1}
E_p	Potential erosion rate	mm y^{-1}
EV	Excess volume of material eroded	km^3
K_b	Bedload delay time	y
GRT	Groundwater residence time	days
K_e	Response of hillslope angle to erosion	ky
K_f	Response of fluvial gradient to uplift	ky
K_{soil}	Soil erodibility	
K_u	Response of hillslope angle to uplift	ky
L	Lithology coefficient	

LT	Length of the transient reach	km
P_a	Yearly precipitation rate	mm y^{-1}
P_g	Precipitation gradient	
ψ	Knickzone migration proportionality	
Q_{bed}	Bedload	m^3 s^{-1}
Q_{bss}	Bedload supply from hillslopes	m^3 s^{-1}
Q_{susp}	Suspended load	m^3 s^{-1}
R	Average runoff	mm y^{-1}
R_h	Response time for hillslopes	My
R_f	Response time for fluvial channel	My
Reg	Regolith thickness	mm
$Relief$	Average relief	m
R_t	Regolith threshold	mm
S_f	Fluvial channel gradient	m m^{-1}
S_h	Average hillslope angle	°
SI	Sediment supply index	
SMC	Snow melt coefficient	
T_a	Average yearly temperature	°C
TC	Transport capacity	kg s^{-1}
θ	Fluvial channel profile concavity	
U	Uplift or fault-slip rate	mm y^{-1}
V	Knickzone migration rate	mm y^{-1}
Veg	Vegetation cover	%
W	Weathering rate	mm y^{-1}

CHAPTER 4

Non-linear response of the Golo River system, Corsica, France, to Late Quaternary climatic and sea level variations

Abstract. Disentangling the impact of climatic and sea level variations on fluvio-deltaic stratigraphy is still an outstanding question in sedimentary geology and geomorphology. We used the Golo River System, Corsica, France, as a natural laboratory to investigate the impact of Late Quaternary climate and sea level oscillations on sediment flux from a catchment and on fluvio-deltaic stratigraphy. We applied a numerical model, PaCMod, which calculates catchment sediment production and transport and compared modeling output to the sedimentary record of the Golo alluvial-coastal plain, whose chronology was reinterpreted using new optical stimulated luminescence (OSL) ages on feldspars. Our modeling, OSL ages, and geomorphological results indicate that the two main phases of braindplain development in the Golo alluvial-coastal plain occurred during the cold-dry phases of MIS5 and during the late MIS4-early MIS3, as a consequence of high catchment erosion rates and low water discharge. Incision and sediment reworking occurred during sea level low stand periods (early MIS4 and late MIS3-MIS2). High sediment flux pulses from the catchment outlet were generated during the late glacial and early Holocene, as a result of the release of sediments previously stored within the catchment and enhanced snowmelt. Our results suggest a non-linear response of the Golo River system to climatic and eustatic changes, caused by sediment storage within the catchment and geomorphological thresholds. This indicates that a direct comparison between palaeo-climate and stratigraphy is not possible without considering catchment sediment storage and sediment transport delays out of the catchment.

4.1 Introduction

Fluvial systems are key elements of the geological cycle because of their fundamental role in reshaping the Earth's surface and in transporting water and sediments from continents to the global ocean. Through such reshaping and transporting processes external forcing, such as climate, tectonics, and eustatism, is recorded in landscapes and in basin stratigraphy. During the last decades, hydrologists, geomorphologists and stratigraphers have developed modeling techniques to simulate erosional and fluvial processes at different spatial and temporal scales (Tucker and Slingerland, 1997; Coulthard et al., 2002; Storms and Swift, 2003; Muto and Steel, 2004; Kettner and Syvitski, 2008; Martin et al., 2011; Rohais et al., 2012). Comparing experimental results to observed stratigraphy and geomorphological data they have been able to test their hypothesis and quantify the impact of external forcing on fluvial systems.

In a comprehensive review of Quaternary and modern systems and experimental work Blum et al. (2013) showed how fluvial systems dynamics and stratigraphic architecture are the result of the complex interaction between sediment supply and variations in accommodation space, function of sea level changes, tectonics and fluvial-bathymetric gradients. In particular, they showed that early sequence stratigraphic model for fluvial valleys, considering complete sediment bypass as a result of sea level fall, do not stand up to theoretical, experimental, and field evidence. Instead, periods of incision correspond with sediment export minima, whereas periods of lateral migration and channel belt construction occur with increased sediment flux.

For example, the Rhine-Meuse fluvial system in the southern Netherlands is an excellent and well-studied system to investigate the impact of climatic and eustatic changes on river systems (Huizink, 1998; Bogaart and van Balen, 2000; Veldkamp and Tebbens, 2001; Bogaart et al., 2003b; Busschers et al., 2007; Vanderberghe 2008; van Balen et al., 2010). During cold-dry glacial phases, periglacial processes and low vegetation cover led to high erosion rates and, consequently, high sediment supply and accumulation of coarse sediments in braidplains and alluvial fans. Aggradation and lateral channel migration during sea level fall were favored by the lengthening of the river longitudinal profile, which extended through the English Channel towards the Atlantic. At the glacial-interglacial transition, during sea level rise, the Rhine and the Meuse River incised the previously deposited sediments as a result of increased fluvial water discharge, and subsequently evolved to meandering systems filling in their valleys with floodplain deposits during interglacial periods.

Analogue models of fan-deltas in flume tanks have illustrated how different parts of the fluvial systems react differentially and inertially to external forcing (Muto and Swenson, 2005; Kim et al., 2006; Petter and Muto, 2008). For example, Van Heijst and Postma (2001) showed that, in the early stages of sea level fall, aggradation occurred in the upper part of the fluvial system, meanwhile an erosional knickpoint developed from the shelf edge and migrated upstream on the continental shelf. Similarly, numerical models have indicated a non-linear response of fluvial systems to climate forcing. This response is controlled by various thresholds, such as bedrock channel incision or landslide initiation (Tucker and Slingerland, 1997), by buffers, such as large floodplains (Metivier and Gaudemer, 1999), and by delays and autogenic behavior (Coulthard and van de Wiel, 2007; Allen, 2008; Jerolmack and Paola, 2010). These studies showed that the record of external forcing in landscapes and stratigraphy is generally better preserved in small source-to-sink systems with little sediment storage in their catchments.

Because of its small size, the well constrained coastal and offshore sedimentary archives, and the limited storage area within the catchment, the Golo River system (Corsica, NW Mediterranean) is an excellent laboratory to investigate the transmission of climatic and eustatic sea level fluctuations across a fluvial system. Recent studies on the catchment and alluvial-coastal plain (Somme et al., 2011; Skyles, 2013; Moreau et al., in prep.), and on the shelf and submarine fans (Deptuck et al., 2005; Gervais et al., 2006a; 2006b; Somme et al., 2012; Calves et al., 2013) have given new insights into the architecture and evolution of the Golo River system, illustrating how major modifications in stratigraphy, sediment storage and dispersal occurred as a response to climatic and eustatic sea level changes. The cut-and-fill pattern of the Golo fluvial terraces and the stacking pattern of sedimentary unit on the shelf were interpreted by Somme et al. (2011) as the result of balance/imbalance between sediment supply and fluvial transport capacity. Still, the link between the timing, the spatial distribution and magnitude of geomorphological changes, and external forcing remains unclear and untested.

The objective of this paper is to reconstruct the sediment flux and fluvial dynamics history of the Golo river system, resulting from changes in external forcing, and to investigate how this history affected the geomorphic and stratigraphic evolution of the Golo catchment and alluvial-coastal plain. We used a numerical model, PaCMod (Forzoni et al., 2013) to simulate catchment evolution, fluvial dynamics, and sediment flux from the Golo catchment. Then we compared modeling results to geomorphological data and new optically stimulated luminescence (OSL) ages from the Golo coastal plain, to unravel how climate-induced fluvial dynamics

interacted with sea level variations during the last glacial-interglacial cycle. Finally, we compared our findings on the Golo fluvial system to other field and modeling studies, adding to the ongoing discussion on long-term climatic and eustatic forcing on landscape evolution and sediment flux from catchments.

4.2 Background

4.2.1 Geological and geomorphological setting

The Golo River is the major fluvial system of the island of Corsica, France (Fig. 4.1). The eastern part of the catchment is underlain by Mesozoic oceanic crust and meta-sedimentary rocks, deformed during the late Cretaceous and Cenozoic (Alpine Corsica), while the western part is underlain by Paleozoic granodioritic rocks (Hercynian Corsica). The present day rugged relief of the catchment is a result of the recent phase of regional uplift (Plio-Quaternary), which rejuvenated the Miocene low-relief landscape (Fellin et al., 2005). In the upland steep-sloped valleys, slope gravitational processes are the main contributor to denudation, and the sediments eroded from hillslopes are deposited in narrow, confined floodplains. Terraced remnants of ancient floodplains occur predominantly in the low relief area close to the Hercynian-Alpine contact, and in the Marana Plain, the alluvial-coastal plain bordering the Tyrrhenian Sea (Somme et al., 2011) (Fig. 4.1).

In Marana Plain, the Golo River accumulated thick conglomeratic wedges during the Pleistocene (Conchon, 1972; Conchon, 1978) and repeatedly incised into these deposits which is likely the result of long term uplift (Fellin et al., 2005) and climatic variations of sea level and of sediment supply (Somme et al., 2011). In the alluvial plain, these coarse braidplain deposits are organized in a cut-and-fill pattern, with the younger units located at progressively lower topographic levels (Fig. 4.2). The modern floodplain of the Golo River is characterized by gravelly-sandy braided fluvial deposits in the west and by finer grained (sandy-silty) meandering fluvial deposits towards the east. Moreau et al. (in prep.) showed that the modern floodplain has developed inside an incised valley, which becomes wider and deeper seawards (Fig. 4.2). At the coast, beach ridges extend both in a north- and southward direction from the river mouth. The areas landward of the beach ridges are characterized by swamps and, in northern part of the Marana Plain, the Biguglia lagoon separates the Corsican mainland from a spit system.
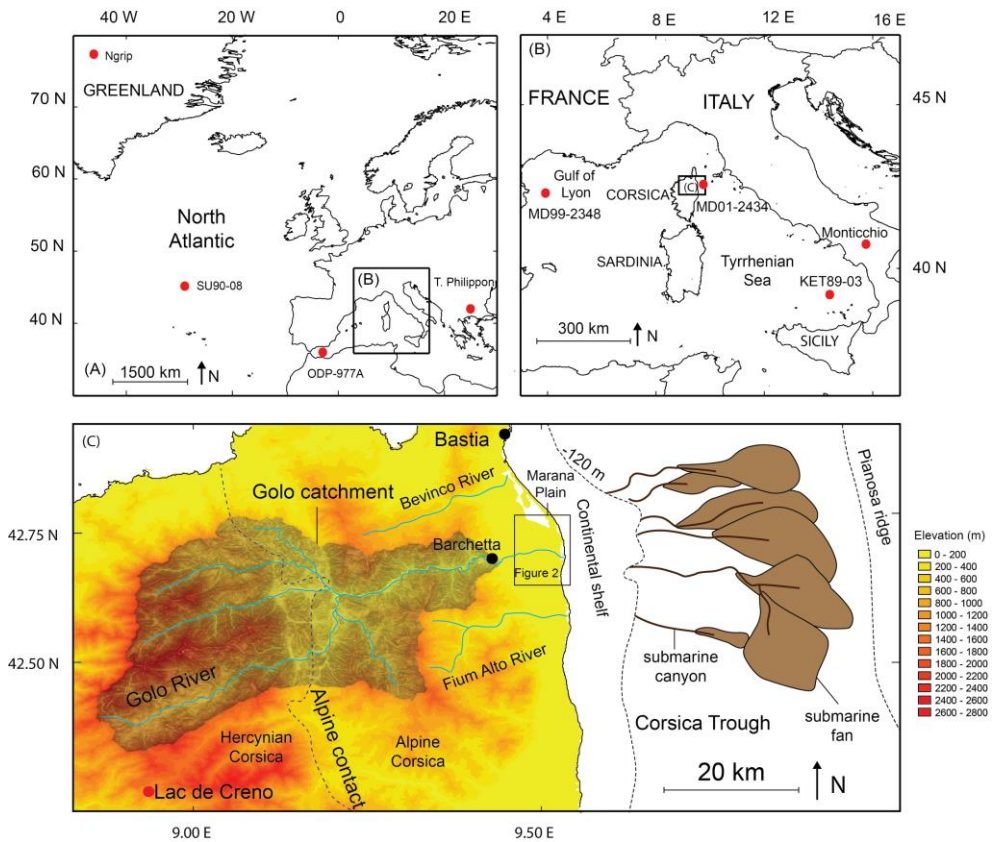
Figure 4.1: location of the study area and of the main palaeo-climatic proxies (A and B); Golo source to sink system (C). References for palaeo-climatic proxies: Ngrip (GRIP, 1993); SU90-08 (Paterne et al., 1999; Kallel et al., 2000); ODP-977A (Martrat et al., 2004); T.Philippon (Tzedakis, 2003); MD99-2348 (Rabineau et al., 2005); MD01-2434 (Toucanne et al., 2011; Calves et al., 2013); KET89-03 (Paterne et al., 1999; Kallel et al., 2000); Monticchio (Ramrath et al., 1999; Allen et al., 2000); Lac de Creno (Reille et al., 1997; Reille et al., 1998).

A chronology of the alluvial-fluvial deposits, based on OSL, has been proposed by Somme et al., (2011) and Skyles (2013). These studies indicated that the modern floodplain, Fy3, developed during the late Glacial-Holocene, filling in an incised valley formed during MIS2, and that the older terraced deposits, Fy2 and Fy1, were accumulated at some time during the last 100 ka. In particular, quartz OSL ages in the Marana Plain (Skyles, 2013) yielded MIS4-early MIS3 ages for Fy2 and a minimal MIS4 age for Fy1. In the methods section we describe new OSL ages from the Marana Plain, and discuss the different OSL age models for the terrace chronology. In the discussion we compare this chronology to geomorphological data and modeling results and discuss the (mis)match between the data.
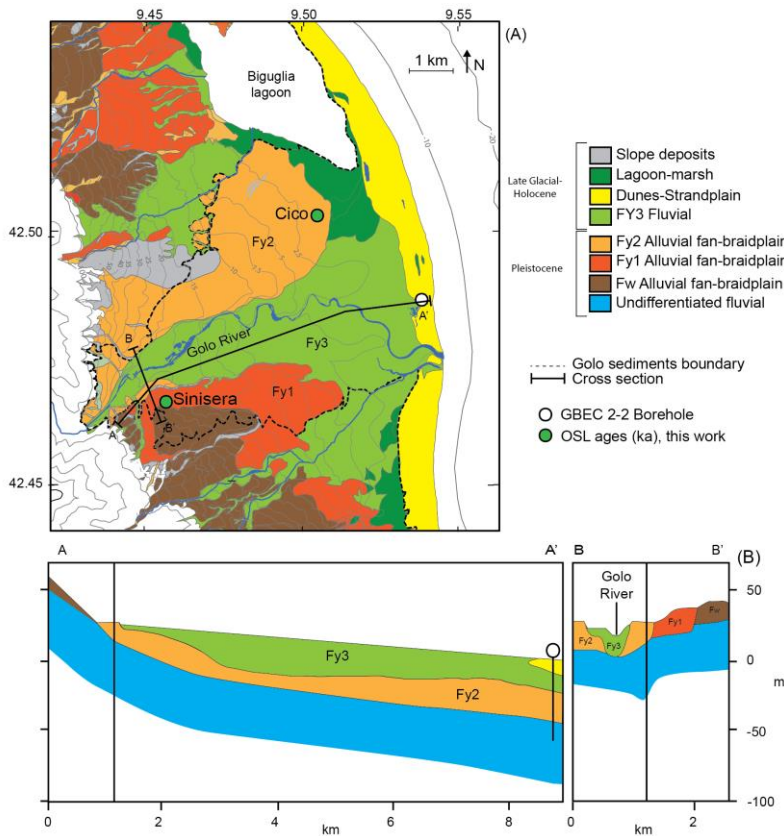
Figure 4.2: geological map of the Marana plain (A) and geological cross sections across the Marana Plain (B) with location of OSL and ^{14}C ages samples and the GBEC2-2 borehole. (A) and (B) are based on Somme et al. (2011), and Moreau et al. (in prep.). The Golo alluvial deposits are organized in a cut-and-fill terrace tread, with modern floodplain deposits Fy3 accumulated in an incised valley in the central part of the Marana Plain.

The offshore part of the Golo source-to-sink system consists of two sedimentary domains: the continental shelf and the slope-basin floor (Calves et al., 2013) (Fig. 4.1). Seismic analysis on the external part of the shelf (Deptuck et al., 2008, Somme et al., 2011) showed different sedimentary wedges stacked during the last glacial-interglacial cycle, characterized by seaward inclined reflectors (clinoforms). Submarine canyons have developed on the external part of the shelf and on the continental slope, and are connected to the basin-floor fans. These deep-marine sedimentary bodies, accumulating in the tectonically subsiding Corsica Trough, are the final sink for the Golo river source-to-sink system, for other smaller river systems on the northeastern margin of Corsica, and for rivers on the Italian northwestern margin.

4.2.2. Late Pleistocene to Present climate and erosion in the Golo catchment

Oxygen-isotopes, sedimentary, and pollen records indicate high amplitude and high frequency fluctuations in the Mediterranean region during the Quaternary (Peyron et al., 1999; Ramrath et al., 1999; Cacho et al., 2002; Tzedakis, 2005; Brauer et al., 2007; Calvès et al., 2012; Toucanne et al., 2012). The correlation between the oxygen isotopes Mediterranean record, the ice core record in Greenland and the sedimentary record in the Atlantic and Northern Europe (Dansgaard et al., 1993; GRIP, 1993; Svenson et al., 2008; Allen et al., 1999; Kallel et al., 2000; Martrat et al., 2004) implies that during the last glacial-interglacial cycle, climatic changes produced a similar environmental response at a continental scale (Fig. 4.3). A millennial scale climatic variability (Dansgaard-Oeschgers, D-O stadials and interstadials) is superimposed on the long term glacial-interglacial variations, as indicated by sea surface temperature reconstructions from the Alboran Sea (Martrat et al., 2004) and the Tyrrhenian Sea (Paterne et al., 1999; Kallel et al., 2000; Kallel et al., 2004), as well as the oxygen isotope record from the Tyrrhenian Sea (Toucanne et al., 2012). The paleoclimatic records from the Alboran Sea and from the Tyrrhenian Sea indicate high temperatures during the interglacial phases, MIS5e (Tyrrhenian stage) and MIS1, as well as during MIS5c and MIS5a. Cold temperatures characterized MIS5d, MIS5b, MIS4, late MIS3 and MIS2, with up to 10 degrees colder than present during the Last Glacial Maximum LGM ($\approx$21 ka). During early MIS3 temperatures were, on average, intermediate between glacial and interglacial conditions.

The onshore pollen record in Corsica (Reille et al., 1997; Reille et al., 1999), in Greece (Tezakis et al., 2003), and in central Italy (Ramrath et al., 1999; Allen et al., 2000) indicate that glacial periods and stadials were dominated by herbaceous, cold-dry steppe taxa, while interglacial periods and interstadials were dominated by arboreal, closed-vegetation taxa. Based on such pollen evidence, Peyron et al. (1999) and Allen et al. (1999) estimated a 20-30 % lower annual precipitation rate during the Last Glacial Maximum LGM (MIS2). On the other hand, Kuhlemann et al.'s (2008) atmospheric circulation modeling results and Kuhlemann et al.'s (2005) glacial equilibrium lines reconstruction suggested increased precipitation (snowfall) on Corsica during the LGM, as a consequence of more frequent storms, despite the aridity on a regional scale. In this paper, we consider the sedimentary record (Kallel et al., 2004; Martrat et al., 2004) as the most informative for palaeo-precipitation, keeping in mind that changes in storm frequency, seasonality, and storm frequency might have been important on a local scale (see discussion).
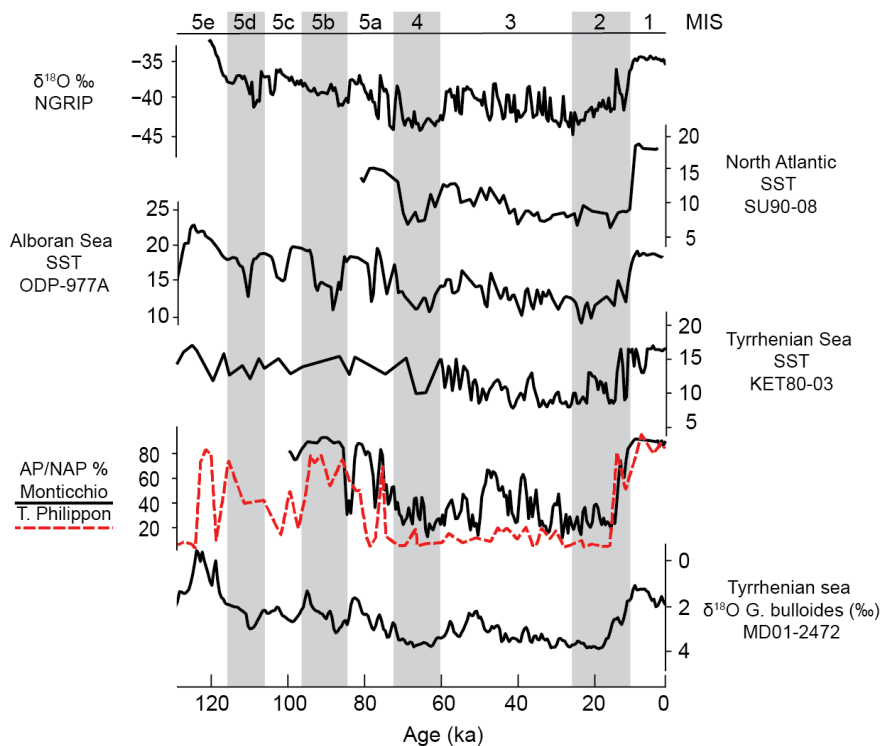
Figure 4.3: correlation between palaeo-climatic proxies for the last 130 ka. SST=sea surface temperature (°C); AP/ NAP=arboreal pollen/ non-arboreal pollen. References for palaeo-climatic proxies: NGRIP (GRIP, 1993); SU90-08 (Paterne et al., 1999; Kallel et al., 2000); ODP-977A (Martrat et al., 2004); T.Philippon (Tzedakis, 2003); MD01-2434 (Toucanne et al., 2011; Calves et al., 2013); KET89-03 (Paterne et al., 1999; Kallel et al., 2000); Monticchio (Ramrath et al., 1999; Allen et al., 2000).

Climatic oscillations importantly affected denudation rates in the Golo catchment (Somme et al., 2011; Calves et al., 2013) with a large increase in sediment production during glacial phases. Such behavior, characteristic for several catchments across Europe (Bogaart et al., 2003, Busschers et al., 2007, Hinderer, 2001, Collier et al., 2000), was the result of sparse vegetation cover, permafrost processes and glacial erosion (Conchon, 1976, Kuhlemann et al., 2005; de Winter et al., 2012). Chemical weathering was high during interglacial periods, as a consequence of higher temperature, precipitation, vegetation cover and the enhanced development of soils (Calves et al., 2013). On a longer time scale, denudation rates, measured by [10]Be cosmogenic nuclides on high elevation Miocene palaeo-surfaces (0.008-0.024 mm/ y) (Kuhlemann et al., 2007), are one order of magnitude lower than Quaternary fluvial incision rates (0.2-0.4 mm/ y) (Fellin et al., 2005) and sediment yield to the Corsica Trough (Calves et al. 2013) (0.04-0.1 mm/ y). This indicates an increase in catchment denudation rate from the

Miocene to present, as a result of post-Miocene uplift and/or increasing amplitude of climate oscillations during the Quaternary.

4.3. Methods

We investigated the impact of climate on environmental conditions, erosion rates and sediment flux using PaCMod, a spatially-lumped model, which calculates long time series (10^3-10^6 years) of fluvial water discharge and sediment load from any given catchment. PaCMod input consists of climatic data derived from proxies (e.g., sea-surface temperatures from ^{18}O of foraminifera tests), drainage basin characteristics and user-defined parameters, i.e., precipitation increase with altitude, snowmelt coefficient, groundwater residence time and direct flow buffer (Forzoni et al., 2013). We compared modeling results to geomorphological and stratigraphic data from the field, namely boreholes, outcrops, shallow geophysics (Moreau et al., in prep.), and new OSL ages from the Marana Plain, in order to disentangle the influence of sea level and climatic variations on the Golo fluvial system during the last glacial-interglacial cycle.

4.3.1.   PaCMod

In PaCMod, the morphology of a real catchment is collapsed into four model domains, where different processes occur and sediment is routed and temporarily stored (hillslopes, fluvial network, catchment lower reaches, and catchment outlet) (Fig. 4.4). Based on climatic and environmental conditions, PaCMod calculates a yearly time series of precipitation, surface runoff, and fluvial water discharge, with two time steps per year, one for flood conditions (peaks) and one for average discharge conditions (average). In the model, precipitation occurs either as rain or snow. Snow accumulates in a snow reservoir. The amount of snow in this reservoir increases when snowfall exceeds snowmelt, whereas it decreases when snowmelt exceeds snowfall. Snowmelt is a function of temperature and of the amount of snow in the snow reservoir.

Hillslope erosion rate is calculated as a function of average hillslope angle, runoff and vegetation cover (Zhang et al., 2002). The fine fraction of eroded sediment is treated as suspended load (Morehead et al., 2003). The suspended load out of the catchment depends on the fine fraction of the eroded sediments and on the fluvial water discharge. The coarse fraction of sediments eroded from hillslopes is treated as bedload supply. The bedload supply is balanced with the fluvial transport capacity at the catchment outlet (Tucker and Slingerland, 1997), which is a function of fluvial channel gradient at the catchment outlet, average bedload grain size, and fluvial water discharge (Fig. 4.5). For the case of the Golo, we assumed that 50% of

the total eroded sediments constitutes the fine fraction and the other 50% the coarse fraction, based on empirical regression curves between catchment area and bedload/suspended load ratio in Alpine catchments (Schlunegger and Hinderer, 2003; Turowski et al., 2010) and considering the hard rocks outcropping lithologies in the catchment (Turowski et al., 2010). We considered the coarsest grain size fraction of the Golo alluvial sediments (100 mm, within the cobble fraction) as representative for the bedload grain-size D_{50} and for the Golo fluvial dynamics evolution, because of its armoring effect on river bed and banks. We assumed that the river was able to switch from a regime of accumulation to a regime of incision only when it was able to transport its coarsest grain size fraction, i.e., during floods-peak transport capacity.

The actual bedload supply $Q_{bactual}$ for each time step is the sum of the bedload supply from that time step and a fraction of the bedload accumulated in a confined floodplain reservoir during previous time steps (geomorphological memory). When $Q_{bactual}$ exceeds either peak or average transport capacity *TC*, the amount of sediments in excess is stored in the confined floodplain reservoir. The bedload out of the catchment equals actual bedload supply $Q_{bactual}$ when transport capacity *TC* (either peak or average) exceeds $Q_{bactual}$, whereas it equals *TC* when $Q_{bactual}$ exceeds *TC*. For a detailed description of PaCMod see Forzoni et al. (2013). We calibrated the PaCMod modeled hydrograph using present day data (Fig. 4.6). Meteorological data from the weather stations of Ajaccio and Bastia (NOAA) for the period 2004-2010 were used as input. We averaged precipitation and temperature from the weather stations of Bastia and Ajaccio and corrected for catchment altitude classes (Forzoni et al., 2013). The modeled hydrograph was compared to the measured water discharge at Barchetta (hydro.eaudefrance website), and it was optimized by tuning the four user-defined parameters (Bogaart et al., 2000; Forzoni et al., 2013) (Table 4.1). The main discrepancies between modeled and measured discharge, which occur during periods of very high discharge, can be explained by the lack of spatial information for the probability and the magnitude of local precipitation events.
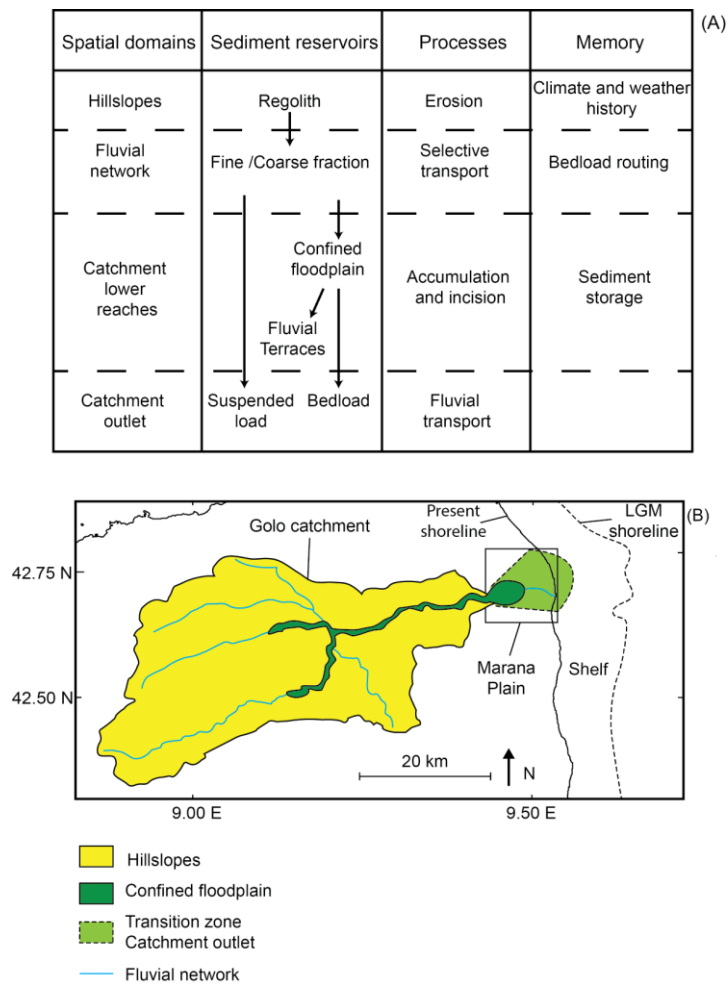
Figure 4.4: (A) Schematic overview of PaCMod modeling approach (from Forzoni et al., 2013), and (B) subdivision of the Golo catchment according to the modeling spatial domains. The four model spatial domains are a simplification of a fluvial system with different environments spatially connected to each other. For the case of the Golo River system, we considered the model spatial domain catchment lower reaches to represent the Late Quaternary Golo alluvial plain, extending from the low lying areas near the alpine-hercyinic contact until the Marana Plain, which is the transition zone from a confined and/ or terraced alluvial plain to an unconfined floodplain/ coastal plain.
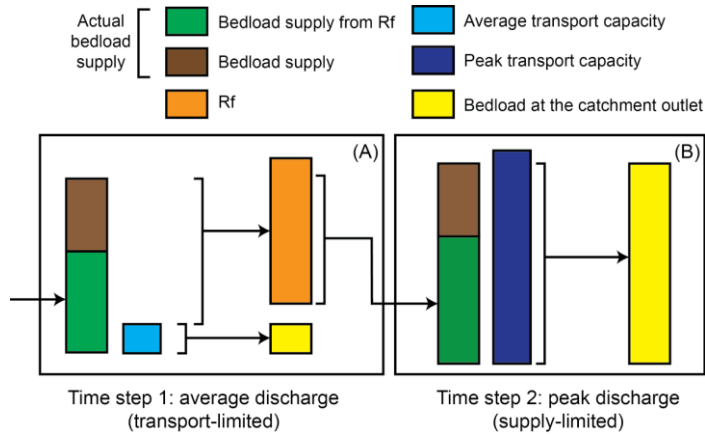
Figure 4.5: flow diagram of PaCMod bedload supply and transport capacity balance illustrating two synthetic time steps, the first with average fluvial discharge (A) and the second with peak fluvial discharge (B). The actual bedload supply in is the sum of bedload supply from the time step and a fraction of the bedload accumulated in the confined floodplain reservoir *Rf* during previous time steps. When the actual bedload supply exceeds transport capacity (A) (transport-limited conditions) the sediment in excess are stored in the confined floodplain reservoir and the bedload out of the catchment equals transport capacity. In the second time step (B) transport capacity exceeds the actual bedload supply (supply-limited conditions). As a consequence the bedload out of the catchment equals the actual bedload supply and no sediment is accumulated in the confined floodplain reservoir.
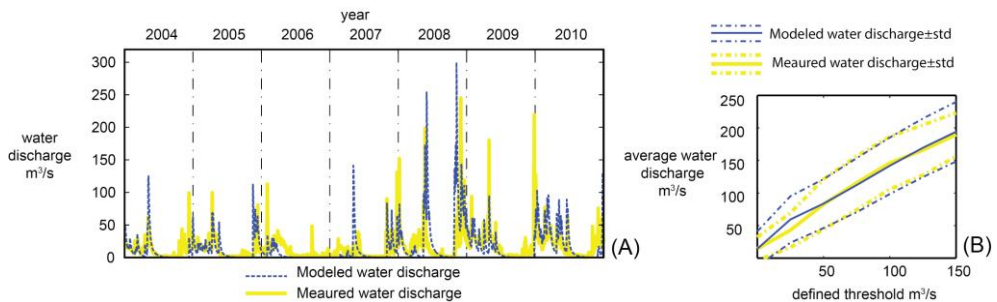

Figure 4.6: (A) Daily measured and modeled discharge for the Golo River. (B) Average daily water discharge above a defined water discharge threshold. We calculated the average water discharge (vertical axis) of the days, when water discharge was above a defined threshold (horizontal axis), and the standard deviation on the average. We used the weather stations used for input were Ajaccio and Bastia (NOAA) and the gauging station at Barchetta (http:/ / www.hydro.eaufrance.fr/) as input for the model calibration.

Table 4.1. Calibrated hydrological parameters

Parameter	Value	Unit
Precipitation gradient	0.00012	mm d^{-1} m^{-1}
Snowmelt coefficient	0.5	mm d^{-1} C^{-1}
Groundwater residence time	70	d
Direct flow buffer	6	d

Table 4.2. Climatic and morphological parameter used

Parameter	Value	Unit	Source
K_{soil}	0.3	tons/ acre	Panagos et al. (2012)
Fraction of floodplain reservoir	80	%	Somme et al. (2011)
D_{50}	10	mm	Moreau et al. (in prep)
Vegetation delay	250	a	Vanderberghe et al. (1994)
Temperature seasonality	6	°	Allen et al. (2000)
Storminess	0.48		Hydrograph analysis
Fluvial channel gradient	0.01	m m^{-1}	Aster GDEM
Average hillslope angle	23	°	Aster GDEM
Concavity exponent	1.1		Aster GDEM

As climatic input for PaCMod simulations, we used the sea-surface palaeo-temperature signal from the Alboran Sea, ODP-977A (Martrat et al., 2004) (Figs. 4.1A and 4.42). The temperature signal was calibrated on present day temperatures at sea-level in Bastia (Corsica), which are, on an annual average, 2° C cooler than in the Alboran Sea. We assumed that precipitation varied in phase with temperature, with 30% less precipitation than Present during the LGM (Peyron et al., 1998). Next, we assigned a value of 0.03 (tons/ acre) for soil erodibility K_{soil}, which is the average soil erodibility coefficient in Corsica measured by Panagos et al., (2012) (Table 4.2). As most of the sediments that accumulated in confined floodplains are reworked (40% to 100%, Somme et al., 2011; Moreau et al., in prep), we applied an

average value of 70 % for the fraction of the confined floodplain reservoir which is available for fluvial transport. Finally, we applied a 250 years delay of vegetation to climatic changes (Vandenberghe, 1994).

4.3.2   Luminescence dating sampling and analysis

Six samples from Golo coastal plain were taken for optically stimulated luminescence (OSL) dating (Table 4.3 and 4.4) in the locations Sinisera and Cico (Fig. 4.2) and were analysed at the Netherlands Centre for Luminescence Dating. The sedimentary succession of the Fy1 terrace at Sinisera and Fy2 terrace at Cico are characterized by poorly-sorted well-rounded conglomerates, with pebbles, granules and sand in a silty matrix, and interbedded lenses of well-sorted cross-bedded sand (Fig. 4.7). The conglomerates were interpreted as hyper-concentrated flow deposits in a braindplain environment (McPherson et al., 1987; Sohn et al., 1999; Benvenuti and Martini, 2002), deposited during high-magnitude, low-frequency flood events. The sand lenses were interpreted as stream flow deposits formed by bar migration of braided streams during average flood events. All OSL samples were taken from the sandy lenses within the conglomeratic succession, except for NCL-5412117 (Table 4.3), which was taken from the colluvial deposits at the top of the Sinisera succession.

OSL dating determines the time of deposition and burial of sand grains. Measurement of the OSL signal on the purified quartz or potassium-rich feldspar mineral fraction reveals how much ionizing radiation the sample received since the last bleaching event. Bleaching occurs when a sand grain is exposed to daylight. Hence, the last bleaching event represent the last time the mineral was at the surface before being buried. The luminescence age (ka) is obtained by dividing the amount of radiation received (equivalent dose, D_e, Gy) by the measurement of the background radiation level at the sample position (dose rate, Gy/ka). More details about the basics on luminescence dating are provided by Preusser et al. (2008).
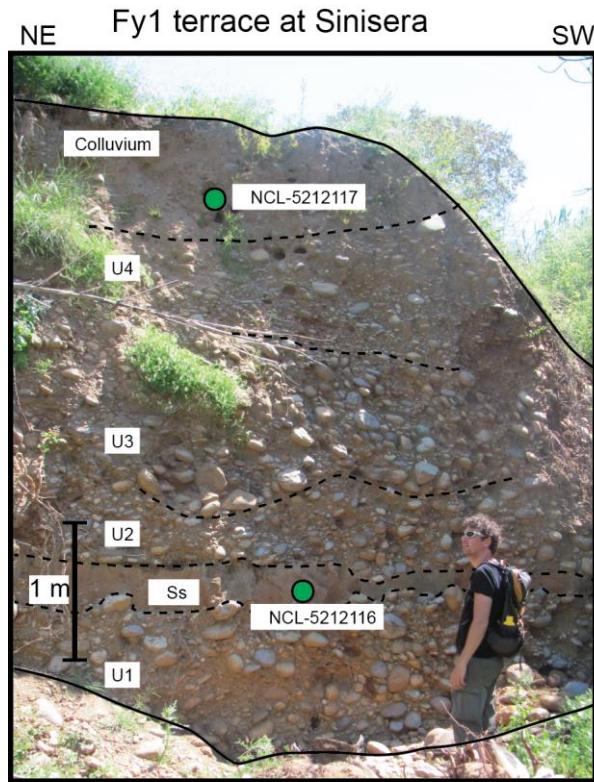
Figure 4.7: Outcrop of the Fy1 terrace at Sinisera. The Fy1 terrace deposits are characterized by vertically stacked units of poorly-sorted conglomeratic braided deposits (U1-U4) with an interbedded sandy lens Ss, in which OSL sample NCL-5412116 was collected. The section is topped by a colluvial cover, in which sample NCL-5412117 was collected.

The young colluvial sample (NCL-5412117) was dated using sand size quartz fraction and stimulating the OSL with blue light emitting diodes (quartz OSL). The measurement procedure and experimental setup is described in Wintle and Murray (2006) and more details are given in the electronic supplement. Because of the high dose rate in our samples, the luminescence signal in our sand-sized quartz minerals of sample NCL-5412116, -118, -119, and -120 was in saturation i.e. the quartz OSL D_e is above the sample depended lower dose saturation limit (Wintle and Murray, 2006) (Table 4.3). Based on the saturation limits (see Fig. S1 of the electronic supplement) of the other four samples dated with quartz, we assigned a minimum quartz OSL age of 30 ka.

For the four samples where quartz OSL was in saturation (NCL-5412116, -118, -119, and -120) and an additional sample from the CICO terrace (NCL-5412CICO), we

measured the Infrared stimulated luminescence (IRSL) from feldspars, as feldspar IRSL saturates at significantly higher D_es than quartz OSL (also see Fig. S2 of the electronic supplement). We used the recently explored post-infrared infrared (pIRIR) luminescence signal (Thomsen et al., 2008), which overcomes problems with regards to signal instability (anomalous fading, e.g. Thiel et al., 2011; Buylaert et al., 2012; Kars et al., 2012). A drawback of the pIRIR signal is slow luminescence signal resetting, which potentially increases the risk of age overestimation due to insufficient signal resetting (Buylaert et al., 2012; Kars et al., 2014). To obtain an insight into the pIRIR D_e scatter in our samples, we carried out feldspar pIRIR single-grain measurements (Reimann et al., 2012).

The feldspar pIRIR D_e was calculated using three procedures: (i) a central age model (Galbraith et al., 1999) for multiple-grain aliquots (MG-CAM), (ii) the central age model for single-grain distributions (SG-CAM); (iii) the bootstrapped minimum age model of Cunningham and Wallinga (2012) for feldspar single-grains (SG-MAM). The MG-CAM and SG-CAM models assume that the enormous scatter in the pIRIR D_e distributions is mainly caused by other factors than incomplete signal resetting (e.g. saturation properties of the feldspar grains, micro-dosimetry). The SG-MAM model is the bootstrapped minimum age model of Cunningham and Wallinga (2012) for feldspar single-grains (SG-MAM), which fits a normal distribution to the younger part of the scattered and skewed D_e distribution and thus assumes that the main sources of D_e scatter is caused by incomplete pIRIR signal resetting prior to burial (incomplete bleaching), implying that the younger part of the distribution yields the accurate age.

The SG-MAM approach was recently successfully applied to late Holocene fluvial deposits from Turkey (van Gorp et al., 2013) in combination with a low temperature pIRIR measurement protocol (Reimann et al., 2011); however, the suitability of this approach for Pleistocene fluvial deposits and the elevated temperature pIRIR measurement protocol as it is used in this study has not been demonstrated yet. The advantage of applying either a CAM or a MAM to feldspar single-grains (SG-CAM and –MAM) is that the age determination is restricted to the brightest as well as most appropriate K-feldspar grains and thus the most precise luminescence dosimeters. The disadvantage of single-grain analysis is that feldspar grains with a pIRIR signal in saturation are rejected from analysis as no reasonable D_e can be assigned. This may bias distributions towards younger ages. In order to evaluate the suitability of the three approaches four our feldspar samples we systematically compare the outcome of the three approaches and

discuss the geochronological implications (section 5.3). More details about the measurements and data analysis are provided in the electronic supplements.

4.4. Results

4.4.1   PaCMod modeling results

The cold-dry glacial phases MIS4 and MIS2 (Figs. 4.8A and 4.8B) were characterized by relatively low vegetation cover (Fig. 4.8C), low evaporation and high amounts of snowfall compared to rainfall (Fig. 4.8D), whereas the opposite occurred during warm-wet phases within MIS5 and in MIS1. The balance between snowfall and snowmelt controlled the development of a snow storage reservoir. When snowfall outpaced snowmelt, during prolonged periods of cold-dry conditions (MIS4, late MIS3 and MIS2), snow storage importantly increased (Fig. 4.8E). The water stored in such snow storage reservoir was released as snowmelt during deglaciation, when temperatures rose in the early MIS3 and at the transition MIS2-MIS1.

During cold-dry periods, the low precipitation rate induced low water discharge (Fig. 4.9A) and, consequently, low fluvial transport capacity (both peak and average) (Fig. 4.9B), whereas the opposite occurred during warm-wet interglacial periods. The low vegetation cover induced high hillslope erosion rates during glacial cold-dry periods, leading to high bedload supply (Fig. 4.9B). During MIS4, MIS3 and MIS2 bedload supply exceeded peak transport capacity. This led to the temporary storage of sediments transported as bedload in the confined floodplain reservoir. As a result, the sediment available from transport (actual bedload supply) was higher than coarse-grained sediments produced by hillslope erosion (bedload supply).

The bedload flux out of the catchment was controlled by the balance between actual bedload supply and transport capacity-water discharge (Fig. 4.9C). The average bedload equaled average transport capacity throughout the whole simulation, as bedload supply exceeded average transport capacity (transport-limited conditions). The peak bedload equaled peak transport capacity during transport-limited conditions (MIS4, MIS3 and MIS2), while it equaled actual bedload supply during supply-limited conditions (MIS5 and MIS1). This resulted in a complex peak bedload flux signal: short phases of high peak bedload flux occurred when peak transport capacity and actual bedload supply were at the same level, whereas low bedload flux occurred with either low supply or low

transport capacity. The suspended load, both peak and average, behaved similarly to the bedload (Fig. 4.9D).
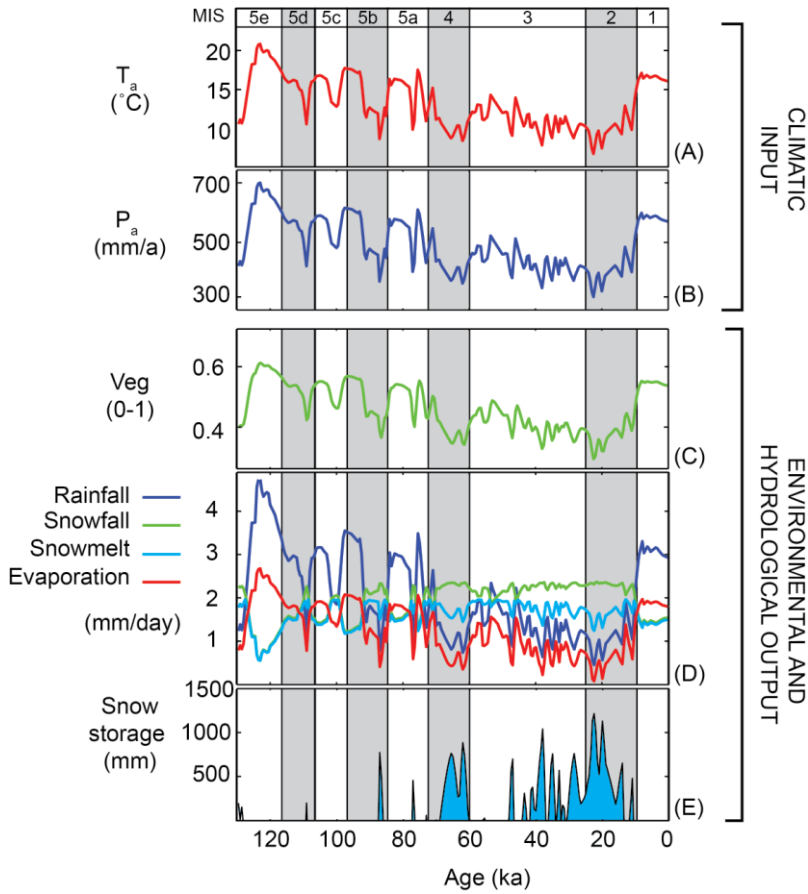

Figure 4.8: (A) Mean annual temperature T_a and (B) total annual precipitation P_a input for PaCMod simulations; (C) modeled vegetation cover *Veg;* (D) hydrological response to climatic and environmental changes; and (E) snow storage evolution. Daily rainfall and snowfall values (D) exceed long term precipitation values (B), as a result of modeled increase of precipitation with altitude (Forzoni et al., 2013).
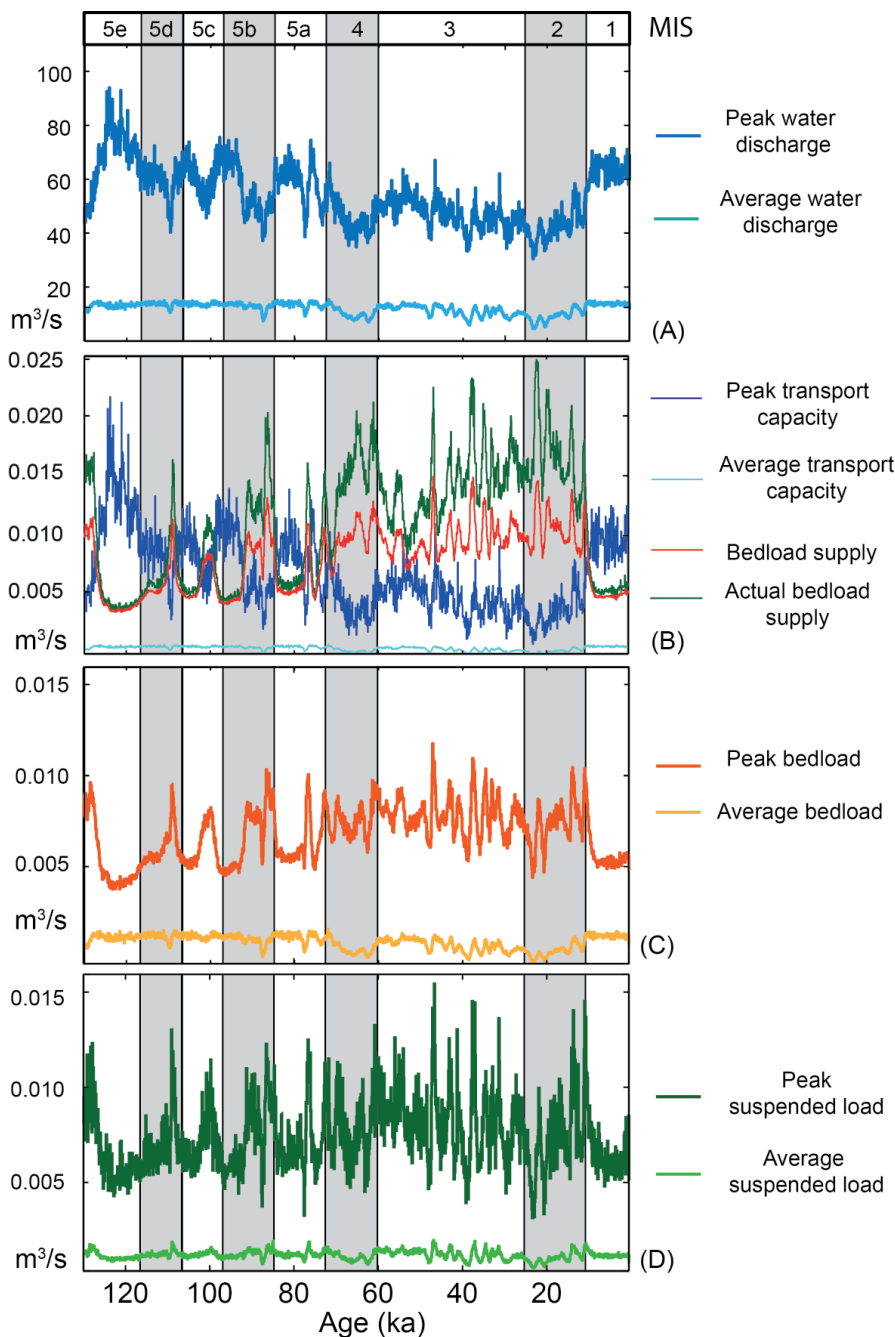
Figure 4.9: modelled fluvial water discharge (A), transport capacity and bedload supply (B), bedload (C), and suspended load (D).
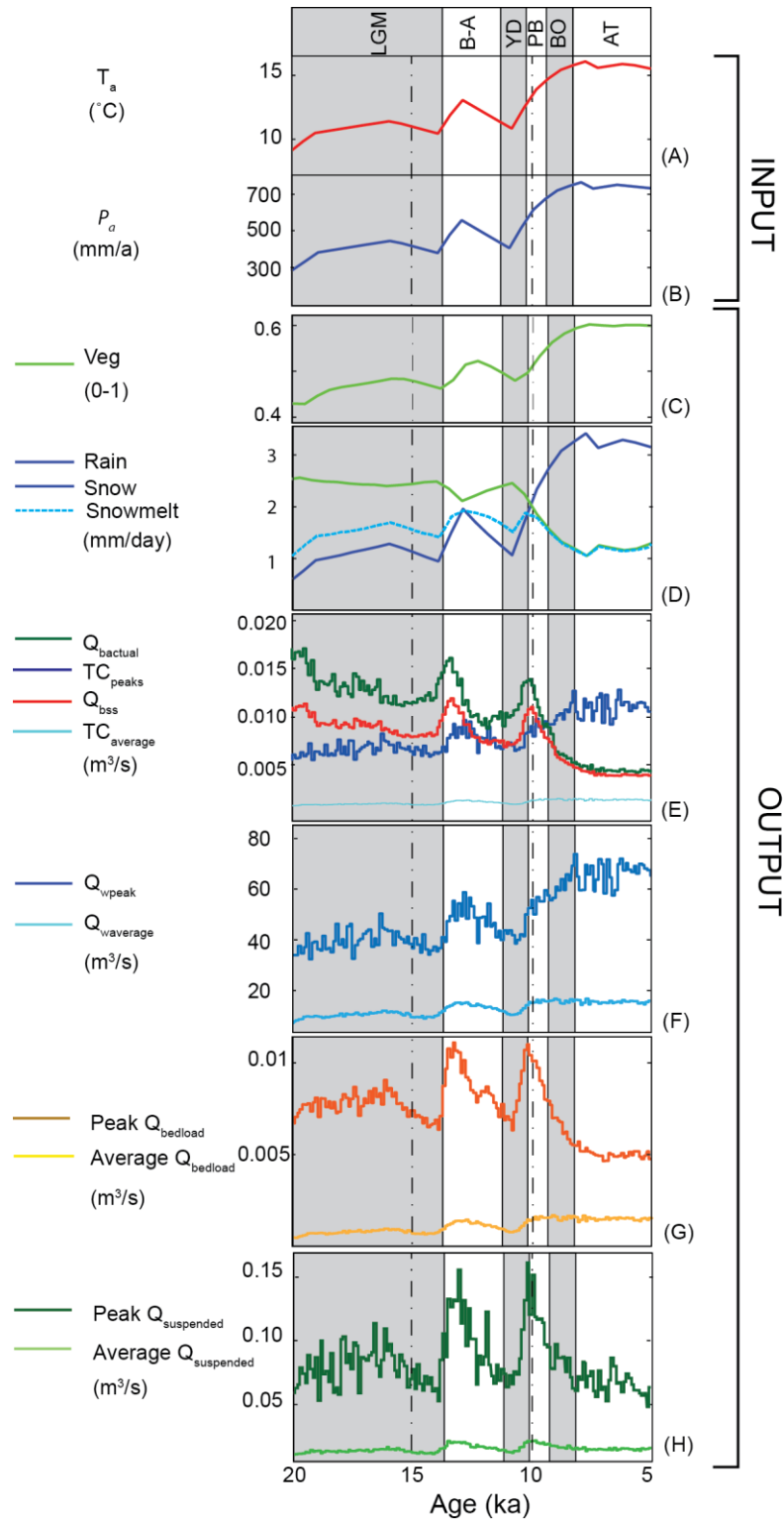
Figure 4.10: model input and output for the Golo simulation between 20 and 5 ka. (A) Input mean annual temperature T_a; (B) input annual precipitation P_a (C) modeled vegetation cover *Veg;* (D) hydrological response to climatic and environmental changes; (E) transport capacity and bedload supply balance; (F) fluvial water discharge; (G) bedload; and (H) suspended load. Q_{wpeak} = peak water discharge; $Q_{waverage}$ = average water discharge; TC_{peaks} = peak transport capacity; $TC_{average}$ = average transport capacity; Q_{bs} = bedload supply; $Q_{bactual}$ = actual bedload supply; $Q_{bedload}$ = bedload at the catchment outlet; $Q_{suspended}$ = suspended load at the catchment outlet. LGM = Last Glacial Maximum; B-A = Bølling-Allerød; YD = Younger Dryas; PB = Preboreal; BO = Boreal; AT= Atlantic.

After reconstructing the sediment flux from the Golo catchment during the last 130 ka, we zoomed in the last deglaciation phase, in order to investigate the impact of climate on sediment transport on a century-millennial time scale using the same input as before (Fig. 4.10). During deglaciation, the increase in temperatures, precipitation, and vegetation cover (Figs. 4.10A-C), led to the increase in fluvial transport capacity and to the decrease in erosion rates and sediment supply from hillslopes (Fig. 4.10E). The bedload and suspended load peaks signals from the Last Glacial Maximum (LGM) to the Holocene (Fig. 4.10G-H) are marked by two distinct pulses of high sediment flux at cold-to-warm transitions: during the Early Bølling-Allerød (B-A), and at the Younger Dryas (YD) to Pre-Boreal (PB) transition (Figs. 4.10G-H). These pulses are a consequence of snow storage (hydrological memory) (Fig. 4.10D), sediment storage in the catchment (geomorphological memory) (Fig. 4.10E), and of the delayed response of vegetation to climate (environmental memory) (Fig. 4.10C).

During cold-warm transitions runoff increased as a result of the increase in precipitation rate, but vegetation cover and consequently soil development lagged behind (250 a) (Fig. 4.10C), leading to high hillslope erosion. Furthermore, the extra amount of snow melt (Fig. 4.10D), deriving from the snow reservoir, amplified the increase in runoff, and induced higher peak water discharge (Fig. 4.10F), and consequently in fluvial transport capacity (Fig. 4.10E). The increase in transport capacity caused the depletion of the sediment reservoir, previously built up during glacial phases, and resulted in the high pulses of peak bedload (Fig. 4.10G) and peak suspended load (Fig. 4.10H) in the Early Bølling-Allerød and at the Younger Dryas and Pre-Boreal transition.

4.4.2. Luminescence dating results

The results of quartz OSL dating and pIRIR feldspar OSL dating are listed in Table 3 and 4 and visualized in Figure 11. The feldspar OSL dating provides three possible pIRIR ages for each sample. The first pIRIR age scenario, calculated by

applying the central age model MG-CAM (weighted average) to multiple-grain aliquot equivalent dose distributions, reveals two age clusters. Samples NCL-5412116 and NCL-5412118 (Fy1 at Sinisera) yield MG-CAM ages of 100±12 and 92±11 ka (MIS5), respectively. Samples NCL-5412119 and NCL5412120 (Fy2 at Cico) yield MG-CAM ages of 57±6 and 44±3 (early MIS3), respectively. The second pIRIR age scenario was calculated by applying the CAM to the feldspar pIRIR single-grain data (SG-CAM). Two age clusters were obtained. Sample NCL-5412116 and NCL-5412118 (Fy1 at Sinisera) yield a single-grain age, SG-CAM, of 76±7 ka (late MIS5). Sample NCL-5412119 and NCL5412120 (Fy2 at Cico) yield SG-CAM ages of 43±7 and 46±3 (MIS 3), respectively.

The third age scenario was calculated using the bootstrapped minimum age model MAM of Cunningham and Wallinga (2012) to the feldspar pIRIR De distributions (SG-MAM). Again, two age clusters are found; sample NCL-5412116 and NCL-5412118 (Fy1) yield single-grain MAM ages of 60±13 and 53±12 ka (MIS 4 to early 3), respectively, suggesting that the boot-MAM ages of these samples are ~40 ka younger than the CAM multiple-grain aliquot estimates. Sample NCL-5412119 and NCL5412120 (Fy2) yield single-grain MAM ages of 38±7 and 35±6 (MIS 3), respectively. This suggests that the age offset of SG-MAM ages compared to the MG-CAM values is ~10 ka for the samples at Cico (Fy2), whereas the offset is ~40 ka for the samples at Sinisera (Fy1). Finally, sample NCL-5412117 was dated using quartz and yielded a 0.35 ± 0.04 ka age. This sample was collected in the colluvial cover at 0.7 m depth from the top of the Fy1 terrace (Figure 7).

4.5. Discussion

PaCMod simulation of the Late Quaternary evolution of the Golo fluvial system indicate that (i) glacial periods were characterized by high hillslope erosion and sediment availability, and low transport capacity and fluvial water discharge, whereas the opposite occurred during interglacial periods; (ii) coarse sediment was stored within the catchment during glacial phases; (iii) pulses of high sediment load out of the catchment outlet occurred at glacial-interglacial transitions, as a consequence of the release of sediments previously stored in the catchment. How does PaCMod output translate, both qualitatively and quantitatively, to stratigraphic data and previous studies on the Golo River? First, we interpreted PaCMod result in terms of fluvial dynamics. Next, we compared the predicted model simulation to stratigraphic and geomorphological data from the Marana plain, to the new OSL ages, and to the sediment yield to submarine fans (Calves et al. 2013). Finally, we interpreted the Marana plain evolution in terms of causative controls.

Table 4.3. Overview and specifications of the new OSL ages in the Marana Plain using quartz OSL.

	Depth (m)	D_e (Gy)	Quartz dose rate	Quartz age (ka)
NCL-5412116	4.3	> 125	4.15 ± 0.12	> 30
NCL-5412117	0.7	**1.45 ± 0.21**	3.44 ± 0.10	**0.42 ± 0.06**
NCL-5412118	4.1	> 150	4.23 ± 0.12	> 30
NCL-5412119	2.0	> 154	4.85 ± 0.14	> 30
NCL-5412120	2.1	> 63	4.64 ± 0.13	> 14

Table 4.4. Overview and specifications of the new OSL ages in the Marana Plain using feldspars OSL. The most reliable De values and ages are presented in bold.

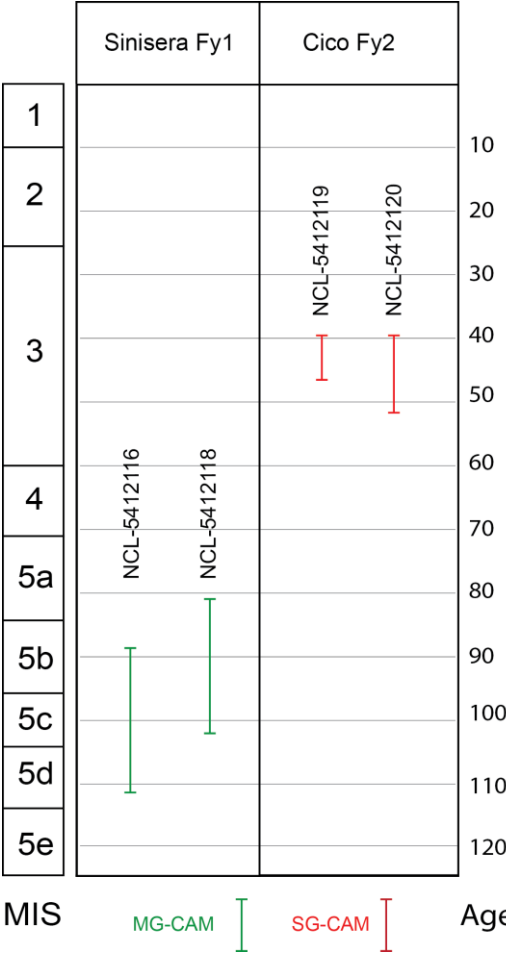|	Depth (m)	MG-CAM De (Gy)	SG-CAM De (Gy)	MG-MAM De (Gy)	Dose rate	MG-CAM Age (ka)	SG-CAM Age (ka)	SG-MAM Age (ka)
NCL-5412116	4.3	**530 ± 59**	410 ± 34	298 ± 64	5.00 ± 0.15	**106 ± 12**	82 ± 7	60 ± 13
NCL-5412118	4.1	**495 ± 53**	414 ± 32	270 ± 61	5.07 ± 0.15	**98 ± 11**	82 ± 7	53 ± 12
NCL-5412119	2.0	352 ± 32	**273 ± 16**	217 ± 37	5.69 ± 0.16	62 ± 6	**48 ± 3**	38 ± 7
NCL-5412120	2.1	270 ± 13	**284 ± 35**	190 ± 52	5.48 ± 0.17	49 ± 3	**52 ± 7**	35 ± 6

Figure 4.11: overview of OSL ages in the Marana Plain in the locations Sinisera and Cico: multiple grain central age model (MG-CAM), and single grain central age model (SG-CAM). For the Sinisera Fy1 terrace the MG-CAM ages are regarded more reliable, whereas for the CICO Fy2 terrace the SG-CAM ages are more reliable (see section 5.3 for details).

Model uncertainty

Before discussing and interpreting the modeling results it is important to acknowledge the limitations and sources of uncertainty of PaCMod simulations. The main limitation of PaCMod is the use of a spatially lumped approach, where all parameters and processes are averaged into single parameters. This approach neglects the detailed properties and processes heterogeneities across the catchment, as well as important processes such as glacial erosion, sediment sorting and grinding. Importantly, the model does not simulate the impact of sea-level changes on fluvial dynamics. Nevertheless, the model has the advantage of being parsimonious with required input, modeled processes, and processing capacity and is able to simulate the first order variations of sediment storage and sediment flux from a catchment (Forzoni et al., 2013).

The main sources of uncertainty are the palaeo-precipitation reconstruction, the choice of the soil erodibility coefficient K_{soil}, the fraction of coarse vs fine of eroded sediments, and the bedload grain-size coefficient D_{50}. In our simulations, we assumed, based on the palynological records (Reille et al., 1997; Ramrath et al., 1999; Allen et al., 2000; Tezakis et al., 2003), that precipitation varied simultaneously with temperature, with cold-dry glacial periods and warm-wet interglacial periods. However, Kuhlemann et al. (2008) argued that precipitation, and in particular snowfall, might have increased in Corsica during glacial periods. This likely induced no relevant change for sediment flux and storage during glacial phases. Still, the enhanced snow-melt might have led to very high sediment flux pulses at the glacial-interglacial transition, even more pronounced than in our simulations.

Next, the choice of the soil erodibility, fractions of eroded sediments, and bedload grain-size is crucial, because these parameters are the main controls on erosion rate, fluvial transport capacity and, consequently, sediment storage or reworking. The value of soil erodibility was based on Panagos et al. (2012). Soil erodibility is usually very difficult to constrain, particularly in the geological past. When reconstructing the Golo sediment budget (section 5.4.) we considered a range of plausible soil erodibility values in order to take uncertainty into account. Assuming unlimited regolith availability, a higher soil erodibility value would lead to higher erosion rates and sediment supply from hillslopes, whereas the opposite occurs with a lower soil erodibility.

Similarly, the fraction of fine versus coarse eroded sediment is a major control on erosion rates. We assumed that 50% of the eroded sediment constitutes the coarse grain-size fraction (bedload supply). This choice was based on measurement and estimation of suspended versus bedload flux from several river systems (Summerfield and Hulton, 1994; Burbank and Anderson, 2008), which indicate a higher bedload/suspended load ratio in small, high-relief catchment, such as the Golo. A lower coarse grain-size fraction would lead to lower bedload supply and hence, lower sediment storage, whereas suspended load would be higher.

The choice of one value for bedload grain size is one of the main limitation when modeling palaeo-sediment flux with PaCMod, as well as with other numerical models (Kettner et al. 2008), because the bedload consists of a distribution of different grain-size classes. Based on field observations (Moreau et al., in prep), we considered the coarsest grain size fraction of the Golo alluvial sediments (100 mm, within the cobble fraction) as representative for the bedload grain size D_{50} and for

the Golo fluvial dynamics evolution, because of its armoring effect on river bed and banks. Finer grain-size classes, such as sand and clay, are more easily transported than pebbles and gravels (higher transport-capacity). The choice of a lower bedload grain size value would lead to lower sediment storage within the catchment and higher sediment flux out of the catchment outlet.

In summary, our parameters choice importantly affected the absolute magnitude of sediment supply and transport capacity variations. However, the timing of these variations would not have changed, at least on a $<10^2$ years' time-scale, as indicated by the similarities between the different palaeo-climatic proxies. Furthermore, the modeled sediment yield from the Golo catchment is comparable to the sediment yield to the Golo submarine fans (Calves et al., 2013), and to fluvial incision rates (Fellin et al., 2005) (see section 5.4.). Consequently, the first order variations of modeled erosion rates and sediment flux from the Golo catchment are robust.

Modeled fluvial dynamics

We inferred the fluvial evolution of the Golo River in terms of accumulation versus incision based on modeled transport capacity and actual bedload supply (Bogaart et al., 2003a). Did a transition from accumulation to incision/bypass occur when the actual bedload supply started decreasing (I), or when peak transport capacity exceeded actual bedload supply (II) or exceeded bedload supply (III)? Figure 4.12A illustrates three different interpretations in terms of accumulation-incision during the last deglaciation. All three interpretations (IV) indicate accumulation during the Last Glacial Maximum to the early Bølling-Allerød B-A, in the Younger Dryas YD, and at the transition YD to Preboreal PB (IV). Incision-bypass occurred from the PB to the Boreal BO.

We applied the same approach on the 130 ka simulation (Fig. 4.12B). All three interpretations indicate accumulation during MIS4, middle-late MIS3 and MIS2, and incision during the warm spells of MIS5, early MIS3 and MIS1. This pattern of accumulation and incision-bypass is comparable to the previously described geomorphological and stratigraphic data from the Marana Plain by Sømme et al., (2011) (Fig. 4.2). Yet, such sediment supply signal cannot by itself explain the long phase of incision during MIS2 and the accumulation of fine grained sediments in the Marana Plain during MIS1. We argue that the incision was produced by the sea level fall below the shelf edge.

Marana Plain terrace chronology

The OSL feldspar dating on Fy1 and Fy2 terraces in the Marana Plain provided three possible ages for each sample: (i) a multiple grain central age model (MG-CAM) age, a single grain central age model (SG-CAM) age, and a single-grain minimum age model (SG-MAM) age (Table 4; Figure 11). For the MG-CAM and SG-CAM we assumed that the large scatter in dose distribution is mainly caused by variations in the saturation properties of the feldspar grains and/or micro-dosimetry, whereas for the SG-MAM it is assumed that the scatter is caused by incomplete pIRIR signal resetting prior to burial (incomplete bleaching).

The feldspar single-grain pIRIR D_e distributions reveal a moderate un-explained scatter after taking the experimental uncertainties into account (termed over-dispersion) with over-dispersion values of 22 to 45 % (see Fig. S4 and S5 of the electronic supplement). The feldspar single-grain pIRIR D_e distributions are mostly symmetric, which indicates that incomplete pIRIR signal resetting is not the main cause for the observed scatter. Incomplete pIRIR signal resetting typically results in strongly asymmetric D_e distributions (e.g. Reimann et al., 2012). Furthermore, the average age offset between SG-MAM and MG-CAM for each sample is smaller in the Cico samples (Fy2), ~10 ka (or even less), than in Sinisera (Fy1), ~40 ka (Table 4). It is unlikely that the age offset due to incomplete pIRIR signal resetting (i.e. the relevance of an unbleached remnant luminescence signal) increases with increasing depositional age. Therefore, we conclude that the SG-MAM is likely to be underestimated and thus the CAM scenarios are likely to be more reliable than the SG-MAM. Note that we subtracted a residual dose from all CAM estimates to account for possible remnant doses at the time of deposition (see section 3.2). As the impact of saturated feldspar grains on the D_e distribution increases with increasing age it is fair to presume that the multiple-grain MG-CAM ages of the samples at Sinisera (Fy1) are likely to be more reliable, whereas for the samples at Cico (Fy2) the single grain SG-CAM is probably more accurate. Bases on this reasoning, we conclude that the samples in Fy2 and Fy1 yield mid MIS3 and MIS5d-MIS5b ages, respectively (Figure 11).

The SG-CAM age range on Fy2 is comparable to the quartz OSL dating of Skyles (2013) on the same terrace. The MG-CAM age range of Fy1 (MIS5) is older than the age obtained by Skyles (2013), namely MIS4-MIS3. However, they considered their Fy1 age as a minimum age due to early saturation of the quartz OSL and probable overestimation of the dose rate. Consequently, the quartz OSL age of Skyles (2013) of the Fy1 terrace is likely older than MIS4, which indicates that our feldspar OSL age of Fy1 is in agreement with their geochronological interpretation. Skyles (2013)

measured significantly lower dose rate in their sample compared to our samples, which were collected in different locations. This suggests that the dose rates in these terrace sediments are relatively heterogeneous and this relatively heterogeneous radiation field may have caused a large part of the un-explained scatter in the pIRIR D_e distributions, which would confirm that the CAM models are more appropriate for age determination than the MAM model. Finally, we argue that the Holocene ages (4-8 ka) obtained by Somme et al., (2011) in the Fy1 and Fy2 terraces represent a recent alluvial cover similarly to our sample NCL-5412117 with a late Holocene age.

The development of alluvial fans and braidplain during cold-dry glacial phases (MIS4 to MIS2) is a common characteristic to other fluvial systems in central Italy (Amorosi et al., 2004; Fontana et al., 2008; Wegmann and Pazzaglia, 2009; Amorosi et al., 2013). The peculiarity of the Golo River system is the braidplain developed also during MIS5 (Fy1 terrace). Sediments from the warm-wet MIS5e (Tyrrhenian or Eemian stage) on the coast of Sardinia and central Italy are typically sandy littoral-coastal deposits (Amorosi et al., 2004, Nisi et al., 2008, Andreucci et al., 2009), therefore very different from the conglomeratic deposits at Sinisera (Fy1). Consequently, we argue that the coarse grained alluvial sediments of Fy1 were likely deposited during the colder stages of MIS5, namely MIS5d and MIS5b. In the upper part of the Marana Plain the MIS5e deposits have likely been reworked by fluvial processes during the formation of the Fy1 terrace, while in the lower part of the plain they might be preserved at depth.
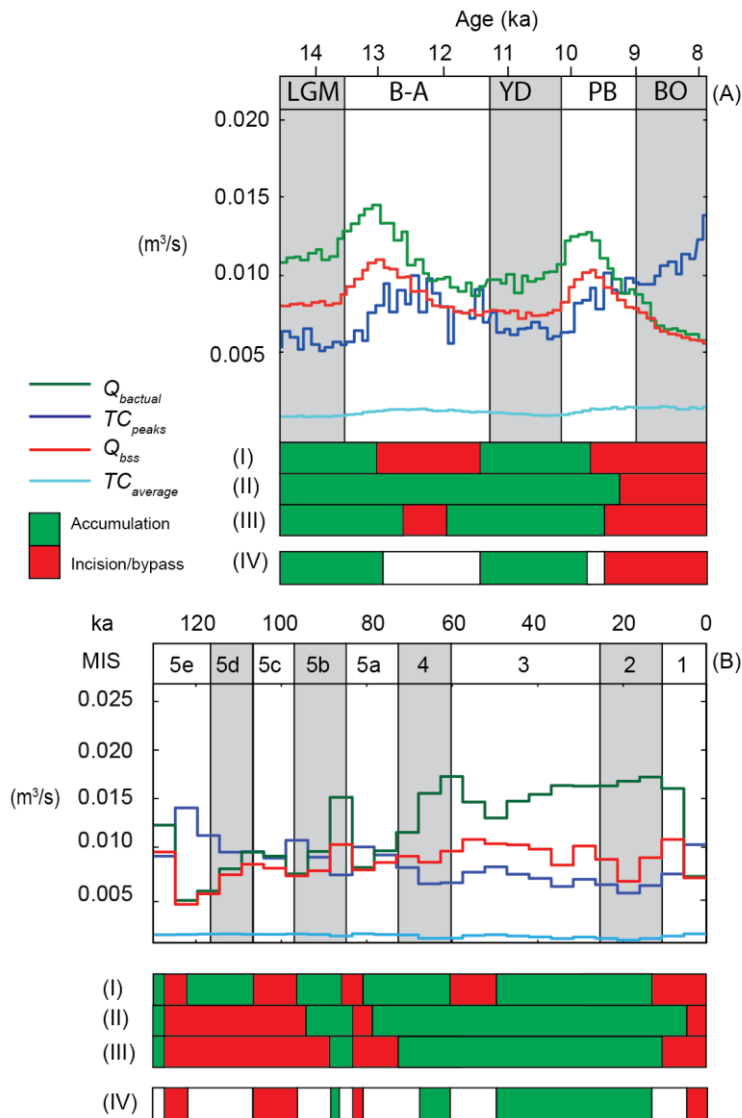
Figure 4.12: relation between bedload supply *Qbs*, actual bedload supply *Qbactual*, peak transport capacity *TCpeaks* and average transport capacity *TCaverage* and interpreted phases of accumulation or incision/ bypass for the Golo (A) during the last deglaciation (100 a temporal resolution) and (B) during the last 130 ka (5 ka temporal resolution). LGM = Last Glacial Maximum; B-A = Bølling-Allerød; YD = Younger Dryas; PB = Preboreal; BO = Boreal. The interpreted fluvial dynamics is based on (I) the increase or decrease in actual bedload supply; (II) the balance between actual bedload supply and peak transport capacity; (III) the balance between bedload supply and peak transport capacity. Interpretation (IV) is the intersection between interpretations (I), (II), and (III).

Sediment budget

We compared the calculated sediment yield to sediment yields and erosion rates from literature (Fig. 4.13). In order to quantify the uncertainty on the model output, we ran three experiments using different values of soil erodibility K_{soil}, the most important of the user-defined parameters (Forzoni et al., 2013). The calculated erosion rates (converted to km^3/ka) are comparable to the sediment yield to the Golo deep-sea fans (Calves et al., 2013), and lie within the range defined by the fluvial incision rates (Fellin et al., 2005) and denudation rates (Kuhlemann et al., 2008). We interpreted the differences between sediment volume from catchment erosion SY1 (km^3) and sediment volume in submarine fans SY2 (km^3) in terms of storage versus reworking of sediments (Fig. 4.14), assuming that most of the sediment delivered to the submarine fans was transported by the Golo and that the sediment yield from smaller rivers in Corsica and northern Italy is less relevant.

The average difference (Fig. 4.14C) between SY1 and SY2 was positive in all epochs except between 40-20 ka, indicating net storage of sediments in the catchment and/or on the shelf between MIS5 and early MIS3 ($4.3\ km^3$). However, due to the poor time constrains of SY1 from MIS5 to MIS3, we cannot exclude short periods of sediment bypass during this period, e.g., during MIS4. Sediments were reworked and bypassed to the submarine fans during late MIS3 to MIS2 (40-20 ka) (average -$0.4\ km^3$). Finally, during deglaciation and in the Holocene (15-0 ka), sediments were stored on the shelf and/or in the catchment ($1.1\ km^3$) (Table 4.5). The calculated volume of sediments stored in the catchment and on the shelf is $\approx 5\ km^3$, which is less that Sømme et al. (2011) reconstruction, with $\approx 3.5\ km^3$ of sediments stored in the catchment and $\approx 3.5\ km^3$ of sediments stored on the shelf. We argue that Sømme et al. (2011) might have overestimated the sediments stored in the Marana Plain by considering a much larger area for the deposition of the sediments from the Golo, whereas an important part of those deposits might have been transported by the smaller rivers draining to Corsican coastal range.

Finally, the difference between SY1 and SY2 might also be caused by the presence of glaciers in the highest part of the catchment during glacial periods (Kuhlemann et al., 2005, Conchon, 1976), which is not simulated by PaCMod. Glaciers enhanced erosion rates during their advance, but they are also an important sediment trap. Consequently, sediment flux out of the catchment might have decreased during glaciers advance and increased during deglaciation (Storms et al. 2012).
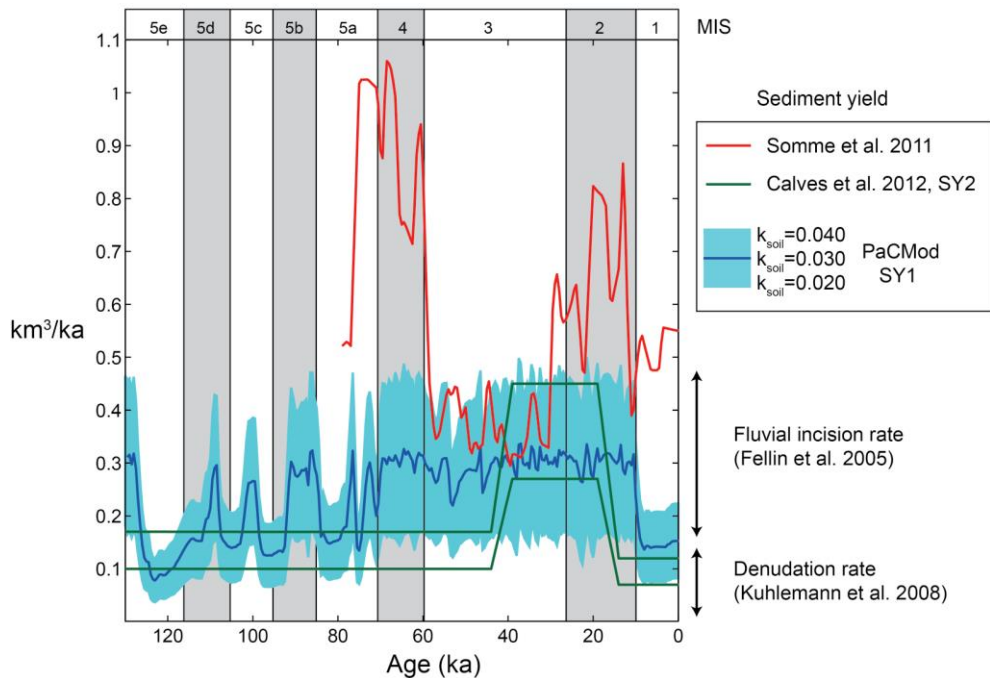
Figure 4.13: comparison between calculated suspended load yield (Somme et al. 2011); sediment yield to the Golo submarine fans (Calves et al. 2012); PaCMod total sediment yield based on calculated erosion rates with three different values of soil erodibility K_{soil}; measured fluvial incision rates in the Golo catchment (Fellin et al., 2005); calculated denudation rate in the Golo catchment (Kuhlemann et al., 2008). Somme et al., (2011) sediment yield is almost one order of magnitude higher than SY1 and SY2, as a consequence of Somme et al. (2011) choice to apply a constant water discharge throughout the whole simulation.

Causative controls

The stratigraphic and geomorphological evolution of the Marana Plain was controlled by the interaction of eustatism (downstream control), sediment and water supply (upstream control), and long term tectonic vertical movements. Figure 4.15 illustrates the temporal evolution of upstream (A) and downstream (C) controls, the spatial differences in vertical movements (D), and a wheeler diagram (B) synthesizing the temporal and spatial evolution of the Marana Plain stratigraphy assuming SG-CAM ages for Fy2 (MIS4-Early MIS3) and MG-CAM ages for Fy1 (MIS5d-MIS5b). While the upstream control determined how much sediment was stored and transported, the downstream control and vertical movements affected accommodation and sediment dispersal.

Table 4.5: sediment volumes, yield and volume differences summary

MIS	5	4	3b	3a-2b	2a	1
Volume PaCMod (km^3)	9.0±1.9	2.9±0.7	6.6±1.4	6.3±1.5	1.4±0.31	1.1±0.3
Volume in submarine fans (km^3)	8.0±2.1	1.3±0.3	4.9±1.2	6.7±1.7	0.5±0.1	1.0±0.2
Yield PaCMod (km^3/ 10^{2}a)	1.5±0.4	2.9±0.7	2.6±1.3	3.1±0.8	2.9±0.5	1.1±0.3
Yield to submarine fans (km^3/ 10^{2}a)	1.3±0.7	1.3±0.7	2.0±0.9	3.4±1.6	1.0±0.4	1.0±0.4
Volume difference (km^3)	1.0±4.0	1.6±1.0	1.7±2.6	-0.4±3.2	0.9±0.4	0.2±0.5

Tectonics

The long term uplift of onshore Corsica during the late Quaternary, indicated by the fluvial terrace treads (Fellin et al., 2005), allowed little accommodation within the catchment during the Late Quaternary and determined a net degradational stacking pattern of alluvial sediment bodies. On the other hand, the long term subsidence of the continental shelf and possibly on the downstream part of the Marana plain (Deptuck et al., 2005; Somme et al., 2011) offered more accommodation, resulting in an aggradational stacking pattern (Fig. 4.2B and 4.16).

Geophysical data in the upper part of the Marana Plain (Moreau et al., in prep) indicate a very thick (>70 m) package of coarse alluvial sediments of unknown age below the Golo floodplain. This suggests that the long term uplift of the Corsican eastern margin from the Miocene (Fellin et al. 2005) might have been unsteady and, in fact, a phase of subsidence likely occurred. We speculate that the switch from subsidence to uplift might be linked to the major geodynamic change in the Tyrrhenian Sea at around 0.7 Ma (Pepe et al., 2010), which might have led to the uplift of the in eastern Corsica anticlinal structure and subsidence in the Corsica Trough synclinal structure (Fellin et al., 2005).
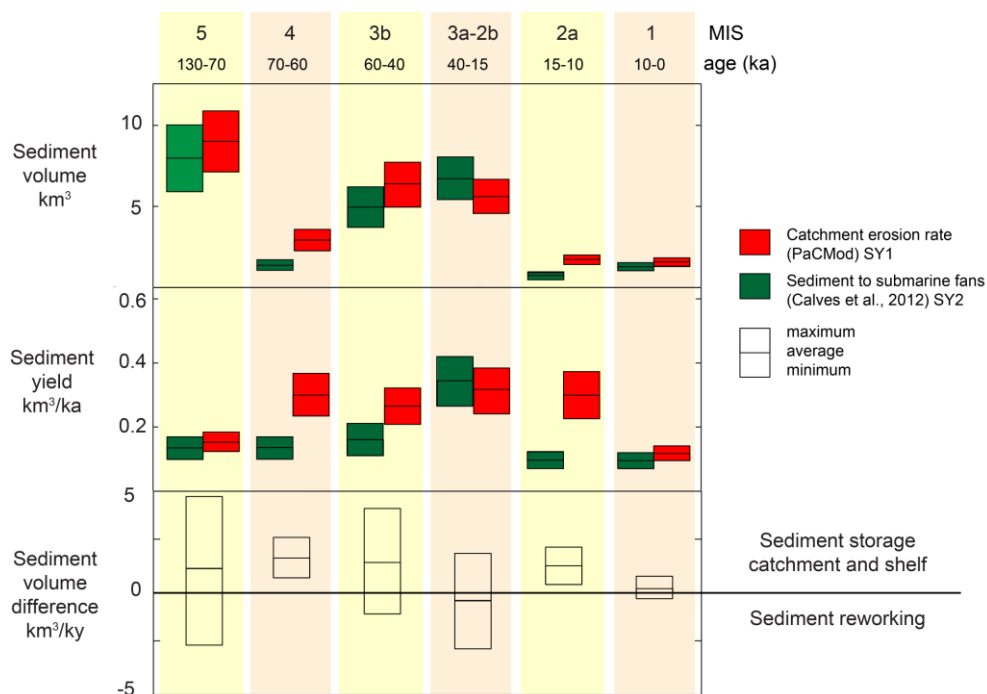
Figure 4.14: comparison between calculated catchment erosion rates (PaCMod) and sediment to submarine fans in (A) volumes, (B) sediment yield, and (C) sediment volume difference for six epochs in the last 130 ka. Values of sediment volumes, sediment yield, and sediment volume difference are show as average, maximum, and minimum, reflecting the uncertainty in model simulations and in the sediment yield to submarine fans (Calves et al., 2012). We interpreted the phases when erosion rates exceeded sediment flux to submarine fans as periods of sediment storage in the catchment and/ or on the continental shelf, whereas sediment reworking when the flux to submarine fans exceeded erosion rates.

Sea level and climatic changes

Accumulation of coarse sediments in braidplains (MIS5d, MIS5b, MIS4-early MIS3) was caused by (a) the high sediment supply, induced by sediment freeing in periods of low vegetation cover, and (b) by the gentle slope of the fluvial gradient in the Marana Plain, compared to the catchment upper reaches and to the continental slope. As the fluvial longitudinal profile was lengthened during the early stages of sea level fall, the Golo River restored its graded profile through aggradation (Fig. 17), similarly to other river systems with a high-relief catchment, such as in the Canterbury Plain, New Zealand (Brown and Naish, 2003) and the Venetian Plain of Northern Italy (Amorosi et al., 2008; Fontana et al., 2008). Furthermore, the low vegetation cover induced river-bank instability, thereby enhancing lateral channel migration and braindplain development. In addition,

based on analogue and numerical modeling experiments (van Heijst and Postma, 2001; van Heijst and Postma, 2001) we argue that the Golo braidplains developed during MIS5 (Fy1) and MIS3 (Fy2), were also incised at its apex simultaneously with progradation at the fan toe. This area of incision-lateral erosion migrated progressively downstream during regression.

The most important phases of incision and sediments reworking in the Golo alluvial-coastal plain occurred during phases of lowest sea level, namely MIS4 and late MIS3-MIS2 (Fig. 17), as a result of the landward migration of an erosional knickpoint. During these periods, most of the sediments produced in the catchment were bypassed to the Golo submarine fans. Afterwards, during the Late-Glacial and early Holocene, sea-level rise caused the drowning of the incised valley and its infilling with marine deposits, possibly alternating or contemporaneous with coarse fluvial deposits under glacial outwash conditions. During the middle and late Holocene, notwithstanding the low sediment supply, the modern deltaic wedge developed and prograded, as a consequence of the slow sea-level rise. Similarly, we argue that a fine-grained deltaic wedge developed during also MIS5e. This is in apparent contradiction with PaCMod experiments, which indicate incision/bypass during MIS5e and MIS1. However, PaCMod only simulates sediment flux and storage as a result of changing climate and neglects sea level variations. We argue that incision occurred in the Holocene and during the warm phases of MIS5 only in the upper reaches of the catchment, beyond the area of influence of sea-level variations, as a result of higher transport capacity, and high vegetation cover, which led to sediment locking in stream banks and forced river to cut and scour their channels.

Valley incision during MIS4 and MIS2 is a common characteristics to the coastal plain of river systems in Italy, such as the Arno River (Amorosi et al., 2013); the Tevere River (Milli et al., 2013); the Ombrone River (Bellotti et al., 2004); and Po River (Amorosi et al., 2004), as well as the well-studied examples on the Texas coast (Blum et al., 2013). What makes the Golo special compared to these systems is (a) the proximity of the coastline to the mountain ranges, i.e., the sediment source, and (b) the narrow continental shelf, which allowed sediments to be bypassed more effectively towards the submarine fans. These characteristics allowed climatic and sea level forcing signals to be transmitted across the fluvial systems within less than few centuries and enhanced the impact of climate-induced sediment supply variations on the alluvial-coastal plain.
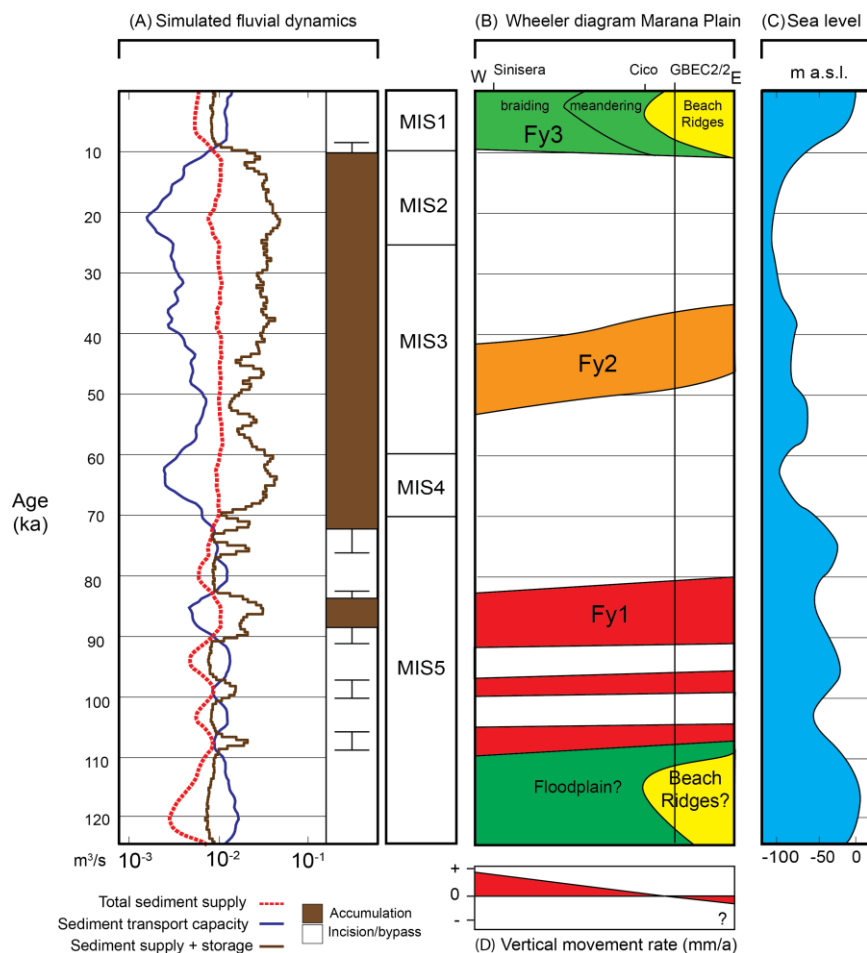
Figure 4.15: Climatic, eustatic, and tectonic controls on the Marana Plain geomorphological evolution. (A) simulated fluvial dynamics: brown indicates accumulation, white indicates incision, and the error bars indicate possible accumulation. (B) Wheeler diagram. (C) Sea level curve from Waelbroeck et al., 2002. (D) Interpreted tectonic vertical movement rates in the Marana Plain based on Fellin et al. (2005).

Fluvial system non-linear response to climate and sea level variations

PaCMod experiments showed that high sediment flux pulses from the catchment were generated at transitions form cold-dry stadials to warm-wet interstadials during deglaciation (Figs. 4.9, 4.10, and 4.12), when bedload supply equaled fluvial transport capacity. Relative low sediment flux occurred during phases of either low transport capacity (cold-dry climate) or low bedload supply (warm-wet climate). Such results indicate a non-linear response of the fluvial system to

climate. Sediment storage, sediment transport and the amplitude of sea level variations were the main causes for this non-linear relation.

First, the sediments stored in the catchment during low-discharge glacial phases, were released during deglaciation, when transport capacity increased as a result of increasing precipitation and snowmelt. This led to the high sediment flux pulses at the cold-warm transitions. Second, peak transport capacity acted as a threshold for fluvial dynamics evolution. Accumulation of coarse material in the catchment did not occur in all phases of high bedload supply, but only in phases when actual bedload supply exceeded peak transport capacity (MIS5d, MIS5b, MIS4-MIS3). Finally, we argue that the impact of sea level variations on the Golo fluvial system was conditioned by the magnitude of these variations (Fig. 4.17). Our interpretation of stratigraphic data indicates that sea level induced major incision in the alluvial-coastal plain only during periods of lowest sea level (MIS4 and MIS2), whereas it promoted aggradation during periods of intermediate sea level (MIS5d, MIS5b, and MIS3).
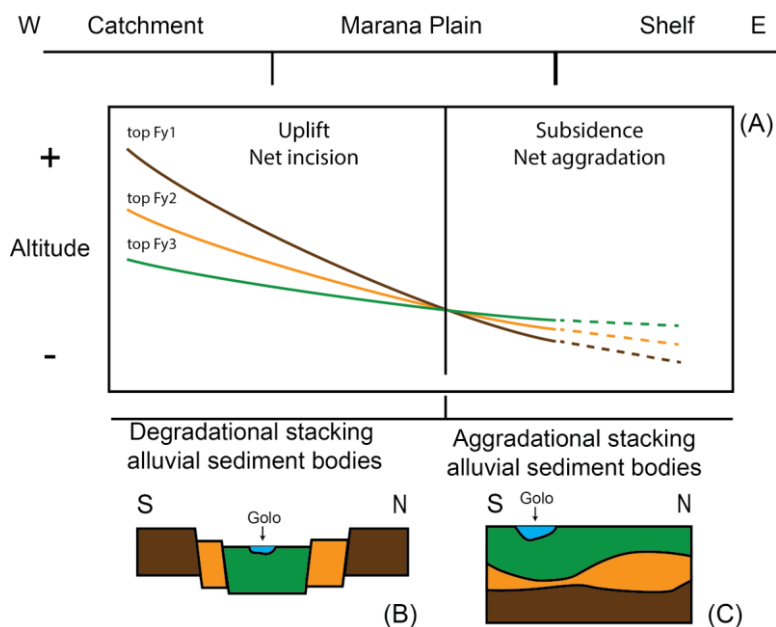
Figure 4.16: (A) Schematic W-E longitudinal profiles of the Golo fluvial alluvial terraces and schematic S-N cross-sections across (B) the upper part and (C) the lower part of the Marana plain. The steepness of the longitudinal profiles increases with depositional age as a result of higher uplift rates in the west compared to the east. The long-term uplift results in net incision with a net degradational stacking of alluvial sediment bodies (Fig. 4.2, cross-section B-B'). The aggradational stacking in the lower part of the

Marana Plain (borehole GBEC2-2) and likely on the shelf is the result of higher accommodation caused by subsidence.
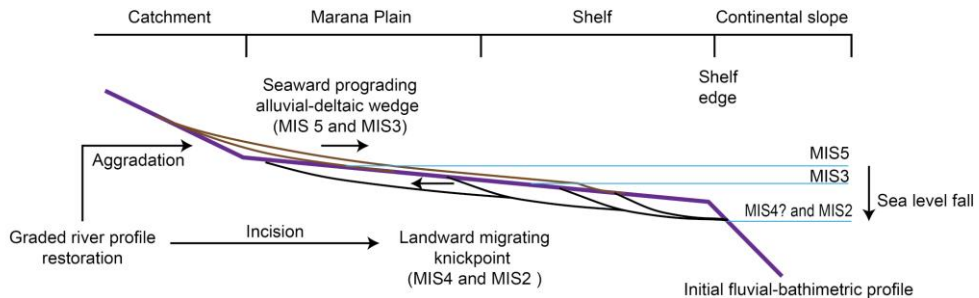

Figure 4.17: schematic evolution of the Golo fluvial-bathymetric profile during sea level fall. As the fluvial longitudinal profile was lengthened during early sea level fall (MIS5 and MIS3), the Golo River restored its graded profile through aggradation. During sea-level low stands (MIS4 and MIS2) an erosional knickpoint migrated upstream inducing incision in the Golo alluvial plain.

4.5. Conclusions

We applied a numerical model PaCMod and compared modeling results to field data and new OSL ages in order to (i) reconstruct the sediment flux and fluvial dynamics history of the Golo river system, and (ii) investigate the impact of external forcing on the geomorphological and stratigraphic evolution of the Golo alluvial-coastal plain. Our results indicate that: (1) the Golo River system response to climate and sea level variations was non-linear, as a result of catchment memory and geomorphological thresholds; (2) the Golo alluvial-coastal plain evolution was controlled by a complex interaction of sediment supply, seal level variations, and tectonics; (3) glacial phases were characterized by high hillslope erosion and sediment storage, and low transport capacity. Interglacial phases were characterized by low hillslope erosion, high water discharges and transport capacity; (4) a large amount of coarse sediment was stored in the catchment during glacial phases, and it was consequently eroded and bypassed to the submarine fans during periods of lowest sea level.

These results support the idea that fluvial stratigraphy should not be interpreted based on sea level fluctuations only, but one should also account for climatic-induced sediment supply variations. The observed non-linear relation between external forcing and fluvial system response suggests that only the events crossing climatic and morphological thresholds are transmitted to the geomorphic-stratigraphic record, implying that the geological record is a filtered translation of external forcing.

CHAPTER 5

Along-strike variations in stratigraphic architecture of shallow marine reservoir analogues: Upper Cretaceous Panther Tongue delta and coeval shoreface, Star Point Sandstone, Wasatch Plateau, central Utah, USA

Abstract. Along-strike variations in sediment supply and process regime may result in different facies distributions and stratigraphic architectures in shallow-marine strata. Data from a large (c. 100 km), nearly continuous outcrop belt aligned oblique to depositional strike was integrated with nearby sub-surface well data and petrological analysis of distal fine-grained deposits, to analyze along-strike variations in stratigraphic architecture within a single parasequence in the upper Cretaceous Star Point Sandstone, Wasatch Plateau, central Utah, USA.

The parasequence comprises wave-dominated shoreface deposits in the southern part of the study area, and represent a single episode of shoreline regression and transgression. Four progradationally stacked bedsets (BS1-BS4) in the distal deposits of the parasequence are the expression of minor variations in relative sea-level, sediment supply and/or wave climate. The four bedsets can be traced to fluvial-dominated deltaic deposits (Panther Tongue) in the northern part of the study area. We interpret the parasequence on the scale of the Wasatch Plateau outcrop belt as the record of deposition in a regressive fluvial- and wave-influenced delta, which is deflected asymmetrically towards the SSW, sub-parallel to the regional paleo-shoreline trend, with a coeval wave-dominated strandplain. The lateral transition from fluvial- to wave-dominated facies is attributed to the localization of a major river acting as a point sediment source in the north, and to wave-induced longshore transport towards the south. Our results imply that characterizing lateral facies distributions and the expression of bedsets is vital for interpreting along-strike variability in controlling mechanisms of stratigraphic architecture, and that external forcing may be recorded differently along depositional strike.

5.1. Introduction

Understanding variable patterns of stratigraphic architecture and associated heterogeneities is crucial for untangling the causative controls on stratigraphy (Charvin et al., 2010), and for predicting the lithological characteristics of subsurface hydrocarbon and groundwater reservoirs (e.g. Hansen and Rasmussen, 2008; Enge and Howell, 2010; Olariu et al., 2010). The architecture of shallow marine deposits is controlled by physical processes (rivers, waves, tides), autogenic behaviors (e.g. delta lobe switching), and accommodation (e.g. Hampson and Storms, 2003; Storms and Hampson, 2005). Ancient regressive shallow marine deposits typically occur as laterally extensive sandstone tongues or parasequences, which represent periods of shoreline progradation (Elliott, 1986; Walker and Plint, 1992; Reynolds, 1999; Clifton, 2006). Each tongue is characterized by a shallowing-upward succession bounded by flooding surfaces that represent shoreline transgression (Van Wagoner et al., 1990; Kamola and Wagoner, 1995).

During the last two decades, several studies have analyzed the high resolution, intra-parasequence stratigraphic architecture and associated heterogeneities of fossil deltas and strandplains and unravel the forcing mechanisms controlling their evolution (Gani and Bhattacharya, 2007; Hampson et al., 2008; Somme et al., 2008; Charvin et al., 2010; Enge et al., 2010a; Enge et al., 2010b; Olariu et al., 2010; Li et al., 2011). For example, Hampson and Storms (2003) and Storms and Hampson (2005) showed that individual clinoforms within a fossil wave-dominated parasequence were formed by enhanced by wave scour and/or sediment starvation, which may have been driven by minor fluctuations in sea-level, sediment supply and/or wave regime over short timescales (10^1-10^3 years). Bhattacharya and Giosan (2003) stressed the necessity of interpreting ancient depositional systems in a larger paleo-geographic context. In particular, their observations from modern asymmetric wave-dominated deltas indicate that most deltas are characterized by major along-strike variations in sedimentary environments and facies associations. Fluvial-dominated delta front deposits can be coeval with wave-dominated shoreface, lagoonal, and barrier-island deposits within a single delta lobe, such as in the modern Danube Delta and Ebro Delta (Somoza et al., 1990; Bhattacharya and Giosan, 2003).

Along-strike differences in subsidence, river-supplied sediment and water, and wave action enhance differences in facies distributions, preservation potential, and expression of sequence stratigraphic surfaces and units in shallow-marine deposits (e.g. Ainsworth et al., 2008, 2011). This implies that different parts of the deltaic or

shoreline system may record a different signal of external forcing change. Therefore it can be a challenging task to connect different along-strike components of ancient shallow marine strata dominated by different sedimentological processes, and to reconstruct the signal of external forcing history (relative sea level, sediment supply, wave climate) recorded in shallow marine sedimentary archives.

Continuous exposures of the Upper Cretaceous Star Point Sandstone in the Wasatch Plateau (central Utah, USA) are aligned sub-parallel to regional depositional strike over a distance of c. 100 km, and provide an opportunity to investigate the along-strike and vertical changes in the intra-parasequence stratigraphic architecture of shallow-marine deposits of mixed wave and fluvial influence. Based on detailed outcrop studies in the northern Wasatch Plateau, the Panther Tongue of the Star Point Sandstone is considered a fluvial-dominated river delta deposited during a forced regression (Newman and Chan, 1991; Posamentier and Morris, 2000; Hwang and Heller, 2002). However, the Panther Tongue also forms the northern continuation of a wave-dominated parasequence deposited principally during normal regression in the southern Wasatch Plateau (parasequence KSp040 of Hampson et al., 2011) (Flores et al., 1984; Dubiel et al., 2000). This apparent contradiction suggests that the internal stratigraphic architecture of the Panther Tongue and KSp040 coastal system on the spatial scale of the Wasatch Plateau outcrop belt is still poorly understood, and that the signal of relative sea-level change may be strongly modified along-strike. The aims of this paper are (1) to present new data and interpretations of the intra-parasequence architecture and along-strike variability of the Panther Tongue delta and KSp040 shoreface deposits; and (2) to relate this architecture to shoreline geomorphological evolution with reference to modern analogues.

5.2. Geological setting and previous work

The Panther Tongue forms part of the shallow-marine Star Point Sandstone, which was deposited during the Santonian-Campanian along the western shoreline of the Cretaceous Western Interior Seaway, a shallow sea that extended from north to south across the North American continent (Fig. 5.1A). The Star Point Sandstone overlies and interfingers with the offshore deposits of the Mancos Shale, and it is overlain by coal-bearing coastal plain deposits of the Blackhawk formation (Fig. 5.1B and 5.1C) (Speiker and Reeside, 1925). The Mancos Shale, Star Point Sandstone, Blackhawk Formation and overlying Castlegate Sandstone form an eastward-prograding wedge of siliciclastic sediment that forms part of a foredeep

fill along the western margin of the Western Interior Seaway. To the west of the seaway laid the Sevier Orogenic Belt, a major mountain range formed as a result of the collision between the North American Plate and the Farallon Plate. Thrust loading and crustal thickening in the Sevier Orogenic Belt provided the topography needed for erosion and transport of sediment towards the Western Interior Seaway, and induced subsidence in the foredeep (e.g. Liu et al., 2014).

During the Santonian-Campanian, the hinterland supplying sediments to the Panther Tongue deltaic system was affected by progressive westward migration of deformation associated with active, SSW-NNE-oriented thrusts and folds (DeCelles and Coogan, 2006). Petrological analysis of the Star Point Sandstone and Blackhawk Formation indicates that the catchment was underlain mainly by sandstones, quarzites and limestones, consistent with exhumation of Precambrian and Palaeozoic basement rocks in the Sevier Orogen (DeCelles and Coogan 2006). The coarser sediments eroded from the Sevier Orogen mountain ranges accumulated in alluvial fan and braidplain deposits of the Indianola Group (Lawton, 1982), whereas sand, silt and clay were transported farther basinwards (e.g. Robinson and Slingerland, 1998).

The Panther Tongue crops out along the eastern edge of the Wasatch Plateau in Central Utah (Fig. 5.2). Most previous studies have focused on outcrops in the area north of the town of Helper (Olariu et al., 2005, 2010; Howell et al., 2008; Enge et al., 2010a, 2010b), in the northern part of the Wasatch Plateau. Here the Panther Tongue is characterized by delta front clinoforms deposited by intermittent gravity flows, and it contains multiple laterally stacked mouth bar bodies (Olariu et al., 2005, 2010; Enge et al., 2010a, 2010b). In sequence stratigraphic terms, the Panther Tongue has been interpreted to record forced regressive or lowstand deposition, due to the large dip extent of the unit (>20 km), an absence of overlying delta plain deposits, and the declining clinoform relief in a down dip direction (Posamentier and Morris, 2000). The delta front clinoforms are top-truncated by a transgressive wave-cut erosion surface capped by thin shallow-marine deposits (Hwang and Heller, 2002).
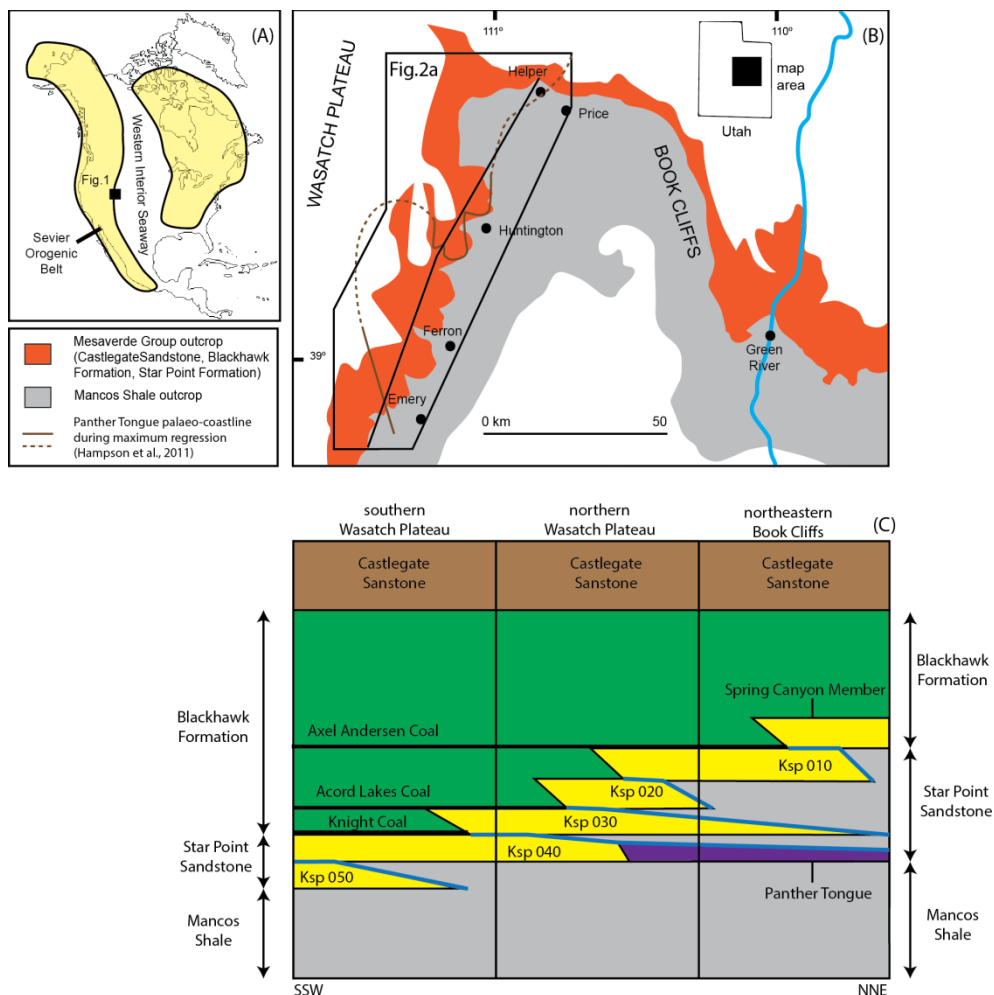
Figure 5.1: (A) Location of the study area on the western margin of the Western Interior Seaway (after Kauffman and Caldwell, 1993); (B), location of the Mesaverde Group (including the Star Point Sandstone, Blackhawk Formation, and Castlegate Sandstone) and Mancos Shale outcrop belt in the Wasatch Plateau and western Book Cliffs; (C) lithostratigraphic summary chart of the Star Point Sandstone and surrounding strata in the Wasatch Plateau and north-western Book Cliffs (after Hampson et al., 2011).
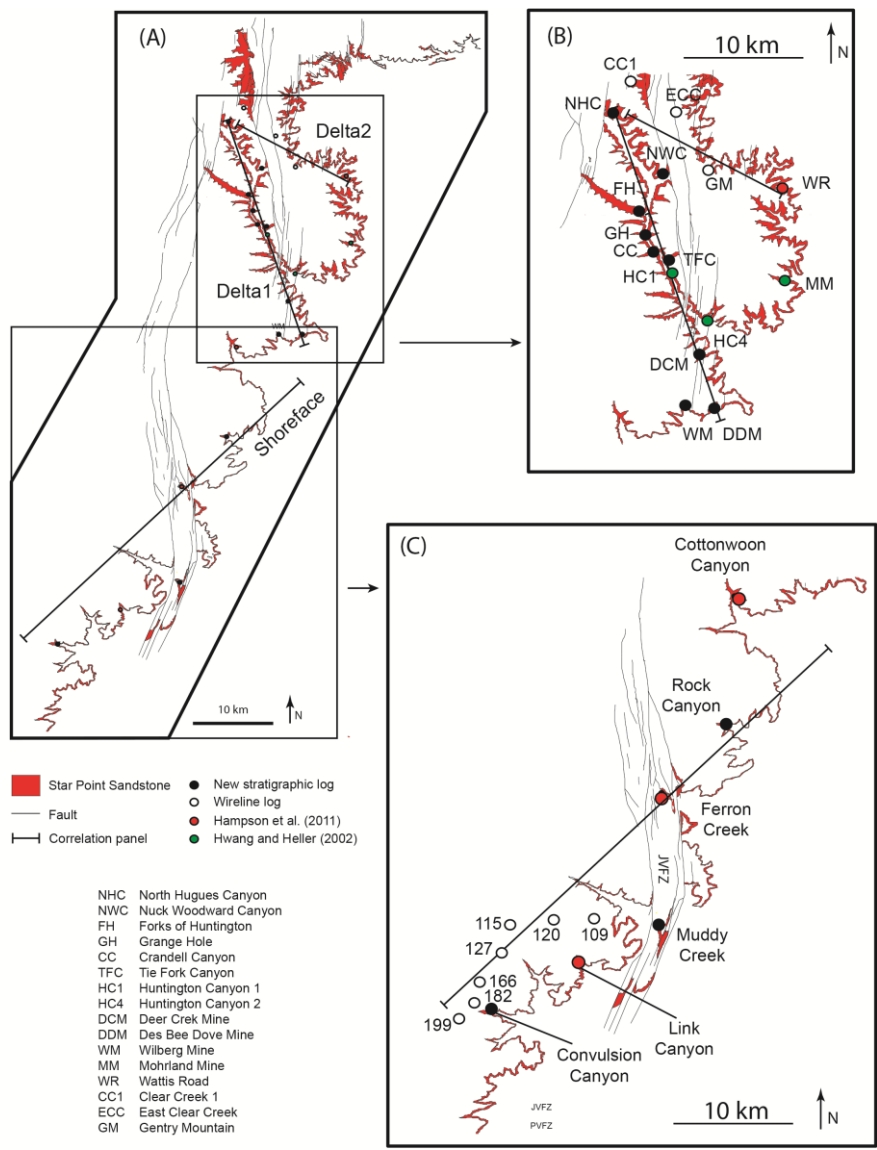
Figure 5.2: (A) Map of the eastern Wasatch Plateau, showing the Star Point Sandstone outcrop belt, location of stratigraphic logs within the Star Point Sandstone and correlation panels. Detailed maps of the Star Point Sandstone outcrop belt, locating stratigraphic logs and cross sections used in this study in: (B) the Huntington Canyon area (after Hwang and Heller 2002; Hampson et al., 2011; Utah Geological Survey, 2014) and (C) the Ferron area (Dubiel et al., 2000; Hampson et al., 2011).

Recent photographic mapping of cliff-face exposures indicates that the deltaic deposits in the northern Wasatch Plateau correlate with the wave-dominated shoreface deposits in the southern Wasatch Plateau (parasequence Ksp040 of Hampson et al., 2011; equivalent to parasequences 1, 2 and 3 of Dubiel et al., 2000). Although the regional paleo-shoreline during the Cretaceous was N-S oriented, the interpreted local shoreline morphology was complex (see interpreted palaeo-coastline by Hampson et al. (2011) in Fig. 5.1B). Paleocurrent direction and clinoforms geometry in the northern Wasatch Plateau indicate progradation of a river-dominated delta towards the south, sub-parallel to the regional shoreline, whereas the wave-dominated shoreface deposits in the southern Wasatch Plateau represent ENE prograding shorelines. In combination, these two components form an eastward prograding deltaic-coastal system, with decreasing river influence and increasing wave influence towards the south.

There is no documented evidence in the southern Wasatch Plateau for shoreface progradation during a relative sea level fall, in contrast to the forced regressive architecture of the Panther Tongue delta front deposits in the northern Wasatch Plateau (Hampson et al., 2011). Hampson et al. (2011) argued that evidence of a relative sea level fall may be below the resolution of their stratigraphic analysis of the southern Wasatch Plateau exposures. Alternatively, the wave-dominated shoreface deposits in the south may not be directly time-equivalent to the fluvial-dominated deltaic deposits in the north.

5.3. Dataset and methods

We measured new stratigraphic logs of the Panther Tongue in the Huntington Canyon area (Fig. 5.2B) and of the Ksp040 parasequence in the cliffs west of Ferron and Emery (Fig. 5.2C). These stratigraphic logs record lithology, grain size, sedimentary structures, trace fossil types, and bioturbation intensity in the form of the bioturbation index (Taylor and Goldring, 1993). Three correlation panels were constructed using the new stratigraphic logs, combined with stratigraphic logs from previous work (Hwang and Heller, 2002; Hampson et al., 2011), interpreted wireline logs (Dubiel et al., 2000) and previously not interpreted wireline logs (Utah Geological Survey, 2014). The correlation between stratigraphic logs is based on the tracing of sequence stratigraphic surfaces and units along cliff faces (cf. Hampson et al., 2011), and existing wireline-log correlations are utilized where appropriate (Dubiel et al., 2000). The logs in each correlation panel are projected into a 2D plane: one correlation panel (labelled "Shoreface" in Fig. 5.2) is oriented oblique to the wave-dominated KSp040 palaeo-coastline in the southern part of the

Wasatch Plateau (Hampson et al. 2011), while the other two panels (labelled "Delta1" and "Delta2" in Figure 5.2) are oriented along local axes of progradation in the fluvial-dominated Panther Tongue delta (Hwang and Heller, 2002; Hampson et al., 2011).

We analyzed sediment samples collected in a vertical profile in the Des Bee Dove Mine location (Fig. 5.2B) in order to investigate the petrological and grain size properties of the fine-grained succession in the lower part of the studied stratigraphic interval, and to correlate stratigraphic surfaces between the "Shoreface" and the "Delta1" panels. All 43 samples were analyzed with X-Ray fluorescence (XRF), resulting in a record of relative element abundances in the context of a vertical chemical signal. A principal component analysis was applied to the XRF data and the results were plotted as log-ratios of the major elements (Bloemsma et al., 2012). Five samples were selected for further analysis with micro CT scans and thin sections, which provided mineralogical composition, average grain size, and grain size fraction volumes. Micro CT-scan images show higher density material in lighter grey tones and lower density material in darker grey tones (Fig. 5.3).

Using image analysis software (ImageJ) (Rasband, 1997), we quantitatively analyzed images from thin sections and CT scans to determine (1) the average particle grain size and (2) the volume of silt-grain and matrix fractions (Fig. 5.3). First, we applied a high color threshold C_{high} to the images, thereby isolating the individual grains. Then we calculated the diameter of the grains using a low grain-size threshold g_{low} (silt-clay, 12.5 μm^2) and a high grain-size threshold g_{high}, considering the latter as the boundary between non-cohesive and cohesive grains (medium silt-fine silt, 167.3 μm^2). Second, we applied a low color threshold C_{low} to the same images thereby marking all the area of the image occupied by grains, and subsequently calculated this area with either a high or a low grain-size threshold. Finally, we interpolated the values of average grain size and grain-size fractions to all the samples in the succession at Des Bee Dove Mine based on the XRF signal, calculating the power function which best fits the relation between either grain size or grain-size fraction and the XRF values. Technical details of the techniques used are described in the Supplement to this paper.
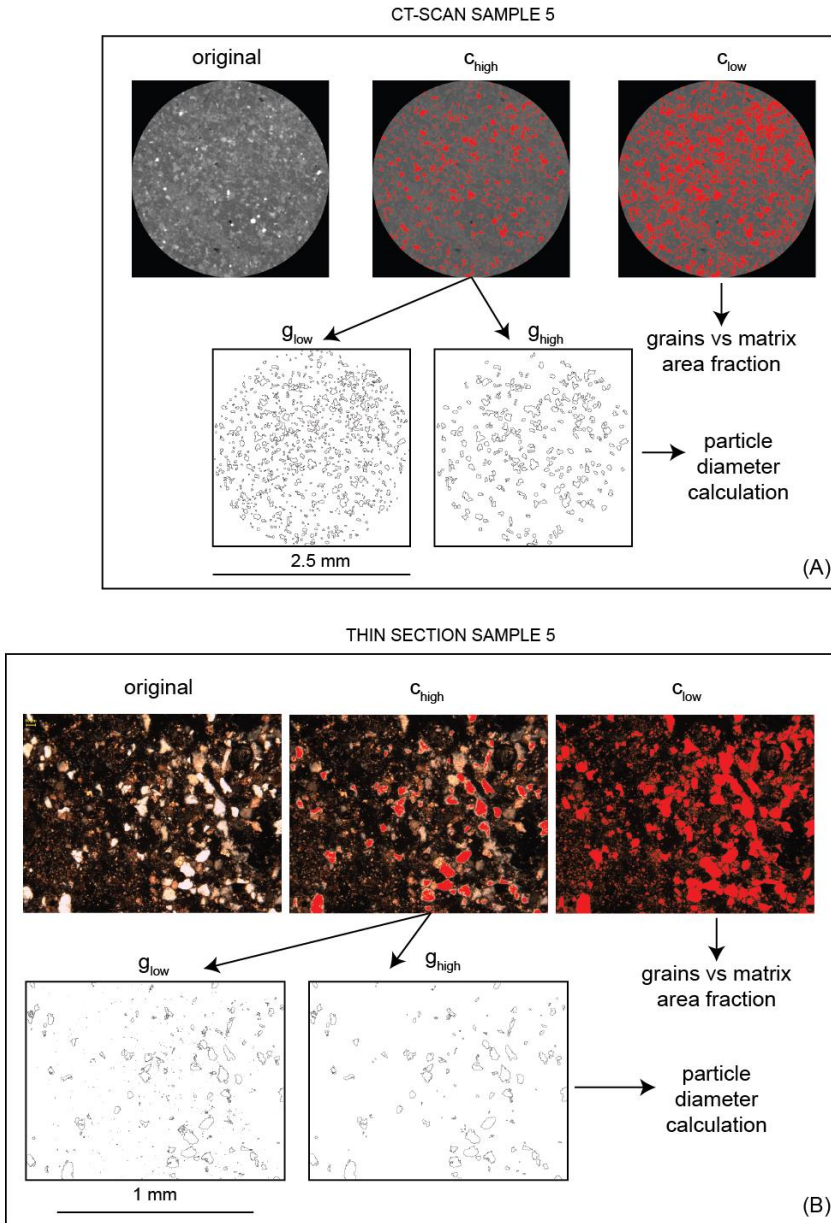
Figure 5.3: Methodological approach for analysis of images from: (A) CT-scans, and (B) thin sections. For every image we used two color thresholds c_{high} and c_{low}. We used the image with the low color threshold to calculate the area occupied by silt-sized grains (colored in red) versus the area occupied by matrix and cement (grains vs matrix area fraction). From the image with the high color threshold we calculated the particle diameter using two grain-size thresholds g_{high} and g_{low}. See section 5.3 for details.

4. Results

Facies and facies successions

We recognized the following eight facies, which correspond to previous facies interpretations of the Star Point Sandstone, the Mancos Shale and the Blackhawk Formation (Newman and Chan, 1991; Dubiel et al., 2000; Enge et al., 2010a; Olariu et al., 2010; Hampson et al., 2011): offshore shelf (OS), distal lower shoreface (dLSF), proximal lower shoreface (pLSF), upper shoreface and foreshore (USF), distal delta front (dDF), proximal delta front (pDF), distributary channel (DC), and floodplain (FP). These facies are summarized in Table 1, and their arrangement into vertical facies successions is summarized below.

Shoreface facies are arranged into vertical successions characterized by a distinctive ordering of facies (from base to top: dLSF, pLSF, USF) and an upward increase in sandstone content (Figs. 5.4, 5.5). Non-amalgamated, hummocky cross-stratified sandstones with interbedded shales, and amalgamated hummocky cross-stratified sandstones are interpreted as distal lower shoreface (dLSF facies) and proximal lower shoreface deposits (pLSF facies), respectively (Fig. 5.4C, D). Sand was deposited during major storm events, whereas mud and silt was deposited during fair weather conditions. Trough and tabular cross-bedded sandstones are interpreted as upper shoreface deposits (USF facies; Fig. 5.4B) deposited during the migration of nearshore sand bars, and locally these are capped by planar-parallel laminated sandstones that record deposition under upper plane bed conditions by swash-backwash processes on the foreshore. Where absent, foreshore deposits were probably eroded by wave action during transgression (Fig. 5.4A) (e.g. Hwang and Heller, 2002). The vertical facies successions are interpreted to represent upward shallowing and regression (Dubiel et al., 2000; Hampson et al., 2011). Trace fossil assemblages are characterized by a mixture of Cruziana and Skolithos ichnofacies in the dLSF and PLSF facies and Skolithos ichnofacies in the USF facies, which indicates deposition in progressively shallower shoreface environments (MacEachern & Bann, 2008).

Delta front deposits at Wattis Road and near Helper (Fig. 5.2B) are arranged into characteristic, upward-coarsening vertical facies successions (from base to top: dDF, pDF) (Figs. 5.6, 5.7). Non-amalgamated, normally graded structureless and laminated sandstones and interbedded shales at the base of the successions are interpreted as distal delta-front deposits (dDF facies; Fig. 5.6C, D). These grade upwards into amalgamated sandstones that contain trough and tabular cross-beds, and are interpreted as proximal delta front deposits (pDF facies; Fig. 5.6A, B). The

vertical facies successions are interpreted to represent gradual upward shallowing and regression (Olariu et al., 2010; Enge et al., 2010a; Hampson et al., 2011). In the Huntington Canyon area (Fig. 5.2B), proximal delta front deposits (pDF facies), directly overlie offshore-shelf mudstones (OS facies), indicating erosion at the base of the delta front. Asymmetrical ripples, steep clinoforms (up to 15°; Fig. 5.7A), and a low bioturbation index in the deposits indicate deposition from unidirectional flow close or at the river mouth bar. However, the pervasive occurrence of hummocky cross-stratified beds and a high degree of sorting suggest that the sand delivered to the mouth bar was reworked by waves (Fig. 5.7C).

Shoreface and delta front deposits overlie thick (>30 m) successions of bioturbated mudstones with interbedded, thin, rippled sandstone beds (Figs. 5.4E, 5.5C, 5.6C, 5.D, 5.7B). These mudstones were interpreted as offshore-shelf deposits (OS facies), deposited from suspended sediment plumes, from major storm events, and from river-derived hyperpycnal flows. Erosionally based, channelized sandstones that truncate and interfinger with the upper parts of delta front and shoreface facies successions are interpreted as distributary channels (Olariu and Bhattacharya, 2006). At Grange Hole and Tie Fork Canyon (Figs. 5.2B, 5.7B, C), distributary channel-fill sandstones are incised into delta front deposits, suggesting a genetic relation between distributary channel and delta front deposits. In other locations (e.g. Convulsion Canyon, Fig. 5.8A and North Hueghes Canyon, Fig. 5.9), distributary channel-fill sandstones cannot be linked to their coeval mouth bars, as they are incised in wave-dominated shoreface deposits. Root-penetrated mudstones and interbedded sandstones and coals are interpreted as floodplain deposits (FP facies).

The upper 0.5-1 m of many shoreface and delta front successions are intensely bioturbated, they overlie hummocky cross-stratified sandstones and shales, and are capped by an erosional surface that is lined by a thin (5-30 cm) bed of coarse-grained sandstone. This vertical transition records upward-deepening and transgression. The erosional surface is thus interpreted as a ravinement surface (*sensu* Swift, 1968), and the overlying deposits as a transgressive lag, as described in detail by Hwang and Heller (2002).

Table 5.1: Summary of facies associations in the Star Point Sandstone, lower Blackhawk Formation, and Mancos Shale (after Newman and Chan, 1991; Dubiel et al., 2000; Enge et al., 2010a; Olariu et al., 2010; Hampson et al., 2011).

| Facies	Lithology and Sedimentary Structures	Process Interpretation
Offshore shelf (O)	Mudstone with rare beds of fine-grained sandstone. Parallel lamination, wave-and current-ripple cross-lamination.	Mud deposition from suspended sediment plumes; sand deposition during major storm events or by river-derived hyperpycnal flows.
Distal lower shoreface (dLSF)	Non-amalgamated beds of fine-grained sandstone with mudstone interbeds. Hummocky cross-stratification, minor wave-ripple cross-lamination.	Sand deposition during major storms events; mud deposition during fair weather periods. Above storm wave-base and below fair-weather wave-base.
Proximal lower shoreface (pLSF)	Amalgamated beds of fine-grained sandstone. Hummocky cross-stratification, minor wave-ripple cross-lamination.	Sand deposition during major storms events; fair weather mudstones are not preserved. Above storm wave-base and below fair-weather wave-base.
Upper shoreface and foreshore (USF)	Fine- to medium-grained sandstone. Trough and tabular cross-beds, wave-ripple cross-lamination, minor planar lamination.	Migration of nearshore bars due to longshore and offshore-directed currents generated by fair weather wave approach. Planar lamination generated under upper plane bed conditions. Above fair-weather wave-base.
Distal delta front (dDF)	Non-amalgamated beds of fine- to medium-grained sandstone with mudstone interbeds. Graded, structureless to laminated sandstone beds. Rare hummocky cross-stratification and wave-ripple cross-lamination.	Sediment gravity flow deposits near toe of delta front; variably reworking by oscillatory flow during major storm events.
Proximal delta front (pDF)	Amalgamated beds of fine- to medium-grained sandstone. Trough and tabular cross-beds, massive to laminated beds. Rare hummocky cross-stratification and wave-ripple cross-lamination.	Migration of dunes and sediment gravity flows down the delta front, and lateral and longitudinal accretion of distributary mouth bars.
Distributary channel	Channelized fine- to coarse-grained sandstone bodies containing trough and tabular cross-beds, soft-sediment folding, scour and lateral accretion surfaces, massive beds.	Migration of sandy dunes and bars within and adjacent to fluvial channels, in overall deltaic setting.
Floodplain	Root-penetrated mudstones with thin beds of fine- to medium-grained sandstone, coal.	Mud deposition from suspension during small floods; sand deposition during major floods. Roots record repeated subaerial exposure. Coal records accumulation of organic material in paleosols during reduced clastic sedimentation.
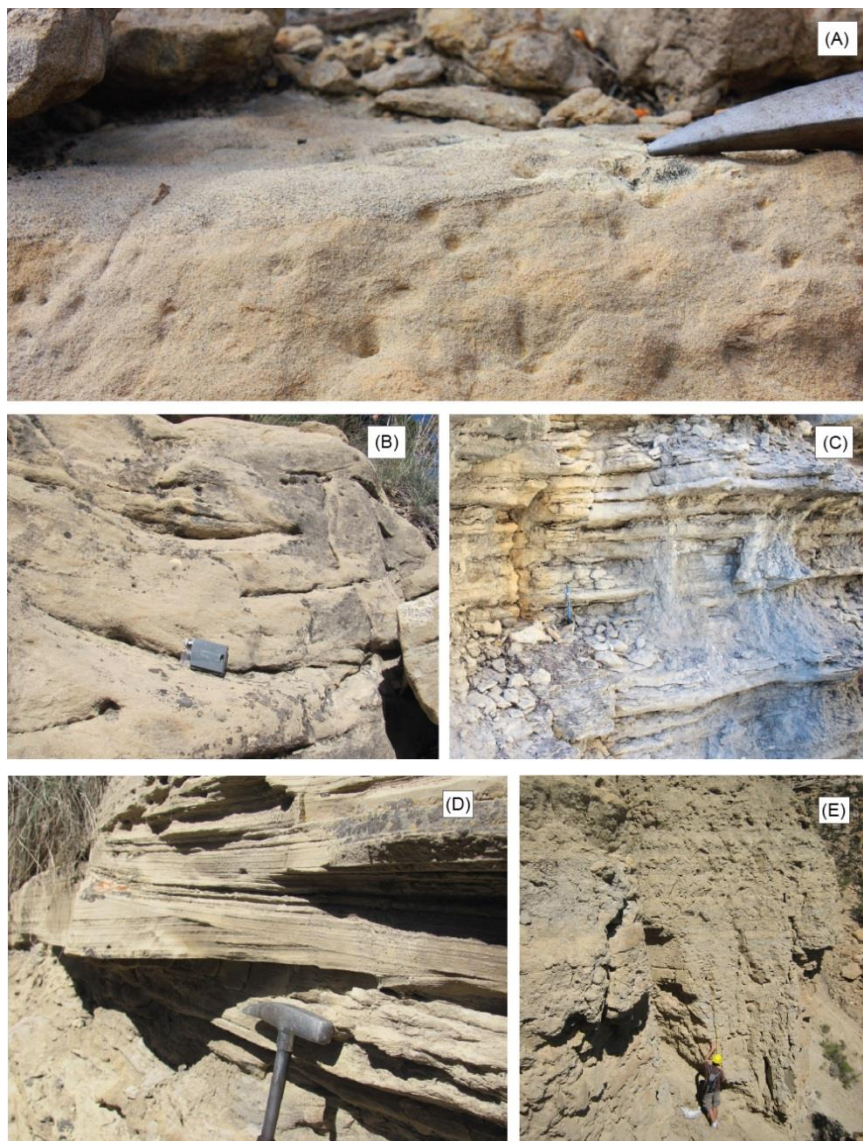
Figure 5.4: Photographs illustrating wave-dominated shoreface facies (Table 1). (A) Erosional scour overlain by well-sorted coarse-grained sandstone and underlain by intensely bioturbated medium-grained sandstone (USF facies) at Dee Bee Dove Mine (Fig. 5.5C). The coarse-grained sandstone is interpreted as a transgressive lag produced by wave-induced erosion and sediment reworking (cf. Hwang and Heller, 2002). (B) trough cross bedding in medium-grained sandstones (USF facies) at Deer Creek. (Fig. 5.5A). (C) fine-grained sandstone beds and siltstone interbeds (dLSF facies); and (D) hummocky cross stratification in one of the sandstone beds (dLSF facies) at Deer Creek (Fig. 5.5A). (E) Bioturbated siltstone beds (OS facies) at Rock Canyon. Localities are shown in Figure 5.2.
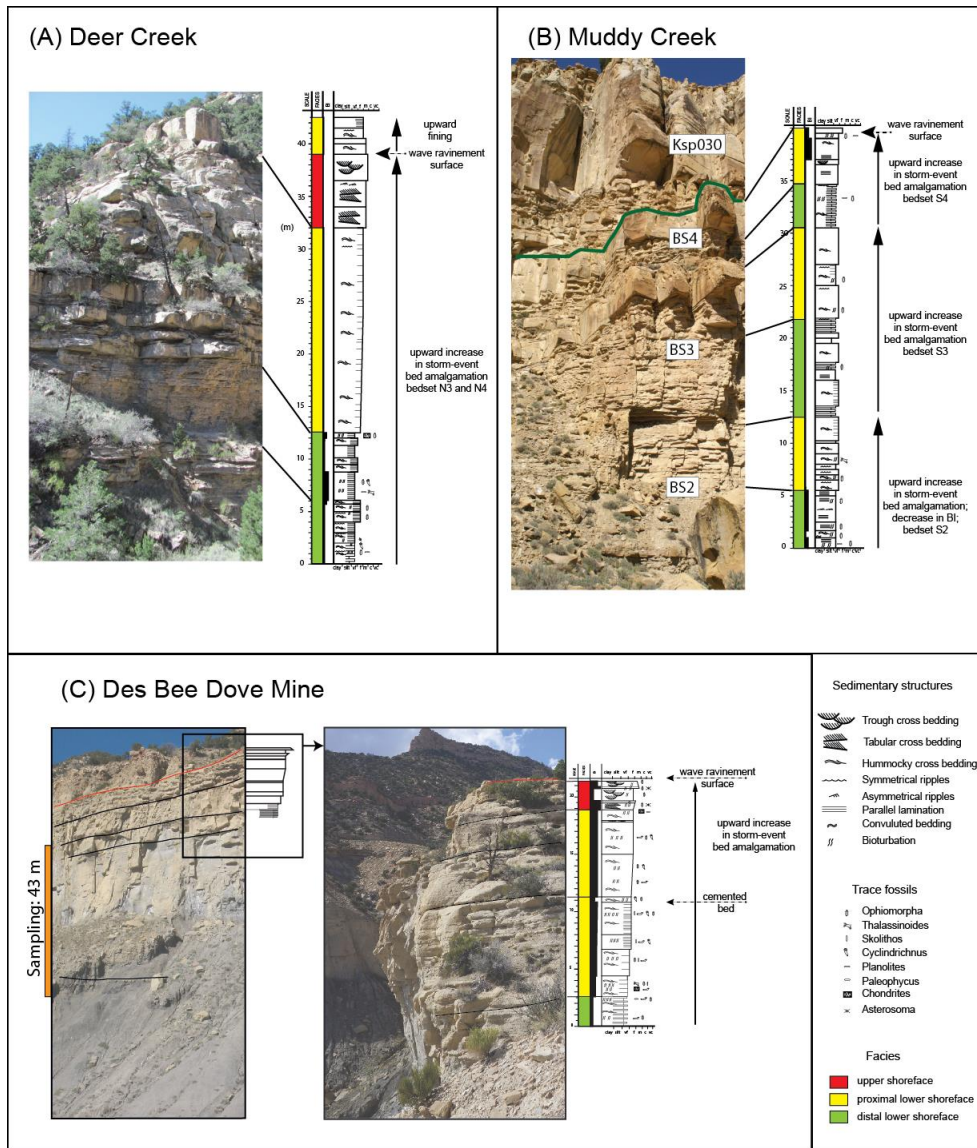
Figure 5.5: Stratigraphic logs and accompanying photos of wave-dominated shoreface facies successions. (A) Upward-shallowing wave-dominated shoreface succession truncated by a wave ravinement surface overlain by fining-upward transgressive deposits at Deer Creek; (B) three upward-coarsening bedsets of variably amalgamated storm-event beds in a wave-dominated lower shoreface succession at Muddy Creek; (C) upward-coarsening wave-dominated shoreface succession truncated by a wave ravinement surface at Des Bee Dove Mine,. A cemented bed separates bedsets 3 and 4. Localities are shown in Figure 5.2.
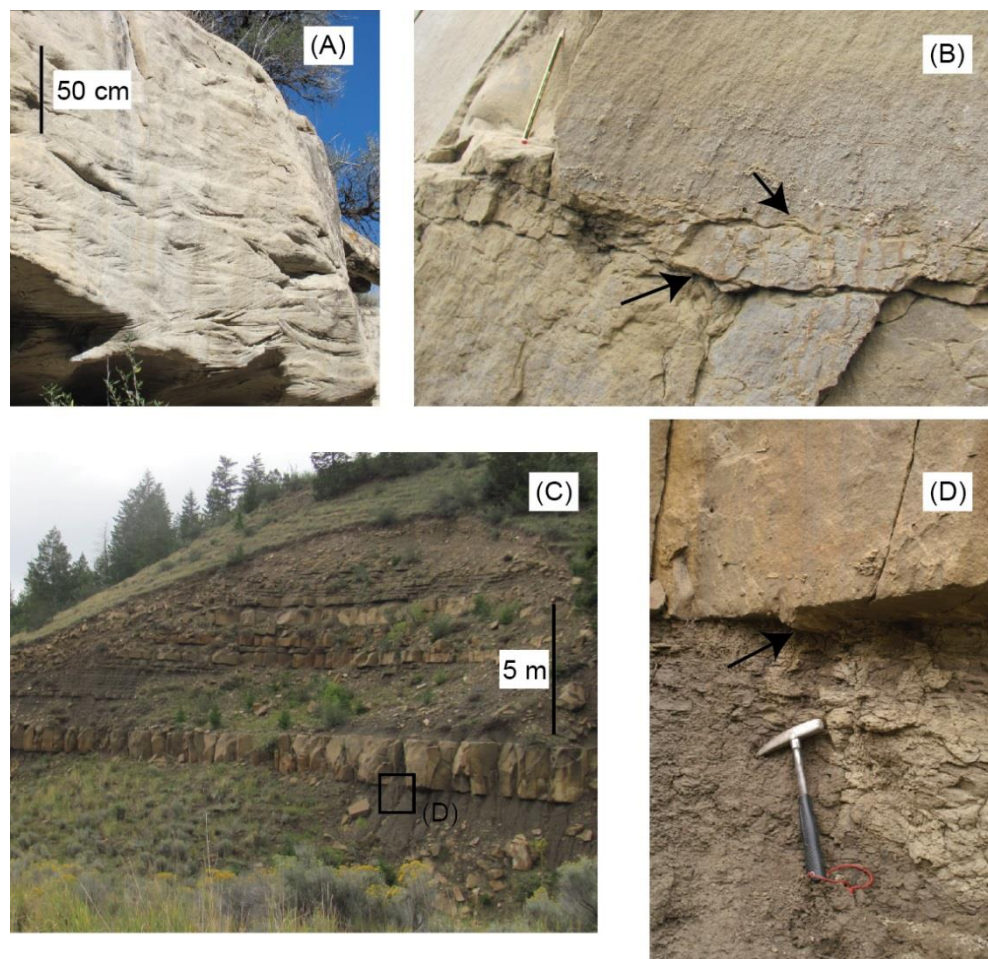
Figure 5.6: Photographs illustrating the fluvial-dominated delta front facies (Table 5.1). (A) trough cross-beds in medium-grained sandstones (pDF facies) at Crandell Cayon (Fig. 5.7A); (B) asymmetrical ripples at bed top, overlain by structureless medium-grained sandstone in lower part of overlying bed (pDF facies) at Tie Fork Canyon (Fig. 5.7C); (C) non-amalgamated sandstone beds and siltstone interbeds (dDF facies) at Wattis Road; and (D) flute casts at base of sandstone bed (dDF facies) at Wattis Road. Localities are shown in Figure 5.2.
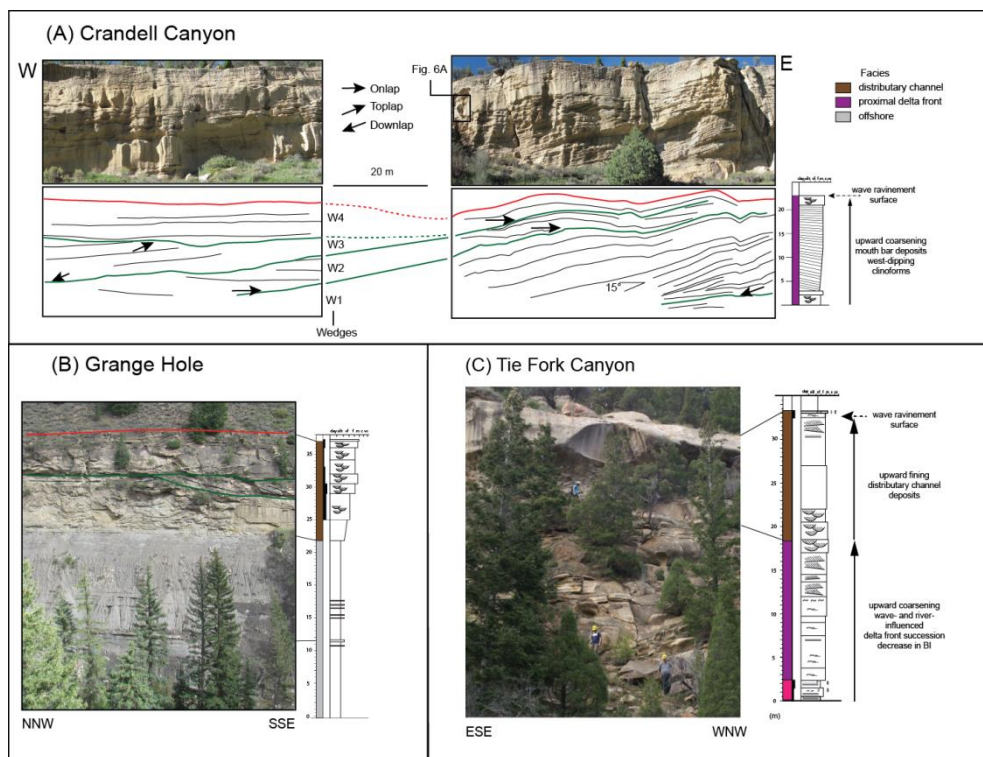
Figure 5.7: Stratigraphic logs and accompanying photos of fluvial-dominated delta front facies successions. (A) Coarsening-upward mouth bar sandstones (pDF facies) at Crandell Canyon, organized into inclined, wedge-shaped units bounded by surfaces of onlap, downlap and erosional truncation. The lowest wedge (W1) is characterized by steep westward-dipping delta front clinoforms that contain trough and tabular cross beds (Fig. 5.6A), indicating dune migration on the delta front. (B) Distributary channel-fill sandstones (DC facies), containing erosional scours and lateral accretion surfaces, overlying offshore mudstones (OS facies) at Grange Hole, indicating significant erosion. (C) Upward-shallowing, wave- and river- influenced delta front succession, overlain by distributary channel-fill deposits and truncated by a wave ravinement surface and lag at Tie Fork Canyon. Localities are shown in Figure 5.2.

"Shoreface" correlation panel

The "Shoreface" correlation panel (Fig. 5.8) obliquely crosses the NNW-SSE oriented, wave-dominated paleo-shoreline of the KSp040 parasequence (Hampson et al., 2011) (Figs. 5.1B, 5.2C). In paleo-landward locations (e.g. Link Canyon), the parasequence is represented by a single upward-coarsening succession that comprises both lower and upper shoreface deposits. This succession records an

overall upward shallowing trend, and meets the criteria necessary to define a parasequence (e.g. Van Wagoner et al., 1990; Hampson et al., 2008). In the southern Wasatch Plateau, the parasequence records 16 km of wave-dominated shoreline progradation (Fig. 5.11B in Hampson et al., 2011). The upper boundary of the parasequence is marked by a flooding surface associated with landward dislocation of the shoreline by 1 to 4 km (Fig. 5.9B in Hampson et al., 2012). Due to the absence of transgressive deposits in this correlation panel, the flooding surface at the top of the parasequence coincides with the maximum regressive surface and a wave ravinement surface.

The three upper bedsets are described by stratigraphic logs (bedsets S2-S4 in Fig. 5.8), while the lowermost bedset was interpreted by Hampson et al. (2011) using outcrop photographs (bedset S1 in Fig. 5.8). The basinward pinch-out of the pLSF facies belts in bedsets S3 and S4 is located c. 10 km further NNE (paleo-seaward) than the corresponding pinch-out in bedset S2 (Fig. 5.8). Bedset boundaries cannot be traced paleo-landward of the pLSF-dLSF facies transition, but are inferred based on geomorphic criteria to be present here as paleo-seaward-dipping clinoforms across which there is no facies dislocation (cf. Hampson et al., 2008; Sømme et al., 2008). Bedsets are inferred to be progradationally stacked with no significant aggradation in paleo-landward locations (dashed correlation lines in Fig. 5.8B). The stratigraphic log at Convulsion Canyon records the most southward (paleo-landward) position of shoreface deposits in the Ksp040 parasequence. Here, the Knight coal seam lies within root-penetrated mudstones (FP facies), which overlies a distributary channel-fill sandstone body incised into wave-dominated shoreface deposits.
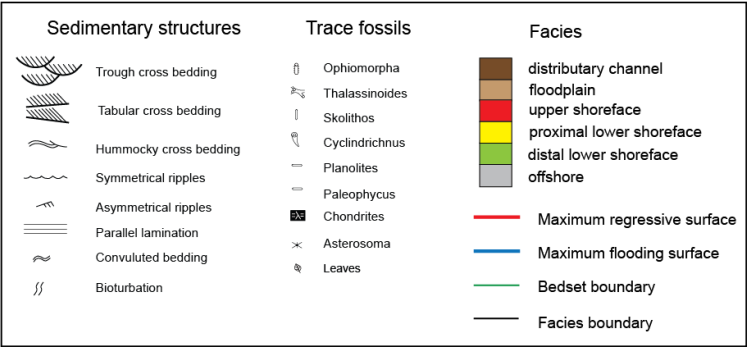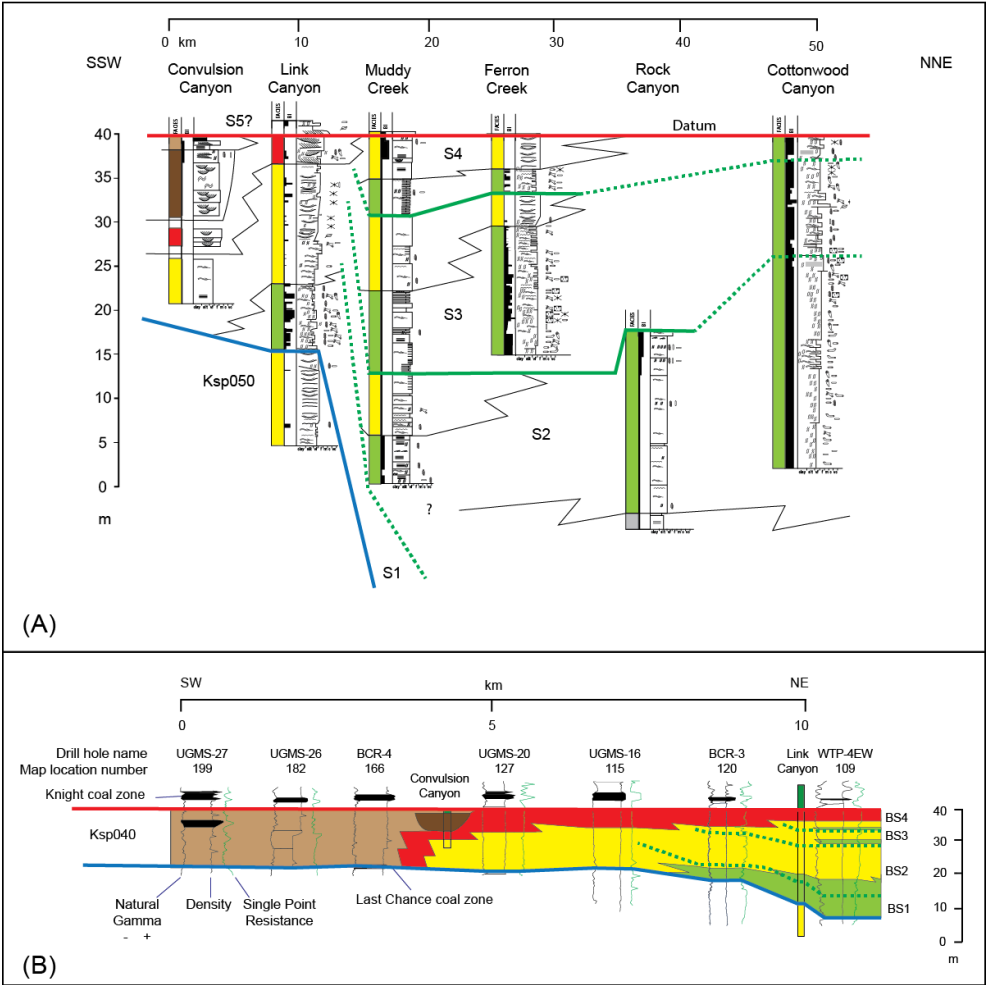
(A)

(B)

Sedimentary structures

Trough cross bedding
Tabular cross bedding
Hummocky cross bedding
Symmetrical ripples
Asymmetrical ripples
Parallel lamination
Convoluted bedding
Bioturbation

Trace fossils

Ophiomorpha
Thalassinoides
Skolithos
Cyclindrichnus
Planolites
Paleophycus
Chondrites
Asterosoma
Leaves

Facies

distributary channel
floodplain
upper shoreface
proximal lower shoreface
distal lower shoreface
offshore

Maximum regressive surface
Maximum flooding surface
Bedset boundary
Facies boundary

Figure 5.8: "Shoreface" correlation panel through wave-dominated shoreface-shelf deposits of the KSp040 parasequence in the southern part of the Wasatch Plateau (Figs. 5.1B, 5.2A). (A) Stratigraphic logs in paleoseaward locations show that the parasequence thickens paleoseaward (NE) and is subdivided into four bedsets (S1-S4) in its distal part. Logs are projected along depositional dip into the plane of the correlation panel (Fig. 5.2B), and the maximum regressive surface at the top of the parasequence is used as a horizontal datum. The horizontal spacing of the logs is not to scale. The apparent paleolandward (SW) dip of bedset boundaries is an artefact caused by using the maximum regressive surface as a horizontal datum, and enhanced by differential compaction. (B) Wireline and stratigraphic logs correlation in paleolandward locations (after Dubiel et al., 2000).

"Delta1" correlation panel

The "Delta1" correlation panel is oriented sub-parallel to the south-southeastward progradation direction of a Panther Tongue delta lobe in Huntington Canyon (Hwang and Heller, 2002) (Fig. 5.1B and 5.9). In the northern Wasatch Plateau, the parasequence records 17 to 25 km of fluvial-dominated deltaic shoreline progradation (Fig. 5.11B in Hampson et al., 2011). The upper boundary of the parasequence is marked by a flooding surface associated with landward dislocation of the shoreline by 16 to 31 km (Fig. 5.9B in Hampson et al., 2012).

Stratigraphic logs in the southern part of the "Delta1" correlation panel are characterized by a thick upward-shallowing, wave-dominated shoreface succession (Des Bee Dove Mine, Deer Creek Mine; Fig. 5.7A, C). A similar upward-shallowing wave-dominated shoreface succession is noted locally in more northerly, proximal locations (Forks of Huntington, Nuck Woodward Canyon; Fig. 5.9). These shoreface deposits are interpreted to occur off the principal axis of delta-lobe progradation, in marginal locations. Locally, shoreface deposits are eroded by a distributary channel-fill sandbody at North Hueghes Canyon (Fig. 5.9); this channelized unit is interpreted to be unrelated to the underlying wave-dominated shoreface deposits, and may have fed a fluvial-dominated delta lobe towards the east (e.g. in bedset N4; Fig. 5.10). At Des Bee Dove Mine the upward-shallowing shoreface succession contains a prominent oxidized, cemented layer within pLSF deposits, which is interpreted to represent a depositional hiatus (cf. Taylor et al., 2000) at a bedset boundary (between bedsets N3 and N4; Fig. 5.9).
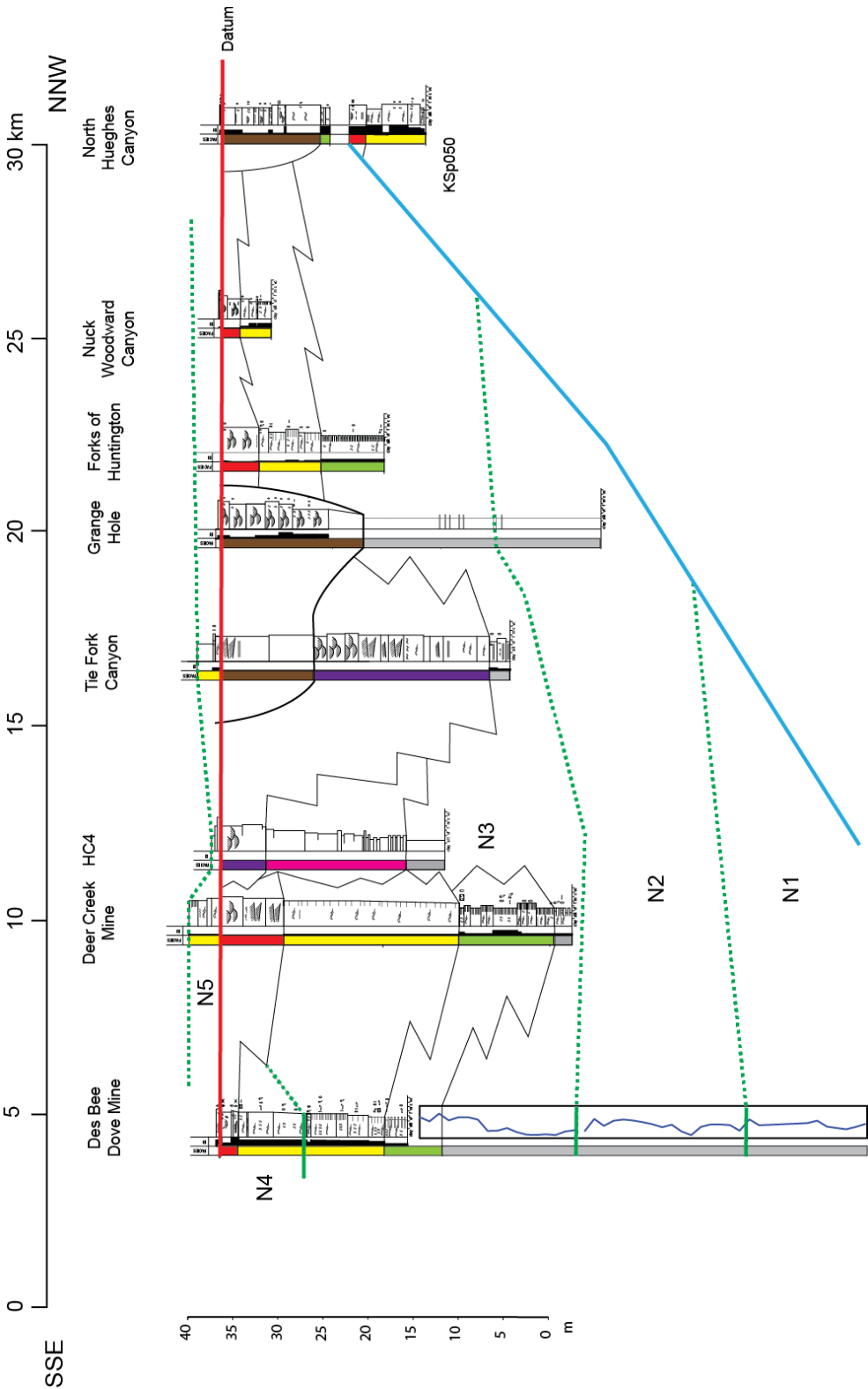
Figure 5.9: "Delta1" correlation panel through wave-dominated shoreface-shelf deposits and river-dominated delta front deposits of the KSp040 parasequence in the southern part of the Wasatch Plateau (Figs. 5.1B, 5.2A). The parasequence is subdivided into five bedsets (N1-N5). Logs are projected along depositional dip into the plane of the correlation panel (Fig. 5.2A), and the maximum regressive surface at the top of the parasequence is used as a horizontal datum. The maximum regressive surface coincides with a ravinement surface which truncates the regressive part of the parasequence (Hwang and Heller, 2002), comprising bedsets N1-N4. Overlying transgressive deposits are assigned to bedset N5.

The central part of the profile contains an upward-shallowing fluvial-dominated delta front succession up to 35 m thick (HC4, HC1, Tie Fork Canyon, Crandell Canyon, Grange Hole; Fig. 5.9). Locally the succession is deeply eroded by distributary channel-fill sandbodies (at HC1, Tie Fork Canyon, Grange Hole; Fig. 5.7B), and is marked by erosion at the base of proximal delta front deposits (HC1; Fig. 5.9). At Crandell Canyon (Fig. 5.9), the upper part of the Panther Tongue delta front succession is subdivided into a series of stacked, laterally offset wedges that contain steep (up to 15°), westward-dipping clinoforms (Fig. 5.7A). These clinoform-bearing wedges are interpreted as laterally and/or longitudinally accreting mouth bars within a mouth-bar assemblage (*sensu* Bhattacharya, 2006; corresponding to mouth bar "elements" in a mouth bar "element complex" *sensu* Vakarelov and Ainsworth, 2013), consistent with previous interpretations of the Panther Tongue succession in Huntington Canyong (Hwang and Heller, 2002) and near Helper (Olariu et al., 2005). The entire upward-shallowing delta front succession is interpreted as a single delta lobe (*sensu* Bhattacharya, 2006; "element complex set" *sensu* Vakarelov and Ainsworth, 2013) that is assigned to bedset N3. Regressive wave-dominated shoreface deposits and regressive fluvial-dominated deltaic deposits throughout the correlation panel are truncated at their top by a transgressive lag capped by thin (<10 m) wave-dominated shoreface deposits (Fig. 5.9) (Hwang and Heller, 2002). These thin transgressive deposits are assigned to bedset N5.

"Delta2" correlation panel

The "Delta2" correlation panel (Fig. 5.10) was constructed from wireline logs (Utah Geological Survey, 2014) and one outcrop stratigraphic log (Wattis Road; Hampson et al., 2011). We interpret vertical trends in sandstone content evident in the gamma ray logs in wells along the panel (Ridge Runner 11-20, East Clear Creek Federal 22-42, Gentry Mountain Unit 1) using observed successions in the nearby North Hueghes Canyon and Wattis Road stratigraphic logs (Figs. 5.2A, 5. 8).
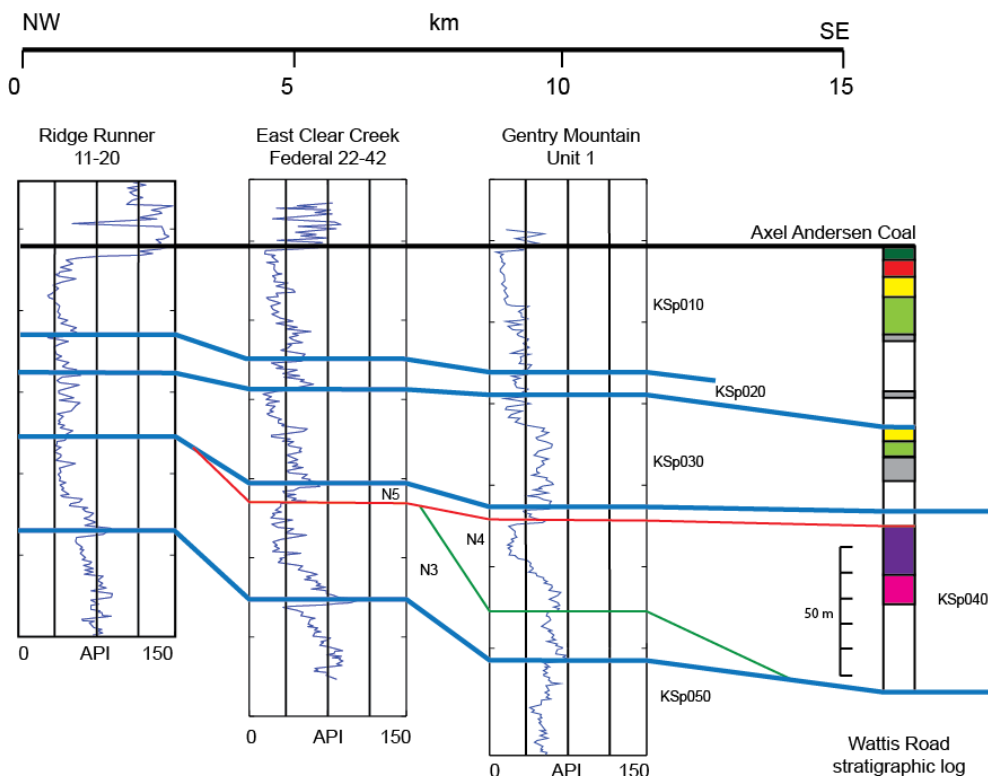
Figure 5.10: "Delta2" correlation panel through river-dominated delta front deposits of the KSp040 parasequence, and overlying and underlying wave-dominated shoreface-shelf deposits of the KSp010, KSp020, KSp030 and KSp050 parasequences (Figs. 5.1B, 5.2A). The parasequence thickens towards the ESE (palaeoseaward) and is subdivided into three bedsets (N3-N5) in its distal part. Logs are projected along depositional dip into the plane of the correlation panel (Fig. 5.2A), and the Axel Andersen coal seam, which locally caps the Star Point Sandstone, is used as a horizontal datum.

In the KSp040 parasequence, offshore shales (facies OS) have uniformly high gamma ray values, distal delta front deposits (facies dDF) have a serrate gamma ray pattern that alternates between high and low values, and proximal delta front and distributary channel deposits (facies pDF, DC) have uniformly low gamma ray values.

Within the KSp040 parasequence, the gamma ray logs indicate several vertically stacked upward-coarsening successions (i.e. with upward-decreasing gamma ray values), which we interpret as bedsets of delta front facies that thin and shale out

towards the east into offshore deposits (Fig. 5.10). Bedsets in the lower part of the parasequence (N3, N4) are interpreted to define a progradational clinoform set (cf. Hampson et al., 2008), whereas the upper part of the parasequence is characterized by an overall upward-fining trend and is interpreted to comprise transgressive deposits (N5) (cf. Hwang and Heller, 2002). The boundary between bedsets N4 and N5 corresponds to a maximum regressive surface amalgamated with a ravinement surface, whereas the upper boundary of N5 is the flooding surface on top of the Ksp040 parasequence.

Petrological trends in offshore shelf deposits

Samples collected at Des Bee Dove Mine (Figures 5.2b, 5.5) were analyzed to investigate variations in grain size and chemical-mineralogical composition within the visually homogeneous succession of offshore deposits.

XRF analysis

XRF analysis on samples collected at 1 m intervals indicates systematic fluctuations of the bulk chemical composition with depth (Fig. 5.11). Most of the variability is caused by changes in the relative abundances of silica, aluminum and calcium, as evidenced by principal component analysis (Fig. 5.11D). We chose to visualize the fluctuations in depth with the log-ratio Si/Al, a proxy for grain size related to the abundance of quartz versus aluminum-bearing minerals (clays, feldspars, micas) (Fig. 5.11A), Si/Ca, related to the abundance of quartz versus calcium-bearing minerals (calcite, dolomite) (Fig. 5.11B), and (K+Fe+Al)/Ca, a function of the abundance of aluminum-bearing versus calcium-bearing minerals (Fig. 5.11C).

The log-ratio plots show cycles in relative elemental abundances, with two Si and Ca minima (Al maxima) at c. 35 m and c. 48 m depth, and two maxima at c. 40 m and c. 55 m depth. The maxima of Si/Al correspond to minima in (Al+Fe+K)/Ca, suggesting a weak positive correlation between the abundance of quartz and calcium-bearing minerals (coarser grain size) and a negative correlation between calcium-bearing minerals and clays-feldspars-micas (finer grain size). Very high abundances of Ca (34.8%), Mg (9.2%) and Fe (60%) are measured at c. 38 m, suggesting the occurrence of cement composed of calcite, (Fe) dolomite and iron (hydro-)oxides. We interpret the cemented layer and the sharp decrease of Si/Al and Si/Ca signals at c. 38 m as the boundary between bedsets N2 and N3. The sharp decrease in chemical signals at 54 m represents the boundary between bedsets N1 and N2.

Thin sections and CT-scans

Quartz (≈85 %) and detrital dolomite and calcite (≈10 %) are the predominant framework grains in all thin sections (Fig. 5.12). These grains are rounded to sub-angular and have a homogeneous particle size distribution. Micas, quartzite lithics, cherts, and feldspars are secondary components. The matrix is composed of clay minerals, organic material, authigenic calcite cement, and iron oxides. In the samples at 25 and 43 m depth, corresponding to a high Si/ Al ratio, the grains are coarser and more abundant than in samples at 34 and 50 m, which correspond to a low Si/ Al ratio. Grains are mixed with the matrix, bedding is faint, and grains have no preferred orientation, which in combination suggest that the samples were affected by bioturbation. The absence of fossils and presence of cement around detrital grains suggests that a fraction of the primary detrital or biogenic calcite was recrystallized during diagenesis.

The CT scan images differentiate Fe-dolomite (white spots), quartz and carbonate grains (light grey areas) and clayey matrix (dark grey areas) (Fig. 5.12). Samples corresponding to a higher Si/ Al ratio (XRF) and coarser grain size (thin sections) show a high abundance of large light grey areas, whereas the finer grained samples (low Si/ Al) exhibit much smaller areas and darker grey tones. The grain sizes and the ratio between the proportions of silt-sized grains and clayey matrix, calculated using image analysis (Fig. 5.3), vary from sample to sample (Fig. 5.12), and are displayed in Figure 11E-H.

All data points and interpolated curves exhibit a clear trend in both particle diameter and grain size fractions (area %), with minima of Si/ Al corresponding to minima in particle diameter and grain size fraction, and vice versa. The analyses using CT scans and thin sections images produced almost identical particle diameter trends, and similar grain size fraction trends. The uncertainty in the absolute values of all different trends is a function of the different image analysis approaches (Fig. 5.3) and in the choice of the sample volume for thin-section analysis. In particular, in the sample at 43 m, the measured grain size is coarser than the interpolated grain size curve (Figure 5.11F). This mismatch is likely due to the choice of a sub-sample for the thin section analysis which has a coarser grain-size than the bulk sample.
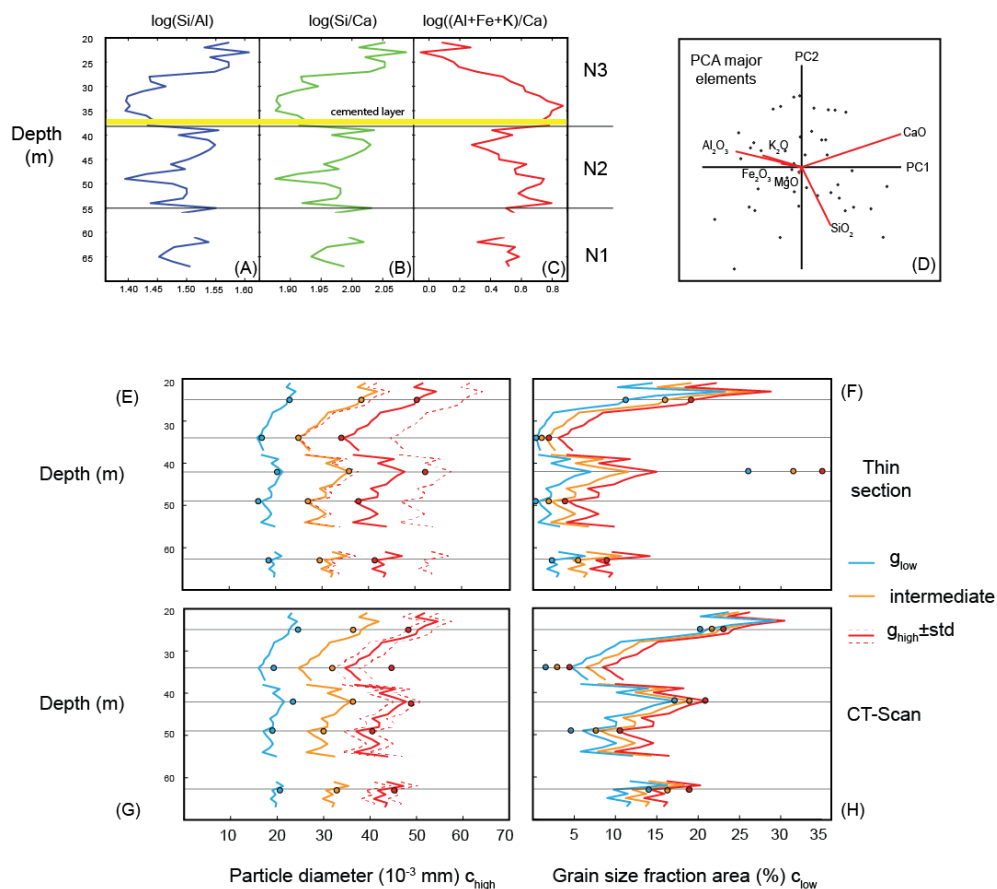
Figure 5.11: Results from the XRF, thin section, and CT scan analyses of rock samples from the offshore deposits succession at Des Bee Dove Mine (Figs. 5.2A, 5.9). (A-C) Log-ratio plots of the major elements in depth. The Si/ Al (Silica/ Aluminum) ratio is a proxy for quartz/ clay ratio and for grain size. The Si/ Ca (Silica/ Calcium) ratio is a proxy for ratio between silica- and carbonate-bearing minerals. The (Al +Fe + K)/ Ca (Aluminum, Iron, Potassium/ Calcium) ratio is a proxy for (clay minerals + feldspars + micas)/ carbonate-bearing minerals. (D) Principal Component Analysis (PCA) of the major elements for the XRF analysis, showing that most of the variability of the chemical composition with depth is caused by silica, aluminum, and calcium variations. Aluminum is strongly correlated to iron and potassium. (E-H) Variation in average grain size and area of grains vs. area of matrix along the sampled section, using thin sections (E, F) and CT scans (G, H). Points indicate measurements, whereas lines show the best-fit power-law function applied to an interpolation of the XRF results (Figure 5.11A-C). The log-ratio value for the cemented layer is not shown as it is off-scale, with a very small log(Si/ Al) and log (Si/ Ca) values.
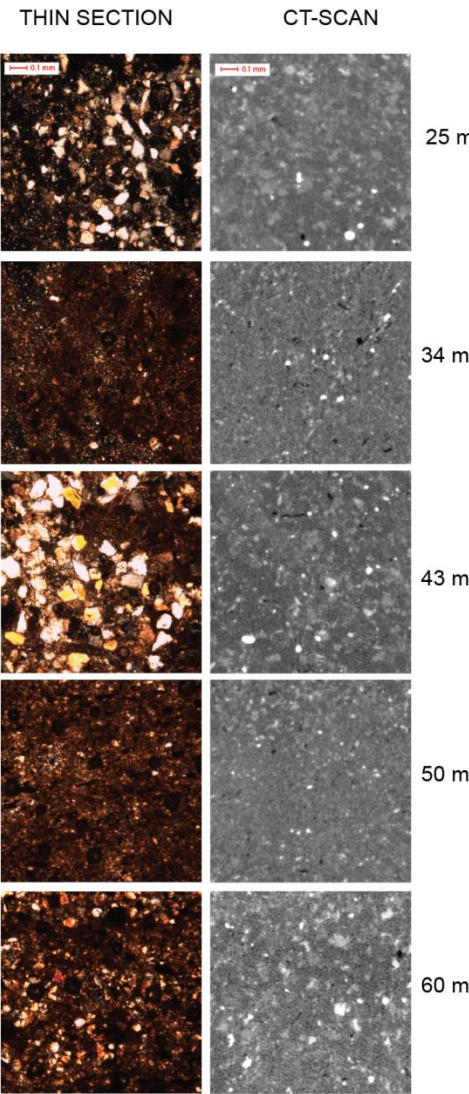
Figure 5.12: Photographs of thin sections (left) and CT scan images (right) for the five studied samples (located in Fig. 5.11D-G). In the CT scan images, white spots represent Fe-dolomite, light grey areas are associated with quartz and carbonate grains, and dark grey areas represent the clayey matrix.

5.5. Discussion

Our results show major along-strike differences in facies and stratigraphic architecture of the KSp040 parasequence. Petrological analysis of XRF, thin section and CT scan data has facilitated recognition of stratigraphic units within offshore-shelf deposits, in which lithological contrasts are too subtle to be recognized in the field. Below, we propose a plausible and simple, regional along-strike correlation of stratigraphic units in the KSp040 parasequence along the Wasatch Plateau outcrop belt, thereby connecting the dip-oriented "Shoreface", "Delta1" and "Delta2" correlation panels (Fig. 13A). Alternative interpretations are possible given the gaps in 3D data coverage of exposures in the outcrop belt, in combination with the subtle nature of stratigraphic features within parasequences, for the reasons outlined below.

The first difficulty in correlating stratigraphic units within parasequences is the historical absence of a generic hierarchical framework of such stratigraphic units that acknowledges the highly variable and commonly subtle architectural ordering within parasequences. The term "bedset" was first defined by Campbell (1967), and then used by Van Wagoner et al. (1990) to refer to intra-parasequence stratigraphic units. It has since been applied to units of different stratigraphic architectural characteristics, spatial scale and inferred temporal scale by many subsequent authors. Here, we use the term "bedset" as a synonym for an "element complex assemblage" in the recent stratigraphic architectural scheme of Vakarelov and Ainsworth (2013). Vakarelov and Ainsworth's (2013) scheme recognizes up to four smaller scales of hierarchically arranged stratigraphic units, which can be readily defined in sub-modern systems using geomorphological criteria but are considerably harder to recognize in ancient strata in the absence of high-quality, continuous exposure. In our interpretation of the KSp040 parasequence, bedset boundaries are marked by hiatuses in deposition that reflect paleogeographic re-organization of the depositional system, but are not marked by major landward dislocations of the shoreline, and increases in water depth (such as those that characterize flooding surfaces bounding parasequences; Hampson et al., 2008).

The bedsets interpreted in the KSp040 parasequence (S1-S4 in Fig. 5.8, N1-N5 in Figs. 5.9, 5.10) are equivalent to fluvial-dominated delta lobes (*sensu* Bhattacharya, 2006) and their contiguous wave-dominated strandplains, spits and barrier islands. We infer that the latter were nourished by sediment transported alongshore by wave-generated currents from a fluvial-dominated delta lobe. The deposits of strandplains, spits, barrier islands and, in particular, delta lobes have complex three-dimensional geometries, such that bedsets and their stratigraphic

components may pinch out laterally, along depositional strike (e.g. bedsets interpreted as beach-ridge sets; Charvin et al. 2010). Furthermore, the multiple scales of intra-parasequence stratigraphic architecture in wave-dominated and, especially, fluvial-dominated deltaic deposits may be difficult to distinguish, which makes consistent interpretation of bedsets a challenging exercise. In combination, these two aspects generate uncertainty in our preferred correlation of stratigraphic architectural units in the KSp040 parasequence.

Correlation between exposures in the southern and the northern Wasatch Plateau is further complicated by the lack of a paleo-horizontal stratigraphic datum and by the thickness differences within the Star Point Sandstone induced by differential subsidence and compaction (e.g. compaction of peat in proximal locations and of mud in distal locations). In parts of the "Shoreface 1" correlation panel, we use three coal seams in the Blackhawk Formation (Knight Coal, Accord Lakes Coal, Axel Anderson Coal) as local stratigraphic datum surfaces (after Hampson et al. 2011, 2012). We use the maximum regressive surface and a coincident ravinement surface as a paleo-horizontal datum in parts of the "Shoreface 1" correlation panel and throughout the "Delta 1" correlation panel, although the surface dipped gently paleoseaward (e.g. Hwang and Heller, 2002). The Axel Andersen Coal seam was used as a paleo-horizontal datum in the "Delta2" correlation panel.

Along-strike correlation and architecture of intra-parasequence stratigraphic units

In the southern Wasatch Plateau, parasequence Ksp040 comprises only wave-dominated shoreface deposits and is subdivided into four progradationally stacked bedsets (S1-S4) (Figs. 5.8, 5.13A). Bedsets are most clearly expressed within lower shoreface deposits, whereas they become less distinct in a paleo-seaward direction as storm event beds thin and shale out. Similarly, bedsets cannot be traced into upper shoreface deposits, indicating that they are not associated with major changes in water depth during deposition. Bedset boundaries are interpreted as non-depositional discontinuities . Each bedset records progradation of a wave-dominated shoreline (i.e. upper shoreface facies belt) by c. 2 to 9 km and of the lower shoreface facies belt by c. 20 to 30 km, relative to the basal bedset boundary (Fig. 5.14B-E). The bedsets are interpreted to be stacked laterally as progradational clinothems in shoreface deposits (cf. Hampson et al., 2008; Sømme et al., 2008), but to have an aggradational component at their shelfal toes such that they extend distally into continuous sheets of offshore shales (e.g. Fig. 5.9).
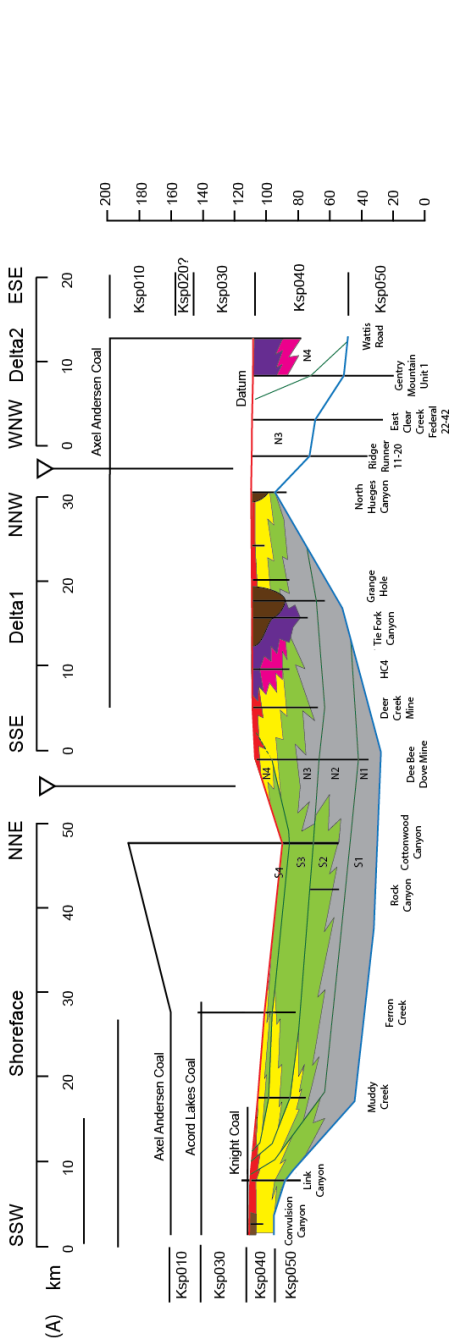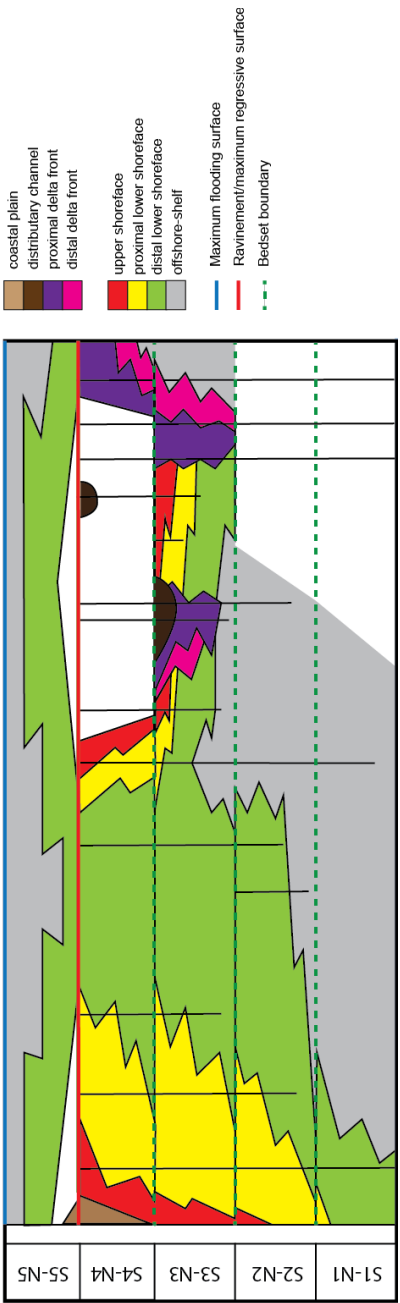
Figure 5.13: (A) regional along-strike correlation between local dip-oriented "Shoreface", "Delta1", and "Delta2" correlation panels (Figs. 5.8, 5.9, 5.10). The Ksp040 parasequence is subdivided into five bedsets that extend across the Wasatch Plateau outcrop belt, recording the stepwise progradation of a wave-dominated shoreface in the south and a wave-influenced, river-dominated delta from the northwest (bedsets S1 / N1 – S4 / N4), followed by retreat of a wave-dominated shoreface (bedset S5 / N5). (B) Wheeler diagram showing the interpreted chronostratigraphic evolution of the Ksp040 parasequence. Each bedset is assigned the same duration, estimated to be c. 100 kyr. Bedset boundaries are shown as dotted lines, as they may be asynchronous surfaces recording non-deposition or erosion.

The relationship between bedsets exposed in the northern Wasatch Plateau (N1-N5) and the well-documented fluvial-dominated deltaic deposits of the Panther Tongue in the northwestern Book Cliffs near Helper (Newman and Chan, 1991; Posamentier and Morris, 2000; Olariu et al., 2005, 2010; Howell et al., 2008; Enge et al., 2010a, 2010b) is unclear due to poor exposure between the two areas. Delta lobe deposits in the Panther Tongue near Helper exhibit little evidence for wave reworking, and built out towards the southeast, parallel to the regional paleoshoreline trend (Fig. 5.14A). Our reconstructions of bedsets in the Wasatch Plateau imply that delta lobe deposits near Helper may be contiguous with bedset N4 (Fig. 5.14E), implying overall southward progradation of a single delta lobe for >50 km, or that a separate (and possibly younger) delta lobe(s) was deposited near Helper. We favor this second interpretation because it entails the development of several relatively small delta lobes, comparable in size to those documented elsewhere in the Star Point Sandstone and Blackhawk Formation (e.g. Hampson and Howell, 2005; Charvin et al., 2010). Furthermore, the very long (>50 km) progradation distance parallel to the regional shoreline is likely unrealistic even for strongly asymmetrical modern deltas with low avulsion frequency (Bhattacharya and Giosan, 2003; Olariu and Bhattacharya, 2006).

We infer that a river draining the Charleston Nebo triangle zone to the north fed the delta lobe(s) near Helper, and a river draining the area west of the Paxton and Pavant thrusts fed the lobes in bedsets N3 and N4 near Huntington Canyon (Fig. 5.14A). Finally, we note that the Panther Tongue extends for at least c. 20 km to the northeast of exposures in Huntington Canyon (Fig. 5.14A), implying that older bedsets containing additional delta lobes (equivalent to bedsets S1 and S2; Fig. 5.14B, C) may occur here. Here, the Panther Tongue is overlain by the Flat Canyon coal (Sanchez, 1990; Fig. 9B in Hampson et al. 2012), implying delta plain aggradation during regression and/or subsequent transgression.

The connection between fluvial-dominated deltaic deposits in the northern Wasatch Plateau and wave-dominated shoreface deposits in the southern Wasatch Plateau is a key for understanding the architecture and the paleogeography of the Ksp040 parasequence. Based on our regional along-strike correlation (Fig. 5.13A), we consider these two geographically distinct deposits containing evidence for different depositional process regimes to be genetically related and time equivalent. We interpret the Ksp040 shoreline on the scale of the Wasatch Plateau outcrop belt as the record of deposition on the fluvial-dominated, downdrift flank of a wave-influenced delta system deflected asymmetrically towards the SSW, sub-parallel to the regional paleo-shoreline trend, and an adjacent wave-dominated strandplain (Fig. 5.14). This lateral transition is controlled by an along-strike decrease towards the south in the relative influence of riverine sediment supply, via a discrete point source(s) in the north, and by a corresponding increase in wave influence (e.g. Hampson et al., 2011). The northerly delta lobes also supplied sediment for wave-induced longshore transport towards the south. In addition, smaller, unmapped, fluvial systems may have supplied extra sediment to the shoreline in the southern Wasatch Plateau. The large volume of sediment fed by river(s) in the north induced a large seaward migration of deltaic shorelines in the northern Wasatch Plateau, compared to the migration distance of the strandplain in the southern Wasatch Plateau during the same time interval (Fig. 5.14).

The along-strike variability observed in the Ksp040 parasequence is intrinsic within modern and ancient wave-modified deltas, such as the modern Ebro Delta, Spain (Jiménez et al., 1997; Somoza et al., 1998) (Fig. 5.15A) and the Cretaceous Notom Delta of the Ferron Sandstone, Utah, USA (Li et al., 2011) (Fig. 5.15D). The Kura Delta, Azerbaijan (Fig. 5.15B), is a modern example of a strongly asymmetrical wave-modified delta of similar size and morphology to the Panther Tongue delta lobes in bedsets N3 and N4 (Fig. 5.14D, E). The Kura Delta is characterized by two fluvial-dominated lobes, an abandoned one in the south, and a southwards deflected active lobe in the north (Mikhailov et al., 2003; Hoogendoorn et al., 2005). A large wave-dominated spit and associated strandplain developed in the area between the two lobes, as a result of southward sediment longshore transport. Based on exposures in the Book Cliffs, parasequence Ab1 in the Aberdeen Member of the Blackhawk Formation (Charvin et al., 2010) represents an ancient analogue of the Panther Tongue delta lobes in bedsets N3 and N4 (Fig. 5.15C). Wave-dominated shoreface and fluvial-dominated delta-front deposits both occur in the Ab1 parasequence, and are interpreted as the updrift and downdrift flanks, respectively, of a single asymmetrical wave-dominated delta

that periodically shifted its position. Fluvial-dominated delta-front deposits observed at outcrop are interpreted as a single delta lobe (Fig. 5.15C; Fig. 5.11E in Charvin et al., 2010) that is comparable in areal extent to one of the Panther Tongue delta lobes (Fig. 5. 14D, E).
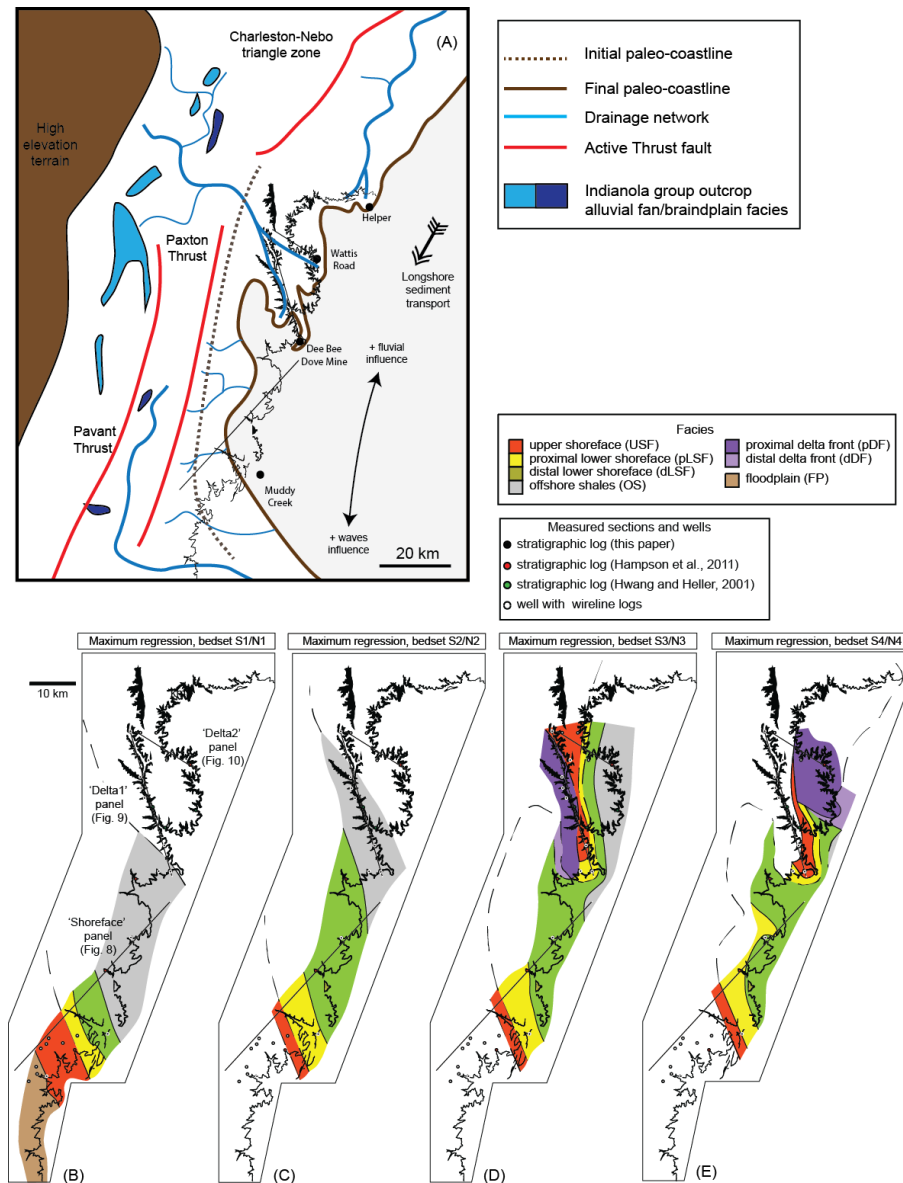
Figure 5.14: (A) Paleogeographic reconstruction of the KSp040 parasequence, comprising the Panther Tongue delta and coeval strandplain, in the context of the source-to-sink sediment routing system, showing active thrust faults, outcrops of coeval Indianola Group alluvial sediments, reconstructed shoreline position maximum regression, and interpreted drainage system (after Johnson, 2003; Horton et al., 2004; DeCelles and Coogan, 2006; Hampson et al., 2011). The delta lobes in the Huntington Canyon and Helper areas are interpreted to have been fed by two different river systems. (B-E) Maps of reconstructed and interpreted facies-belt extent at maximum regression in bedsets of the KSp040 parasequence, in ascending stratigraphic order: B) bedset S1 / N1; C) bedset S2 / N2; D) bedset S3 / N3); and E) bedset S4 / N4.

The interpreted chronostratigraphic framework of the Ksp040 parasequence and its constituent bedsets is illustrated in Figure 5.13B. This framework is highly schematic given the absence of high-resolution dates within the Ksp040 parasequence, and uncertainty in the precise position of some facies belt pinch-out positions within bedsets. Figure 5.13B shows the stepwise regression of a wave-dominated shoreface from the WSW and a fluvial-dominated, wave-influenced delta from the NNW. Bedset boundaries formed during pauses in regression.

Causative controls on stratigraphic architecture

Stacking of bedsets S1, S2 and S3 in the southern Wasatch Plateau contains a vertical, aggradational component, implying overall normal regression during their deposition, which may have contributed to accumulation of the Knight Coal seam and associated coastal plain deposits (Figs. 5.8, 5.13). The stacking pattern of inferred, correlative bedsets N1, N2 and N3 in the northern Wasatch Plateau cannot be characterized because only bedset N3 is exposed (Figs. 5.9, 5.10, 5.13) However, accumulation of the Flat Canyon Coal seam directly above sandstones of the Panther Tongue in locations northeast of the outcrop belt (Sanchez, 1990; Fig. 5.9B in Hampson et al. 2012) may also indicate overall normal regression during deposition of these bedsets.

In the northern Wasatch Plateau, bedsets N3 and N4 both contain features that indicate forced regression during their deposition (Posamentier et al. 1992; Plint and Nummedal 2000; Posamentier and Morris 2000): (1) widespread areal extents and large progradation distances, (2) absence of coeval delta plain deposits, and (3) incision of distributary channels into distal delta front and offshore shelf deposits (Figs. 5.7B, 5.9). Stacking of these bedsets is also interpreted to lack an aggradational component, consistent with their deposition under forced regressive conditions of falling relative sea level. The stacking of bedsets S3 and S4 in the southern Wasatch Plateau is ambiguous, and can be interpreted as either normal or forced regressive, while the bedsets lack internal evidence of forced regression (e.g.

development of a "sharp-based shoreface" *sensu* Plint, 1988). Thus, a common relative sea-level control can be interpreted for both the southern and northern Wasatch Plateau, despite a higher tectonic subsidence rate in the northern Wasatch Plateau (Hampson et al., 2011).

The greater progradational and areal extent of bedsets N3 and N4 in the northern Wasatch Plateau, relative to bedsets S3 and S4 in the southern Wasatch Plateau, reflects greater local sediment supply, via a riverine point source(s). There is a correspondingly higher degree of lateral stacking of bedsets, relative to vertical stacking, in the northern Wasatch Plateau (e.g. contrast the correlation panels in Figs. 5.9, 5.10 with that in Fig. 5.8). Variations in paleobathymetry reinforce these patterns, with vertical stacking of bedsets being more pronounced in the distal parts of the "Shoreface" and "Delta1" correlation panels (Figs. 5.8, 5.9) that extend beyond the pinchout of shoreface deposits in the underlying KSp050 parasequence. The progradational extents of bedsets S2, S3 and S4 (Fig. 5.14C-E) are also smaller than that of bedset S1 (Fig. 5.14B), because they record advance of the shoreline into deeper paleobathymetry beyond the KSp050 paleoshoreline. The greater local sediment supply to the Panther Tongue delta lobes of the northern Wasatch Plateau may have been related to high discharge of river water, which would have enhanced fluvial erosion and forced more rapid deltaic progradation (e.g. Van den Berg den Saparoea and Postma, 2008). Thus, the presence of incised distributary channels and large progradation distances in the Panther Tongue delta lobes may be attributed, at least in part, to a hinterland-associated climatic or tectonic control on discharge, rather than to sea-level fall.

In the context of our regional correlation of bedsets between the northern and southern Wasatch Plateau (Fig. 5.13A) and associated paleogeographic reconstructions (Fig. 5.14B-E), bedset boundaries most likely formed by erosion and/or non-deposition in response to changes in riverine sediment supply from the catchment, paleogeographic reorganization during delta-lobe switching, longshore sediment transport to the south, and/or variations in wave climate (cf. Storms and Hampson 2005; Sømme et al., 2008; Charvin et al., 2011). These potential formative mechanisms were probably linked, with, for example, decreases in sediment supply and wave-climate energy in southerly locations being caused by paleogeographic re-organization due to delta-lobe switching in the north (cf. Sømme et al., 2008). These various formative mechanisms may also have been forced, at least to some degree, by minor (meter-scale) changes in relative sea level. Future investigation using numerical stratigraphic models may

quantitatively test the relative effects and potential linkage of these formative mechanisms on the stratigraphic architecture of the Ksp040 parasequence.
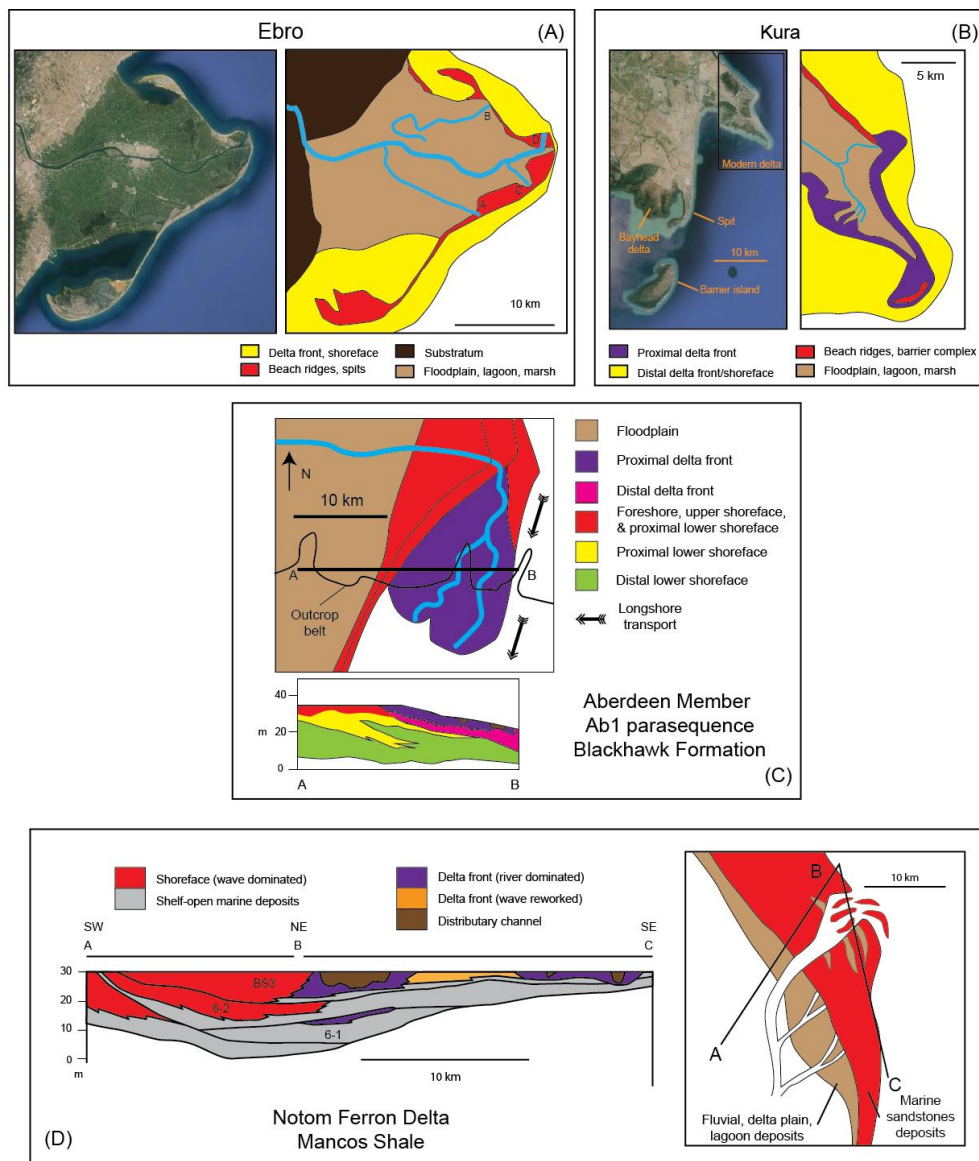

Figure 5.15: Analogues for the KSp040 parasequence shoreline, comprising the fluvial-dominated Panther Tongue delta and coeval wave-dominated strandplain. (A) Ebro Delta, Mediterranean Sea, Spain (Jiménez et al., 1997; Somoza et al., 1998); (B) Kura Delta, Caspian Sea, Azerbaijan (Mikhailov et al., 2003; Hoogendoorn et al., 2005); (C) late Cretaceous "Ab1 parasequence", Aberdeen Member, Blackhawk Formation, Book Cliffs, Utah, USA (Charvin et al., 2010); (D) "parasequence 6" of the late Cretaceous Notom Delta, Ferron Sandstone Member, Mancos Shale, Utah, USA (Li et al., 2010).

6. Conclusions

The internal stratigraphic architecture of the KSp040 parasequence, Star Point Sandstone in the Wasatch Plateau (Utah, USA) has been characterized using an integrated dataset comprising outcrop observations, subsurface well data, and petrological analysis of distal fine-grained deposits. The parasequence is subdivided into five bedsets that are correlated and found to extend across the whole Wasatch Plateau outcrop belt (c. 100 km along depositional strike). The lower four bedsets record the stepwise progradation of a wave-dominated shoreface in the south (bedsets S1-S4) and a fluvial-dominated, wave-influenced delta in the north (bedsets N1-N4). The fifth bedset (N5) records retreat of a wave-dominated shoreline. A clear mineralogical and grain-size signal of the bedsets is recorded in offshore shale deposits. Thus, petrological and image analysis (XRF, CT scans, thin sections) provide valuable data to constrain stratigraphic architectural analysis.

The four bedsets in the progradational part of the parasequence record deposition on the fluvial-dominated, downdrift flank of a wave-influenced delta system deflected asymmetrically towards the SSW, sub-parallel to the regional paleo-shoreline trend, and an adjacent wave-dominated strandplain. In the north of the study area, each bedset represents a fluvial-dominated delta lobe with wave-modified geomorphological features, such as spits, and is characterized by large local progradation distances (c. 18-32 km). Further south, each bedset represents c. 2-9 km progradation of a contiguous, near-linear, wave-dominated strandplain. Bedset boundaries record erosion and/or non-deposition in response to potentially linked changes in riverine sediment supply from the catchment, paleogeographic reorganization during delta-lobe switching, longshore sediment transport to the south, variations in wave climate, and/or minor (meter-scale) changes in relative sea level. The modern Kura Delta, Azerbaijan, is analogous in terms of area, geomorphology, and historical evolution.

Bedset stacking and internal architecture is interpreted to record normal regression with a component of aggradation (bedsets S1 / N1 and S2 / N2) that transitions into forced regression (bedsets S3 / N3 and S4 / N4). Thus, a common relative sea-level control can be interpreted for both the southern and northern Wasatch Plateau. The progradation distance within each bedset, and the lateral stacking of bedsets, reflect local sediment supply, sediment dispersal mechanisms and paleobathymetry. Pronounced delta lobe progradation in the northern Wasatch Plateau reflects high sediment supply from fluvial point source(s) across a relatively shallow sea floor. More uniform and slower shoreface progradation in

the northern Wasatch Plateau reflects relatively homogeneous supply of longshore-transported sediment across a relatively deep sea floor.

The observed lateral variability in architecture within bedsets of the KSp040 parasequence indicates that depositional systems should be interpreted based on their larger paleogeography context. Different parts of the shoreline reacted differently to the same changes in external forcing, which consequently, have a different stratigraphic expression along the regional depositional strike. The relatively continuous style of vertical sedimentation in distal lower shoreface and offshore shelf deposits preserve the most complete archive for reconstructing external forcing variations in the linked deltaic and strandplain setting of the KSp040 parasequence.

CHAPTER 6

General conclusions

6.1. Synthesis

The objectives of this PhD project are (i) to develop and apply a catchment model, to simulate the sediment flux response of river systems to climatic and tectonic forcing, and (ii) to investigate the impact of external forcing on fluvio-deltaic stratigraphic architecture and geomorphological evolution.

First, a numerical model, PaCMod, was developed and tested, which simulates sediment production, erosion, transport, and storage within any given climatically- and tectonically-perturbed catchment (Chapter 2 and 3). PaCMod was applied to reconstruct the sedimentary history of a well-studied, Late Quaternary river system, the Golo, France. Modelling results were compared to new sediment ages, and topographic, sedimentological, and geophysical data acquired in the field, to investigate the impact of climate and sea-level forcing on the geomorphic and stratigraphic evolution of the Golo river system (Chapter 4). Finally, the architecture and the heterogeneities of the Cretaceous Panther Tongue delta, Utah, were studied by means of outcrop observations, stratigraphic logs correlation, and petrological analysis of rock samples (Chapter 5).

6.2. Numerical model relevance and validity

The numerical model PaCMod, was developed to bridge the gap between spatially-lumped and cellular models, by parameterizing the transient geomorphological response of catchments to climatic and tectonic forcing, and sediment storage within the catchment. Notwithstanding the high level of parameterization and the numerous assumptions used, the model is able to capture the first order non-linear response of a catchment to external forcing, caused by the interaction of processes operating at different spatial and temporal scales, and by feedback mechanisms. The modeled water and sediment flux outputs were validated using the Meuse River (Netherlands), the Waipaoa River (New Zealand), and the Po River (Italy) as test cases for climatic forcing and the Celano catchment (Italy) as a test case for tectonic forcing.

The main limitation of the model is the averaging of geomorphic processes and catchment properties into single parameters. Our model uses a spatially lumped approach, which neglects the detailed property and process heterogeneities across the catchment, as well as important processes such as glacial erosion, sediment sorting and grinding. Nevertheless, the model has the advantage of being parsimonious with required input, modeled processes, and processing capacity, in contrast to more complex cellular models, and is therefore particularly suited to ancient sediment routing systems.

6.3. Forcing signal transmission

PaCMod simulations of the Celano (chapter 3) and the Golo catchment (chapter 4) have shown that the sediment flux output from a catchment is complex and not linearly related to the external climatic and tectonic forcing acting on the catchment. Sediment and water storage within the catchment (hillslopes, floodplains, glaciers), and the inertial response of landscapes (hillslopes, vegetation) hamper the transmission of external forcing out of the catchment, into the stratigraphic record. Modeling results using PaCMod and a stratigraphic model, 2Dstratsim, showed that long response times of hillslopes and fluvial channel to tectonics buffer the transmission of a tectonic signal to sediment flux and stratigraphy, whereas long response times to climate tend to amplify the climatic signal. Furthermore, catchment response time modulates sediment supply to basins and thus significantly affects shoreline trajectories, stratal architecture, grain size trends and the visibility of sequence stratigraphic surfaces in borehole logs.

Similarly, modeling results and field data from the Golo River System indicate that the system response to climate and sea level variations was non-linear, as a result of catchment memory (sediment storage, ice storage in glaciers) and geomorphological thresholds (balance between sediment erosion and fluvial transport capacity). The Golo alluvial-coastal plain evolution was controlled by a complex interaction of millennial scale variations in sediment supply and sea level variations, and long-term tectonic-induced vertical movements. In particular, the proposed geomorphological reconstruction indicates that a large amount of coarse sediment was stored in the catchment during glacial phases, and it was consequently eroded and bypassed to the submarine fans during periods of lowest sea level stand.

These results imply that stratigraphy records a complex signal that cannot be understood without reference to landscape response times and sediment supply.

Furthermore, the observed non-linear relation between external forcing and fluvial system response suggests that only the events crossing climatic and morphological thresholds are transmitted to the geomorphic-stratigraphic record, implying that the geological record is a filtered translation of external forcing. With prior knowledge on first order catchment properties, climatic, and tectonic conditions future research may predict under which conditions and how external forcing is translated to a sediment flux and sedimentary archive for any specific catchment. Thereby, the stratigraphic record can be better interpreted in terms of external forcing.

6.4. External forcing impact on shallow marine stratigraphy

In shallow marine settings the upstream forcing signal is modified by marine processes and its record is controlled by the different processes acting in different sedimentary environments. The proposed correlation of outcrop, petrological, and subsurface well data of KSp040 parasequence, Star Point Sandstone, Utah, indicates that the shallow marine deposits of the Ksp040 parasequence are subdivided into five bedsets. The four bedsets in the progradational part of the parasequence record deposition on the fluvial-dominated, downdrift flank of a wave-influenced delta system deflected asymmetrically towards the SSW, sub-parallel to the regional paleo-shoreline trend, and an adjacent wave-dominated strandplain. Bedset boundaries record erosion and/or non-deposition in response to potentially linked changes in riverine sediment supply from the catchment, paleogeographic reorganisation during delta-lobe switching, longshore sediment transport to the south, variations in wave climate, and/or minor (metre-scale) changes in relative sea level.

Bedset stacking and internal architecture is interpreted to record a major sea-level cycle with normal regression (bedsets 1-2), forced regression (bedsets 3-4), and transgression (bedset 5). The progradation distance within each bedset, and the lateral stacking of bedsets, reflect local sediment supply, sediment dispersal mechanisms and paleobathymetry. Pronounced but localised delta lobe progradation in the northern Wasatch Plateau reflects high sediment supply from fluvial point source(s) across a relatively shallow sea floor. More uniform and slower shoreface progradation in the southern Wasatch Plateau reflects relatively homogeneous supply of longshore-transported sediment across a relatively deep sea floor. These results suggest that different parts of the shoreline reacted differently to the same changes in external forcing, which consequently, have a different stratigraphic expression along depositional strike.

6.5. Future study

In this study the new catchment model was successfully tested and applied, new insights were obtained on the architecture of the Golo and the Panther Tongue deltaic systems, and on the transmission of external forcing signal into river systems and fluvio-deltaic stratigraphy. However, several methodological and scientific questions need to be addressed with future research.

First, a more extensive model parameter calibration should be performed using cellular models as a comparison for a short simulation of a well-constrained system. Some model routines, like the hydrological routine, can be rewritten to simulate only the most important processes, thereby reducing the number of input parameters. A standard model routine should be written to quantify model output uncertainty. An empirical relation between catchment response time, lithology, tectonics, and climate may be extracted using a large dataset of different catchments (see discussion in chapter 3).

Second, the Golo delta's Pleistocene-Holocene evolution should be investigated using a stratigraphic model, comparing the model output to observed stratigraphic data and to new seismic and dating data from the offshore part of the system. A similar approach can be used for other systems in the area, for example the Ombrone, Tiber, and Arno Rivers to disentangle the impact of climatic and human forcing on deltaic stratigraphy. New OSL samples should be collected within the same stratigraphic/ geomorphic unit to investigate the impact of travel distance and/ or transport process on OSL signal bleaching.

Finally, future work on the Ksp040 in Utah should focus on more continuous outcrop observations in key areas in the Huntington Canyon using, for example, a drone or Lidar, to better constrain the geometries of the mouth bars and distributary channels deposits. Petrological analysis should be performed on samples from the area of Helper, to understand sediment provenance and the genetic/ spatial/ temporal relation between the delta lobes along the Ksp040 shoreline. A stratigraphic numerical model (2Dstratsim) should be applied in an inversion scheme, to disentangle the causative controls on the Ksp040 stratigraphic architecture, namely relative sea-level, sediment supply, and wave regime.

APPENDIX A

PaCMod modules

A1. Weather and hydrological module

Daily precipitation (mm d^{-1}) is simulated as the combination of a seasonal variations component (P_s) and on a random component (P_n) (Eq. A1). The seasonal variations depend on the average daily precipitation P_m and on the difference between mean precipitation during the wet and the dry seasons P_{amp} (Eq. A2). The random component with average 0.5, P_{n1} (eq. A3) is compared to the probability of a wet day P_w (0-1): the relation between P_{n1} and P_w determines whether it will rain or not on day (i) (Eq. A4), while P_s and P_w determine the precipitation event magnitude P_m.

$$P_{m(i)} = \frac{P_{s(i)} \cdot P_{n(i)}}{P_w} \tag{A1}$$

$$P_{s(i)} = \left\{ \sin\left[2\pi \cdot \frac{i + day}{365} \right] \cdot P_{amp)} \right\} \cdot P_m \tag{A2}$$

where *day* defines the day of the year with the highest average precipitation.

$$P_{n1(i)} = random(0.5) \tag{A3}$$

$$if\ P_{n1(i)} < P_w \qquad\qquad P_{n(i)} = P_{n1(i)} \tag{A4}$$

$$if\ P_{n1(i)} > P_w \qquad\qquad P_{n(i)} = 0$$

P_w can be calculated based on present-day precipitation data, or it can be treated as a user defined parameter: the probability of a wet day is inversely proportional to storm intensity or storminess. Given the same amount of annual precipitation, with high storminess (low P_w) few high magnitude precipitation events will occur and vice versa.
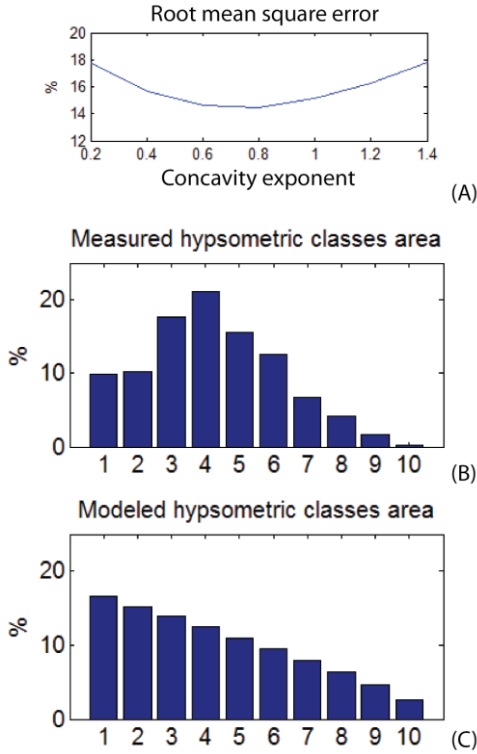
Figure A1: (A) Root mean square error of hypsometric classes area scenarios with respect to measured areas (Meuse River catchment), using different concavity exponent values: the smallest error is at 0.8; (B) measured and (C) modeled (concavity exponent=0.8) hypsometric classes area. The main source of error arises from neglecting the big convexity of the measured hypsometric classes area, which derives from the widespread extent of plateaus between 100 and 400 m altitude. Despite the mismatch between the modeled and the measured hypsometric classes area, the modeled hydrograph of the Meuse River matches closely the measured one.

A2. Hypsometric classes

The relative areal extent of each class, H_{area1}, is calculated using a user defined exponent (eq. A5) and concavity exponent (Fig. A1). For class (h) from 1 to 10:

$$H_{area1(h)} = h^{concavityexponent} \tag{A5}$$

$$H_{area(h)} = \left(\frac{H_{area1(h)}}{\Sigma H_{area1}}\right) \cdot A \tag{A6}$$

The absolute area of each class, H_{area} (km^2), is then calculated (Eq. A6) depending on the total catchment area A (km^2). These hypsometric class areas can be calculated with a DEM in order to calibrate the concavity exponent. We thereby assume that 10 classes are representative for the whole catchment and that the areal extent of each class decreases with altitude. The concavity exponent determines the rate of decrease in areal extent. A source of error will arise in case of the presence of high altitude plateaus in the catchment.

A3. Transport capacity

The hydraulic radius of the river *Rh* (m) (Eq. A7), which is the ratio of the channel's cross-sectional area of the flow to its wetted perimeter, is calculated using Bogaart et al. method (2003a), based on the width/depth ratio *WDR*, on bankfull discharge Q_p, and on fluvial channel gradient *Sf* (m/km):

$$Rh = Q_p \cdot \frac{1}{(W \cdot S_f{}^2)^{0.6}} \tag{A7}$$

$$W = c1 \cdot Q^{C2} \cdot WDR \cdot 50 \cdot Rh^{0.6} \tag{A8}$$

where *c*1 and *c*2 are coefficients that depend on the channel pattern (Bogaart et al., 2003a). For a braiding channel the width depth ratio *WDR* is assumed to be 300, while for a meandering channel *WDR* is 30 (Bogaart and van Balen, 2000). Bottom shear stress, τ (kg m^{-1} s^{-2}) is defined as:

$$\tau = \rho \cdot g \cdot R \cdot S_f \tag{A9}$$

where ρ (kg m^{-3}) is the water density and *g* is the gravitational coefficient. When bottom shear stress exceeds the critical shear stress τ_c for a particular grain size (USACE, 2007) (Eq. A10 and A11) sediment transport occurs.

$$\tau_c = (\rho_s - \rho) \cdot D_{50} \cdot g \cdot (0.22 \cdot \beta + 0.06 \cdot 10^{-7.7 \cdot \beta})) \tag{A10}$$

$$\beta = \left\{ \frac{1}{n} \cdot \left[\left(\frac{\rho_s}{\rho} - 1 \right) \cdot g \cdot D^3 \right] \right\}^{-0.6} \tag{A11}$$

Where ρ_s is the sediment density (kg m^{-3}), ρ is the water density, and *n* is Manning's flow resistance (s m$^{1/3}$), which is assumed to be 1.3·10^{-6} (Bogaart et al., 2003a). The transport capacity *TC* (m^3 s^{-1}) for a particular grain size is defined as (Tucker and Slingerland, 1996)

$$TC = \frac{W}{\left[\left(\frac{\rho_s}{\rho} \right) * \rho^{0.5} * g \right]} * (\tau - \tau c) * (\tau^{0.5} - \tau_c{}^{0.5}) \tag{A12}$$

APPENDIX B

Modeling catchment response to tectonics

In this appendix we describe (i) how we calculated the response times of tectonically perturbed catchments; (ii) how we constrained the coefficients, the regolith threshold, the concavity of the longitudinal river profile; and (iii) how we defined the relation between response time coefficients and response times using geomorphological data from three tectonically-perturbed catchments in Central Italy: Rio Torto, Celano, and l'Apa (Whittaker et al., 2010).

B1. Response time to tectonics

First, we calculated the response time of hillslopes R_h to tectonics, based on the area of the catchment affected by tectonic-induced incision. We defined A' as the spatial extent (km^2) of the incised transient reach (c.f. Cowie et al., 2008; Whittaker et al., 2010), and we used it to constrain knickzone migration rate, V. For upland rivers, knickzone migration rate (mm y^{-1}) (eq. B1) is defined by Whittaker et al. (2008) and Whittaker and Boulton, (2012) as a function of changing drainage area with downstream distance A_c (km^2) and a proportionality coefficient Ψ, which is a function of fault throw rate, U (mm y^{-1}) (eq. B2).

$$V = \Psi^b \cdot A_c{}^{0.5} \tag{B1}$$

$$\Psi = C_e \cdot U \tag{B2}$$

A_c is the difference between total catchment area A and A', Ψ is a function of fault slip-rate U (mm y^{-1}) (Whittaker and Boulton, 2012) and the coefficient b = 0.67 is based on the data analysis of Whittaker and Boulton (2012). In order to establish a quantitative relation between Ψ and U, we introduce a proportionality coefficient C_e, which describes catchment erosion efficiency depending on both climate and lithology (Whittaker and Boulton, 2012). A' is described as a function of the length of the transient reach LT. We applied the formula and the coefficients C and α from Mesa and Gupta (1987) (eq. B3), a reformulation of Hack's law, which describes the spatial layout in steady-state catchments, with α typically ~ 0.5 and C ~ 1.4. However, its applicability to transient-state catchments is debated (Mesa and Gupta, 1987) and the choice of C and α have a non-negligible impact on the

calculation of response times (Figure B1). Furthermore, real catchments lose drainage area with upstream distance in a stepwise way (e.g., due to confluences) that may not, in detail, follow Hack's law. The length of the transient reach at time t is a function of time and knickzone migration velocity (eq. B4). We used equations B1-B4 to calculate the response times of the three catchments in Central Italy. In the case of the Celano catchment, the spatial extent of the transient incised reach, A' is ca. 30% of the total drainage area, A (Whittaker et al., 2008) ($A_c = 70\%$). Figure B1b shows the evolution of A_c after the increase of fault slip-rate using three different C_e coefficients. The condition of A_c/A at 70 % at 700 ky is verified with $C_e = 0.00022$ mm (table B1). A condition of near-equilibrium (response time) ($A_c/A = 10\%$) is reached at 4600 ky. The experiment results for all three catchments indicate response times in the order of 10^6 years, becoming progressively longer with lower fault-slip rates (table B1), whereas C_e coefficients are almost identical, consistent with the similar lithology and climate for the three catchments.

$$A_c = \left(\frac{L}{C}\right)^{\frac{1}{\alpha}} \tag{B3}$$

$$LT(t) = LT(t-1) - V(t) \cdot dt \tag{B4}$$
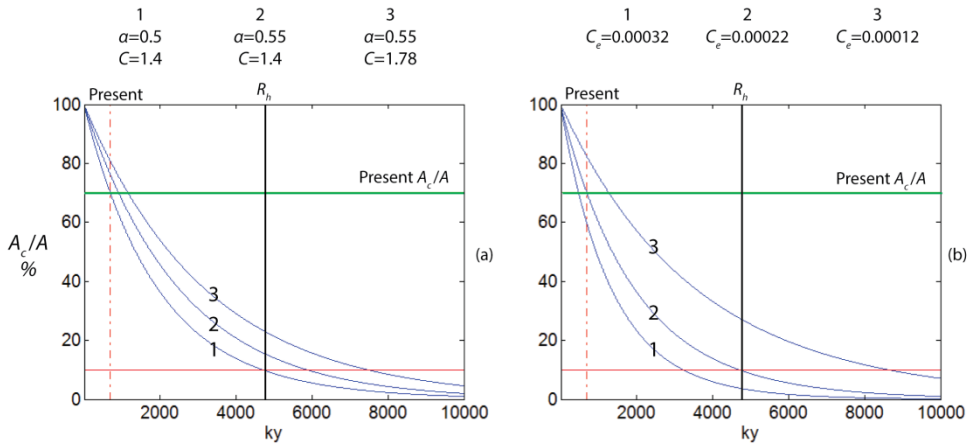
Figure B1: evolution of the ratio between transient state catchment area and total catchment area A_c/A, and hillslopes response time R_h for the Celano catchment as a function of (a) coefficients C and α (equation 13), and (b) erosion efficiency C_e. For the Rio Torto α is ~ 0.5 and C = 1.78 (case 3). High α, C and C_e values lead to longer R_h.
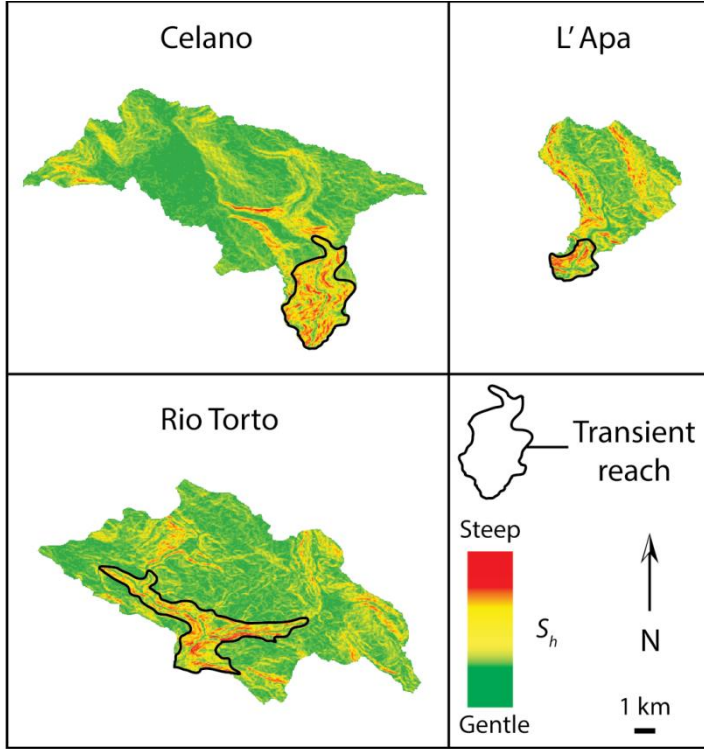
Figure B2: DEM based average hillslope angle S_h of the investigated catchments

B2. Model parameters

In order to constrain the hillslope evolution coefficients *c1* and *c2* in equation 1, we used the previously calculated response times (table B1), the average hillslope angle, S_h, and fluvial channel gradient, S_f, for each catchment, calculated with a DEM (ASTER-GDEM) (Figure B2). At present, each catchment is subdivided in a lower reach, characterized by steep S_h and S_f; and an upper reach, not yet affected by the erosive wave, with gentle S_h and S_f. We assumed that S_h and S_f in the upper reach represent the original S_h and S_f for the whole catchment before the propagation of the wave of erosion (i.e., before 700 ky BP) (see table B2). For the three analyzed catchments, the higher uplift rate *U* corresponds to a larger increase of S_h. This supports our modeling approach, with S_h as a function of *U* (eq. 1-2).
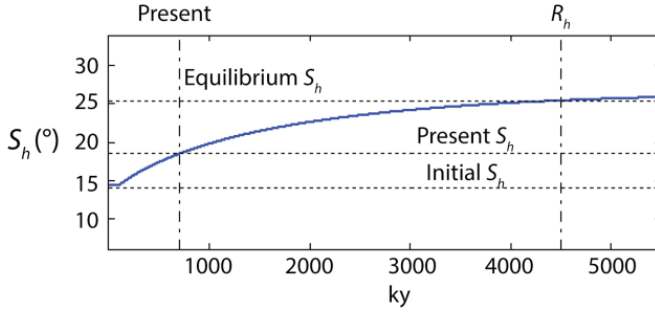
Figure B3: average hillslope angle S_h evolution and response time R_h for the Celano catchment

In our simulations, U increased at 700 ky BP, and climatic conditions were constant throughout the whole simulation. With a trial-error approach, we isolated the combination of parameters $c1$ and $c2$ which fits (i) measured S_h prior to 700 ky BP, (ii) present day S_h, and (iii) the calculated response time for each catchment (Figure A3). With a similar approach, we calibrated the value of concavity of the longitudinal river profile θ (Fig 7a), using a coefficient of erosion $x = 10^{-6}$. Finally, we calibrated regolith threshold R_t based on the excess volume of material eroded from the lower reach EV, previously estimated by Whittaker et al (2010). Since the lower reach is, at present, in detachment-limited conditions (Whittaker et al., 2010), while the upper reach is not, we assumed that R_t was crossed after the increase in fault slip-rate. We constrained R_t by comparing the measured and the modeled volume of the eroded material (Figure B4b and B4c).

For the three Abruzzi catchments, θ is inversely correlated to fault slip-rate (table B2). For the L'Apa, $c1$ is much higher than for the other two catchments, because of the high initial S_h. If we consider only the Celano and Rio Torto, which have a similar initial S_h, $c1$ is directly related to U and to the change in S_h (table B2). The parameter $c2$ does not play an important role on the model output, and its value is identical for all three catchments. Considering only the Celano and Rio Torto, R_t is inversely related to U. This can be explained by the fact that a stronger tectonic perturbation led hillslopes to detachment-limited conditions. The low R_t value in the L'Apa is probably due to the high initial S_h.
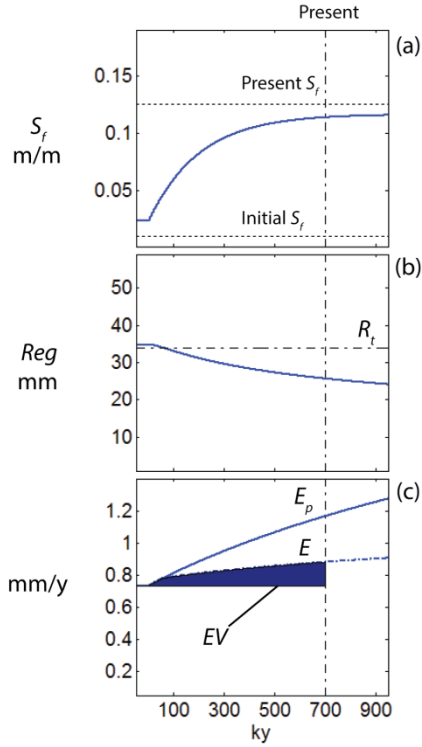
Figure B4: evolution of the Celano catchment morphological parameters: (a) fluvial channel gradient S_f; (b) regolith thickness Reg; (c) actual erosion rate E, potential erosion rate E_p and excess volume of material eroded from the lower reach EV. When Reg is below regolith threshold R_t E is lower than Ep.

The relation between response time coefficient of hillslopes to erosion K_e, response time coefficient of hillslopes to uplift K_u, and response time for hillslopes, R_h (My), was calculated numerically. We ran a number of experiments with different K_e and K_u

and calculated the resulting R_h. Subsequently, we applied a polynomial regression to fit the calculated relation (eq. B5). With the same approach we calculated the relation between response time for fluvial channel gradient R_f and response time coefficient of fluvial channel gradient to uplift (eq. B6).

$$R_h = 208 - 3.5 \cdot K_e^{0.7} + 0.55 \cdot K_u^{1.17} \tag{B5}$$

$$R_f = 2.214 \cdot K_f \tag{B6}$$

Table B1: boundary conditions for the three catchments, ratio between transient state catchment area and total catchment area A_t/A, uplift rate U; calculated erosion efficiency coefficient C_e, Ψ, and response time for hillslopes R_h for the three catchments

Catchment	A_c/A	U	C_e	Ψ	R_h
Celano	70	1.6	2.2	3.0	4.6
Rio Torto	80	1.0	2.0	1.9	7.5
L'Apa	90	0.3	2.0	0.8	17

Table B2: measured and calibrated parameters for the three Abruzzi catchments

Catchment	U	EV	$S_h(°)$	$S_h(°)$	$S_h(°)$	$c1$	$c2$	θ	R_t
Celano	1.6	2.8	13.9	18.5	4.6	25	0.3	0.54	34
Rio Torto	1.0	1.6	13.0	16.2	3.2	22	0.3	0.51	37
L'Apa	0.3	0.2	20.3	22.5	2.2	130	0.3	0.46	22

BIBLIOGRAPHY

Ahnert F. 1970. Functional relationships between denudation, relief, and uplift in large mid-latitude drainage basins. *American Journal of Science* **268** : 243–263.

Ainsworth, R.B., Flint, S.S., and Howell, J.A., 2008, Predicting coastal depositional style: influence of basin morphology and accommodation to sediment supply ratio within a sequence stratigraphic framework, in Hampson, G.J., Steel, R.J., Burgess, P.M., and Dalrymple, R.W., eds., Recent Advances in Models of Siliciclastic Shallow-Marine Stratigraphy: SEPM, Special Publication 90, p. 237-263.

Ainsworth, R.B., Vakarelov, B.K., and Nanson, R.A., 2011, Dynamic spatial and temporal prediction of changes in depositional processes on clastic shorelines: toward improved subsurface uncertainty reduction and management: American Association of Petroleum Geologists, Bulletin, v. 95, p. 267–297.

Alizai, A., Carter, A., Clift, P.D., Van Laningham, S., Williams, J.C., Kumar, R., 2011. Sediment provenance, reworking and transport processes in the Indus River by U–Pb dating of detrital zircon grains. Global and Planetary Change 76 (1-2), 33–55.

Allen PA. 2008. Time scales of tectonic landscapes and their sediment routing systems. *Geological Society, London, Special Publications* **296** : 7–28.

Allen, J.R.M., Brandt, U., Brauer, A., Hubberten, H., Huntley, B., Kramlk, M., Mackensen, A., Mingram, J., Negendank, È.F.W., Nowaczyk, N.R., Watts, W.A., Wulf, S., Zolitschka, B., 1999. Rapid environmental changes in southern Europe during the last glacial period. Letters to Nature 400, 1–4.

Amorosi, A., Colalongo, M.., Fiorini, F., Fusco, F., Pasini, G., Vaiani, S.., Sarti, G., 2004. Palaeogeographic and palaeoclimatic evolution of the Po Plain from 150-ky core records. Glob. Planet. Change 40, 55–78.

Amorosi, A., Rossi, V., Sarti, G., Mattei, R., 2013. Coalescent valley fills from the late Quaternary record of Tuscany (Italy). Quat. Int. 288, 129–138.

Andreucci, S., Pascucci, V., Murray, A.S., Clemmensen, L.B., 2009. Late Pleistocene coastal evolution of San Giovanni di Sinis, west Sardinia (Western Mediterranean). Sediment. Geol. 216, 104–116.

Armitage JJ, Duller RA, Whittaker AC, Allen PA. 2011. Transformation of tectonic and climatic signals from source to sedimentary archive. *Nature Geoscience* **4** : 231–235.

Attal M, Tucker GE, Whittaker AC, Cowie PA, Roberts GP. 2008. Modeling fluvial incision and transient landscape evolution : Influence of dynamic channel adjustment. *Journal of Geophysical Research* **113** : 1–16.

Bellotti, P., Caputo, C., Davoli, L., Evangelista, S., Garzanti, E., Pugliese, F., Valeri P., 2004. Morpho-sedimentary characteristics and Holocene evolution of the emergent part of the Ombrone River delta (southern Toscany). Geomorphology 61, 71–90.

Benvenuti, M., Martini, P., 2002. Analysis of terrestrial hyperconcentrated flows and their deposits. Spec. Publs. Int. Ass. Sediment. 32, 167–193.

Berryman, K., Marden, M., Eden, D., Mazengarb, C., Ota, Y., Moriya, I., 2000. Tectonic and paleoclimatic significance of Quaternary river terraces of the Waipaoa River, east coast, North Island, New Zealand. New Zealand Journal of Geology and Geophysics 43, 229–245.

Bhattacharya JP, MacEachern JA. 2009. Hyperpycnal rivers and prodeltaic shelves in the Cretaceous seaway of North America. *Journal of Sedimentary Geology* **79**: 184–209.

Bhattacharya, J.P., 2006, Deltas, *in* H. W. Posamentier, and R. Walker, eds., Facies models revisited, SEPM Special Publication 84, p. 237-292.

Bhattacharya, J.P., Giosan, L., 2003. Wave-influenced deltas: geomorphological implications for facies reconstruction. Sedimentology 50, 187–210.

Binnie SA, Phillips WM, Summerfield MA, Fifield LK. 2007. Tectonic uplift , threshold hillslopes , and denudation rates in a developing mountain range. *Geology* **35**(8) : 743–746.

Bloemsma, M.R., Zabel, M., Stuut, J.B.W., Tjallingii, R., Collins, J.A., and Weltje, G.J., 2012, Modelling the joint variability of grain size and chemical composition in sediments: Sedimentary Geology, v. 280, p. 135-148.

Blum, D.M., Törnquist, T., 2000. Fluvial responses to climate and sea-level change: a review and look forward. Sedimentoloty 47, 2–48.

Blum, M., Martin, J., Milliken, K., Garvin, M., 2013. Paleovalley systems: Insights from Quaternary analogs and experiments. Earth-Science Rev. 116, 128–169.

Blum, M.D., Aslan, A., 2006. Signatures of climate vs. sea-level change within incised valley-fill successions: Quaternary examples from the Texas GULF Coast. Sediment. Geol. 190, 177–211.

Bogaart PW, Troch PA. 2006. Curvature distribution within hillslopes and catchments and its effect on the hydrological response. *Hydrology and Earth System Sciences* **10** : 925–936.

Bogaart PW, Van Balen RT, Kasse C, Vandenberghe J. 2003a. Process-based modelling of fluvial system response to rapid climate change – 2: Application to the River Maas (The Netherlands) during the last glacial-interglacial transition. *Quaternary Science Reviews* **22**: 2077–2095.

Bogaart PW, Van Balen RT, Kasse C, Vandenberghe J. 2003b. Process-based modelling of fluvial system response to rapid climate change – 1: model formulation and generic applications. *Quaternary Science Reviews* **22**: 2097–2110.

Bogaart, P.W., van Balen, R.T., 2000. Numerical modeling of the response of alluvial rivers to Quaternary climate change. Glob. Planet. Change 27, 147–163.

Brauer, A., Allen, J.R.M., Mingram, J., Dulski, P., Wulf, S., Huntley, B., 2007. Evidence for last interglacial chronology and environmental change from Southern Europe. Proc. Natl. Acad. Sci. U. S. A. 104, 450–5.

Brazier RE, Beven KJ, Freer J, Rowan JS. 2000. Equifinality and uncertainty in phisically based soil erosion models: application of the glue methodology to WEPP-the water erosion prediction project- for sites in the UK and USA. *Earth Surf. Process. Landforms* **25** : 825–845.

Brommer, M.B., Weltje, G.J., Trincardi, F., 2009. Reconstruction of sediment supply from mass accumulation rates in the northern Adriatic Basin (Italy) over the past 19,000 years. Journal of Geophysical Research 114, 1–15.

Brown, L.J., 1995. Holocene shoreline depositional processes at Poverty Bay, a tectonically active area, northeastern north island, New Zealand. Quaternary International 26, 21–33.

Browne, G.H., Naish, T.R. 2003. Facies development and sequence architecture of a Late Quaternary fluvial-marine transition, Canterbury Plains and shelf, New

Zealand: implications for forced regressive deposits. Sedimentary Geology 158(1/ 2), 57–86.

Burbank, D.W., Anderson, R.S., 2008. Tectonic Geomorphology 2001. Blackwell Science, Malden, 274 pp.

Burgess PM, Lammers H, van Oosterhout C, Granjeon D. 2006. Multivariate sequence stratigraphy: tackling complexity and uncertainty with stratigraphic forward modeling, multiple scenarios, and conditional frequency maps. *AAPG Bulletin* **90**(12): 1883–1901.

Busschers FS, Kasse C, Van Balen RT, Vandenberghe J, Cohen KM, Weerts HJT, Wallinga J, Johns C, Cleveringa P, Bunnik FPM. 2007.Late Pleistocene evolution of the Rhine-Meuse system in the southern North Sea basin: imprints of climate change, sea-level oscillations and glacio-isostasy. *Quaternary Science Reviews* **26**: 3216–3248.

Buylaert, J.P., Jain, M., Murray, A.S., Thomsen, K.J., Thiel, C., Sohbati, R., 2012. A robust feldspar luminescence dating method for Middle and Late Pleistocene sediments. Boreas 41, 435–451.

Cacho, I., Grimalt, J.O., Canals, M., 2002. Response of the Western Mediterranean Sea to rapid climatic variability during the last 50 , 000 years : a molecular biomarker approach. Journal of the Marine Systems 34, 253–272.

Calvès, G., Toucanne, S., Jouet, G., Charrier, S., Thereau, E., Etoubleau, J., Marsset, T., Droz, L., Bez, M., Abreu, V., Jorry, S., Mulder, T., Lericolais, G., 2012. Inferring denudation variations from the sediment record; an example of the last glacial cycle record of the Golo Basin and watershed, East Corsica, western Mediterranean sea. Basin Res. 24, 1–22.

Campbell, C.V., 1967, Lamina, laminaset, bed and bedset: Sedimentology, v. 8, p. 7-26.

Carretier S, Lucazeau F. 2005. How does alluvial sedimentation at range fronts modify the erosional dynamics of mountain catchments ?. *Basin Research* **17** : 361–381.

Castelltort S, Van Den Driessche J. 2003. How plausible are high-frequency sediment supply-driven cycles in the stratigraphic record?. *Sedimentary Geology* **157** : 3–13.

Cavinato GP, Carusi C, Dall'Asta M, Miccadei E, Piacentini T. 2002. Sedimentary and tectonic evolution of Plio-Pleistocene alluvial and lacustrine deposits of Fucino Basin (central Italy). *Sedimentary Geology* **148** : 29–59.

Charvin K, Hampson GJ, Gallagher KI, Storms JEA, Labourdette R. 2011. Characterization of controls on high-resolution stratigraphic architecture in wave dominated shoreface-shelf parasequences using inverse numerical modeling. *Journal of Sedimentary Research* **81** : 562–578

Charvin, K., Hampson, G.J., Gallagher, K.L., and Labourdette, R., 2010, High-resolution stratigraphic architecture within an interpreted asymmetrical wave-dominated deltaic parasequence: Sedimentology, v. 57, p. 760-785.

Charvin, K., Hampson, G.J., Gallagher, K.L., and Labourdette, R., 2010, High-resolution stratigraphic architecture within an interpreted asymmetrical wave-dominated deltaic parasequence: Sedimentology, v. 57, p. 760-785.

Charvin, K., Hampson, G.J., Gallagher, K.L., Storms, J.E.A. and Labourdette, R., 2011, Characterization of controls on high-resolution stratigraphic architecture in wave-dominated shoreface-shelf parasequences using inverse numerical modelling: Journal of Sedimentary Research, v. 81, p. 562-578.

Church, M., Slaymaker, O., 1989. Disequilibrium of Holocene sediment yield in glaciated British Columbia. Nature 337, 452–454.

Clifton, E.H., 2006, A re-examination of facies models for clastic shorelines. In: Facies Models Revisited (Eds H.W. Posamentier and R.G. Walker), SEPM Spec. Publ., 84, 293– 337.

Clifton, E.H., 2006, A re-examination of facies models for clastic shorelines. In: Facies Models Revisited (Eds H.W. Posamentier and R.G. Walker), SEPM Spec. Publ., 84, 293– 337.

Collier, R.E.L., Leeder, M.R., Trout, M., Ferentinos, G., Lyberis, E., Leeder, M.R., Trout, M., Papatheodorou, G., 2000. High sediment yields and cool , wet winters : Test of last glacial paleoclimates in the northern Mediterranean. Geology 28, 999– 1002.

Conchon, O., 1972. Caractères généraux et chronologie relative des alluvions fluviatiles rubéfiées de quelques vallées de Corse orientale. Bulletin de l'Association francaise pour l'etude du quaternaire 9, 171–184.

Conchon, O., 1978. Quaternary studies in Corsica, France.. Quaternary Research 9, 41–53.

Coulthard TJ, Macklin MG, Kirkby MJ. 2002. A cellular model of Holocene upland river basin and alluvial fan evolution. *Earth Surface Processes and Landforms* **27** : 269–288.

Coulthard TJ., Van de Wiel MJ. 2013. Climate, tectonics or morphology: what signals can we see in drainage basin sediment yelds?. *Earth Surface Dynamics* **1** : 13–27.

Coulthard, T.J., Lewin, J., Macklin, M.G., 2005. Modelling differential catchment response to environmental change. Geomorphology 69, 222–241.

Coulthard, T.J., Van De Wiel, M.J., 2007. Quantifying fluvial non linearity and finding self-organized criticality? Insights from simulations of river basin evolution. Geomorphology 91, 216–235.

Couture, N.J., Pollard, W.H., 2007. Modeling geomorphic response to climate change. Climatic Change 85, 407–431.

Cowie PA, Whittaker AC, Attal M, Roberts G, Tucker GE. 2008. New constraints on sediment-flux – dependent river incision : Implications for extracting tectonic signals from river profiles. *Geology* **36**(7) : 535–538.

Cunningham, A.C., Wallinga, J., 2012.. Realizing the potential of fluvial archives using robust OSL chronologies. Quaternary Geochronology 12, 98-106.

Dansgaard, W., Johnsen, S.J., Clausen, H.B., Dahl-Jensen, D., Gundestrup, N.S., Hammer, C.U., Hvidberg, C.S., Steffensen, J.P., Sveinbjornsdottir. A.E., Jouzel, J., Bond, G., 1993. Evidence for general instability of past climate from a 250 kyr ice-core record. Letters to Nature 364, 218–220.

Davidson SK, North CP. Geomorphological regional curves for prediction of drainage area and screening modern analogues for rivers in the rock record. *Journal of sedimentary Research* **79**: 773–792

de Jager, G., Van Doren, J.F.M., Jansen, J.D., Luthi, S.M., 2009. An evaluation of relevant geological parameters for predicting the flow behavior of channelized reservoirs. Petroleum Geoscience 15 (4), 345–354.

de Winter, I.L., Storms J.E.A., Overeem I., 2012. Numerical modeling of glacial sediment production and transport during deglaciation. Geomorphology 167-168, 102-114

DeCelles, P.G., and Coogan, J.C., 2006, Regional structure and kinematic history of the Sevier fold-and-thrust belt, central Utah: Geological Society of America, Bulletin, v. 118, p. 841-864.

Densmore AL, Allen PA., Simpson G. 2007. Development and response of a coupled catchment fan system under changing tectonic and climatic forcing. *Journal of Geophysical Research* **112** : 1–16.

Deptuck, M.E., Piper, D.J.W., Savoye, B., Gervais, A., 2008. Dimensions and architecture of late Pleistocene submarine lobes off the northern margin of East Corsica. Sedimentology 55, 869–898.

Doomen, A.M.C., Wijma, E., Zwolsman, J.J.G., Middelkoop, H., 2008. Predicting suspended sediment concentrations in the Meuse River using a supply-based rating curve. Hydrological Processes 22, 1846–1856.

Dubiel, R.F., Kirschbaum, M.A., Roberts, L.N.R., Mercier, T.J., and Heinrich, A., 2000, Geology and coal resources of the Blackhawk Formation in the Southern Wasatch Plateau, Central Utah, in Kirschbaum, M.A., Roberts, L.N.R., and Biewick, L.R.H., eds., Geologic Assessment of Coal in the Colorado Plateau: Arizona, Colorado, New Mexico, and Utah: U.S. Geological Survey, Professional Paper 1625-B, Chapter S (CD-ROM only).

Elliott, T., 1986, Clastic shorelines. In: Sedimentary Environ- ments and Facies (Ed. H.G. Reading), pp. 143–177. Black- well Scientific Publications, Oxford.

Enge, H.D., and Howell, J.A,, 2010, Impact of deltaic clinothems on reservoir performance: dynamic studies of reservoir analogs from the Ferron Sandstone Member and Panther Tongue, Utah: AAPG Bulletin, v. 94, p. 139-161.

Enge, H.D., Howell, J.A., and Buckley, S.J., 2010a, Quantifying clinothem geometry in a forced-regressive river-dominated delta, Panther Tongue Member, Utah, USA: Sedimentology, v. 57, p. 1750-1770.

Enge, H.D., Howell, J.A., and Buckley, S.J., 2010b, The geometry and internal architecture of stream mouth bars in the Panther Tongue and the Ferron Sandstone members, Utah, USA: Journal of Sedimentary Research, v. 80, p. 1018-1031.

Fellin, M.G., 2005. Relief evolution in northern Corsica, western Mediterranean: Constraints on uplift and erosion on long-term and short-term timescales. J. Geophys. Res. 110, 1–16.

Fletcher, W.J., Sánchez Goñi, M.F., 2008. Orbital- and sub-orbital-scale climate impacts on vegetation of the western Mediterranean basin over the last 48,000 yr. Quat. Res. 70, 451–464.

Flores, R.M., Blanchard, L.F., Sanchez, J.D., Marley, W.E., and Muldoon, W.J., 1984, Paleogeographic controls of coal accumulation, Cretaceous Blackhawk Formation and Star Point Sandstone, Wasatch Plateau, Utah: Geological Society of America, Bulletin, v. 95, p. 540-550.

Fontana, A., Mozzi, P., Bondesan, A., 2008. Alluvial megafans in the Venetian–Friulian Plain, north-eastern Italy: Evidence of sedimentary and erosive phases during Late Pleistocene and Holocene. Quat. Int. 189, 71–90.

Forzoni A, Jager GDJ, Storms, JEA. 2013. A spatially lumped model to investigate downstream sediment flux propagation within a fluvial catchment. *Geomorphology* **193** : 65–80.

Foster, G., Carter, L., 1997. Mud sedimentation on the continental shelf at an accretionary margin - Poverty Bay, New Zealand. New Zealand Journal of Geology and Geophysics 40, 157–173.

Frostick, L.E., Jones, S.J., 2002. Impact of periodicity on sediment flux in alluvial systems: grain to basin scale. Geological Society, London, Special Publications 191 (1), 81–95.

Fryirs KA, Brierley GJ, Preston NJ, Kasai M. 2007. Buffers, barriers and blankets: The (dis)connectivity of catchment-scale sediment cascades. *Catena* **70** : 49–67.

Fryirs KA. 2013. (Dis)Connectivity in catchment sediment cascades: a fresh look at sediment delivery problem. *Earth Surface Processes and Landforms* **38**: 30–46.

Gabet EJ, Pratt-sitaula BA, Burbank DW. 2004. Climatic controls on hillslope angle and relief in the Himalayas. *Geology* **32**(7) : 629–632.

Galbraith, R.F., Roberts, R.G., Laslett, G.M., Yoshida, H., Olley, J.M., 1999. Optical dating of single and multiple grains of quartz from Jinmium rock shelter, northern Australia: Part I. Experimental design and statistical models. Archaeometry 41, 339–364.

Galloway, W.E., 1975, Process framework for describing the morphologic and stratigraphic evolution of deltaic deposi- tional systems. In: Deltas, Models for Exploration (Ed. M.L. Broussard), pp. 87–98. Houston Geological Society, Houston.

Gani, M.R. and Battacharya, J.P., 2007, Basic building blocks and process variability of a Cretaceous delta: internal facies architecture reveals a more dynamic interaction of river, wave and tidal processes than is indicated by external shape. J. Sed. Res., 77, 284–302.

Gaudemer Y, Me F. 1999. Stability of output fluxes of large rivers in South and East Asia during the last 2 million years: implications on floodplain processes. Basin Research **11** : 293–303.

Gervais, A., Mulder, T., Savoye, B., Gonthier, E., 2006a. Sediment distribution and evolution of sedimentary processes in a small sandy turbidite system (Golo system, Mediterranean Sea: implications for various geometries based on core framework. Geo-Marine letters 26, 373–395.

Gervais, A., Savoye, B., Mulder, T., Gonthier, E., 2006b. Sandy modern turbidite lobes: A new insight from high resolution seismic data. Mar. Pet. Geol., 23, 485–502.

GRIP, 1993. Climate instability during the last interglacial period recorded in the GRIP ice core. Nature 364, 203–207.

Hampson, G.J., and Howell, J.A., 2005, Sedimentologic and geomorphic characterization of ancient wave-dominated shorelines: examples from the Late Cretaceous Blackhawk Formation, Book Cliffs, Utah, *in* Bhattacharya, J.P., and Giosan, L., eds., River Deltas – Concepts, Models, and Examples: SEPM, Special Publication 83, p. 133-154.

Hampson, G.J., Gani, M.R., Sahoo, H., Rittersbacher, A., Irfan, N., Ranson, A., Jewell, T.O., Gani, N.D.S., Howell, J.A., Buckley, S.J., and Bracken, B., 2012, Alluvial-to-coastal plain stratigraphic architecture and large-scale patterns of fluvial sandbody distribution in a progradational clastic wedge: Upper Cretaceous Blackhawk Formation, Wasatch Plateau, central Utah, USA: Sedimentology, v. 59, p. 2226-2258.

Hampson, G.J., Gani, M.R., Sharman, K.E., Irfan, N., and Bracken, B., 2011, Along-strike and down-dip variations in shallow-marine sequence stratigraphic architecture: Upper Cretaceous Star Point Sandstone, Wasatch Plateau, Central Utah, USA: Journal of Sedimentary Research, v. 81, p. 159-184.

Hampson, G.J., Rodriguez, A.B., Storms, J.E.A., Johnson, H.D., and Meyer, C.T., 2008, Geomorphology and high-resolution stratigraphy of wave-dominated shoreline deposits: impact on reservoir-scale facies architecture, in Hampson, G.J., Steel, R.J., Burgess, P.M., and Dalrymple, R.W., eds., Recent Advances in Models of Siliciclastic Shallow-Marine Stratigraphy: SEPM, Special Publication 90, p. 117-142.

Hampson, G.J., Steel, R.J., Burgess, P.M., and Dalrymple, R.W., eds., Recent Advances in Models of Siliciclastic Shallow-Marine Stratigraphy: SEPM, Special Publication 90, p. 3-12.

Hampson, G.J., Storms, J.E.A., 2003. Geomorphological and sequence stratigraphic variability in wave-dominated, shoreface-shelf parasequences. Sedimentology 50, 667–701.

Hansen, J.P. V., and Rasmussen, E.S., 2008, Structural, sedimentologic, and sea-level controls on sand distribution in a steep-clinoform asymmetric wave-influenced delta: Miocene Billund Sand, Eastern Danish North Sea and Jylland: Journal of Sedimentary Research, v. 78, p. 130–146.

Harvey AM. 2002. Effective timescales of coupling within fluvial systems. *Geomorphology* **44** : 175–201.

Harvey, a. ., 2002. The role of base-level change in the dissection of alluvial fans: case studies from southeast Spain and Nevada. Geomorphology 45, 67–87.

Heimsath AM, E. Dietrich W, Nishiizumi K, Finkel RC. 1999. Cosmogenic nuclides, topography, and the spatial variation of soil depth. *Geomorphology* **27** : 151–172.

Helland-Hansen W, Hampson GJ. 2009. Trajectory analysis: concepts and applications. *Basin Research* **21** : 454–483.

Hinderer, M., 2001. Late Quaternary denudation of the Alps , valley and lake fillings and modern river loads. Geodinamica Acta 14, 231–263.

Hoek, W.Z., 1997. Late-glacial and early Holocene climatic events and chronology of vegetation development in the Netherlands. Vegetation History and Archaeobotany 6 (4), 197–213.

Hogg, R.V. J. Ledolter, 1987. Engineering Statistics, MacMillan, New York.

Holbrook, J. M., Bhattacharya, J., 2012. What Happened to My Marine Reservoir? Implications of Falling Stage and Lowstand Fluvial Sediment Storage during " Sequence-Boundary " Scour for Sand Starvation of Coastal Marine Reservoirs. adapted from poster presentation, AAPG Annual Convention and Exhibition, Long Beach, California

Hoogendoorn RM, Overeem I, Storms JEA. 2008. Process-response modelling of fluvio-deltaic stratigraphy. *Computers & Geosciences* **34** : 1394–1416.

Hoogendoorn, R.M., Boels, J.F., Kroonenberg, S.B., Simmons, M.D., Aliyeva, E., Babazadeh, A.D., and Huseynov, D., 2005, Development of the Kura delta, Azerbaijan: a record of Holocene Caspian sea-level changes: Marine Geology, v. 222-223, p. 359-380.

Horton, B.K., Constenius, K.N., and DeCelles, P.G., 2004, Tectonic control on coarse-grained foreland-basin sequences: an example from the Cordilleran foreland basin, Utah: Geology, v. 32, p. 637-640.

Howell, J.A., Vassel, Å., and Aune, T., 2008, Modelling of dipping clinoform barriers within deltaic outcrop analogues from the Cretaceous Western Interior Basin, USA, in Robinson, A., Griffiths, P., Price, S. Hegre, J., and Muggeridge, A., eds., The Future of Geological Modelling in Hydrocarbon Development: Geological Society of London, Special Publication 309, p. 99-121.

Howell, J.A., Vassel, Å., and Aune, T., 2008, Modelling of dipping clinoform barriers within deltaic outcrop analogues from the Cretaceous Western Interior Basin, USA, in Robinson, A., Griffiths, P., Price, S. Hegre, J., and Muggeridge, A., eds., The Future of Geological Modelling in Hydrocarbon Development: Geological Society of London, Special Publication 309, p. 99-121.

Huizink, M., 1999. Lateglacial river sediment budgets in the Maas valley, the Netherlands. Earth Surf. Process. Landforms 24, 93-109.

Hutton, E.W.H., Syvitski, J.P.M., 2008. Sedflux 2.0: An advanced process-response model that generates three-dimensional stratigraphy. Comput. Geosci. 34, 1319–1337.

Hwang, I-G., and Heller, P.L., 2002, Anatomy of a transgressive lag: Panther Tongue Sandstone, Star Point Formation, central Utah: Sedimentology, v. 49, p. 977-999.

Jerolmack DJ, Paola C. 2010. Shredding of environmental signals by sediment transport. *Geophysical Research Letters* **37** : 1–5.

Jiménez, J.A., Sánchez-Arcilla, A., Valdermoro, H.I., Gracia, V. and Nieto, F., 1997, Processes reshaping the Ebro Delta: Marine Geology, v. 144, p. 59-79.

Kallel, N., Duplessy, J.C., Labeyrie L., Fontugne., Paterne., 2004. Mediterranean sea palaeohydrology and pluvial periods during the late Quaternary. In R.W. Battarbee et al. (eds) Past Climate Variability through Europe and Africa. Springer, Dordrecht, The Netherlands.

Kallel, N., Duplessy, J.-C., Labeyrie, L., Fontugne, M., Paterne, M., Montacer, M., 2000. Mediterranean pluvial periods and sapropel formation over the last 200 000 years. Palaeogeogr. Palaeoclimatol. Palaeoecol. 157, 45–58.

Kamola, D.L., and Van Wagoner, J.C., 1995, Stratigraphy and facies architecture of parasequences with examples from the Spring Canyon Member, Blackhawk

Formation, Utah, *in* Van Wagoner, J.C., and Bertram, G.T., eds., Sequence Stratigraphy of Foreland Basin Deposits: Outcrop and Subsurface Examples from the Cretaceous of North America: American Association of Petroleum Geologists, Memoir 64, p. 27-54.

Kars, R.H., Busschers, F.S., Wallinga, J., 2012. Validating post IR-IRSL dating on K-feldspars through comparison with quartz OSL ages. Quaternary Geochronology 12, 74-86

Kars, R.H., Reimann, T., Ankjærgaard, C., Wallinga, J., 2014. Bleaching of the post-IR IRSL signal: new insights for feldspar luminescence dating. Boreas

Kauffman, E.G., and Caldwell, W.G.E., 1993, The Western Interior Basin in space and time, in Caldwell, W.G.E., and Kauffman, E.G., eds., Evolution of the Western Interior Basin: Geological Association of Canada, Special Paper 39, p. 1-30.

Kettner, A. J., Gomez, B., Syvitski, J. P. M., 2009. Modeling suspended sediment discharge from the Waipaoa River system, New Zealand: The last 3000 years. Water Resources Research 43 (7), W07411.

Kettner, A.J., Syvitski, J.P.M., 2008. HydroTrend v.3.0: A climate-driven hydrological transport model that simulates discharge and sediment load leaving a river system. Computers & Geosciences 34 (10), 1170–1183.

Kim, W., Paola, C., Swenson, J.B., Voller, V.R., 2006. Shoreline response to autogenic processes of sediment storage and release in the fluvial system. J. Geophys. Res. 111, F04013.

King, G.E., Sanderson, D.C.W., Robinson, R.A.J., Finch, A.A., 2014. Understanding processes of sediment bleaching in glacial setting using a portable OSL reader. Boreas 10, 0300-9483.

Kirby E, Whipple K. 2001. Quantifying differential rock-uplift rates via stream profile analysis. *Geology* **29**(5) : 415–418.

Kubo Y, Syvitski JPM, Hutton EWH, Kettner AJ. 2006. Inverse modeling of post Last Glacial Maximum transgressive sedimentation using 2D-SedFlux: application to the northern Adriatic Sea. *Marine Geology* **234**: 233–243.

Kuhlemann, J., Borg, K., Bons, P.D., Danišík, M., Frisch, W., 2007. Erosion rates on subalpine paleosurfaces in the western Mediterranean by in-situ 10Be concentrations in granites: implications for surface processes and long-term landscape evolution in Corsica (France). Int. J. Earth Sci. 97, 549–564.

Kuhlemann, J., Frisch, W., Székely, B., Dunkl, I., Danišik, M., Krumrei, I., 2005. Würmian maximum glaciation in Corsica. Austrian Journal of Earth Sciences 97.

Kuhlemann, J., Rohling, E.J., Krumrei, I., Kubik, P., Ivy-Ochs, S., Kucera, M., 2008. Regional synthesis of Mediterranean atmospheric circulation during the Last Glacial Maximum. Science 321, 1338–40.

Lawton, T.F., 1982, Lithofacies correlations within the upper Cretaceous Indianola group, central Utah, Utah Geol. Assoc. Publication 10, 199–214.

Le Dortz, K., Meyer, B., Sebrier, M., Braucher, R., Bourles, D., Benedetti, L., Nazari, H., Foroutan, M., 2012. Interpreting scattered in-situ produced cosmogenic nuclide depth-profile data. Quaternary Geochronology 11, 98–115.

Leeder, M.R., Harris, T., Kirkby, M.J., 1998. Sediment supply and climate change: implications for basin stratigraphy. Basin Research 10 (1), 7–18.

Leigh, D.S., 2006. Terminal Pleistocene braided to meandering transition in rivers of the Southeastern USA. Catena 66 (1-2), 155–160.

Leigh, D.S., 2008. Geomorphology Late Quaternary climates and river channels of the Atlantic Coastal Plain , Southeastern USA. Geomorphology 101, 90–108.

Leigh, D.S., Srivastava, P., Brook, G., 2004. Late Pleistocene braided rivers of the Atlantic Coastal Plain, USA. Quaternary Science Reviews 23 (1-2), 65–84.

Li, W., Bhattacharya, J.P., Zhu, Y., Garza, D. And Blankenship, E., 2011, Evaluating delta asymmetry using three-dimensional facies architecture and ichnological analysis, Ferron 'Notom Delta', Capital Reef, Utah, USA: Sedimentology, v. 58, p. 478-507.

Linacre, E. T., 1977. A simple formula for estimating evaporation rates in various climates, using temperature data alone. Agricultural Meteorology 18, 409–424.

Liu, S., Nummedal, D., and Gurnis, M., 2014, Dynamic versus flexural controls of Late Cretaceous Western Interior Basin, USA: Earth and Plantary Science Letters, v. 389, p. 221-239.

Macklin MG, Woodward JC. 2009. River systems and environmental change. Woodward (ed.). *The Physical Geography of the Mediterranean*. Oxford University Press, Oxford, 319–352.

Marden, M., Mazengarb, C., Palmer, A., Berryman, K., Rowan, D., 2008. Last glacial aggradation and postglacial sediment production from the non-glacial Waipaoa

and Waimata catchments , Hikurangi Margin, North Island , New Zealand. Geomorphology 99, 404–419.

Martin, J., Cantelli, a., Paola, C., Blum, M., Wolinsky, M., 2010. Quantitative Modeling of the Evolution and Geometry of Incised Valleys. J. Sediment. Res. 81, 64–79.

Martrat, B., Grimalt, J.O., Lopez-Martinez, C., Cacho, I., Sierro, F.J., Flores, J.A., Zahn, R., Canals, M., Curtis, J.H., Hodell, D. a, 2004. Abrupt temperature changes in the Western Mediterranean over the past 250,000 years. Science 306, 1762–5.

McPherson, J.G., Shanmugam, G., Moiola, R.J. 1987. Fan-deltas and braid-deltas: varieties of coarse-grained deltas. Geological Society of America Bulletin 99, 331– 340.

Meade, R.H., 1982. Sources, sinks and storage of river sediment in the Atlantic drainage of the United States. The Journal of Geology 90 (3), 235–252.

Merritts, D. J., K. R. Vincent, E. E. Wohl, 1994. Long river profiles, tectonism and eustasy: a guide to interpreting fluvial terraces. Journal of Geophysical research 99 (7), 14031–14050.

Mesa OJ, Gupta VK. 1987. On the Main Channel Length-Area Relationship for Channel Networks. *Water Resources Research* **23**(11) : 2119–2122.

Metivier, F., Y., Gaudemer, Y, 1999. Stability of output fluxes of large rivers in South and East Asia during the last 2 million years: implications on floodplain processes. Basin Research 11(4), 293–303.

Mikhailov, V.N., Kravtsova, V.I., and Magritskii, D.V, 2003. Hydrological and morphological processes in the Kura River delta: Water Resources, 30, 541–554.

Millar, G., 2000. Influence of bank vegetation on alluvial channel patterns. Water Resources Research 36(4), 1109–1118.

Milli, S., D'Ambrogi, C., Bellotti, P., Calderoni, G., Carboni, M.G., Celant, A., Di Bella, L., Di Rita, F., Frezza, V., Magri, D., Pichezzi, R.M., Ricci, V., 2013. The transition from wave-dominated estuary to wave-dominated delta: the Late Quaternary stratigraphic architecture of the Tiber River succession (Italy). Sedimentary Geology 284-285, 159–180.

Milliman JD, Syvitski JPM. 1992. Geomorphic/Tectonic Control of Sediment Discharge to the Ocean: The Importance of Small Mountainous Rivers. *The Journal of Geology* **100** : 525–544.

Moglen GE, Eltahir EAB, Bras RL. 1998. On the sensitivity of drainage density to climate change. *Water Resource Research* **34**(4) : 855–862.

Montgomery DR, Brandon MT. 2002. Topographic controls on erosion rates in tectonically active mountain ranges. *Earth and Planetary Science Letters* **201** : 481–489.

Morehead MD, Syvitski JP, Hutton EWH, Peckham SD. 2003. Modeling the temporal variability in the flux of sediment from ungauged river basins. *Global and Planetary Change* **39** : 95–110.

Murillo-Muñoz, R., G.J., Klaassen, 2006. Downstream fining of sediments in the Meuse river. Proceedings of the International Conference of Fluvial Hydraulics, Lisbon, Portugal, Taylor and Francis.

Muto, T., Steel, R.J., 2004. Autogenic response of fluvial deltas to steady sea-level fall: Implications from flume-tank experiments. Geology 32, 401.

Muto, T., Swenson, J.B., 2005. Large-scale fluvial grade as a nonequilibrium state in linked depositional systems: Theory and experiment. J. Geophys. Res. 110, F03002.

Newman, K.F., and Chan, M.A., 1991, Depositional facies and sequences in the Upper Cretaceous Panther Tongue Member of the Star Point Formation, Wasatch Plateau, Utah, in Chidsey, T.C., Jr., ed., Geology of East-Central Utah: Utah Geological Association, Publication 19, p. 65–75.

Nicholas AP, Quine TA. 2010. Quantitative assessment of landform equifinality and palaeoenvironmental reconstruction using geomorphic models. *Geomorphology* **121** : 167–183.

Nisi, M.F., Antonioli, F., Pra, G.D., Leoni, G., Silenzi, S., 2003. Coastal deformation between the Versilia and the Garigliano plains (Italy) since the last interglacial stage. J. Quat. Sci. 18, 709–721.

Olariu, C., and Bhattacharya, J.P., 2006, Terminal Distributary Channels and Delta Front Architecture of River-Dominated Delta Systems: Journal of Sedimentary Research, v. 76, p. 212–233.

Olariu, C., Bhattacharya, J.P., 2006. Terminal Distributary Channels and Delta Front Architecture of River-Dominated Delta Systems. J. Sediment. Res. 76, 212–233.

Olariu, C., Bhattacharya, J.P., Xu, X., Aiken, C.L.V., Zeng, X., and McMechan, G.A., 2005, Integrated study of ancient delta-front deposits, using outcrop, ground-penetrating radar, and three-dimensional photorealistic data: Cretaceous Panther

Tongue Sandstone, Utah, USA, in Bhattacharya, J.P., and Giosan, L., eds., River Deltas – Concepts, Models, and Examples: SEPM, Special Publication 83, p. 155-178.

Olariu, C., Steel, R.J., and Petter, A.L., 2010, Delta-front hyperpycnal bed geometry and implications for reservoir modeling: Cretaceous Panther Tongue delta, Book Cliffs, Utah: American Association of Petroleum Geologists, Bulletin, v. 94, p. 819-845.

Overeem I, Veldkamp A, Tebbens L, Kroonenberg SB. 2003. Modelling Holocene stratigraphy and depocenter migration of the Volga delta due to Caspian sea-level change. *Sedimentary Geology* **159**: 159–175.

Panagos, P., Meusburger, K., Alewell, C., Montanarella, L., 2012. Soil erodibility estimation using LUCAS point survey data of Europe. Environ. Model. Softw. 30, 143–145.

Paterne, M., Kallel, N., Labeyrie, L., Vautravers, M., Duplessy, J.-C., Rossignol-Strick, M., Cortijo, E., Arnold, M., Fontugne, M., 1999. Hydrological relationship between the North Atlantic Ocean and the Mediterranean Sea during the past 15-75 kyr. Paleoceanography 14, 626.

Pepe, F., Sulli, A., Bertotti, G., Cella, F. 2010. Architecture and Neogene to Recent evolution of the western Calabrian continental margin: an upper plate perspective to the Ionian subduction system, central Mediterranean. Tectonics 29, TC3007.

Petter, a. L., Muto, T., 2008. Sustained Alluvial Aggradation and Autogenic Detachment of the Alluvial River from the Shoreline in Response to Steady Fall of Relative Sea Level. J. Sediment. Res. 78, 98–111.

Peyron, O., Cheddadi, R., Tarasov, P., Reille, M., 1998. Climatic Reconstruction in Europe for 18,000 YR BP from Pollen Data. Quaternary Research 49, 183–196.

Phillips JD, Marion DA, Luckow K, Adams KR. 2005. Nonequilibrium regolith thickness in the Ouachita Mountains. *The Journal of Geology* **113** : 325–340.

Phillips, J. D., Gomez B., 2007. Controls on sediment export from the Waipaoa River basin , New Zealand. Basin Research 19, 241–252.

Phillips, J. D., Marden, M., Gomez. B., 2007. Residence time of alluvium in an aggrading fluvial system. Earth Surface Processes and Landforms, 32, 307–316.

Phillips, J. D., Slattery, M.C., 2006. Sediment storage, sea level ,and sediment delivery to the ocean by coastal plain rivers. Progress in Physical Geography 4, 513–530.

Phillips, J., 2003. Alluvial storage and the long-term stability of sediment yields. Basin Research 15, 153–163.

Plint, A.G., 1988, Sharp-based shoreface sequences and "offshore bars" in the Cardium formation of Alberta: their relationship to relative changes in sea level, *in* Wilgus, C.K., Hastings, B.S., Kendall, C.G.St.C., Posamentier, H.W., Ross, C.A., and Van Wagoner, J.C., eds., Sea-Level Changes: An Integrated Approach: SEPM, Special Publication 42, p. 357-370.

Plint, A.G., and Nummedal, D., 2000, The falling stage systems tract: recognition and importance in sequence stratigraphic analysis, *in* Hunt, D., and Gawthorpe, R.L., eds., Sedimentary Responses to Forced Regression: Geological Society of London, Special Publication 172, p. 1-18.

Posamentier, H.W, Allen, H.W, James, D.P, and Tesson, M., 1992, Forced regressions in a sequence stratigraphic framework: concepts, examples and sequence stratigraphic significance: American Association of Petroleum Geologists, Bulletin, v. 76, p. 1687-1709.

Posamentier, H.W., and Morris, W.R., 2000, Aspects of the stratal architecture of forced regressive deposits, in Hunt, D., and Gawthorpe, R.L., eds., Sedimentary Responses to Forced Regression: Geological Society of London, Special Publication 172, p. 19-46.

Preusser, F., Degering, D., Fuchs, M., Hilgers, A., Kadereit, A., Klasen, N., Krbetschek, M., Richter, D., Spencer, J.Q.G., 2008. Luminescence dating: basics, methods and applications. Eiszeitalter und Gegenwart (Quaternary Science Journal) 57, 95–149.

Ramrath, A., Zolitschka, B., Wulf, S., Negendank, K.F.W., 1999. Late Pleistocene climatic variations as recorded in two Italian maar lakes (Lago di Mezzano, Lago Grande di Monticchio). Quaternary Science Reviews 18, 977–992.

Rasband, W.A., 1997-2014, ImageJ, U. S. National Institutes of Health, Bethesda, Maryland, USA: http://imagej.nih.gov/ij/

Reille, M., Gamisans, J., Andrieu, V., 1997. The late-glacial at Lac de Creno (Corsica, France): a key site in the western Mediterranean basin. New Phytol, 135, 547–559.

Reille, M., Gamisans, J., Andrieu-Ponel, V., Beaulieu, J.L., 1999. The Holocene at Lac de Creno, Corsica, France: a key site for the whole island. New Phytol. 141, 291–307.

Reimann, T., Thomsen, K.J., Jain, M., Murray, A.S., Frechen, M., 2012. Single-grain dating of young feldspars using the pIRIR procedure. Quaternary Geochronology 11, 28-41.

Reimann, T., Tsukamoto, S., Naumann, M., Frechen, M., 2011. The potential of using K-rich feldspars for optical dating of young coastal sediments e a test case from Darss-Zingst peninsula (southern Baltic Sea coast). Quaternary Geochronology 6, 207-222.

Reynolds, A.D., 1999, Dimensions of paralic sandstone bodies. AAPG Bull., 83, 211–229.

Robinson, R.A.J., and Slingerland, R.L., 1998, Grain-size trends, basin subsidence and sediment supply in the Campanian Castlegate Sandstone and equivalent conglomerates of central Utah: Basin Research, v. 10, p. 109-127.

Roering JJ, Perron JT, Kirchner JW. 2007. Functional relationships between denudation and hillslope form and relief. *Earth and Planetary Science Letters* **264** : 245–258.

Rohais S, Bonnet S, Eschard R. 2012. Sedimentary record of tectonic and climatic erosional perturbations in an experimental coupled catchment-fan system. *Basin Research* **24** : 198–212.

Ruddiman WF. 2001. Earth's climate: past and future. W. H. Freeman and Company. New York.

Sanchez, J.D. (1990) Stratigraphic framework, coal zone correlations, and depositional environment of the Upper Cretaceous Blackhawk Formation and Star Point Sandstone in the Scofield and Beaver Creek areas, Nephi 30°x60° quadrangle, Wasatch Plateau coal field, Carbon County, Utah. U.S. Geol. Surv., Coal Investigations Map C-128B, scale 1:24,000.

Saparoea, A.H.V.D.B. Van, Postma, G., 2008. Control of climate change on the yield of river systems. In: Hampson G.J., Steel, R.J., Burgess, P.M., and Dalrymple, R.W., eds., 2008, Recent advances in models of siliciclastic shallow-marine stratigraphy, SEPM, Special Publication 90.

Schlunegger, F., and Hinderer, M., 2003. Pleistocene/ Holocene climate change, re-establishment of fluvial drainage network and increase in relief in the Swiss Alps. Terra Nova 15: 88-95.

Sierro, F.J., Andersen, N., Bassetti, M.A., Berné, S., Canals, M., Curtis, J.H., Dennielou, B., Flores, J.A., Frigola, J., Gonzalez-Mora, B., Grimalt, J.O., Hodell, D.A., Jouet, G.,

Pérez-Folgado, M. and Schneider, R., 2009. Phase relationship between sea level and abrupt climate change. Quaternary Science Reviews 28, 2867-2881.

Simpson G, Castellort S. 2012. Model shows that rivers transmit high-frequency climate cycles to the sedimentary record. *Geology* **40**(12): 1131–1134.

Skyles, E.M., 2013. Alluvial geochronology and watershed analysis of the Golo River, Northeastern Corsica, France. Master of Science Thesis, Utah State University, Logan, Utah, USA.

Snyder NP, Whipple KX, Tucker GE, Merritts DJ. 2003. Channel response to tectonic forcing: field analysis of stream morphology and hydrology in the Mendocino triple junction region, northern California. *Geomorphology* **53** : 97–127.

Sohn, Y.K., Rhee, C.Q., Kim, B.C., 1999. Debris flow and hyperconcentrated flood-flow deposits in an alluvial fan, north-western part of the Cretaceous Yongdong Basin, Central Korea. The Journal of Geology 107, 111–132.

Sømme, T.O., Howell, J.A., Hampson, G.J., and Storms, J.E.A., 2008, Architecture and genesis of intra-parasequence discontinuity surfaces in wave-dominated deltaic deposits: Upper Cretaceous Sunnyside Member, Blackhawk Formation, Book Cliffs, Utah, USA, in Hampson, G.J., Steel, R.J., Burgess, P.M., and Dalrymple, R.W., eds., Recent Advances in Models of Siliciclastic Shallow-Marine Stratigraphy: SEPM, Special Publication 90, p. 421-441.

Sømme, T.O., Piper, D.J.W., Deptuck, M.E., Helland-Hansen, W., 2011. Linking Onshore-Offshore Sediment Dispersal in the Golo Source-to-Sink System (Corsica, France) During the Late Quaternary. Journal of Sedimentary Research 81 (2), 118–137.

Somoza, L., Barnolas, A., Arasa, A. and Maestro, A., 1990, Architectural stacking patterns of the Ebro Delta controlled by Holocene high-frequency eustatic fluctuations, delta-lobe switching and subsidence processes, Sedimentary Geology, v. 117, p. 11-32

Spieker, E.M., and Reeside, J.B., 1925, Cretaceous and Tertiary Formations of the Wasatch Plateau, Utah: Geological Society of America, Bulletin, v. 36, p. 435–454.

Storms, J. E. A., Swift, D. J. P. 2003. Shallow-marine sequences as the building blocks of stratigraphy: insights from numerical modelling. Basin Research 15, 287–303.

Storms, J.E.A., 2003. Event-based stratigraphic simulation of wave-dominated shallow-marine environments. Marine Geology 199 (1-2), 83–100.

Storms, J.E.A., and Hampson, G.J., 2005, Mechanisms for forming discontinuity surfaces within shoreface-shelf parasequences: sea level, sediment supply or wave regime?: Journal of Sedimentary Research, v. 75, p. 67-81.

Storms, J.E.A., de Winter I.L., Overeem, I., Drijkoningen G.G., Lykke-Andersen H., 2012. The Holocene sedimentary history of the Kangerlussuaq Fjord-valley fill, West Greenland. Quat. Sci. Rev. 1-22.

Strudley MW, Murray AB, Haff PK. 2006. Regolith thickness instability and the formation of tors in arid environments. *Journal of Geophysical Research* **111** : 1–16.

Summerfield MA, Hulton NJ. 1994. Natural controls of fluvial denudation rates in major world drainage basins. *Journal of Geophysical Research* **99** : 13,871–13,883.

Summerfield MA. 1991. Global Geomorphology. Prentice Hall. Edinburgh.

Svensson, a., Andersen, K.K., Bigler, M., Clausen, H.B., Dahl-Jensen, D., Davies, S.M., Johnsen, S.J., Muscheler, R., Parrenin, F., Rasmussen, S.O., Röthlisberger, R., Seierstad, I., Steffensen, J.P., Vinther, B.M., 2008. A 60 000 year Greenland stratigraphic ice core chronology. Clim. Past. 4, 47–57.

Swift, D.J.P., 1968, Coastal erosion and transgressive stratigraphy: Journal of Geology, v. 76, p. 444-456.

Syvitski JPM, Milliman JD. 2007. Geology , geography , and humans battle for dominance over the delivery of fluvial sediment to the coastal ocean. *The Journal of Geology* **115** : 1–19.

Syvitski, J.P., Morehead, M.D., Nicholson, M., 1998. Hydrotrend: a Climate-Driven Hydrologic-Transport Model for Predicting Discharge and Sediment Load To Lakes or Oceans. Computers & Geosciences 24 (1), 51–68.

Taylor, A.M., and Goldring, R., 1993, Description and analysis of bioturbation and ichnofabric: Geological Society of London, Journal, v. 150, p. 141-148.

Taylor, K.G., Gawthorpe, R.L., Curtis, C.D., Marshall, J.D., and Awwiller, D.N., 2000, Carbonate cementation in a sequence-stratigraphic framework: Upper Cretaceous sandstones, Book Cliffs, Utah-Colorado: Journal of Sedimentary Research, v. 70, p. 360-372.

Tebbens, L. A., Veldkamp, A., Van Dijke, J.J., Schoorl, J.M., 2000b. Modeling longitudinal-profile development in response to Late Quaternary tectonics, climate and sea-level changes: the River Meuse. Global and Planetary Change 27 (1-4), 165–186.

Tebbens, L.A., Veldkamp, A, 2000. Late Quaternary evolution of fluvial sediment composition: a modeling case study of the River Meuse. Global and Planetary Change 27 (1-4), 187–206.

Tebbens, L.A., Veldkamp, A, Westerhoff, W., Kroonenberg, S.B., 2000a. Fluvial incision and channel downcutting as a response to Late-glacial and Early Holocene climate change: the lower reach of the River Meuse (Maas). Journal of Quaternary science 14 (1), 59–75.

Thiel, C. Buylaert, J.P., Murray, A.S, Terhorst, B., Hofer, I., Tsukamoto, S., Frechen, M., 2011.. Luminescence dating of the Stratzing loess profile (Austria) – Testing the potential of an elevated temperature post-IR IRSL protocol. Quaternary International 234, 23-31.

Thomsen, K. J., Murray, A. S., Jain, M. and Bøtter-Jensen, L., 2008. Laboratory fading rates of various luminescence signals from feldspar-rich sediment extracts. Radiation Measurements 43, 1474-1486.

Toucanne, S., Jouet, G., Ducassou, E., Bassetti, M.-A., Dennielou, B., Angue Minto'o, C.M., Lahmi, M., Touyet, N., Charlier, K., Lericolais, G., Mulder, T., 2012. A 130,000-year record of Levantine Intermediate Water flow variability in the Corsica Trough, western Mediterranean Sea. Quat. Sci. Rev. 33, 55–73.

Trimble, S.W., 1977. The fallacy of stream equilibrium in contemporary denudation studies. American Journal of Science 277, 876–887.

Tucker GE, Mccoy SW, Whittaker AC, Roberts GP, Lancaster ST, Phillips R. 2011. Geomorphic significance of postglacial bedrock scarps on normal - fault footwalls. *Journal of Geophysical Research* **116** : 1–14.

Tucker GE, Slingerland R. 1996. Predicting sediment flux from fold and thrust belts. *Basin Research* **8** : 329–349.

Tucker GE, Slingerland R. 1997. Drainage basin responses to climate change. *Water Resources Research* **33** : 2031.

Turowski, J.M., Rickenmann, D., Dadson, S.J., 2010. The partitioning of the total sediment load of a river into suspended and bedload: a review of empirical data. Sedimentology 57: 1126-1146.

Tzedakis, P.C., 2005. Towards an understanding of the response of southern European vegetation to orbital and suborbital climate variability. Quat. Sci. Rev. 24, 1585–1599.

Upton, P., A. Kettner, J., Gomez, B., Orpin, A.R., Litchfield, N., Page, M.J., 2012. Simulating post-LGM riverine fluxes to the coastal zone: The Waipaoa River System, New Zealand. Computers and Geosciences, 1–10.

USACE, Stream Restoration Design National Engineering Handbook, Chapter 8, Threshold Channel Design, United States Department of Agriculture, Predicting Rainfall Erosion losses (1978),

Utah Geological Survey, 2014,

Vakarelov, B., and Ainsworth, R.B., 2013, A hierarchical approach to architectural classification in marginal-marine systems: bridging the gap between sedimentology and sequence stratigraphy: AAPG Bulletin, v. 97, p. 1121–1141.

van Balen, R.T., Busschers, F.S., Tucker, G.E., 2010. Modeling the response of the Rhine–Meuse fluvial system to Late Pleistocene climate change. Geomorphology 114 (3), 440–452.

Van de Wiel MJ, Coulthard TJ. 2010. Self-organized criticality in river basins: challenging sedimentary records of environmental change. *Geology* **38** : 87–90.

Van der Berg Saparoes APH, Postma G. 2008. Control of climate change on the yield of river stystems. In Hampson, G.J., Steel, R.J., Burgess, P.M., Dalrymple, R.W., eds., Recent advances in models of siliciclastic shallow-marine stratigraphy, SEPM, Special Publication 90.

Van der Zwan CJ. 2002. The impact of Milankovitch-scale climatic forcing on sediment supply. *Sedimentary Geology* **147**: 271–294.

Van Gorp, W., Veldkamp, A., Temme, A.J.A.M., Maddy, D., Demir, T., van der Schriek, T., Reimann, T., Wallinga, J., Wijbrans, J., Schoorl, J.M., 2013. Fluvial response to Holocene volcanic damming and breaching in the Gediz and Geren rivers, western Turkey. Geomorphology 201, 430-448.

Van Heijst, M.W.I.M., Postma, G., 2001. Fluvial response to sea-level changes: a quantitative analogue, experimental approach. Basin Res. 13, 269–292.

Van Strien WJ. 2010. The impact of discharge, supply and base-level cyclicity on (fan)delta development. MSc Thesis, Utrecht University, the Netherlands.

Van Wagoner, J.C., Mitchum, R.M., Campion, K.M., and Rahmanian, V.D., 1990, Siliciclastic Sequence Stratigraphy in Well Logs, Cores, and Outcrops: Association of Petroleum Geologists, Methods in Exploration 7, 55 p.

Vandenberghe, J., 2008. The fluvial cycle at cold–warm–cold transitions in lowland regions: A refinement of theory. Geomorphology 98 (3-4), 275–284.

Vanderberghe, J., Kasse, C., Bohncke, S., Kozarski, S., 1994. Climate-related river activity at the Weichselian- Holocene transition: a comparative study of the Warta and Maas rivers. Terra Nova 6, 476–485.

Veldkamp, A, van Dijke, J.., 2000. Simulating internal and external controls on fluvial terrace stratigraphy: a qualitative comparison with the Maas record. Geomorphology 33 (3-4), 225–236.

Veldkamp, A., Tebbens, L.A., 2001. Registration of abrupt climate changes within fluvial systems: insights from numerical modelling experiments. Global and Planetary Change 28, 129–144.

Vis, G.J., Kasse, C., Vandenberghe, J., 2008. Late Pleistocene and Holocene palaeogeography of the Lower Tagus Valley (Portugal): effects of relative sea level, valley morphology and sediment supply. Quaternary Science Reviews 27 (17-18), 1682–1709.

Walker, R.G. and Plint, A.G., 1992, Wave and storm-dominated shallow marine systems. In: Facies Models: Response to Sea-Level Change (Eds R.G. Walker and N.P. James), pp. 219–238. Geological Association of Canada, St John's, Newfoundland.

Walling D.E., 1983. The sediment delivery problem. Journal of Hydrology 65, 209–237.

Ward, P.J., 2008. River Meuse suspended sediment yield : a new estimate and past estimates revisited. Netherlands Journal of Geosciences 87 (2), 189–193.

Wegmann, K.W., Pazzaglia, F.J., 2009. Late Quaternary fluvial terraces of the Romagna and Marche Apennines, Italy: Climatic, lithologic, and tectonic controls on terrace genesis in an active orogen. Quat. Sci. Rev. 28, 137–165.

Weltje GJ, Meijer XD, de Boer PL. 1998. Stratigraphic inversion of siliciclastic basin fills: a note on the distinction between supply signals resulting from tectonic and climatic forcing. *Basin Research* **10** : 129–153.

Whipple KX, Kirby E, Brocklehurst SH. 1999. Geomorphic limits to climate-induced increases in topographic relief. *Nature 401* : 39–43.

Whipple KX, Tucker GE. 2002. Implications of sediment-flux-dependent river incision models for landscape evolution. Journal of Geophysical research **107**

Whipple KX. 2004. Bedrock rivers and the geomorphology of active orogens. *Annual Review of Planetary Sciences* **32** : 151-185.

Whipple, K. X., G. E. Tucker, 1999. Dynamics of the stream-power incision model: implications for height limit of mountain ranges, landscape response timescale and research needs. Journal of Geophysical research 104 (8), 14661–17674.

Whittaker AC, Attal M, Allen PA. 2010. Characterising the origin, nature and fate of sediment exported from catchments perturbed by active tectonics. *Basin Research* : 809–828.

Whittaker AC, Attal M, Cowie PA, Tucker GE, Roberts G. 2008. Decoding temporal and spatial patterns of fault uplift using transient river long profiles. *Geomorphology* **100** : 506–526.

Whittaker AC, Boulton SJ. 2012. Tectonic and climatic controls on knickpoint retreat rates and landscape response times. *Journal of Geophysical Research* **117** : 1–19.

Whittaker AC., Cowie PA, Attal M, Tucker GE, Whittaker AC, Cowie PA, Roberts GP. 2007. Contrasting transient and steady-state rivers crossing active normal faults : new field observations from the Central Apennines , Italy. *Basin Research*.

Wintle, A.G., Murray, A.S., 2006. A review of quartz optically stimulated luminescence characteristics and their relevance in single-aliquot regeneration dating protocols. Radiation Measurements 41, 369-391.

Wittmann, H., von Blanckenburg, F., 2009. Cosmogenic nuclide budgeting of floodplain sediment transfer. Geomorphology 109 (3-4), 246–256.

Zachos J, Pagani M, Sloan L, Thomas E, Billups K. 2001. Trends, rhythms, and aberrations in global climate 65 Ma to present. *Science* **292** : 686–93.

Zhang X, Drake N, Wainwright J. 2002. Scaling land surface parameters for global-scale soil erosion estimation. *Water Resources Research* **38** (9) : 1180

Web references

http:// topsoil.nserl.purdue.edu/ usle/ AH_537.pdf

http:// www.nae.usace.army.mil/ reg/ nrrbs/ chapters/ Chapter-08.pdf

http:// www.rijkswaterstaat.nl

http://edenz.niwa.co.nz/map/nz

http://www.ncdc.noaa.gov/paleo/icecore/greenland/ngrip/ngrip-data.html

TUTIEMPO.NET,
http://www.tutiempo.net/en/Climate/Gisborne_Aerodrome/01-1981/932910.htm

USDA, United States Department of Agriculture, Agricultural research service,
RUSLE, http://www.ars.usda.gov/Research/docs.htm?docid=5971

USGS Hydro1k Elevation Derivative Database,
http://eros.usgs.gov/#/Find_Data/Products_and_Data_Available/gtopo30/hydro

Royal Netherlands Meteorological Institute, KNMI, http://www.knmi.nl

SAGE, University of Wisconsin-Madison, http://www.sage.wisc.edu/riverdata/

SUMMARY

Summary

This thesis investigates the impact of climatic, tectonic, and sea-level changes (external forcing) on river systems (source-to-sink) and how these changes are recorded in the stratigraphic record. Investigating and quantifying this impact in present day river systems and sedimentary basins using numerical models and data from the field (e.g., outcrops) is fundamental for reconstructing geological history and for predicting the future evolution of river deltas. Furthermore, understanding the evolution of river systems is crucial for predicting stratigraphic architectures in the sub-surface, and hence for characterizing hydrocarbon reservoirs.

River systems are the key motor in transporting water and sediments from continents to the ocean. Tectonics, climate, and sea-level chance are the main controls on their evolution. It becomes increasingly difficult to quantify the impact of these controls the further back in geological time due to the uncertainty in boundary conditions and to the complexity of river system. This complexity is induced by the transient response of these systems to forcing and by sediment storage within the systems. Numerical models are useful tools to simulate present and past Earth's surface processes, and to understand how these processes operate/ operated. The level of complexity of models is a function of the uncertainty in boundary conditions and of the spatial/ temporal resolution of the desired output.

In chapters 2 and 3 the numerical model PaCMod is described. The model was developed to bridge the gap between simple spatially-lumped models and detailed, complex cellular models, by parameterizing the transient geomorphological response of fluvial systems to climatic and tectonic forcing and sediment storage within the catchment. PaCMod calculates long time series of water and sediment flux from any given catchment. The three dimensional morphology of a real catchment is collapsed into four model domains, where different processes occur and sediment is routed and temporarily stored. In the

second version of the model (Chapter 3), PaCMod was implemented with new routines to simulate the evolution of landscape morphology and erosion rates under tectonic and climatic forcing. Notwithstanding the high level of parameterization and the numerous assumptions used, the model is able to capture the first order non-linear response of a catchment to external forcing, caused by the interaction of processes operating at different spatial and temporal scales, and by feedback mechanisms. The modeled water and sediment flux outputs were validated using the Meuse River (Netherlands), the Waipaoa River (New Zealand), and the Po River (Italy) as test cases for climatic forcing and the Celano catchment (Italy) as a test case for tectonic forcing.

PaCMod simulations of the Celano catchment (Chapter 3) have shown that sediment and water storage within the catchment and the inertial response of landscapes (hillslopes, vegetation) to forcing hamper the transmission of external forcing out of the catchment, into the stratigraphic record. Modeling results using PaCMod and a stratigraphic model, 2Dstratsim, showed that long response times of hillslopes and fluvial channel to tectonics buffer the transmission of a tectonic signal to sediment flux and stratigraphy, whereas long response times to climate tend to amplify the climatic signal. Furthermore, catchment response time modulates sediment supply to basins and thus significantly affects shoreline trajectories, stratal architectures and grain size trends.

PaCMod was then applied to reconstruct the sedimentary history of a Late Quaternary river system, the Golo, France (Chapter 4). Modelling results, new sediment ages, topographic, sedimentological, and geophysical data acquired in the field indicate that the Golo response to climate and sea level variations was non-linear, as a result of catchment memory (sediment storage, ice storage in glaciers) and geomorphological thresholds (balance between sediment erosion and fluvial transport capacity). The Golo alluvial-coastal plain evolution was controlled by a complex interaction of millennial scale variations in sediment supply and sea level variations, and long-term tectonic-induced vertical movements. In particular, the proposed geomorphological reconstruction indicates that a large amount of coarse sediment was stored in the catchment during glacial phases, and it was consequently eroded and bypassed to the submarine fans during periods of lowest sea level stand.

Finally, an ancient deltaic system with poorly-constrained boundary conditions was investigated, the Panther Tongue delta, KSp040 parasequence, Star Point Sandstone, on the Wasatch Plateau (Utah, USA) (Chapter 5). The architecture and

the heterogeneities of this Cretaceous river delta were studied by means of outcrop observations, stratigraphic logs correlation, and petrological analysis of rock samples. The proposed interpretation indicates that the shallow marine deposits of the Ksp040 parasequence are subdivided into five bedsets which record progradation on the fluvial-dominated, downdrift flank of an asymmetric, wave-influenced delta and an adjacent wave-dominated strandplain. Bedset boundaries record erosion and/ or non-deposition in response to potentially linked changes in riverine sediment supply from the catchment, delta-lobe switch, longshore sediment transport to the south, variations in wave climate, and/ or minor changes in relative sea level. Pronounced but localised delta lobe progradation in the northern Wasatch Plateau reflects high sediment supply from fluvial point source(s) across a relatively shallow sea floor. More uniform and slower shoreface progradation in the southern Wasatch Plateau reflects relatively homogeneous supply of longshore-transported sediment across a relatively deep sea floor.

To conclude, this thesis describes a newly developed numerical tool to simulate the complex fluvial system sediment flux response to external forcing on a geological time scale. Numerical modelling simulations, combined with field data indicated that the late Quaternary evolution of the Golo River system (France) was controlled by a complex interaction of sea-level and climatic forcing. Stratigraphic analysis in the Panther Tongue delta (Utah) showed how different parts of an ancient shoreline reacted differently to the same changes in external forcing, which consequently, have a different stratigraphic expression along depositional strike.

SAMENVATTING

Dit proefschrift onderzoekt de invloed van klimatologische, tektonische, en zeeniveau veranderingen (externe forcing) op riviersystemen (source-to-sink) en hoe deze veranderingen worden geregistreerd in de stratigrafische archieven. Het onderzoeken van de effecten van deze veranderingen in zowel bestaande riviersystemen als sedimentaire bekkens met behulp van numerieke modellen en data uit het veld is van fundamenteel belang voor de reconstructie van de geologische geschiedenis en voor het voorspellen van de toekomstige evolutie van rivierdelta's. Begrip van de evolutie van rivier systemen is daarnaast cruciaal voor het voorspellen van de stratigrafische architectuur in de ondergrond en dus voor het karakteriseren van koolwaterstof reservoirs.

Riviersystemen zijn de belangrijkste motor van het transport van water en sedimenten van continenten naar de oceaan. Tektoniek, klimaat en zeespiegel zijn de belangrijkste factoren die hun evolutie bepalen. Het kwantificeren van de impact van deze factoren wordt steeds moeilijker naarmate we verder teruggaan in de geologische tijd vanwege de onzekerheid in de randvoorwaarden en de complexiteit van riviersystemen. Deze complexiteit wordt veroorzaakt door de respons van deze systemen op externe forcing en door sediment opslag in de systemen. Numerieke modellen zijn nuttige hulpmiddelen voor het simuleren van huidige en historische processen op het aardoppervlak en om te begrijpen hoe deze processen opereren of opereerden. De complexiteit van modellen is een functie van de onzekerheid in randvoorwaarden en de ruimtelijke / temporele resolutie van het gewenste resultaat.

In de hoofdstukken 2 en 3 wordt het numerieke model PaCMod wordt beschreven. Het model is ontwikkeld om de kloof tussen enerzijds eenvoudige, nul-dimensionele modellen en anderzijds gedetailleerde, complexe modellen te overbruggen door het parametriseren van de voorbijgaande geomorfologische respons van riviersystemen op klimatologische en tektonische veranderingen en van sediment opslag binnen het stroomgebied. PaCMod berekent lange tijdreeksen van water en sediment flux van een bepaald stroomgebied. De drie dimensionale morfologie van de stroomgebied wordt geparameteriseerd in vier model

domeinen, waar verschillende processen plaatsvinden en sediment wordt omgeleid en tijdelijk opgeslagen. In de tweede versie van het model (hoofdstuk 3), werd PaCMod geïmplementeerd met nieuwe routines om de evolutie van het landschap morfologie en erosie te simuleren onder tektonische en klimatologische forcing. Ondanks de hoge parameterizatie en de aannames, kan het model de eerste orde, niet-lineaire responsie van een stroomgebied op externe forcing simularen die veroorzaakt is door de interactie van processen die op verschillende ruimtelijke en temporele schalen werken en door terugkoppelingsmechanismen . De gemodelleerde water en sediment flux output zijn gevalideerd met de Maas (Nederland), de Waipaoa River (Nieuw-Zeeland), en de Po (Italië) als testcases voor klimatologische forcing en de Celano stroomgebied (Italië) als een testcase voor tektonische forcing.

PaCMod simulaties van de Celano stroomgebied (hoofdstuk 3) hebben aangetoond dat het sediment en waterberging in het stroomgebied en de infertiele reactie van landschappen (hillslopes, vegetatie) op forcing de overdracht van externe forcing uit het stroomgebied naar sedimentaire bekkens belemmeren. Model resultaten gegenereerd met PaCMod en een stratigrafische model "2Dstratsim", toonden aan dat een lange responstijd van hillslopes naar tektoniek de overdracht bufferen van een tektonische signaal naar sediment flux en stratigrafie, terwijl lange reactietijden op klimaat veranderingen de neiging hebben om de klimatologische signaal te versterken. Bovendien moduleren de reactietijden van rivier systemen het sediment transport naar sedimentaire bekkens en dus heeft een aanzienlijke invloed op kustlijn veranderingen, stratigrafische architecturen en korrelgrootte trends. PaCMod werd vervolgens toegepast op de reconstructie van de sedimentaire geschiedenis van een Laat-Quartair rivier systeem, de Golo, Frankrijk (hoofdstuk 4). Model resultaten, nieuwe sediment ouderdom, topografisch, sedimentologische en geofysische gegevens hebben getoond dat de reactie van de Golo klimaat en zeeniveau variaties non-lineair is als gevolg van stroomgebied geheugen (sediment opslag, ijs opslag in gletsjers) en geomorfologische drempelwaarden (balans tussen sediment erosie en binnenvaartvervoer capaciteit). De alluviale kustvlakte evolutie van de Golo werd bestuurd door een complexe interactie van duizendjarige schaal variaties in de aanvoer van sediment en zeespiegel variaties en door lange termijn tektonische-geïnduceerde verticale bewegingen. Met name de voorgestelde geomorfologische reconstructie geeft aan dat een grote hoeveelheid grof sediment werd opgeslagen in het stroomgebied tijdens glaciale fasen, en daarna werd uitgehold en doorgelaten naar diepzee fans tijdens perioden van laagste zeeniveau.

Tot slot, werd een oude deltaïsche systeem met slecht-gedefinieerde randvoorwaarden onderzocht, de Panther Tong delta, KSp040 parasequence, Star Point zandsteen, op de Wasatch Plateau (Utah, USA) (hoofdstuk 5). De architectuur en de heterogeniteit van deze rivierdelta uit het Krijt werden bestudeerd door middel van ontsluitingen, stratigrafische logs correlatie, en petrologische analyse van gesteente monsters. De voorgestelde correlatie geeft aan dat de ondiepe mariene afzettingen van de Ksp040 parasequence zijn onderverdeeld in vijf bedsets, die representeert progradatie van een rivier-gedomineerd, downdrift flank van een asymmetrische,-wave beïnvloed delta en een aangrenzende golf gedomineerde strandplain. Bedset grenzen representeren erosie en / of niet-depositie in reactie op potentieel verbonden veranderingen in riviergebieden sediment aanvoer vanuit het stroomgebied, (delta-lobe switch), sedimenttransport naar het zuiden parallel aan de kust, variaties in golfklimaat, en / of kleine veranderingen in de relatieve zeespiegel. Uitgesproken maar gelokaliseerde delta lobes progradatie in de noordelijke Wasatch Plateau weerspiegelt een hoge aanvoer van sediment uit fluviatiele puntbron (s) over een relatief ondiepe zeebodem. Gelijkmatiger en langzame vooroever progradatie in de zuidelijke Wasatch Plateau weerspiegelt relatief homogene levering van sediment getransporteerd langs de kust.

Tot slot, beschrijft dit proefschrift een nieuw ontwikkel algoritme om de complexe reactie van fluviatiele systemen op externe forcing op een geologische tijdschaal te simuleren. Numerieke model simulaties gecombineerd met veldgegevens hebben aangetoond dat de laat Quartair evolutie van het Golo rivier systeem (Frankrijk) werd bestuurd door een complexe interactie van de zeespiegel variaties en het klimaat forcing. Stratigrafische analyse in de Panther Tongue delta (Utah) heeft laten zien hoe de verschillende delen van een oude

CURRICULUM VITAE

Andrea Forzoni was born in Pistoia, Italy, on November 26 1985. He graduated from secondary school ITC Pacini, Pistoia, in 2004. Between 2004 and 2008 he studied at the faculty of Earth Sciences at the University of Florence for his Bachelor degree. After that, he studied Earth Sciences at the Vrije Universiteit Amsterdam and obtained his MSc degree in 2010 "with distinction". In 2010 Andrea started his PhD research entitled 'Untangling the sediment flux control on sedimentary basin stratigraphy' with the Applied Geology Group at the Delft University of Technology. The research was supervised by Dr Joep Storms (daily supervisor) and Prof. Stefan Luthi (Promotor). This research was funded by an NWO (Netherlands organization for scientific research) VIDI grant to Joep Storms. This research resulted in two published peer-reviewed papers, two papers submitted to international journals, and several conferences abstract. Andrea currently lives in the Hague and he is working as a post-doc at the Delft University of Technology.

ACKNOWLEDGMENTS

Tjerk, and Joorn, to my good friends David, Alessandro, Luca, Filippo, Sally, Caroline, Henriette, Lauri, Elisabeth, Elisa, Francesco.

Dear dad, mam and Annalisa thanks for your support, trust, and love. I could not have done this without you.

LIST OF PUBLICATIONS, CONFERENCE PROCEEDINGS AND ABSTRACTS

Publications

Forzoni A., Storms. J.E.A, Whittaker A.C., de Jager G. (2014). Delayed delivery from the sediment factory: Modeling the impact of catchment response time to tectonics on sediment flux and fluvio-deltaic stratigraphy. Earth Surface Processes and Landforms, 689-704.

van Balen R.T., Forzoni A., van Dam J.A. (2013). Active faulting and folding along the Jumilla Fault Zone, northeastern Betics, Spain. Geomorphology, in press.

Forzoni A., de Jager G., Storms J.E.A. (2013). A spatially lumped model to investigate downstream sediment flux propagation within a fluvial catchment. Geomorphology, 193, 65-80.

Conference proceedings and abstracts

Forzoni A., Hampson G.J., Storms J.E.A. (2014). Vertical and lateral heterogeneities in shallow marine reservoir analogues: the Panther Tongue (para)sequence, Utah. William Smith Meeting 2014. London, UK, The Geological Society of London.

Forzoni A., Storms J.E.A., Moreau J., Jouet G., Reimann T., de Jager G. (2014). Upstream versus downstream forcing: the response of the Golo River system, Corsica, to late Quaternary climatic and eustatic oscillastions. Nederlands aardwetenschappelijk congres 12.

Forzoni A., Storms J.E.A., Moreau J., Jouet G., de Jager G., Reimann T. (2013) The impact of Late Quaternary climate oscillations on the Golo River system, Corsica, France. American geophysical union fall meeting 2013, San Francisco.

Forzoni A., de Jager G., Storms J.E.A. (2012). Impact of external forcing and catchment response on sediment flux, EGU general assembly 2012.

Forzoni A., de Jager G., Storms J.E.A. (2012). External forcing and catchment response control on sediment flux. Nederlands aardwetenschappelijk congres 11.

Forzoni A., de Jager G., Storms J.E.A. (2011). An integrated source-to-sink model simulating sediment flux through a river system and fluvio-deltaic stratigraphy. Frontiers Meeting 2011. London, UK, The Geological Society of London.

Forzoni A., de Jager G., Storms J.E.A. (2011). An integrated source-to-sink model simulation sediment flux through a river system and fluvio-deltaic stratigraphy. EGU General Assembly 2011.